frontiers | Research Topics

Advances in geo-resources and geo-energy extraction and exploitation: Theories, technologies, and numerical simulation

Edited by
Yingfeng Sun, Yanan Gao
and Jianwei Tian

Published in
Frontiers in Earth Science

ISSN 1664-8714
ISBN 978-2-8325-4751-9
DOI 10.3389/978-2-8325-4751-9

About Frontiers

Frontiers is more than just an open access publisher of scholarly articles: it is a pioneering approach to the world of academia, radically improving the way scholarly research is managed. The grand vision of Frontiers is a world where all people have an equal opportunity to seek, share and generate knowledge. Frontiers provides immediate and permanent online open access to all its publications, but this alone is not enough to realize our grand goals.

Frontiers journal series

The Frontiers journal series is a multi-tier and interdisciplinary set of open-access, online journals, promising a paradigm shift from the current review, selection and dissemination processes in academic publishing. All Frontiers journals are driven by researchers for researchers; therefore, they constitute a service to the scholarly community. At the same time, the *Frontiers journal series* operates on a revolutionary invention, the tiered publishing system, initially addressing specific communities of scholars, and gradually climbing up to broader public understanding, thus serving the interests of the lay society, too.

Dedication to quality

Each Frontiers article is a landmark of the highest quality, thanks to genuinely collaborative interactions between authors and review editors, who include some of the world's best academicians. Research must be certified by peers before entering a stream of knowledge that may eventually reach the public - and shape society; therefore, Frontiers only applies the most rigorous and unbiased reviews. Frontiers revolutionizes research publishing by freely delivering the most outstanding research, evaluated with no bias from both the academic and social point of view. By applying the most advanced information technologies, Frontiers is catapulting scholarly publishing into a new generation.

What are Frontiers Research Topics?

Frontiers Research Topics are very popular trademarks of the *Frontiers journals series*: they are collections of at least ten articles, all centered on a particular subject. With their unique mix of varied contributions from Original Research to Review Articles, Frontiers Research Topics unify the most influential researchers, the latest key findings and historical advances in a hot research area.

Find out more on how to host your own Frontiers Research Topic or contribute to one as an author by contacting the Frontiers editorial office: frontiersin.org/about/contact

Advances in geo-resources and geo-energy extraction and exploitation: Theories, technologies, and numerical simulation

Topic editors

Yingfeng Sun — University of Science and Technology Beijing, China
Yanan Gao — China University of Mining and Technology, China
Jianwei Tian — Technical University of Denmark, Denmark

Citation

Sun, Y., Gao, Y., Tian, J., eds. (2024). *Advances in geo-resources and geo-energy extraction and exploitation: Theories, technologies, and numerical simulation*. Lausanne: Frontiers Media SA. doi: 10.3389/978-2-8325-4751-9

Table of contents

frontiers | Frontiers in Earth Science

TYPE Methods
PUBLISHED 13 January 2023
DOI 10.3389/feart.2022.1040464

OPEN ACCESS

EDITED BY
Xia Yan,
China University of Petroleum (East China), China

REVIEWED BY
Jinding Zhang,
China University of Petroleum (East China), China
Zhao Zhang,
Shandong University, China

*CORRESPONDENCE
Weiqiang Guo,
guoweiqiang95@163.com

SPECIALTY SECTION
This article was submitted to Economic Geology, a section of the journal Frontiers in Earth Science

RECEIVED 09 September 2022
ACCEPTED 20 October 2022
PUBLISHED 13 January 2023

CITATION
Liu G, Guo W, Fu E, Yang C and Li J (2023), Dynamic optimization of open-pit coal mine production scheduling based on ARIMA and fuzzy structured element.
Front. Earth Sci. 10:1040464.
doi: 10.3389/feart.2022.1040464

Dynamic optimization of open-pit coal mine production scheduling based on ARIMA and fuzzy structured element

Guangwei Liu[1], Weiqiang Guo[1]*, Ensan Fu[1,2], Chuanda Yang[3] and Jiaming Li[1]

[1]College of Mining Engineering, Liaoning Technical University, Fuxin, China, [2]Information Institute, Ministry of Emergency Management of the PRC, Beijing, China, [3]National Energy Investment Group Co. Ltd., Coal Branch, Beijing, China

A dynamic optimization method was created to address the production schedule issue in an open-pit coal mine while taking into account the characteristics of the fuzzy structured element. The fuzzy mining capacities of all "geologically optimal push-back bodies" were then examined using the moving cove method. One of the most crucial elements in the process of open-pit coal mine production scheduling optimization is coal pricing. As a result, this work also presents a dynamic optimization technique for production scheduling that incorporates the prediction of economic time series and the generation of dynamic economic indices. An appropriate time series model is created to forecast the future coal price based on previous data on coal prices. The prediction results are used in the calculation of optimal mining body generation to dynamically obtain the optimal production scheduling model. The Baorixile Open-pit Coal Mine in China's Inner Mongolia Autonomous Region is using this method. The Autoregressive Integrated Moving Average Model ARIMA is constructed to anticipate the coal price in the future 23 years by evaluating and processing the coal price from 2009 to 2022, and the ideal production scheduling scheme of the mine economics is afterwards identified. The ideal fuzzy coal mining volume, the potential production life, and the fuzzy total net present value (*NPV*) of the annual production scheduling are all provided at the same time. The optimization findings can better give fundamental support for mine design and future production since the fuzzy problem is accurately expressed by correct formulations.

KEYWORDS

open-pit coal mine, production schedule, fuzzy dynamic programming, fuzzy structured element, ARIMA

1 Introduction

A prominent place is held by open-pit coal mines in the worldwide coal industry. The share of open-pit coal mining in major coal-mining nations like the United States, Australia, Russia, and India is more than 50%, and some countries reach more than 90% (He et al., 2006; Zheng et al., 2014; Wang et al., 2022). The main objective of the OPCMPS is to choose a coal and waste rock extraction sequence that is technically viable and has the greatest possible total economic advantages. The term "technically feasible" refers to the OPCMPS having to adhere to a number of technical requirements; to maximize the entire *NPV* realized by deposit mining is to obtain the "greatest possible total economic advantages" (Ramazan, 2007; Osanloo et al., 2008; Khan and Niemann-Delius, 2018; Gilani et al., 2020; Fathollahzadeh et al., 2021). Saving non-renewable resources, safeguarding the ecosystem on which people depend for existence, and enhancing total economic gains throughout the mining life cycle are all greatly aided by the OPCMPS in the mine design (Nelson and Goldstern, 1980; Fytas, 1986; Chicoisne et al., 2012; Alipour et al., 2020). Therefore, the optimization design of OPCMPS has been extensively researched since the 1980s and 1990s (Caccetta and Hill, 2003; Bienstock and Zuckerberg, 2009; Boland et al., 2009).

The production scheduling issue has been the subject of much study effort by many professionals and academics. For short-term production scheduling: A multidestination mixed integer linear programming model for short-term open pit mine production scheduling was proposed by Eivazy and Askari-Nasab (2012). The model takes into consideration choices regarding buffer and blending stocks, horizontally directed mining, and ramps. It decreases the whole cost of mining operations, including extraction, processing, transporting, rehandling, and rehabilitation. The following items were presented by Blom et al. (2017): A tool for constructing multiple, diverse, short-term schedules that meet a variety of common objectives without the need for iterative parameter adjustment; and a novel concurrent rolling horizon-based algorithm for the generation of multiple distinct production schedules, each optimized concerning a series of objectives. Using hierarchical decomposition (HDP), Blom et al. (2018) introduced a unique hierarchical decomposition-based approach (HDP). It also provides an experimental comparison of this technique with a scheduling approach based on receding horizon controls. HDP may be used to solve any scheduling issue, not only those that arise in the mining industry. Upadhyay and Askari-Nasab (2018) provide a simulation-optimization framework/tool to take into account uncertainty in mining operations for reliable short-term production planning and proactive decision making. With the use of a goal programming-based mine operational optimization tool and a discrete event simulation model of mine operations, this framework/tool creates a short-term schedule based on uncertainty. For long-term production scheduling: Tolouei et al. (2021a) presented hybrid models to elucidate the long-term production scheduling problem regarding grade uncertainty, and the results show that the models generate a near-optimal solution within a reasonable time. The same year, due to the deterministic assumption and grade uncertainty, Tolouei et al. (2021b) proposed hybrid models that combine the Lagrangian relaxation (LR) approach with meta-heuristic techniques, the bat algorithm, and particle swarm optimization to solve the LTPSP. Utilizing meta-heuristic techniques, the Lagrange multipliers have been updated. The results from the case studies show that, in comparison to other strategies, the LR-bat algorithm hybrid approach may provide a solution that is near to optimum in terms of cumulative *NPV*, average ore grade, and computing time during a 12-years production period. Khan (2018) uses two distinct computationally effective population-based metaheuristic techniques, based on particle swarm optimization (PSO) and the bat algorithm, to solve one specific stochastic variant of the open pit mine scheduling problem, i.e., the two stage stochastic programming model with recourse for figuring out the long-term production schedule of an open pit mine under the condition of grade uncertainty. Turan and Onur (2022) improved cone extraction sequencing to ascertain the ultimate pit limit. Following that, a long-term production schedule was created utilizing the modified floating cone method's cone extraction approach and parametric analysis strategy. This method allows for the mining of ore blocks with the same annual production quantity throughout the course of each cycle.

Almost all of the above studies take metal open-pit mines as the research object. It can be found that a large number of researchers have focused their attention on the optimization of production scheduling in open-pit metal mines, but rarely on the optimization of production scheduling in open-pit coal mines. Therefore, Gu et al. (2011) proposed a dynamic sorting method for open-pit coal mines to simultaneously optimize the final pit and production scheduling of mines. The method can simultaneously solve the optimal final pit, mine life, annual recoverable amount of waste rock and coal, and mining sequence. Its flexibility is that it can easily incorporate constraints such as maximum strip ratio, maximum and minimum mining capacity. However, the preparation of an open-pit coal mine production plan should take into account the number of equipment, the number of personnel, the width of the security platform, and the production capacity of available equipment; the maximization of overall economic benefits should be based on the perspective of dynamic economics to maximize the total *NPV*. In actual production, due to the influence of equipment failure, inaccurate geological model caused by insufficient geological exploration, landslide of working slope, weather and other factors, the actual annual coal mining volume and stripping volume are uncertain and fuzzy, which will lead to the total *NPV* is also fuzzy. In the process of calculating the *NPV*, the coal price is often calculated with the

average value of coal price in recent years, without considering the variability of coal price. How to solve the reliability of economic parameters is also the key issue in the dynamic optimization of production scheduling. Therefore, based on the research of literature (Gu et al., 2011), this study proposes a dynamic optimization method of mine production scheduling based on fuzzy mining quantity and fuzzy stripping quantity of production plan determined by economic time series prediction production cost and coal sales price combined with the fuzzy structural element. The dynamic optimization of production scheduling considering economic variability and fuzzy stripping quantity is realized, and the fuzzy interval of maximum *NPV* is obtained. At the same time, the possibility of each value in the interval is given. The effectiveness of the method is verified by an example.

The following sections present the framework and application of the approach. Section 2 introduces the principle of fuzzy structure element; Section 3 explains the dynamic optimization method of geologically optimal mining limit and production scheduling described in the literature (Gu et al., 2011); Section 4 describes the principle of the price time series prediction method; Section 5 contains all the details and processes of the proposed method; To demonstrate the viability of the dynamic optimization approach suggested in this work, a real mine is used in Section 6; Section 7 presents the contribution of this paper to the research field and the characterization of the proposed method, and discusses the experimental results; And, finally, the conclusions are presented in Section 8.

2 Related theory of the fuzzy structured element

In 2002, Guo Sicong presented the fuzzy structure element analysis approach as a solution to the metadata fuzzy operation issue (GUO, 2002a; GUO, 2002b; GUO, 2009; Guo and Song, 2011). This article introduces the fuzzy structured element to achieve OPCMPS dynamic optimization. The basic concept, theorem, and properties of the fuzzy structured element are briefly introduced in this section.

2.1 Fuzzy structured element of the fuzzy number

2.1.1 Definition 1

Let E is a fuzzy set on the real number field R, and $E(x)$ represents the membership function of E, and $x \in R$. Then, E is called a fuzzy structured element on R, if

- $E(x) = 1$.
- $E(x)$ is a function of monotone increasing and right continuous on $[(-1, 0)$, monotone decreasing and left continuous on $(0, 1)]$.
- $E(x) = 0$, When $x \in (-\infty, -1)$ or $x \in (1, +\infty)$.

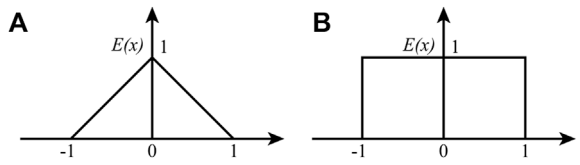

FIGURE 1
Fuzzy structured element. **(A)** Triangle structured element; **(B)**Rectangle structured element.

For example, E also is known as a triangle structured element, The graph membership function is shown in Figure 1A, if E has a membership function:

$$E(x) = \begin{cases} 1 + x, & -1 \le x \le 0 \\ 1 - x, & 0 \le x \le 1 \\ 0, & \text{otherwise} \end{cases} \tag{1}$$

Then E also known as a rectangle structured element, the graph membership function is shown in Figure 1B, if E has a membership function:

$$E(x) = \begin{cases} 1, & -1 \le x \le 1 \\ 0, & \text{otherwise} \end{cases} \tag{2}$$

2.1.2 Definition 2

E is called a canonical fuzzy structural element, if E satisfies the following conditions:

- $\forall x \in (-1, 1)$, $E(x) > 0$.
- $E(x)$ is a function of strictly increasing monotonically and continuous on $[(-1, 0)$, strictly decreasing monotonically and continuous on $(0, 1)]$.

Then, E is called a symmetric fuzzy structural element. if $E(x) = E(-x)$.

2.1.3 Theorem 1

Let E be a fuzzy structured element and $E(x)$ is its membership function, the function $f(x)$ is continuous and monotone on $[-1,1]$, then $f(E)$ is a fuzzy number, and the membership function of $f(E)$ is $E(f^{-1}(x))$, (where $f^{-1}(x)$ is rotational symmetry function for variable x and y, if f is a strictly monotone function, then $f^{-1}(x)$ is the inverse function of $f(x)$).

2.1.4 Theorem 2

For a given canonical fuzzy structured element E and any finite fuzzy number A, there always exists a monotone bounded function $f(x)$ on $[-1,1]$, having the form $A = f(E)$, and $u_{A\sim}(x) = E(f^{-1}(x))$.

2.1.5 Character 1

Let A and B are fuzzy numbers generated linearly by the fuzzy structure element E. Let $A = a + \alpha E$, $B = b + \beta E$, then, $A + B = (a+b) + (\alpha+\beta)E = c + \gamma E$, $u_{A+B}(x) = E(\frac{x-c}{\gamma}) = E(\frac{x-(a+b)}{\alpha+\beta})$; $kA = ka + k\alpha E$; $u_{kA}(x) = E(\frac{x-ka}{k\alpha})$

2.2 Fuzzy numbers structured element weighted order

2.2.1 Definition 3

Let $A, B \in N_{\sim c}(R)$, $A = f(E)$, $B = g(E)$, E is a canonical fuzzy structure element, $E(x)$ is a membership function. f and g are the same ordered monotonic functions of membership on $[-1, 1]$. Then the relation "$\lesssim$" determined by Eq. 3 is the fuzzy numbers structured element weighted order.

$$A \lesssim B \Leftrightarrow F(A, B) = \int_{-1}^{1} E(x)(f(x) - g(x))dx \le 0 \quad (3)$$

Let A is a triangular fuzzy number, $A = (a; a^-, a^+)$ for short, if the membership function of the fuzzy number A is:

$$E(x) = \begin{cases} \dfrac{x - a + a^-}{a^-}, & a - a^- \le x \le a \\ \dfrac{a + a^+ - x}{a^+}, & a \le x \le a + a^+ \\ 0 & \text{otherwise} \end{cases} \quad (4)$$

2.2.2 Theorem 3

If $A = (a; a^-, a^+)$ and $B = (b; b^-, b^+)$ are fuzzy numbers, then E is the triangular fuzzy structural element, then:

$$A \lesssim B \Leftrightarrow a + \frac{a^+ - a^-}{6} \le b + \frac{b^+ - b^-}{6} \quad (5)$$

The proof of the above theorems can be found in References (Caccetta and Hill, 2003; Bienstock and Zuckerberg, 2009; Boland et al., 2009; Eivazy and Askari-Nasab, 2012).

3 Geologically optimum final pits and their dynamic programming

The highest coal amount among all final pits with volume V in the mining region where the working slope angle does not exceed β is referred to as the geologically optimum final pit. The final pit optimization of OPCMPS is based on the pre-designed annual total mining volume (the sum of the coal mining volume and the stripping volume), and it is based on the corresponding mining parameters to determine the optimal state of the end of every year, which is the state of maximum coal volume in the same mining volume. So it is also possible to achieve the ideal coal mining and stripping volumes. There are multiple states in the mining areas that meet the annual mining volume. It is naturally known that the maximum coal mining volume in the total mining volume that meets the requirements should be the optimization, that is, the OPCMPS that meets the technical feasibility and the maximum total *NPV* should be found from a series of geological optimum mining pits, and the total *NPV* is related to the coal mining volume, stripping volume and mining cost.

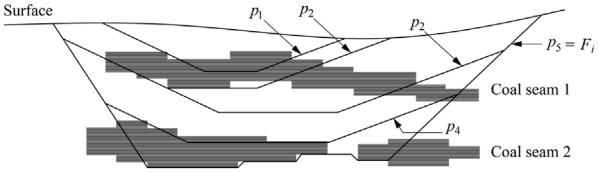

FIGURE 2
Push-backs in a final pit.

Therefore, according to the thought of the Reference (Gu et al., 2011), it is assumed that M geological optimum mining pits are obtained in final pits, i.e., $\{p\}_m = \{p_1, p_2, \ldots, p_m\}$, where p_1 is the smallest pit and p_m is the largest pit, each element in the sequence may be the optimum one. As shown in Figure 2.

- Stage decision variables: in the state p_i, the coal volume is q_i and the stripping volume is w_i.
- State variables: $s(t, i)$ represents the i state of the t stage, corresponding to the kth mining body of $\{p\}_m$. $S(t\text{-}1, i)$ represents the j state of the t-1 stage, corresponding to the kth mining body of $\{p\}_m$.
- State transition equation: let the coal content of the first k mining bodies be q_k and the stripping amount be w_i.
- Objective function: the state transfer profit of each stage is:

$$G_{(t,i)}^{(t-1,j)} = (p_t - c_t)q_{(t,i)}^{(t-1,j)} - b_t w_{(t,i)}^{(t-1,j)} - z_t\left(q_{(t,i)}^{(t-1,j)} + w_{(t,i)}^{(t-1,j)}\right) \quad (6)$$

Where p_t is the unit coal price in stage t, c_t is the unit coal mining cost in stage t, b_t is the unit stripping cost in stage t.

NPV refers to the sum of the annual net cash flow by the industry to the base year present value at the beginning of the calculation period in the economic or physical life cycle of the project. When $NPV \ge 0$, the project is feasible, and when $NPV \le 0$, the project is not feasible. *NPV* is a relatively scientific evaluation method of investment scheme. After the time attribute of the ore block and the ore price at corresponding time points are known, the *NPV* of the boundary scheme can be

calculated according to the concept of *NPV*. According to economic theory, the total *NPV* should be used as the standard to evaluate the subsequence profit of mining bodies. In view of this, let the maximum *NPV* from state 0 to state $s(t-1,\ j)$ be $NPV_{(t-1,j)}$, and transfer to state $s(t,\ i)$ be $NPV_{(t,j)}$, then:

$$NPV_{(t,i)} = \max_{j\in J(t,i)}\left\{NPV_{(t-1,j)} + \frac{G_{(t,i)}^{(t-1,j)}}{(1+d)^t}\right\} \tag{7}$$

Where $J(t,\ i)$ is the decision set, which represents a state set of state $s(t,\ i)$ that may be transferred from stage t-1 to the next stage.

4 Price time series prediction method

Given the dominant position of coal in China's energy market, fluctuating coal prices not only determine the survival of coal enterprises but also directly affects economic growth, energy security and industrial raw material supply (Li and Lin, 2017; Jiang et al., 2018; Wang et al., 2020; Zhang et al., 2020; Liu, 2021). Therefore, this paper combines economic time series with production scheduling optimization for the first time. Oskar Morgenstern, German Realmist (Clements and Hendry, 1998), first systematically discussed the method of economic forecasting in 1928. Box et al. (2015) proposed the famous Auto-Regressive Moving Average (ARMA) model in 1976, and then Harvey (1990) and Hendry and Doornik (1994) improved it. Auto-Regressive Integrated Moving Average (ARIMA) model is a well-known statistical technique for predicting time series. Numerous studies have demonstrated that the ARIMA model is effective in predicting outcomes in linear time series analysis with high levels of accuracy (Contreras et al., 2003; Li, 2021). Its benefits include a straightforward model and the absence of any additional exogenous variables. There are certain restrictions, though. For example, the time series data must be steady or stable after differential differentiation. In essence, it only detects linear correlations and ignores nonlinear ones. Comparing the ARIMA model to approaches like machine learning, its simplicity may assure the efficiency in the dynamic optimization process of open-pit coal mine production scheduling. The ARIMA model's forecast accuracy matches the necessary forecasting criteria. The model can be expressed as ARIMA (p, d, q), where p is the autoregressive order, d is the different order, and q is the moving average order. When $d = 0$, the model can be expressed as ARMA (p, q), namely the autoregressive moving average model; but when p, d, and q are not equal to 0, the model is expressed as ARIMA (p, d, and q), that is, the autoregressive summation moving average model. ARIMA (p, q) model refers to the linear function that the time series can be expressed as the current and previous random error term and the previous value, and its expression is shown in Eq. 8, where y_t is the time series; θ is the moving average coefficient; φ is a self-regression coefficient; u_t is an independent white noise sequence, and obeys the normal distribution with a mean value of 0 and variance of σ_u^2.

$$y_t = \varphi_1 y_{t-1} + \varphi_2 y_{t-2} + \cdots + \varphi_p y_{t-p} + u_t - \left(\theta_1 u_{t-1} + \theta_2 u_{t-2} + \cdots + \theta_p u_{t-p}\right) \tag{8}$$

ARIMA (p, d, q) is a random sequence model with a d-order difference of time series, its expression is shown in Eq. 9, where B^k is a delay operator and can be expressed as y_{t-k}/y_t.

$$y_t = \frac{\left(1-\theta_1 B-\theta_2 B^2-\ldots-\theta_q B^q\right)u_t}{1-\varphi_1 B-\varphi_2 B^2-\ldots-\varphi_p B^p} \tag{9}$$

Time series prediction analysis mainly includes the following steps:

Step-1. Sequence autocorrelation and partial correlation analysis

The simple correlation between each sequence value that constitutes a time series is called autocorrelation, and the autocorrelation coefficient r_k is calculated by Eq. 10, where n is the sample size, k is the lag period, and $\bar{y}$ is the arithmetic mean of the sample data.

$$r_k = \frac{\sum_{j=1}^{n-k}(y_1-\bar{y})(y_{t+k}-\bar{y})}{\sum_{j=1}^{n}(y_t-\bar{y})^2} \tag{10}$$

Partial autocorrelation refers to the conditional correlation between y_t and y_{t-k} under the given conditions of y_{t-1}, y_{t-2}, …, y_{t-k+1} for time series y_t. The partial autocorrelation coefficient is calculated by Eq. 11. When k=1, a=b.

$$\varphi_{kk} = \frac{r_k - \sum_{j=1}^{k-1}\varphi_{k-1,j}r_{k-j}}{1-\sum_{j=1}^{k-1}\varphi_{k-1,j}r_j} \tag{11}$$

The autocorrelation and partial autocorrelation of sequences are an important basis for judging the stability of sequences and selecting the type and order of prediction models.

Step-2. Model-based parameter estimation

The commonly used model parameter estimation methods include Yule-Walker correlation moment estimation, least-squares estimation, maximum likelihood estimation and entropy estimation methods. The first method is mainly for the AR model, and the second method is generally for the MA model. The mixture of the two methods can be used for the ARMA model.

Step-3. Predictive analysis

Time series prediction refers to the prediction of future y_{t+l} $(l>0)$ in $t+l$ period if y_t is known. Since the time t is known, the predicted value of y_{t+l} can be called the first step prediction starting from the time t. It is stated that to obtain the best prediction effect, the mean square error between the predicted value and the true value y_{t+l} is required to be minimized, that is, to minimize $E[y_{t+l}-\hat{y}_l]^2$. The predicted minimum variance is obtained from the conditional expectation of y_{t+l}, that is, $\hat{y}_l(l)=E(y_{t+l}|y_t, y_{t-1}, \cdots\cdots)$. Therefore, as long as the model of y_t is established, $\hat{y}_l(l)$ can be derived. The reversal form of ARMA prediction is shown in Eq. 12, that is, the predicted value $\hat{y}_l(l)$ is the linear combination of all the data at present and in the past, and the coefficient w_j is determined by the inverse function.

$$\hat{y}_t(l)=\sum_{j=1}^{\infty} w_j y_{t+1-j} \tag{12}$$

5 Dynamic sequencing of geological optimum final pit based on structure element theory

Annual actual coal mining and stripping values tend to fluctuate around planned values because they have uncertainty in production. Therefore, the maximum total net present value OPCMPS should be made in the final mining pit, and the annual coal mining and stripping should be regarded as fuzzy numbers. Since the fuzzy number represented by the fuzzy structured element can avoid the complex traversal problem based on the traditional expansion principle in the operation process, the fuzzy structured elements are used to represent the fuzzy coal mining volume and the fuzzy stripping volume.

Let q_i is the fuzzy coal mining volume in state i, w_i is the fuzzy stripping volume in state i, and they are linearly generated by symmetric fuzzy structured elements. Let $q\_i=a_i+b_iE$, $w\_i=c_i+d_iE$, then $f(x)$ and $g(x)$, two same ordered monotonic functions, can be found on $[-1, 1]$ through Theorem 1. Let $f_i(x)=a_i+b_ix$, $g_i(x)=c_i+d_ix$, $q\_i=f_i(E)$ and $w\_i=g_i(E)$. So, in the process of state transferred of state $s(t-1, j)$ to $s(t, j)$ from stage t-1to stage t, the analytic expression of each index generated by the liner structured element is as follows:

(1) The fuzzy coal mining volume is:

$$\underset{\sim}{q}_{(t,i)}^{(t-1,j)}=q\_k-q\_n=f_k(E)-f_n(E)=(a_k-a_n)+(b_k-b_n)E \tag{13}$$

Its membership function is:

$$u_{\underset{\sim}{q}_{(t,i)}^{(t-1,j)}}(x)=E\left(\left(f_k+f_n^{\tau 1}\right)^{-1}(E)\right)=E\left(\frac{x+a_n-a_k}{b_k+b_n}\right) \tag{14}$$

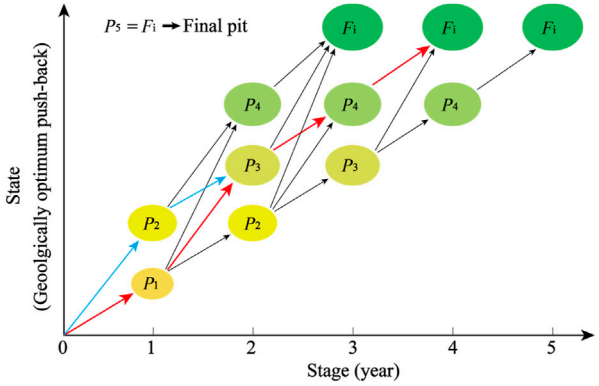

FIGURE 3
The dynamic programming scheme for push-back.

(2) The fuzzy stripping volume is:

$$\begin{aligned}\underset{\sim}{w}_{(t,i)}^{(t-1,j)}&=w\_k-w\_n=g_k(E)-g_n(E)\\&=(c_k-c_n)+(d_k+d_n)E\end{aligned} \tag{15}$$

Its membership function is:

$$u_{\underset{\sim}{q}_{(t,i)}^{(t-1,j)}}(x)=E\left(\left(g_k+g_n^{\tau 2}\right)^{-1}(E)\right)=E\left(\frac{x+c_n-c_k}{d_k+d_n}\right) \tag{16}$$

(3) The fuzzy state transferred profit is:

$$\begin{aligned}\underset{\sim}{G}_{(t,i)}^{(t-1,j)}&=p_t\underset{\sim}{q}_{(t,i)}^{(t-1,j)}-c_t\underset{\sim}{q}_{(t,i)}^{(t-1,j)}-b_t\underset{\sim}{w}_{(t,i)}^{(t-1,j)}-z_t\left(\underset{\sim}{q}_{(t,i)}^{(t-1,j)}+\underset{\sim}{w}_{(t,i)}^{(t-1,j)}\right)\\&=(p_t-c_t-z_t)[(a_k-a_n)+(b_k+b_n)E]-(b_t+z_t)[(c_k-c_n)\\&\quad+(d_k+d_n)E]\end{aligned} \tag{17}$$

Its membership function is:

$$\begin{aligned}u_{\underset{\sim}{G}_{(t,i)}^{(t-1,j)}}(x)&=E\left(\left((p_t+c_t+z_t)\left(f_k-f_n^{\tau_1}\right)^{-1}(E)\right)\right.\\&\quad\left.+(b_t+z_t)\left(\left(g_k+g_n^{\tau_2}\right)^{-1}(E)\right)\right)\\&=E\left(\frac{x+(c_t+z_t-p_t)(a_k-a_n)+(b_t+z_t)(c_k+c_n)}{(p_t+c_t+z_t)(b_k+b_n)+(b_t+z_t)(d_k+d_n)}\right)\end{aligned} \tag{18}$$

(4) Accordingly, the fuzzy NPV transferred to the state $s(t, i)$ is:

$$\underset{\sim}{NPV}_{(t,i)}=\max_{j\in J_{(t,i)}}\left\{\underset{\sim}{NPV}_{(t-1,j)}+\frac{\underset{\sim}{G}_{(t,i)}^{(t-1,j)}}{(1+d)^t}\right\} \tag{19}$$

Its membership function is:

$$u_{\underset{\sim}{NPV}_{(t,i)}}(x)=\max_{j\in J_{(t,i)}}\left\{u_{\underset{\sim}{NPV}_{(t-1,j)}}(x)+\frac{u_{\underset{\sim}{G}_{(t,i)}^{(t-1,j)}}(x)}{(1+d)^t}\right\} \tag{20}$$

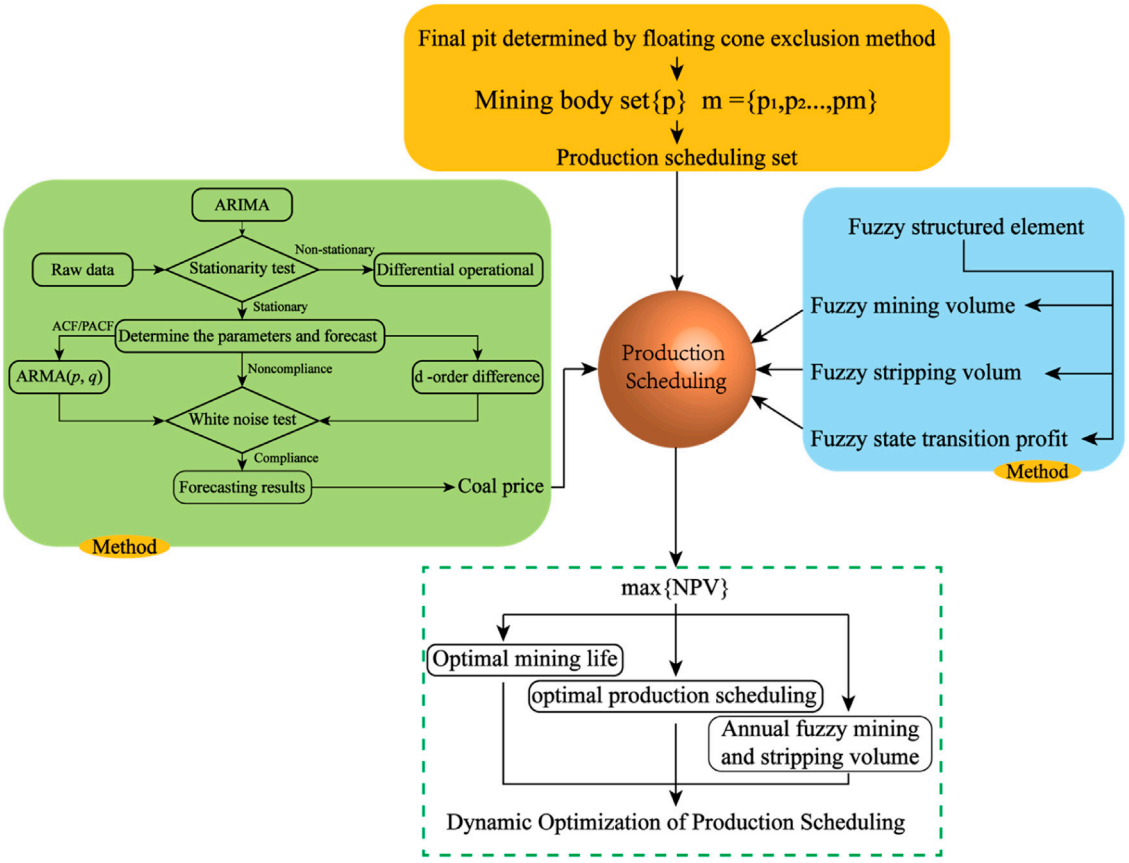

FIGURE 4
Dynamic optimization of OPCMPS flow.

To explain the solving process of the model, take Figure 2 as an example for a brief illustration. It can be seen from Figure 2 that 5 geologically optimum pits are produced in the final mining pit, and the possible state transferred mode is shown in Figure 3 (In the actual calculation, tens or hundreds or even more optimum mining pits will be produced. Therefore, a state transferred mode should be drawn base on the actual situation.). Suppose that a sequence of 5 geologically optimum push-backs within a geologically optimum pit F_i has been generated as shown by p_1 to p_5 in Figure 2. A dynamic programming scheme is set up as shown in Figure 3. The horizontal axis of Figure 3 represents stages with each stage being a planning period (usually a year). The number of stages is equal to the number of push-back volumes, represented by circles. The states of each stage are the push-backs in ascending order of push-back volume, represented by circles. The two states of stage 1 are push-backs p_1 and p_2, which means that at the end of the first year, the working slope may be mined (pushed) to p_1 or p_2. The last state (push-back) and the number of states for a stage depend on the constraint on the maximum yearly production capacity.

If the fuzzy *NPV* of path $\{p_0 \rightarrow p_1 \rightarrow p_3 \rightarrow F_i\}$ in Figure 3 is the largest, the order of states on the path represents the optimal OPCMPS, and it can be seen that:

- The mining life is 3 years (the end of the third year push to the final mining final pit F_i.)
- State sequence. Push-back to state p_1 at the end of the first year; Push-back to state p_3 at the end of the second year; And push-back to state p_5 at the end of the third year.
- Through Eq. 13, it can be obtained that the fuzzy coal mining volume at the end of the 1st, 2nd, and 3rd year are $q\sim1$, $q\sim3 - q\sim1$ and $q\sim5 - q\sim3$ respectively. It can be obtained through Eq. 15 that the fuzzy stripping volume at the end of the 1st, 2nd, and 3rd year are $w\sim1$, $w\sim3 - w\sim1$ and $w\sim5 - w\sim3$ respectively. Similarly, the fuzzy profit and the fuzzy *NPV* of state transferred can be obtained by using Eqs. 17, 19 respectively. Finally, the flow chart of the dynamic optimization of OPCMPS with the proposed method is shown in Figure 4.

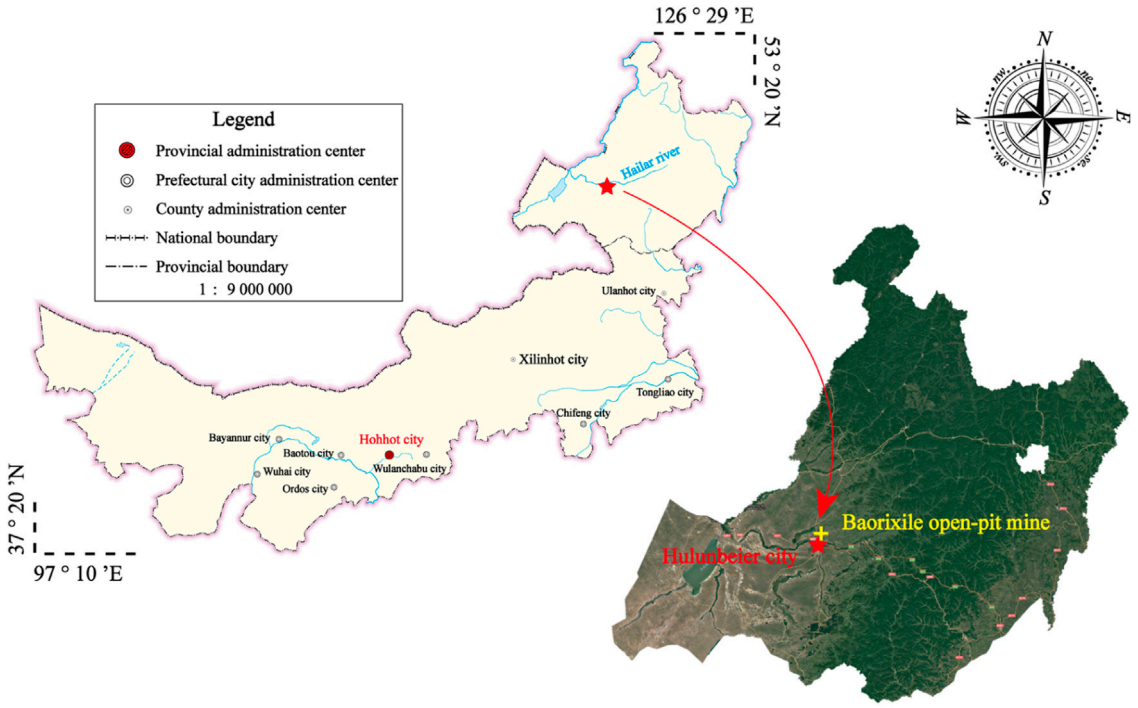

FIGURE 5
The location of the Baorixile open-pit mine.

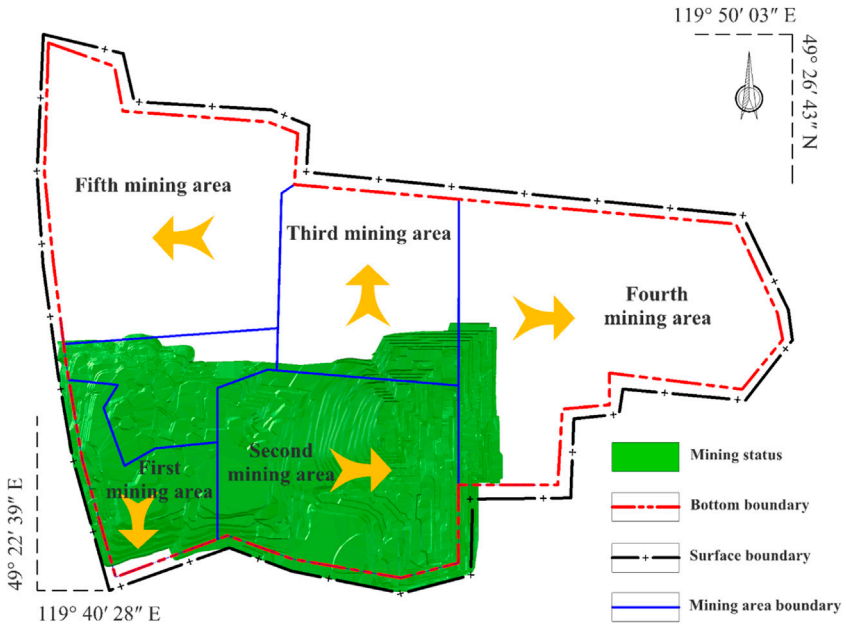

FIGURE 6
The mining area division of the Baorixile open-pit coal mine.

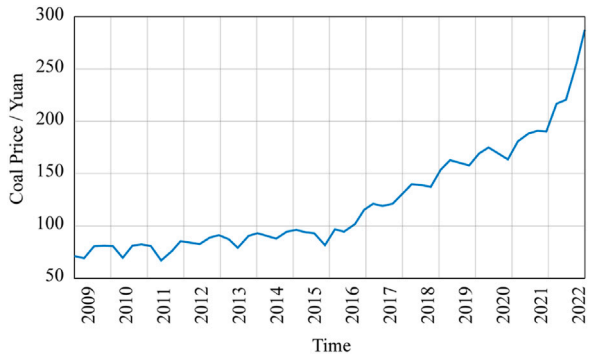

FIGURE 7
Coal price (2009Q1-2022Q2).

6 Application of the proposed optimization approach to a large open-pit coal mine

6.1 Case background

The Chenbaerhuqi coal field in Hulunbuir City, Inner Mongolia Autonomous Region of China, is where the Baorixile open-pit mine is situated (as shown in Figure 5). The mine's external perimeter spans a 50.72 km^2 region, measuring 5.86 km in width from north to south and 10.98 km in length from east to west. The mining adopts semi-continuous technology of single bucket excavator—dump truck—semi-fixed crushing station—belt conveyor, the stripping adopts discontinuous technology of

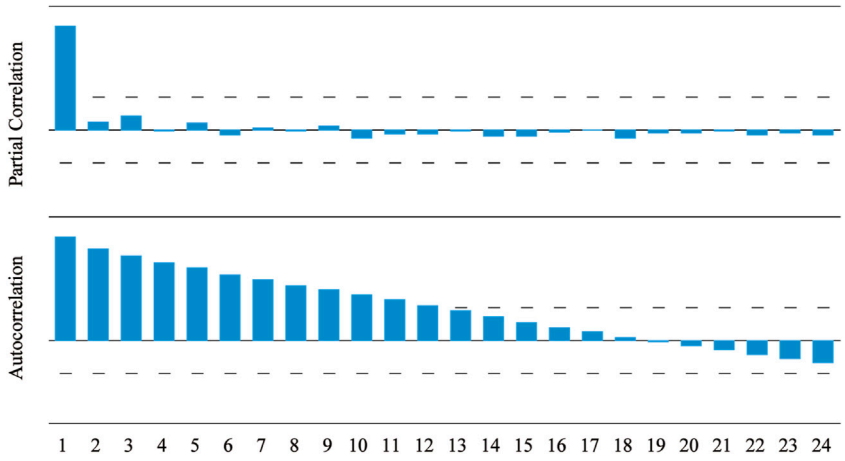

FIGURE 8
Stationarity test of the coal price time series.

TABLE 1 Autocorrelation and Partial Correlation coefficient of the coal prices series.

Number	Autocorrelation	Partial correlation	Prob	Number	Autocorrelation	Partial correlation	Prob
1	0.870	0.870	0.000	13	0.249	−0.014	0.000
2	0.774	0.072	0.000	14	0.203	−0.055	0.000
3	0.717	0.12	0.000	15	0.153	−0.051	0.000
4	0.655	−0.011	0.000	16	0.109	−0.024	0.000
5	0.609	0.058	0.000	17	0.075	0.002	0.000
6	0.555	−0.046	0.000	18	0.031	−0.07	0.000
7	0.508	0.018	0.000	19	−0.010	−0.028	0.000
8	0.466	−0.014	0.000	20	−0.048	−0.029	0.000
9	0.433	0.037	0.000	21	−0.081	−0.014	0.000
10	0.387	−0.068	0.000	22	−0.115	−0.045	0.000
11	0.337	−0.038	0.000	23	−0.149	−0.027	0.000
12	0.291	−0.037	0.000	24	−0.184	−0.046	0.000

TABLE 2 The unit root test of first-order difference sequence.

Null hypothesis: D (PRICE) has a unit root

Exogenous: Constant

Lag length: 3 (automatic—based on SIC, maxlag=10)

		t-Statistic	Prob.*
Augmented Dickey-Fuller test statistic		1.065629	**0.9967**
Test critical values	1% level	−3.571310	
	5% level	−2.922449	
	10% level	−2.599224	

Prob.*, indicates emphasis. The size of the Prob.* value reflects the stability of the data series.

TABLE 3 The unit root test of second-order difference sequence.

Null hypothesis: D (PRICE,2) has a unit root

Exogenous: constant

Lag length: 2 (automatic—based on SIC, maxlag=10)

		t-Statistic	Prob.*
Augmented dickey-fuller test statistic		−9.583848	**0.0000**
Tesactt critical values	1% level	−3.571310	
	5% level	−2.922449	
	10% level	−2.599224	

Prob.*, indicates emphasis. The size of the Prob.* value reflects the stability of the data series.

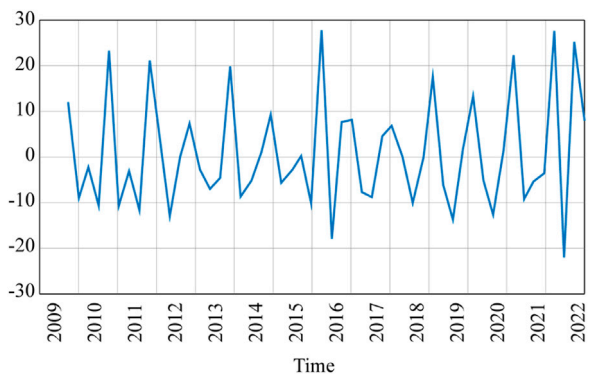

FIGURE 9
Second-order difference results of coal price time series.

single bucket excavator—dump truck—bulldozer. The whole open-pit mine is split into 5 mining regions based on careful consideration of the immediate economic advantages, long-term development of the open-pit mine, and the relationship between production continuity across mining areas. Figure 6 shows each mining area's location and mining order. There are a total of five near-horizontal coal seams that can be mined. The coal volume still recoverable as of 31 December 2021, is 860.66 Mt. Baorixile open-pit coal mine has completed the mining task of the second mining area, and is making a production transition to the third mining area and the fourth mining area. However, during the turning period of the mining area, it is faced with the problem of difficult production connections. It is necessary to carry out a reasonable life cycle OPCMPS task based on the current situation.

6.2 Time series prediction of coal price parameters

ARIMA model refers to the model established by transforming non-stationary time series into stationary time series and then regressing the lag value of a dependent variable with the current value and lag value of the error term. The actual historical coal sales prices of the mine from the first quarter of 2009 to the second quarter of 2022 were gathered as the basic data for the time series prediction analysis of coal sales prices through coordination and communication with the staff of the Zhanihe Open-pit Coal Mine's production technology department. The coal price sequence is shown in Figure 7, and determines whether the sequence is stable.

It can be seen from Figure 7 that the change in coal price fluctuates seasonally, and its trend is rising. The time series of prices does not have the characteristics of zero mean, and its variance is constantly changing, so it can be preliminarily determined that the time series of coal price is unstable.

In Figure 8; Table 1, it can be found that the decline rate of the autocorrelation coefficient is very slow. The autocorrelation coefficient before the 13 period is always outside the confidence interval. The partial autocorrelation coefficient decreases greatly after the first lag period and is not statistically significant. The autocorrelation coefficient value CA and the partial autocorrelation coefficient value CPA do not appear truncation and tailing, which further illustrates that the coal price time series is non-stationary.

The differential processing of coal price time series is to eliminate the fluctuation and the dependence on time, so that the data tends to be stable. The unit root test results after differential processing are shown in Tables 2, 3. After the first-order difference, the unit root test is performed, and the results show that there is a unit root, and $p>0.05$. The first-order difference sequence is unstable. After the second-order difference, the unit root test is performed, and the results showed no unit root and the $p<0.05$. After the second-order difference sequence is stable. Therefore, I = 2 in the ARIMA model.

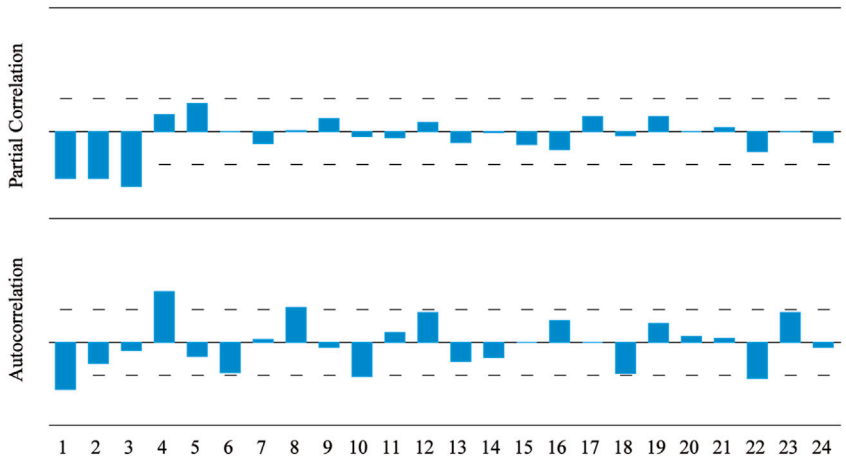

FIGURE 10
Stationarity test of the Second-order difference results.

TABLE 4 Autocorrelation and Partial Correlation coefficient of the Second-order difference results.

Number	Autocorrelation	Partial correlation	Prob	Number	Autocorrelation	Partial correlation	Prob
1	−0.401	−0.401	0.003	13	−0.162	−0.093	0.000
2	−0.174	−0.399	0.005	14	−0.124	−0.014	0.000
3	−0.071	−0.467	0.013	15	0.003	−0.110	0.000
4	0.432	0.140	0.000	16	0.188	−0.151	0.000
5	−0.122	0.232	0.000	17	0.005	0.123	0.000
6	−0.252	−0.002	0.000	18	−0.255	−0.034	0.000
7	0.027	−0.100	0.000	19	0.160	0.130	0.000
8	0.287	0.016	0.000	20	0.055	0.005	0.000
9	−0.047	0.115	0.000	21	0.035	0.037	0.000
10	−0.282	−0.041	0.000	22	−0.300	−0.168	0.000
11	0.086	−0.050	0.000	23	0.250	0.008	0.000
12	0.253	0.076	0.000	24	−0.043	−0.097	0.000

Figure 9 shows that the second-order difference sequence is a stationary sequence with zero mean and variance. In Figure 10; Table 4, it can be seen that the image of the partial autocorrelation coefficient starts from $p = 4$, suddenly approaches the centre line, and hovers on both sides of the zero value. Therefore, it can be preliminarily concluded that the p is obtained on the (He et al., 2006; Wang et al., 2022). Similarly, through the change trend of the autocorrelation coefficient, it can be basically determined that the q is obtained on the (Ramazan, 2007; Wang et al., 2022), which can constitute ARIMA (1,2,1), ARIMA (1,2,2), ARIMA (1,2,3), ARIMA (1,2,4), ARIMA (2,2,1), ARIMA (2,2,2), ARIMA (2,2,3), ARIMA (2,2,4), ARIMA (3,2,1), ARIMA (3,2,2), ARIMA (3,2,3), ARIMA (3,2,4) these 12 models. Then by comparing the AIC, SC, MAPE and RMSE of each ARIMA model, an optimal coal price forecasting model is determined.

Table 5 shows that the ARIMA (2, 2, 1) model has the largest corrected Adjusted-R^2 and the smallest AIC, SC, MAPE, and RMSE. Therefore, ARIMA (2, 2, 1) is tentatively used as the prediction model of coal price. However, coal price has some seasonal fluctuations, the difference needs to lag 4 to eliminate the impact of seasonal fluctuations. The calculated results are shown in Table 2.

Table 6 shows that the ARIMA (1, 2, 4) model has the highest corrected Adjusted-R^2 and the lowest AIC, SC, MAPE, and RMSE values across all models. Therefore, ARIMA (1, 2, 4) is used as the prediction model of coal price.

Figure 11 shows that the effect of using this model to predict the coal price is better, but the effect of short-term prediction will be better. The ARIMA model only considers the characteristics of the coal price time series itself, without considering the influence of some uncertain factors. With the extension of the test time, the prediction error of the model will also increase. Therefore, with the

TABLE 5 The parameter comparison of each model's test index.

Index	ARIMA (1,2,1)	ARIMA (1,2,2)	ARIMA (1,2,3)	ARIMA (1,2,4)	ARIMA (2,2,1)	ARIMA (2,2,2)	ARIMA (2,2,3)	ARIMA (2,2,4)	ARIMA (3,2,1)	ARIMA (3,2,2)	ARIMA (3,2,3)	ARIMA (3,2,4)
Adjusted-R^2	0.351697	0.352447	0.139293	0.311184	**0.394786**	0.279782	0.066860	0.151594	0.356335	0.001429	0.094755	0.151327
AIC	7.514608	7.513726	7.784217	7.573689	**7.449272**	7.696297	7.869510	7.776217	7.507592	7.928901	7.898818	7.779057
SC	7.627180	7.626297	7.896789	7.686260	**7.561843**	7.808869	7.982082	7.888789	7.620164	8.041473	8.011390	7.891629
MAPE	6.576058	6.573973	8.285324	6.847210	**5.991413**	6.680915	7.673681	7.285152	6.719789	8.376965	8.502531	7.482382
RMSE	9.717137	9.713131	11.16802	10.01724	**9.454456**	10.66723	11.68773	11.14531	9.854205	12.19098	11.98773	11.26219

Prob.*, indicates emphasis. The size of the Prob.* value reflects the stability of the data series.

TABLE 6 The parameter comparison of each model's test index (eliminate seasonal fluctuations).

Index	ARIMA (1, 2, 1)	ARIMA (1, 2, 2)	ARIMA (1, 2, 3)	ARIMA (1, 2, 4)	ARIMA (2, 2, 1)	ARIMA (2, 2, 2)	ARIMA (2, 2, 3)	ARIMA (2, 2, 4)	ARIMA (3, 2, 1)	ARIMA (3, 2, 2)	ARIMA (3, 2, 3)	ARIMA (3, 2, 4)
Adjusted-R^2	0.282660	0.302913	0.224594	**0.401740**	0.282594	0.144170	0.013991	0.207111	0.292092	0.123519	−0.015869	0.149244
AIC	7.505304	7.487031	7.574546	**7.373051**	7.505778	7.703474	7.814235	7.635996	7.493233	7.721904	7.841370	7.692927
SC	7.622254	7.603981	7.691496	**7.490001**	7.622728	7.820424	7.931185	7.752946	7.610183	7.838854	7.958320	7.809877
MAPE	5.495101	5.439750	5.682568	**5.072340**	5.430309	6.579909	6.998548	6.020232	5.687182	6.844513	7.251816	6.197987
RMSE	9.637975	9.514886	10.00691	**8.884206**	9.725911	10.72635	11.41146	10.29992	9.765165	10.89394	11.70910	10.75731

Prob.*, indicates emphasis. The size of the Prob.* value reflects the stability of the data series.

10.3389/feart.2022.1040464

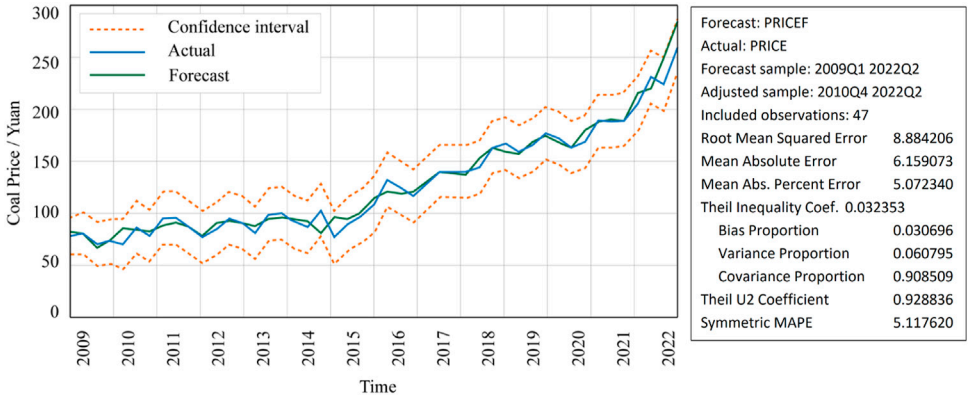

FIGURE 11
The result of the coal prediction model based on ARIMA.

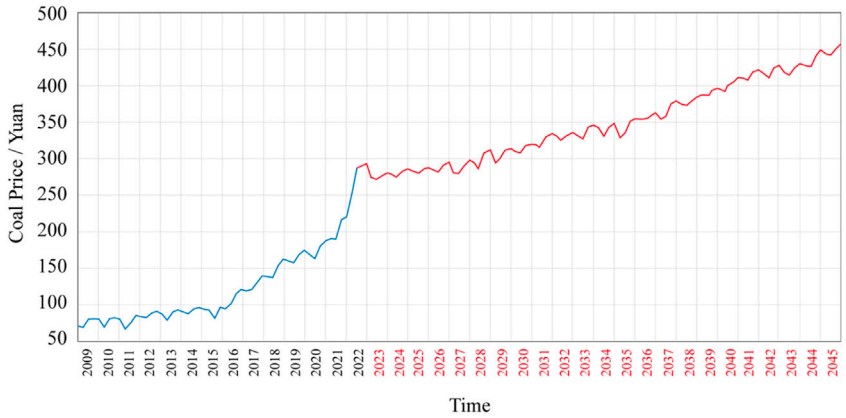

FIGURE 12
The result of coal price forecast in the next 23 years based on ARIMA.

TABLE 7 The optimization results of OPCMPS.

Year/a	Fuzzy mining volume×10^4/t	Fuzzy stripping volume×10^4/m^3	Fuzzy *NPV*×10^4/yuan	Mining body sequence
1	2419.83+0.43*E*	11784.57+0.85*E*	14885.487+0.4579*E*	1
2	2511.23+0.74*E*	13054.28+1.55*E*	15774.121+0.6547*E*	15
3	3482.69+1.87*E*	12977.65+2.88*E*	19124.855+0.8741*E*	24
—	—	—	—	—
21	3518.47+3.76*E*	12984.22+4.56*E*	24154.787+1.7789*E*	98
21	3520.45+3.97*E*	11045.54+4.79*E*	24277.365+1.8745*E*	110
23	1807.32+4.19*E*	4526.32+5.18*E*	10485.354+2.0078*E*	128
Fuzzy total *NPV* ×10^4/yuan 418453.714+31.1163				

growth of the year, the sample data of coal price prediction can be dynamically updated every year to achieve more accurate prediction results of future coal prices. This model is used to predict the coal price in the next 23 years. The result of coal price forecast based on ARIMA (1, 2, 4) is shown in the red curve Figure 12.

6.3 Application of proposed optimization approach

In the preparation of the OPCMPS process, according to the actual situation of the mine, set the mining body of coal increment of about 2.3 million tons, the recovery rate of 95%, stop working slope angle of 8°, and the annual production capacity of about 25 million tons. The production cost of coal mining is 96.27 yuan/t, the stripping cost is 7 yuan/m^3, the price of raw coal is 220.25 yuan/t, the cost rise rate is 3%, the price rise rate is 5%, and the annual discount rate is 7.5%. The coal price predicted by ARIMA is combined with the dynamic sorting of the geological optimal mining body based on the structural element theory proposed in this paper.

AutoCAD is a popular computer-aided design (CAD) and drawing software program. By autodesk, who also developed and sold it. The AutoCAD application is a great and well-liked tool that creates any sort of schemes and drawings with high precision and quality. Additionally, it aids in fully recognizing the creative potential of program users. In order to automate their design work, millions of professionals, scientists, engineers, and students now often utilize the AutoCAD system (Cao and Miyamoto, 2003). Based on AutoCAD, the secondary development is carried out to establish a three-dimensional deposit block model, and a total of 128 geological optimal mining bodies are generated.

Taking E as a triangular structure element, Its membership function is $E(x) = \begin{cases} 1+x, -1 \le x \le 0 \\ 1-x, \ 0 \le x \le 1 \end{cases}$, The fuzzy mining quantity and fuzzy stripping quantity of 128 geological optimal mining bodies can be expressed by the triangular fuzzy number. Taking No. 1 geologically optimal mining body as an example, let $f(x) = 2419.83 + 0.18x$, $g_1(x) = 2419.83 + 0.18x$, then $q_1(x) = f_1(E) = 2419.83 + 0.18E$, $w_1 = g_1(E) = 11784.57 + 0.85E$. Others can be analogized. Let $p_t = 0.022(1+0.05)^t$, $c_t = 0.0096(1+0.03)^t$, $b_t = 0.0007(1+0.03)^t$, $d = 0.0075$, $z_t = 0.001 + 0.001h_t$, h_t is calculated according to the specific situation of the mining body. Therefore, according to the fuzzy coal mining amount, fuzzy stripping amount and set technical parameters, the software is used to perform fuzzy dynamic sorting on the sequence composed of 128 geological optimal mining bodies. The optimization results of OPCMPS are shown in Table 3.

Table 7 shows that when the sequence of geologically optimal mining body is $\{p_1 \rightarrow p_{15} \rightarrow p_{24} \rightarrow \ldots \rightarrow p_{98} \rightarrow p_{110} \rightarrow p_{128}\}$, the maximum fuzzy total *NPV* is $(418453.714+31.1163E) \times 10^4$ yuan. It can be seen that the optimal mining life is 23 years. The annual amount of fuzzy coal mining and stripping can be determined in Table 3. The membership degree of fuzzy total *NPV* is:

$$u_{\underset{\sim}{NPV}_{(32,128)}}(x) = \begin{cases} 1 + \dfrac{x - 418453.714}{31.1163}; 418422.5977 \le x \le 418453.714 \\ 1 - \dfrac{x - 418453.714}{31.1163}; 418453.714 \le x \le 418484.8303 \end{cases}$$

In addition to the first and 2nd years when the mining field is in the turning period of the mining area and the last year when the mining task is completed, the annual fuzzy coal mining volume fluctuates greatly. Others are 35 million tons.

7 Discussions

There have been many studies on production scheduling in the field of open-pit metal mines, but there have been very few studies in this area for open-pit coal mines with stratified ore bodies. From the viewpoint of fuzzy economics, this study suggests a novel mathematical model of the total *NPV* of opencast coal mine production scheduling, while the majority of other studies on this topic have been built by taking into account various limitations. Additionally, this study offers a method for projecting coal prices based on economic time series, and it dynamically executes the production scheduling optimization design from a dynamic economics perspective to account for the effects of price fluctuations on the total *NPV*. The novel approach that has been suggested would undoubtedly aid in the design and construction of open-pit coal mines and offer fresh perspectives to experts working in this area. Additionally, the production schedule optimization technique suggested in this study can be used as a guide for open-pit metal miners.

The size of the sample data set will have an impact on the forecast accuracy, which is one drawback of the price prediction approach. This paper's case study research findings demonstrate that the proposed production scheduling model may simultaneously achieve the best production capacity, excavation order, and production life. But because the mine only began selling coal in 2009, there is only a limited sample data set that can be used to anticipate coal prices. However, there is a technique for optimization and adjustment, which allows for the correction of the current year's coal price and the dynamic updating and adjusting of the future production schedule throughout the development and building of mines.

8 Conclusion

The traditional optimization method of OPCMPS adopts accurate calculation, which somewhat ignores the mining process's uncertainty. Based on the production scheduling optimization method proposed in Reference (Gu et al., 2011), this paper introduces the fuzzy structural

element theory to establish the fuzzy optimization model of fuzzy coal mining volume, fuzzy stripping volume and fuzzy total *NPV* and their respective membership function expressions. At the same time, considering the volatility of coal prices over time, the ARIMA prediction model is used for prediction. Through the analysis of coal prices from 2009 to 2022, the prediction model was determined as ARIMA (1, 2, 4), and the model was applied to predict coal prices in the next 23 years. The optimal mining sequence of the optimal geological body and the fuzzy coal mining volume, fuzzy stripping volume and fuzzy *NPV* of each optimal geological body is obtained by combining the constructed fuzzy optimization model, the predicted coal price and the moving cone exclusion method. The maximum total *NPV* is (418453.714 + 31.1163 E) $\times 10^4$ yuan, and the optimal mining period of the mine is 23 years.

Data availability statement

The original contributions presented in the study are included in the article/supplementary material, further inquiries can be directed to the corresponding author.

Author contributions

All authors listed have made a substantial, direct, and intellectual contribution to the work and approved it for publication.

Funding

This research was supported by the National Natural Science Foundation of China (Grant no. 51974144) and the Discipline Innovation Team of Liaoning Technical University (LNTU20TD-07). The "Jie Bang Gua Shuai" (Take the Lead) of the Key Scientific and Technological Project for Liaoning Province additionally provided financial assistance for this study under the grant number [2021JH1/10400011].

Conflict of interest

The author CY was employed by National Energy Investment Group Co. Ltd.

The remaining authors declare that the research was conducted in the absence of any commercial or financial relationships that could be construed as a potential conflict of interest.

Publisher's note

All claims expressed in this article are solely those of the authors and do not necessarily represent those of their affiliated organizations, or those of the publisher, the editors and the reviewers. Any product that may be evaluated in this article, or claim that may be made by its manufacturer, is not guaranteed or endorsed by the publisher.

References

Alipour, A., Khodaiari, A. A., Jafari, A., and Tavakkoli-Moghaddam, R. (2020). Production scheduling of open-pit mines using genetic algorithm: A case study. *Int. J. Manag. Sci. Eng. Manag.* 15 (3), 176–183. doi:10.1080/17509653.2019.1683090

Bienstock, D., and Zuckerberg, M. (2009). A new LP algorithm for precedence constrained production scheduling. *Optim. Online*, 1–33.

Blom, M., Pearce, A. R., and Stuckey, P. J. (2018). Multi-objective short-term production scheduling for open-pit mines: A hierarchical decomposition-based algorithm. *Eng. Optim.* 50 (12), 2143–2160. doi:10.1080/0305215x.2018.1429601

Blom, M., Pearce, A. R., and Stuckey, P. J. (2017). Short-term scheduling of an open-pit mine with multiple objectives. *Eng. Optim.* 49 (5), 777–795. doi:10.1080/0305215x.2016.1218002

Boland, N., Dumitrescu, I., Froyland, G., and Gleixner, A. M. (2009). LP-based disaggregation approaches to solving the open pit mining production scheduling problem with block processing selectivity. *Comput. Operations Res.* 36 (4), 1064–1089. doi:10.1016/j.cor.2007.12.006

Box, G. E. P., Jenkins, G. M., and Reinsel, G. C., (2015). *Time series analysis: Forecasting and control*. Hoboken, New Jersey, United States: John Wiley & Sons.

Caccetta, L., and Hill, S. P. (2003). An application of branch and cut to open pit mine scheduling. *J. Glob. Optim.* 27 (2), 349–365. doi:10.1023/a:1024835022186

Cao, W., and Miyamoto, Y. (2003). Direct slicing from AutoCAD solid models for rapid prototyping. *Int. J. Adv. Manuf. Technol.* 21 (10), 739–742. doi:10.1007/s00170-002-1316-0

Chicoisne, R., Espinoza, D., Goycoolea, M., Moreno, E., and Rubio, E. (2012). A new algorithm for the open-pit mine production scheduling problem. *Operations Res.* 60 (3), 517–528. doi:10.1287/opre.1120.1050

Clements, M. P., and Hendry, D. F. (1998). *Forecasting economic time series*. Cambridge, United Kingdom: Cambridge University Press.

Contreras, J., Espinola, R., Nogales, F. J., and Conejo, A. (2003). ARIMA models to predict next-day electricity prices. *IEEE Trans. Power Syst.* 18 (3), 1014–1020. doi:10.1109/tpwrs.2002.804943

Eivazy, H., and Askari-Nasab, H. (2012). A mixed integer linear programming model for short-term open pit mine production scheduling. *Min. Technol.* 121 (2), 97–108. doi:10.1179/1743286312y.0000000006

Fathollahzadeh, K., Mardaneh, E., Cigla, M., and Asad, M. W. A. (2021). A mathematical model for open pit mine production scheduling with Grade Engineering® and stockpiling. *Int. J. Min. Sci. Technol.* 31 (4), 717–728. doi:10.1016/j.ijmst.2021.03.011

Fytas, K. (1986). "A computerized model of open pit short and long range production scheduling," in Proceeding of the 19th A PCOM Symposium (SME-AME), New York, 109–119.

Gilani, S. O., Sattarvand, J., Hajihassani, M., and Abdullah, S. S. (2020). A stochastic particle swarm based model for long term production planning of open pit mines considering the geological uncertainty. *Resour. Policy* 68, 101738. doi:10.1016/j.resourpol.2020.101738

Gu, X. W., Wang, P. F., Wang, Q., Zheng, Y. Y., Liu, J. P., and Chen, B. (2011). Simultaneous optimization of final pit and production schedule in open-pit coal mines. *Adv. Mat. Res.* 323, 222–228. doi:10.4028/www.scientific.net/AMR.323.222

Guo, S. C. (2009). Comparison and ordering of fuzzy numbers based on method of structured element. *Syst. Eng. - Theory & Pract.* 29 (3), 106–111. doi:10.1016/s1874-8651(10)60013-0

Guo, S. C. (2002a). *Method of structuring element in fuzzy analysis (I)*. Fuxin: Journal of Liaoning Technical University, 670–673.

Guo, S. C. (2002b). *Method of structuring element in fuzzy analysis (II)*. Fuxin: Journal of Liaoning Technical University, 808–810.

Guo, S. C., and Song, T. (2011). Operations and measurement of interval-valued fuzzy numbers based on the method of structured element. *Fuzzy Inf. Eng.* 3 (1), 101–110. doi:10.1007/s12543-011-0069-6

Harvey, A. C. (1990). *Forecasting, structural time series models and the Kalman filter*, Cambridge, UK: Cambridge University Press.

He, G. J., Liu, S. S., Si, l., Gao, Q., Ma, J., and Zhao, J. L. (2006). *Study on coal cost of major coal-producing countries abroad. Selected articles on coal economics in 2006*, 177–270. Beijing: China Coal Industry Publishing House.

Hendry, D. F., and Doornik, J. A. (1994). Modelling linear dynamic econometric systems[J]. *Scott. J. Polit. Econ.* 41 (1), 1–33. doi:10.1111/j.1467-9485.1994.tb01107.x

Jiang, S., Yang, C., Guo, J., and Ding, Z. (2018). ARIMA forecasting of China's coal consumption, price and investment by 2030. *Energy Sources, Part B Econ. Plan. Policy* 13 (3), 190–195. doi:10.1080/15567249.2017.1423413

Khan, A., and Niemann-Delius, C. (2018). A Differential Evolution based approach for the production scheduling of open pit mines with or without the condition of grade uncertainty. *Appl. Soft Comput.* 66, 428–437. doi:10.1016/j.asoc.2018.02.010

Khan, A. (2018). Long-term production scheduling of open pit mines using particle swarm and bat algorithms under grade uncertainty. *J. South. Afr. Inst. Min. Metall.* 118 (4), 361–368. doi:10.17159/2411-9717/2018/v118n4a5

Li, H. (2021). Prediction of coal price based on ARIMA model. *Front. Econ. Manag.* 2 (8), 155–163. doi:10.9734/ajeba/2022/v22i830590

Li, K., and Lin, B. (2017). Economic growth model, structural transformation, and green productivity in China. *Appl. Energy* 187, 489–500. doi:10.1016/j.apenergy.2016.11.075

Liu, X. (2021). Research on the forecast of coal price based on LSTM with improved Adam optimizer. *J. Phys. Conf. Ser.* 1941 (1), 012069. doi:10.1088/1742-6596/1941/1/012069

Nelson, L. R., and Goldstern, M. R. (1980). "Interactive short range mine planning a case study," in Weiss a Computer Methods for the 80's in the Mineral Industry (SME-AME), New York: AIME, 592–600.

Osanloo, M., Gholamnejad, J., and Karimi, B. (2008). Long-term open pit mine production planning: A review of models and algorithms. *Int. J. Min. Reclam. Environ.* 22 (1), 3–35. doi:10.1080/17480930601118947

Ramazan, S. (2007). The new fundamental tree algorithm for production scheduling of open pit mines. *Eur. J. Operational Res.* 177 (2), 1153–1166. doi:10.1016/j.ejor.2005.12.035

Tolouei, K., Moosavi, E., Bangian Tabrizi, A. H., and Afzal, P. (2021). Application of an improved Lagrangian relaxation approach in the constrained long-term production scheduling problem under grade uncertainty. *Eng. Optim.* 53 (5), 735–753. doi:10.1080/0305215x.2020.1746295

Tolouei, K., Moosavi, E., Tabrizi, A. H. B., Afzal, P., and Bazzazi, A. A. (2021). An optimisation approach for uncertainty-based long-term production scheduling in open-pit mines using meta-heuristic algorithms. *Int. J. Min. Reclam. Environ.* 35 (2), 115–140. doi:10.1080/17480930.2020.1773119

Turan, G., and Onur, A. H. (2022). Optimization of open-pit mine design and production planning with an improved floating cone algorithm. *Optim. Eng.*, 1–25. doi:10.1007/s11081-022-09725-4

Upadhyay, S. P., and Askari-Nasab, H. (2018). Simulation and optimization approach for uncertainty-based short-term planning in open pit mines. *Int. J. Min. Sci. Technol.* 28 (2), 153–166. doi:10.1016/j.ijmst.2017.12.003

Wang, L. L., Li, Y., Zhang, J. J., Qian, M., and Cao, Y. (2022). Analysis on the difference of reconstructed soil moisture content in a grassland open-pit mining area of China. *Agronomy* 12 (5), 1061. doi:10.3390/agronomy12051061

Wang, X., Liu, C., Chen, S., Chen, L., and Li, K. (2020). Impact of coal sector's de-capacity policy on coal price. *Appl. Energy* 265, 114802. doi:10.1016/j.apenergy.2020.114802

Zhang, X., Liu, C., and Qian, Y. (2020). Coal price forecast based on ARIMA model. *Fin. For.* 9 (4), 180. doi:10.18282/ff.v9i4.1530

Zheng, F. W., Zhen, X., and Chen, C. X. (2014). Development status and trend of world open-pit coal mine. *Chain Coal* 40, 113–116. doi:10.19880/j.cnki.ccm.2014.11.028

frontiers | Frontiers in Earth Science

TYPE Original Research
PUBLISHED 20 January 2023
DOI 10.3389/feart.2023.1125689

OPEN ACCESS

EDITED BY
Jianwei Tian,
Technical University of Denmark, Denmark

REVIEWED BY
Jianwei Li,
Inner Mongolia University of Science and Technology, China
Wenlong Shen,
Henan Polytechnic University, China
Jingxuan Yang,
China University of Mining and Technology, China

*CORRESPONDENCE
Yixin Zhao,
zhaoyx@cumtb.edu.cn

SPECIALTY SECTION
This article was submitted to Environmental Informatics and Remote Sensing, a section of the journal Frontiers in Earth Science

RECEIVED 16 December 2022
ACCEPTED 09 January 2023
PUBLISHED 20 January 2023

CITATION
Yang Y, Zhao Y, Ma J and Han P (2023), Study on stability and bearing characteristics of macroscopic pressure arch of surrounding rock in western deep buried stope of China.
Front. Earth Sci. 11:1125689.
doi: 10.3389/feart.2023.1125689

Study on stability and bearing characteristics of macroscopic pressure arch of surrounding rock in western deep buried stope of China

Yuliang Yang[1,2,3], Yixin Zhao[1,2]*, Jianqi Ma[1,2] and Penghua Han[1,2]

[1]Beijing Key Laboratory for Precise Mining of Intergrown Energy and Resources, China University of Mining and Technology (Beijing), Beijing, China, [2]School of Energy and Mining Engineering, China University of Mining and Technology (Beijing), Beijing, China, [3]School of Coal Engineering, Shanxi Datong University, Datong, Shanxi, China

In view of the obvious loose and weak occurrence characteristics of the deeply buried thick weakly cemented stratum in the western mining area of China, the bearing characteristics and stability mechanism of the macrography surrounding rock pressure arch (SRPA) are studied. Firstly, considering the engineering characteristics of deep mining, a SRPA model with trapezoidal load was constructed based on the three-hinged arch theory, the shape characteristic, rise-span ratio and arch thickness equations were derived, the arch thickness under different stress paths is analyzed to characterize the bearing performance of pressure arch. Secondly, the internal force distribution law and destabilization damage type were studied by establishing a two-dimensional bearing SRPA model through arch without articulation theory. The instability type and location can be accurately judged and verified by simulation of similar materials. The results show that, the rational arch axis of SRPA is a cubic parabola with opening downward, its rise-span ratio is between 0.3 and 0.5. Increasing the rise-span ratio and lateral pressure coefficient can promote the stable bearing capacity of arch. Axial force distribution on the SRPA section is basically consistent with the arch axis, and the arch has the best bearing characteristics. The positive bending moment occurs in the ranges of [0°, 30°] and [81°, 90°] on both sides of the symmetry axis, where is prone to tensile failure. The maximum shear force is concentrated on the arch waist and skewback, and these sections are prone to shear failure. The instability modes of SRPA can be divided into "skewback—vault (arch waist)" and "vault (arch waist)—skewback". The research results have theoretical guiding significance for mining roof management.

KEYWORDS

arch thickness, rise-span ratio, surrounding rock pressure arch, stability mechanism, weakly cemented stratum

1 Introduction

A series of mining damage and environmental problems caused by coal mining are related to strata movements; therefore, revealing the bearing characteristics of mining overburden is the key to understand the movement law of overburden in stope (Ning et al., 2017; Genis et al., 2018; Li et al., 2020; Zhang et al., 2021). The mining area in western China is a typical Cretaceous and Jurassic coal-rich area, and the stratum in this area has the

particularity of diagenetic environment, diagenetic age, and sedimentary process. Rocks often exhibit low strength, weak cementation, large porosity, easy weathering, sensitivity to disturbance, etc., thus, many scholars collectively refer to this layer type as weakly cemented stratum (Zhao and Liu 2021). The stratum has poor self-stabilization ability due to mining disturbances, and accidents such as partial roof caving, coal wall spalling, and step sinking often occur in the mining process. At present, the shallow resources with buried depth of 100–300 m in typical western mining areas are gradually being exhausted, and coal mining gradually enters depths of 400–700 m. With the continuous increase in mining depth and intensity, large areas of coal wall spalling, large shrinkage of the hydraulic support column, and even support crushing appear frequently during the mining process (Mark, 2019; Bednarek and Majcherczyk 2020; Zhang et al., 2020). It was found out that the mining area with rich groundwater, such as in Shaanxi, Mongolia, etc., can show a deep mechanical state when the mining depth is 400–500 m (Xie et al., 2015; Zhang et al., 2019). Existing analyses of the bearing characteristics and stability of the overlying strata spatial structure in the mining field focus mainly on the cracked overlying strata in the beam or plate structure. The previous research results have proven that weakly cemented rocks have obvious loose and weak characteristics (Sun et al., 2019), and their bearing performance under the influence of disturbance is characterized by the pressure arch structure.

Surrounding rock pressure arches (SRPAs) exist widely in underground cavern engineering, such as mining fields and tunnels (Dancygier et al., 2016; Wang et al., 2019a; Oge 2020). As a classical problem of geomechanics, SRPAs have always been a research hotspot, including the stress distribution in pressure arch (Pardo and Saez 2014; Shabanimashcool and Li 2015), and application of the pressure arch in geotechnical engineering (Chen and Martin 2002; Yang et al., 2021). Since Platt's collapse arch theory and the "pressure arch hypothesis" of mining overlying strata were proposed, the arch shape of the fracture boundary line of the mining rock and the arch effect of stress self-adjustment have been widely considered (Das 2000; Poulsen 2010; Kong et al., 2018). The earliest theory using the arching effect of surrounding rock to explain the ground pressure during longwall mining is the stress arch hypothesis (Kratzsch 1983). In this hypothesis, the stress arch is regarded as the bearing structure during overlying strata movement. Based on the research of the macroscopic SRPA, the theory of internal and external stress fields of the overlying strata spatial structure in the mining field, the near-field "cracked arch" and the far-field "stress arch" structure model were proposed. The "double arch" model of the mining field overlying strata is the mechanical expression of the self-bearing characteristics of the rock body and the arch effect of compressive stress (Wen et al., 2015). Zou (1989) analyzed a series of mechanical phenomena caused by mining activities from the point of view of the stress field and deduced that there was a "large structure" in the form of a macroscopic pressure arch in the overlying strata in the longwall working face. Du et al., 2011 discussed the stress transfer in surrounding rock during the advancing process of the working face combining numerical simulation and similar physical model methods, indicating that high stress concentration areas are formed in the far-field high level rock layer and surrounding rocks on both sides, which is called mining SRPA. There is no unified standard for the morphological characteristics of SRPA in rock movement. On the one hand, a theoretical model of the stress arch is established based on the three-hinged arch model in structural mechanics, the stress on the vertical boundary being a uniform load, and the stress on the horizontal boundary being a uniform load or trapezoidal load (Xia et al., 2018; Wang et al., 2019b; Kong et al., 2021). On the other hand, the derivation of morphological characteristic equations and instability discrimination were carried out based on Platt's pressure arch theory and the Terzaghi soil arch effect assuming the arch to be a semicircular, semielliptical and parabolic model (Pardo et al., 2014; Zhao et al., 2021); however, which is the most reasonable arch axis has not been considered according to engineering practice. Regarding the bearing characteristics and stability analysis of SRPA, previous studies were conducted mainly from the distribution characteristics and deflection direction of the principal stress in surrounding rock through numerous numerical simulations (Yavuz 2004; El Kamash et al., 2021). There is no index to characterize the load-bearing performance of the SRPA and the factors affecting the characteristics of the arch effect area. Meanwhile, the instability area of the SRPA is not accurately judged according to the stability criterion.

In this paper, the bearing characteristics and stabilization mechanism of the macroscopic SRPA are investigated with respect to the occurrence characteristics of the deeply buried giant-thickness and weakly cemented stratum in the western mining area. First, based on the three-hinged arch theory a mechanical model of the macroscopic pressure arch was established. The boundary conditions were trapezoidal loads in both the vertical and horizontal directions, consistent with actual engineering practice. Then, the axis equation and rise-span relationship of SRPA were deduced. Second, the range of the arch area under different stress paths was determined according to the morphology of the arch axis, combining with the inner and outer boundary positions of the pressure arch. The arch thickness and its bearing characteristics were studied. Finally, based on the arch without articulation theory, combining with the calculated arch axis equation, a two-dimensional mechanical model of SRPA was established to study the distribution of internal forces and failure types when the model was loaded.

2 Theoretical model

The SRPA is the mechanical root cause of the elevated abutment pressure of the coal rock body around the working face and dramatic mine pressure behaviors. The SRPA a redistribution of stress state caused by the self-adjustment of overlying strata to resist the uneven deformation of the medium caused by mining, that is, the principal stress changes, the direction is deflected, and the load transfer path deviates from the arch structure tangential compression area (Jaouhar et al., 2018). At the same time, the load is transferred to the stable rock mass at the skewback position, giving full play to its self-bearing capacity manifestation. The characteristics of SRPA conform to the arch without articulation in structural mechanics, which is a typical cubic statically indeterminate structure. In the calculation of the internal force distribution law of the statically indeterminate arch, the equation of the arch axis and the variation law of the arch section must be

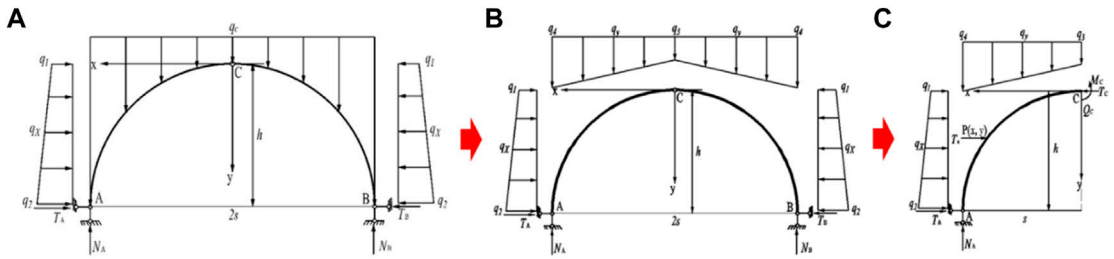

FIGURE 1
Diagram of SRPA (Surrounding rock pressure arch): **(A)** Stress analysis of filling load; **(B)** Stress analysis of trapezoidal load state; **(C)** Left half-span isolator.

determined. Due to the complicated analysis process of statically indeterminate problems, studies have shown that if the influence of axial deformation is neglected when calculating statically indeterminate arch structures, the reasonable axis of statically indeterminate arches is the same as the corresponding three-hinged arch (Jiang et al., 2008). In this paper, the reasonable arch axis of the three-hinged arch is used as the reasonable arch axis of the SRPA. The axis equation of the SRPA is calculated, and then the arch without articulation is taken as the research object to calculate the internal force distribution law of the SRPA.

2.1 Assumptions and boundary conditions

Before theoretical analysis, the model is simplified as follows.

- The SRPA dynamically evolves with the mining influence, and the pressure arch in the far-field under the condition of full mining (the working face length is equal to the advancing length) was selected for analysis, as shown in Figure 3.
- The physical and mechanical properties of the giant-thick weakly cemented laminated rock mass are relatively similar. The tensile strength of weakly cemented rock is less than 2 MPa, the compressive strength is less than 20 MPa, the elastic modulus is less than 2 GPa, and the cohesion is less than 10 MPa. So we assumed that the surrounding rock is a homogeneous and continuous medium (Li et al., 2016).
- The SRPA is a shell structure with a certain thickness, and the centroid line of the arch structure is the research object when analyzing the characteristics of the pressure arch shape.
- The SRPA contains an unstable and broken rock mass, and the supporting reaction force to the arch is not considered in the model construction process.
- The SRPA formed under certain buried depth conditions, For the convenience of calculation, the boundary conditions are set as follows: The vault bears a centrally symmetrical vertical trapezoidal load, and both sides of the arch bear a horizontal linear trapezoidal load.

2.2 Morphological characteristics

The three-hinged arch rational arch axis equation of structural mechanics is used as the morphological characteristic equation of the SRPA. For SRPA, to maintain balance and stability, the bending moment M and the shear force Q on the section where the arch axis located must be zero. To study the morphological characteristics of SRPA (rational arch axis and rise-span ratio), a mechanical model is established, as shown in Figure 1. Among them; Figure 1A shows the actual load distribution state of SRPA in deep mining area. The vault bears a centrally symmetrical filling load, and both sides of the arch bear a horizontal linear trapezoidal load. For convenience of calculation, the vertical stress of overlying is equivalent to trapezoidal load, as shown in Figure 2B.

As displayed in Figure 1A, the force analysis shows that the horizontal thrusts T_A and T_B and the vertical reaction forces N_A and N_B act on the front and rear arch feet A and B, respectively, and the horizontal trapezoidal load $q_x = (q_2 - q_1)y/h + q_1$ while, the vertical trapezoidal load $q_y = (q_4 - q_3)x/s + q_3$ are act on any Section P (x, y). For trapezoidal load $q_1 = \lambda\gamma(H - h)$, $q_2 = \lambda\gamma H$, $q_3 = \gamma(H - h)$ and $q_4 = \gamma H$, in these formulae h is arch rise, s is half of the arch span, λ is the lateral pressure coefficient, γ is the density of the rock mass; and H is the mining depth.

$$\text{Horizontal thrust: } T_x = \int_0^y q_x \mathrm{d}y = \frac{(q_2 - q_1)y^2}{2h} + q_1 y, \tag{1}$$

$$\text{Vertical pressure: } T_y = \int_0^x q_y \mathrm{d}x = \frac{(q_4 - q_3)x^2}{2s} + q_3 x. \tag{2}$$

Taking any point P (x, y) on the left span axis of the SRPA, as shown in Figure 1B, a force analysis is performed and according to the moment balance equation, obtained as follows:

$$T_c y = \frac{x(q_4 + 2q_3)}{3(q_4 + q_3)} \cdot T_y + \frac{y(q_2 + 2q_1)}{3(q_2 + q_1)} \cdot T_x, \tag{3}$$

where T_c is the horizontal force at point C of the vault, $\frac{y(q_2+2q_1)}{3(q_2+q_1)}$ and $\frac{x(q_4+2q_3)}{3(q_4+q_3)}$ are the concentrated load action points of the horizontal trapezoidal stress and the vertical trapezoidal stress, respectively.

Substituting Eqs. 1–2 into Eq. 3, the following equation is obtained as follows

$$T_c = \frac{[(3H - 2h)\gamma](\lambda s y^3 + h x^3) + [2(3H - 2h)(H - h)\gamma](\lambda y^2 + s x^2)}{6(2H - h)s y}. \tag{4}$$

According to the force balance condition in the X-axis direction

$$T_c = T_x + f s q_y, \tag{5}$$

where f is the coal-rock friction factor, which is related to the hardness of the coal and rock mass. Generally, the harder the rock is, the larger the value (Cai 2013).

Substituting Eqs. 1–2 into Eq. 5, the following equation can be obtained

$$T_c = \frac{1}{2}\lambda\gamma y^2 + \lambda\gamma(H-h)y + \gamma sfH + \gamma hf(x-s). \tag{6}$$

By combining Eqs. 4, 6, the axis equation of the SRPA can be obtained as follows

$$\begin{aligned}&\frac{(3H-2h)\gamma h}{6(2H-h)s}x^3 + \frac{(3H-2h)(H-h)\gamma}{3(2H-h)}x^2\\ &= \frac{\gamma\lambda(3H-h)}{6(2H-h)}y^3 + \frac{(3H-h)(H-h)\lambda\gamma}{3(2H-h)}y^2 + \gamma sf(H-h)y\\ &\quad + \gamma hfx \; yx \in [0,s],\ y \in [0,\mathrm{h}].\end{aligned} \tag{7}$$

The axis equation of SRPA can be written as

$$a\cdot y^3 + b\cdot y^2 + c\cdot y + d = 0, \tag{8}$$

where

$$\begin{cases} a = \dfrac{\gamma\lambda(3H-h)}{6(2H-h)} \\ b = \dfrac{(3H-h)(H-h)\lambda\gamma}{3(2H-h)} \\ c = \gamma sf(H-h) + \gamma hfx \\ d = -\left[\dfrac{(3H-2h)\gamma h}{6(2H-h)s}x^3 + \dfrac{(3H-2h)(H-h)\gamma}{3(2H-h)}x^2\right]. \end{cases} \tag{9}$$

Eq. 8 is a cubic equation of one variable. In the range of $x \in [0,s]$, $y \in [0,h]$, it has a unique real number root

$$y = m + n - \frac{b}{3a}, \tag{10}$$

where

$$\begin{cases} m = \sqrt[3]{u+v} \\ n = \dfrac{b^2 - 3ac}{9am}\cdot \end{cases} \tag{11}$$

In Eq. 11, u and v are calculated by the following equations

$$\begin{cases} u = \dfrac{9abc - 27a^2d - 2b^3}{54a^3} \\ v = \dfrac{\sqrt{3\left(4ac^3 - b^2c^2 - 18abcd + 27a^2d^2 + 4b^3d\right)}}{18a^2} \end{cases}. \tag{12}$$

Substituting x=s and y=h into Eq. 7, then the relationship between the arch rise (h) and span (2 s) of the SRPA can be derived, expressed by

$$\frac{(3H-2h)^2s^2}{(2H-h)} - 6Hhfs - (3H-h)\lambda h^2 = 0. \tag{13}$$

2.3 Internal force distribution

The reasonable axis of the SRPA is a unary cubic function curve, and the rational axis equation of the arch is established based on the bending moment of any section of the three-hinged arch structure being zero. When the arch without an articulation structure is used for internal force analysis, the bending moment, shear force and axial force still need to be generated due to the influence of the additional internal force of the statically indeterminate structure. Therefore, based on determining the reasonable axis of the SRPA, the internal force distribution law of the SRPA is analyzed through the force method equation of the cubic statically indeterminate problem of the arch without articulation in structural mechanics. A coordinate system is established, as shown in Figure 2A, with the origin at the center of the arch without an articulation structure. Due to the symmetry of the arch structure, establishing half of the structure for analysis (see Figure 2B) and cutting along the middle of the arch with three unknown forces X_1, X_2, and X_3 in the cross section, which are the bending moment, axial force and shear force respectively. Due to the symmetry of the structure and load, the antisymmetric internal shear force on the central section is 0, that is X_3=0. X_1, and X_2 can be solved according to the force method equations.

$$\begin{cases} \delta_{11}X_1 + \Delta_{1p} = 0 \\ \delta_{22}X_2 + \Delta_{2p} = 0, \end{cases} \tag{14}$$

where δ_{11} and δ_{22} are the displacements generated under the action of unit force $\overline{X_1} = 1$, $\overline{X_2} = 1$ and $\Delta_{1\mathrm{p}}$ and $\Delta_{2\mathrm{p}}$ represent the displacements of point C along the X_1 and X_2 directions under the action of external force.

According to the displacement calculation equation of the statically determinate structure, the rotation angle and displacement δ_{11} and δ_{22} of point C under the action of unit force $\overline{X_1} = 1$, $\overline{X_2} = 1$ can be calculated as follows

$$\begin{cases} \delta_{11} = \dfrac{1}{EI}\displaystyle\int_0^s \sqrt{1+y'}\,\mathrm{d}x \\ \delta_{22} = \dfrac{1}{EI}\displaystyle\int_0^s \mathrm{y}^2\sqrt{1+y'}\,\mathrm{d}x. \end{cases} \tag{15}$$

The bending moment of any section under an external load can be written as

$$M_c = \frac{x(q_4+2q_3)}{3(q_4+q_3)}\cdot T_y + \frac{y(q_2+2q_1)}{3(q_2+q_1)}\cdot T_x. \tag{16}$$

Accordingly, the displacements $\Delta_{1\mathrm{p}}$ and $\Delta_{2\mathrm{p}}$ of point C under an external load can be calculated as follows

$$\begin{cases} \Delta_{1p} = \dfrac{\displaystyle\int_0^s M_c\sqrt{1+y'}\,\mathrm{d}x}{EI} \\ \Delta_{2p} = \dfrac{\displaystyle\int_0^s M_c\mathrm{y}^2\sqrt{1+y'}\,\mathrm{d}x}{EI} \end{cases}. \tag{17}$$

Substituting Eqs. 15, 17 into Eq. 14, can be obtained as follows

$$\begin{cases} X_1 = \dfrac{\displaystyle\int_0^s M_c\sqrt{1+y'}\,\mathrm{d}x}{\displaystyle\int_0^s \sqrt{1+y'}\,\mathrm{d}x} \\ X_2 = \dfrac{\displaystyle\int_0^s M_c\mathrm{y}^2\sqrt{1+y'}\,\mathrm{d}x}{\displaystyle\int_0^s \mathrm{y}^2\sqrt{1+y'}\,\mathrm{d}x} \end{cases}. \tag{18}$$

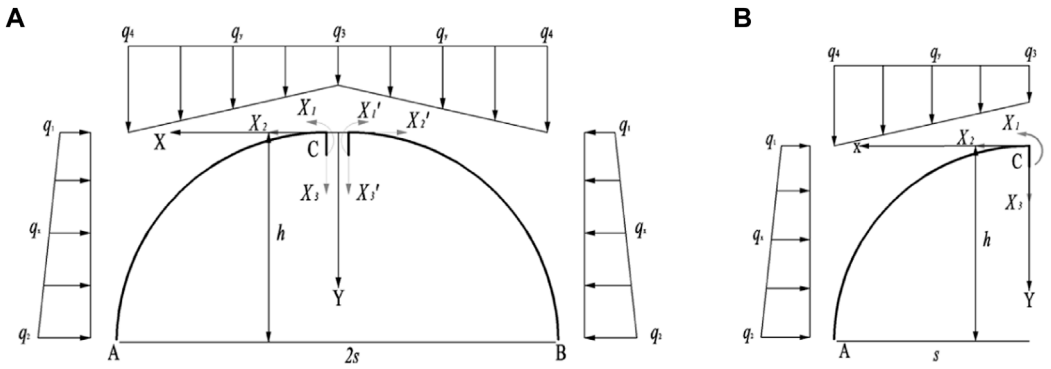

FIGURE 2
Calculating model of internal force of SRPA (Surrounding rock pressure arch): **(A)** Stress analysis, **(B)** Left half-span isolator.

Substituting Eqs. 1, 2, 16, into Eq. 18, the following equation can be obtained

$$\begin{cases} X_1 = \dfrac{\int_0^s \left[\dfrac{x(q_4+2q_3)}{3(q_4+q_3)}\cdot\left[\dfrac{(q_4-q_3)x^2}{2s}+q_3x\right]+\dfrac{y(q_2+2q_1)}{3(q_2+q_1)}\cdot\left[\dfrac{(q_2-q_1)y^2}{2h}+q_1y\right]\right]\sqrt{1+y'}\,\mathrm{d}x}{\int_0^s \sqrt{1+y'}\,\mathrm{d}x} \\ X_2 = \dfrac{\int_0^s \left[\dfrac{x(q_4+2q_3)}{3(q_4+q_3)}\cdot\left[\dfrac{(q_4-q_3)x^2}{2s}+q_3x\right]+\dfrac{y(q_2+2q_1)}{3(q_2+q_1)}\cdot\left[\dfrac{(q_2-q_1)y^2}{2h}+q_1y\right]\right]y^2\sqrt{1+y'}\,\mathrm{d}x}{\int_0^s y^2\sqrt{1+y'}\,\mathrm{d}x} \end{cases} \tag{19}$$

After calculating the redundant unknown forces X_1 and X_2 of the statically indeterminate structure, the internal force formula of any section of the arch without articulation can be obtained according to the equilibrium conditions of the isolated body, as shown below

$$\begin{cases} M(x) = M_c + X_1 + X_2 \cdot y \\ Q(x) = X_2 \cdot \sin\theta - T_x \cdot \sin\theta - T_y \cdot \cos\theta \\ N(x) = X_2 \cdot \cos\theta + T_y \cdot \sin\theta - T_x \cdot \cos\theta \end{cases} \tag{20}$$

where $M(x)$, $Q(x)$ and $N(x)$ are the bending moment, shear force and axial force of any section of arch without articulation respectively; and $\sin\theta = y'/\sqrt{1+(y')^2}$, $\cos\theta = 1/\sqrt{1+(y')^2}$.

Substituting Eqs. 1, 2, 16, 19 into Eq. 20, the internal force distribution of any section of SRPA can be written as

$$\begin{cases} M(x) = \left\{\dfrac{x(q_4+2q_3)}{3(q_4+q_3)}\cdot\left[\dfrac{(q_4-q_3)x^2}{2s}+q_3x\right]+\dfrac{y(q_2+2q_1)}{3(q_2+q_1)}\cdot\left[\dfrac{(q_2-q_1)y^2}{2h}+q_1y\right]\right\}+ \\ \dfrac{\int_0^s \left\{\dfrac{x(q_4+2q_3)}{3(q_4+q_3)}\cdot\left[\dfrac{(q_4-q_3)x^2}{2s}+q_3x\right]+\dfrac{y(q_2+2q_1)}{3(q_2+q_1)}\cdot\left[\dfrac{(q_2-q_1)y^2}{2h}+q_1y\right]\right\}\sqrt{1+y'}\,\mathrm{d}x}{\int_0^s \sqrt{1+y'}\,\mathrm{d}x}+ \\ \left\{\dfrac{x(q_4+2q_3)}{3(q_4+q_3)}\cdot\left[\dfrac{(q_4-q_3)x^2}{2s}+q_3x\right]+\dfrac{y(q_2+2q_1)}{3(q_2+q_1)}\cdot\left[\dfrac{(q_2-q_1)y^2}{2h}+q_1y\right]\right\}\cdot y \\ N(x) = \dfrac{\int_0^s \left\{\dfrac{x(q_4+2q_3)}{3(q_4+q_3)}\cdot\left[\dfrac{(q_4-q_3)x^2}{2s}+q_3x\right]+\dfrac{y(q_2+2q_1)}{3(q_2+q_1)}\cdot\left[\dfrac{(q_2-q_1)y^2}{2h}+q_1y\right]\right\}y^2\sqrt{1+y'}\,\mathrm{d}x}{\int_0^s y^2\sqrt{1+y'}\,\mathrm{d}x}\cdot\dfrac{1}{\sqrt{1+(y')^2}}\cdot \\ +\left[\dfrac{(q_4-q_3)x^2}{2s}+q_3x\right]\cdot\dfrac{y'}{\sqrt{1+(y')^2}}-\left[\dfrac{(q_2-q_1)y^2}{2h}+q_1y\right]\cdot\dfrac{1}{\sqrt{1+(y')^2}} \\ Q(x) = \dfrac{\int_0^s \left\{\dfrac{x(q_4+2q_3)}{3(q_4+q_3)}\cdot\left[\dfrac{(q_4-q_3)x^2}{2s}+q_3x\right]+\dfrac{y(q_2+2q_1)}{3(q_2+q_1)}\cdot\left[\dfrac{(q_2-q_1)y^2}{2h}+q_1y\right]\right\}y^2\sqrt{1+y'}\,\mathrm{d}x}{\int_0^s y^2\sqrt{1+y'}\,\mathrm{d}x}\cdot\dfrac{y'}{\sqrt{1+(y')^2}}\cdot \\ -\left[\dfrac{(q_2-q_1)y^2}{2h}+q_1y\right]\cdot\dfrac{y'}{\sqrt{1+(y')^2}}-\left[\dfrac{(q_4-q_3)x^2}{2s}+q_3x\right]\cdot\dfrac{1}{\sqrt{1+(y')^2}} \end{cases} \tag{21}$$

3 Model application and discussion

3.1 Research background

The Hongqinghe Coal Mine is located in the Dongsheng Coalfield, which is a typical mine with weakly cemented strata, and the main mining coal seam is 3^{-1}, with an average burial depth of 650 m, an average thickness of 6 m and an average dip angle of 2°. The working face adopts the comprehensive mechanized coal mining method of single inclined longwall mining with full height at one time, and the roof is managed by the full caving method. The length of the working face is approximately 300 m, the strike length is approximately 3,300 m, and the average propulsion speed is 12 m/d. The measured uniaxial compressive strength of rock is 11.56–37.89 MPa, the tensile strength is 0.74–2.4 MPa, the cohesion is 0.66–6.77 MPa, the internal friction angle is 10.56–30.65, and the friction coefficient of the coal and rock is approximately 0.22–0.34. The lateral pressure coefficient is between 0.8 and 1.5 (Sun et al., 2019). The immediate roof is a composite roof composed of mudstone, carbonaceous mudstone and coarse sandstone with an average thickness of 12 m, and the main roof is fine sandstone with an average thickness of 20 m. Above the main roof are mainly Jurassic and cretaceous weakly cemented strata. The occurrence characteristics and fracture morphology of overlying strata rocks are shown in Figure 3.

3.2 Reasonable axis analysis

The rational arch axis equation is an important characterization of the morphological characteristics of SRPA. According to the calculation results of Eq. 9, the rational arch axis equation of SRPA is a unary cubic function. In the range of $x \in [0, s]$, $y \in [0, h]$, selecting λ=1.2, f=0.3 and γ=27 kN/m^3, the morphological characteristics of the rational axis of the pressure arch in the far field surrounding rock in the full mining stage of the Hongqinghe Coal Mine are described in combination with Eq. 10.

As shown in Figure 4, the morphological characteristics are a cubic parabola with a downward opening, which is different from the axis equations of semicircle, semi-ellipse and quadratic parabola obtained

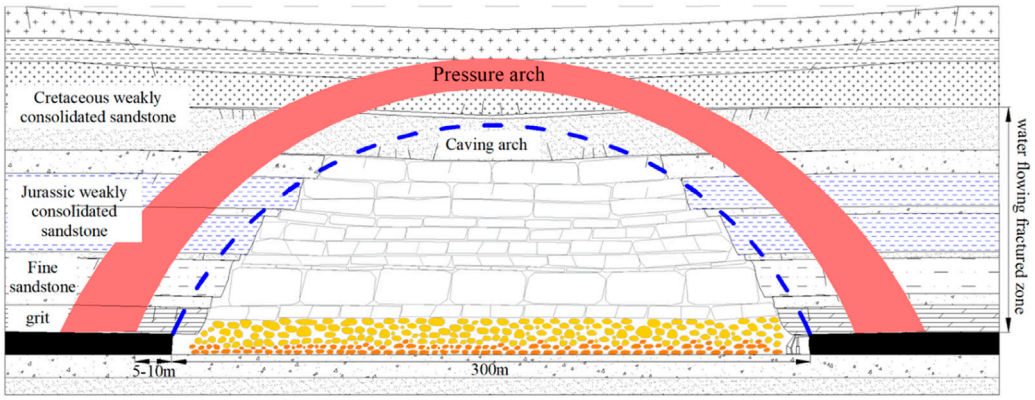

FIGURE 3
Occurrence characteristics and fracture morphology of overlying strata in Hongqinghe Coal Mine.

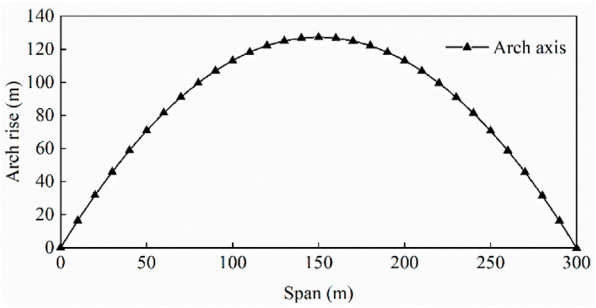

FIGURE 4
Morphological characteristic curve of SRPA (Surrounding rock pressure arch).

by uniformly distributed load studies (Xia et al., 2018, Wang et al., 2019), thus, the change of boundary conditions affects the shape of arch axis. The height of SRPA at the stage of full mining is 127 m. According to the prediction model of the water-conducting fracture zone (He et al., 2020), the height of the water-conducting fracture zone at the stage of full mining of the Hongqinghe Coal Mine is 105.5–114 m. Combined with Figure 3, the limit equilibrium zone range is 5–10 m. The calculated development height of the water-conducting fracture zone is 117–122 m, similar to the prediction model.

3.3 Rise-span relationship analysis

The rise-span relationship of the SRPA can be used to characterize the degree of the arch structure frankness and steepness, and it is an important index to reflect the force characteristics and distribution in arch. According to Eq. 13, the rise-span relationship of SRPA is related to mining depth H, friction factor f of the coal-rock mass, and lateral pressure coefficient λ. According to the measured data of the Hongqinghe Coal Mine, different parameters in Table 1 are selected and substituted into Eq. 13 to calculate, and the variation of SRPA rise-span ratio with lateral pressure coefficient λ and friction factor f of coal and rock mass is obtained.

As shown in Figure 5, according to the field-measured data, the rise-span ratio is between 0.3 and 0.5, and the long axis of the SRPA is the span, which is a flat arch structure along the advancing direction of the working face. The rise-span ratio increases non-linearly with lateral pressure coefficient increasing. When $\lambda < 1$, the growth rate is larger, and when $\lambda > 1$, the growth rate is slower. Lithology change has a significant influence on the mechanical characteristics of SRPA. With the enhancement of lithology, the larger the rise-span ratio of SRPA is, the less the influence of the lateral pressure coefficient is. Under the same lateral pressure coefficient, the harder the overlying strata are, the smaller the flattening rate. The analysis results are consistent with the numerical results in the literature obtained by Zhao (Zhao 2018).

3.4 Internal force analysis

The internal force distribution of SRPA is related to the morphological characteristics of the arch and external load. Since it is difficult to find the analytical solution for the calculation result of Eq. 21, Mathematica software is used to find the numerical solution. According to the actual data of the Hongqinghe Coal Mine, λ=1.2, f=0.3 and γ=27 kN/m^3 are selected, and the internal force distribution in the unhinged arch is calculated.

The illustration is displayed in Figure 6: under the trapezoidal load, the internal force distribution law of any section of the SRPA is as follows:

- The internal force at any section of SRPA has shear force, bending moment and axial force, and the axial force is always greater than the bending moment, and shear force. According to the provisions of “structural mechanics”, the axial forces in the figure are pressures, so the SRPA is maintained mainly by axial compression of any section to maintain the stability and bearing characteristics of the pressure arch.
- The axial compression of any section of SRPA is axially symmetric, and the distribution characteristics are basically

TABLE 1 Parameter assignment of SRPA (Surrounding rock pressure arch).

The parameter name	Value	The total number
Lateral pressure coefficient λ	0.8, 0.9, 1.0, 1.1, 1.2, 1.3, 1.4, 1.5	8
The friction factor f	0.22, 0.24, 0.26, 0.28, 0.3, 0.32, 0.34	7

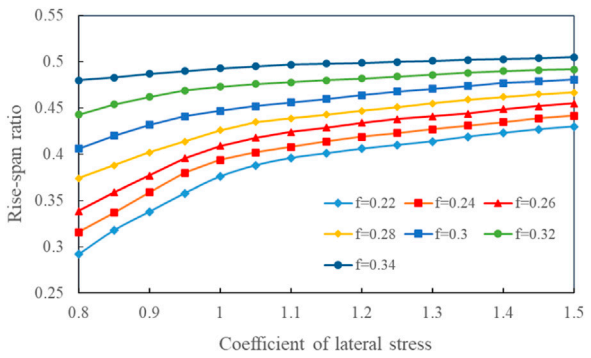

FIGURE 5
Variation law of rise-pan ratio of SRPA (Surrounding rock pressure arch).

consistent with the arch axis equation. In this case, the SRPA can achieve the best bearing performance. The pressure value increases from 77 kN at the vault position to 114 kN at the skewback position, by 48%.

- The bending moment of any section of SRPA is also axially symmetric, and three regions can be defined. The bending moment of any section of SRPA is greater than zero in the range of [0°, 30°] and [81°, 90°] on both sides of the axis of SRPA symmetry. According to the provisions of the bending moment direction in Figure 2 (counterclockwise is positive), the bending moment of any section of this region is taken for analysis. The bending moment of any section of the arch is tensile stress inside and compressive stress outside, and the SRPA is vulnerable to tensile failure in this region. Within the range of [30°, 81°] of the SRPA symmetry axis, the bending moment of the section is less than zero, indicating that the inner side of the arch is subjected to compressive stress, while the outer side is tensile stress.
- The shear force at any section of SRPA still presents an axisymmetric distribution, which can be divided into two parts. The value of shear stress is greater than zero in the range of [0°, 62°] on both sides of the SRPA symmetry axis, and the shear direction is directed to the center of the SRPA. Within the range of [62°, 90°], the sectional shear is less than zero, indicating that the shear direction deviates from the center of the SRPA.

4 Analysis of mechanical properties

4.1 Bearing characteristics

The reasonable axis equation and rise-span relationship are calculated by the SRPA model, and the calculation process of pressure arch is simplified into a compressive stress line, but in fact, the pressure arch is a shell structure with a certain thickness. Meanwhile, to form a stable bearing structure, SRPA should satisfy the arch structure of the rise-span relationship and arch thickness. Here, the thickness of the pressure arch is used to characterize its bearing characteristics. The thickness indicates the degree and range of the disturbed surrounding rock, which means that a small arch thickness can bear the small load of the arch itself and surrounding rock, and a large thickness can bear a larger surrounding rock load. Additionally, the thickness of the arch is determined mainly by the position of the inner and outer boundary lines of the pressure arch.

Currently, the determination of the inner and outer boundaries of the pressure arch is focused mainly on tunnel excavation, which is determined by the stress field characteristics. Three main criteria judge the outer boundary of the pressure arch: tangential stress, principal stress deflection, and the maximum principal stress judging criterion. Two main criteria determine the inner boundary of the pressure arch: The tangential stress judging criterion and the extreme value of the principal stress inside the arch (Chen et al., 2011; Rezaei et al., 2015, He and Zhang 2015). However, the mining field surrounding rock is different from small section excavation projects such as tunnels and caverns. As the coal seam continues to be mined, it is damaged rock range and the structural characteristics of the pressure arch develop dynamically upward, resulting in different stress distribution characteristics of the rock in different areas. It is unreasonable if the boundary location of different paths is determined by using the criterion of determining the boundary inside and outside the arch of the same SRPA. Therefore, it is necessary to determine the optimal arch range according to the judging criterion of the inner and outer boundaries of different stress paths. The stress examination path of the SRPA is defined as the vertical path from the center of the vault upward (such as "J" path in Figure 7), the arc path of arch waist backward to the arch body (such as "B-I" path in Figure 7) and the horizontal path of the skewback away from the arch body (such as "A" path in Figure 7). To facilitate the analysis, this study considers mainly the variability of stress distribution characteristics of the vault path and skewback path, the arch waist and skewback path are approximately the same, and the stress increasing is expressed as the abutment pressure magnitude of each stratified overlying stratum.

The outer boundary of the vault path can be discerned according to the definition of the SRPA. After coal mining, the surrounding rock formed a circular flow line of the maximum principal stress, and the direction of the maximum principal stress was deflected above the vault of the pressure arch. Assuming that the maximum compressive stress inside the arch is vertical, the maximum compressive stress from the arch upward turned from vertical to horizontal, and the maximum principal stress deflection point is taken as the base point of the outer boundary of the pressure arch, i.e., the main stress deflection judging criterion. Description of the degree of deflection of the maximum principal stress vector at various points in the surrounding rock after

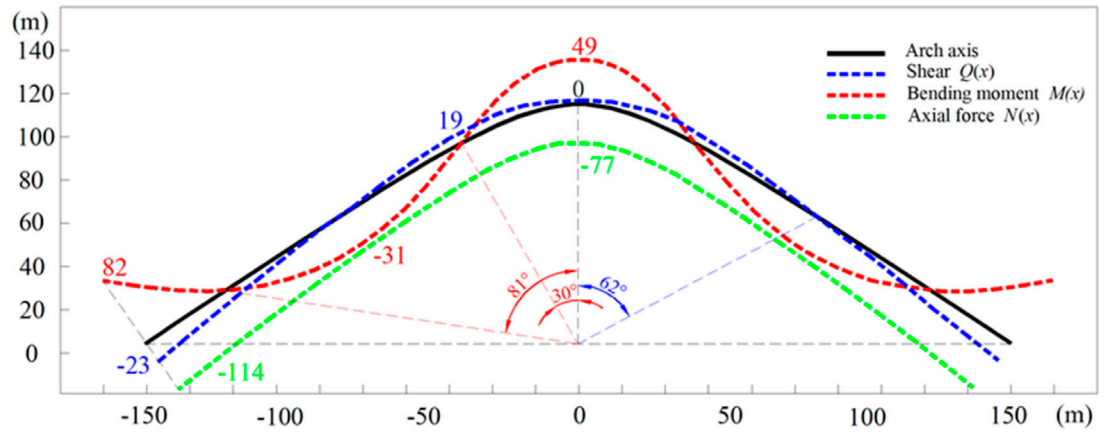

FIGURE 6
Distribution rule of internal force of SRPA (Unit of bending moment: kNm; Unit of shear and axial force: kN).

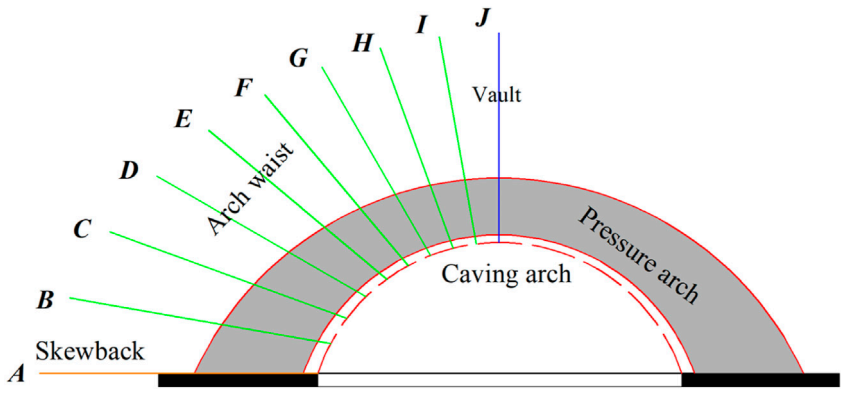

FIGURE 7
Schematic diagram of the stress examination path.

mining relative to its original direction can be expressed as the relative magnitude of the maximum principal stress compared to the vertical stress or horizontal stress. For example, for a stratum where the vertical stress is the maximum principal stress, an index of relative deflection δ is introduced to indicate the degree of deviation of the maximum principal stress vector from the vertical direction, as shown in Figure 8 (point A), which is defined as follows.

$$\delta = \frac{(\sigma_{\max} - \sigma_z)}{\sigma_{\max}}, \tag{22}$$

where $\sigma_{\max}$ is the maximum principal stress, and σ_z is the vertical stress.

To facilitate the calculation, the direction of the maximum principal stress vector gradually reverts to the vertical direction when $\delta < 5\%$; however, the physical significance expressed by the relative deflection index is not considered when $\delta > 5\%$.

The outer boundary of the skewback path can be analyzed according to the stress characteristics of the skewback position. The skewback position stress state is the range of unstable loads transmitted above the arch or the degree of stress concentration in the skewback part, i.e., the elastic zone range of over-abutment pressure at the working surface. The tangential stress increase factor D is introduced to reflect the degree of stress concentration at the skewback location and the arch effect pressure transfer range, such as the location shown at point C in Figure 8. For the convenience of calculation, D=1.05 is defined as the outer boundary of the skewback path.

$$D = \frac{\sigma_{zz}}{\sigma_{zz-ini}}, \tag{23}$$

where σ_{zz} is the tangential stress of the skewback path and $\sigma_{zz\text{-}ini}$ is the tangential stress of the skewback path in the original rock stress state.

For the vault and skewback path, inner boundary determination can be based on the maximum main stress extreme value determination criteria of the SRPA. After mining, the tangential stress gradually increases, and then gradually returns to the original stress. The point at maximum tangential stress is taken as the inner boundary of the pressure arch. The specific applicable criterion is shown in Table 2, and the locations of the inner and outer boundary lines are shown in Figure 8 (point B, D).

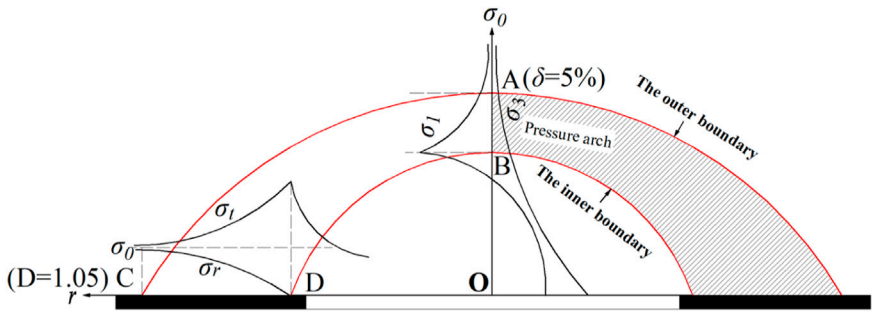

FIGURE 8
Location of inner and outer boundaries of different stress paths in the SRPA (Surrounding rock pressure arch).

TABLE 2 Criterions for the application of different stress examination paths.

Pressure arch boundary judging criterions	Examination paths		
	Vault	Arch waist	Skewback
Outer boundary	Relative deflection index	Tangential stress increase factor	Tangential stress increase factor
Inner boundary	Maximum principal stress extremes	Tangential stress extremes	Tangential stress extremes

The relative deflection index of the SRPA vault path is difficult to find by theoretical calculation, but it can be found by numerical simulation of the deflection characteristics of the principal stress (Kong et al., 2018), which is not discussed here. To study the influencing factors and variation laws of the SRPA thickness, the theoretical formula for calculating the arch thickness is proposed through the limit equilibrium conditions at the skewback.

$$\sigma_{tA} = \sigma_{rA}\tan^2\left(45^\circ + \frac{\varphi}{2}\right) + 2C\tan\left(45^\circ + \frac{\varphi}{2}\right), \tag{24}$$

where σ_{tA} and σ_{rA} are the tangential stress and radial stress at skewback A, respectively; C is the cohesion; and φ is the internal friction angle.

$$\sigma_{tf} = \frac{T_c}{t\sin\varphi} = \frac{\lambda rHh + rsfH - 1/2\lambda rh^2}{t\sin\varphi}, \tag{25}$$

$$\sigma_{rf} = \frac{rhs}{2\sin\varphi}, \tag{26}$$

where σ_{tf} and σ_{rf} are the tangential and radial stress extremes at the base of the SRPA, respectively, and t is the thickness of the SRPA.

Substitute Eqs. 24, 25 into Eq. 26 to simplify, we can obtain the thickness of SRPA

$$t = \frac{\lambda rHh + rsfH - \frac{1}{2}\lambda rh^2}{rh\tan^2\left(45^\circ + \frac{\varphi}{2}\right) + 2C\tan\left(45^\circ + \frac{\varphi}{2}\right)\sin\varphi}. \tag{27}$$

Eq. 27 shows that the arch thickness is affected mainly by the lateral pressure coefficient λ, the friction factor f of coal-rock body, the internal friction angle φ of overlying strata, the cohesion C and the burial depth H. According to the actual measurement data of the Hongqinghe Coal Mine, the values assigned to different parameters are listed in Table 3.

According to the analysis of all curve changes in Figure 9, when the rise-span ratio is in the range of 0.2–0.4, the thickness of the SRPA grows slowly with the increase of the rise-span ratio under the same parameter. When in the range of 0.4–0.6, the arch thickness increases rapidly with increasing rise-span ratio increasing, indicating that larger rise-span ratio can achieve the stable bearing characteristics. As shown in Figure 9A, when the rise-span ratio of SRPA is kept constant, the arch thickness increases as the lateral pressure coefficient rising. The larger the growth rate of the lateral pressure coefficient is, the more obvious the bearing characteristics of the arch, indicating that the increase in the lateral pressure coefficient has significant beneficial effects on the arch stability. As shown in Figure 9B, when the rise-span ratio of SRPA remains constant, the arch thickness increases basically linearly with lithological enhancement. For every 0.1 increase in friction factor, the arch thickness increases by 10.0% on average, illustrating that harder rocks increase the bearing performance of the arch, which can ensure the overhanging overlying strata load is effectively transferred to unmined rock formation in far field. As shown in Figures 9C, D, with the increase in cohesion and internal friction angle of the overlying strata, the tensile and shear strength gradually increase, but the SRPA thickness gradually decreases at the same time. The smaller the cohesion and internal friction angle are, the greater range of the surrounding rock for stress adjustment, and the larger arch thickness is needed to maintain a stable bearing. In Figure 9D, when the rise-span ratio is less than 3.5, the arch thickness is shown to be largely unaffected by the cohesion. According to the results of Section 3.2, the rise-span ratio of the weakly cemented stratum lies between 0.3 and 0.5 at the fully mining stage. According to the analysis of the actual measurement data of the Hongqinghe Coal Mine, the arch thickness of the weakly cemented stratum in the fully mining stage is within 28–47 m.

TABLE 3 Assignment of overlying strata parameters.

The parameter name	Value	The total number
Lateral pressure coefficient λ	0.6, 0.8, 1.0, 1.2, 1.4, 1.6	6
The friction factor f	0.15, 0.2, 0.25, 0.3, 0.35, 0.4	6
The angle of internal friction φ (°)	10°, 15°, 20°, 25°, 30°, 35°	6
Cohesion C (MPa)	0, 2, 4, 6, 8, 10, 12	7

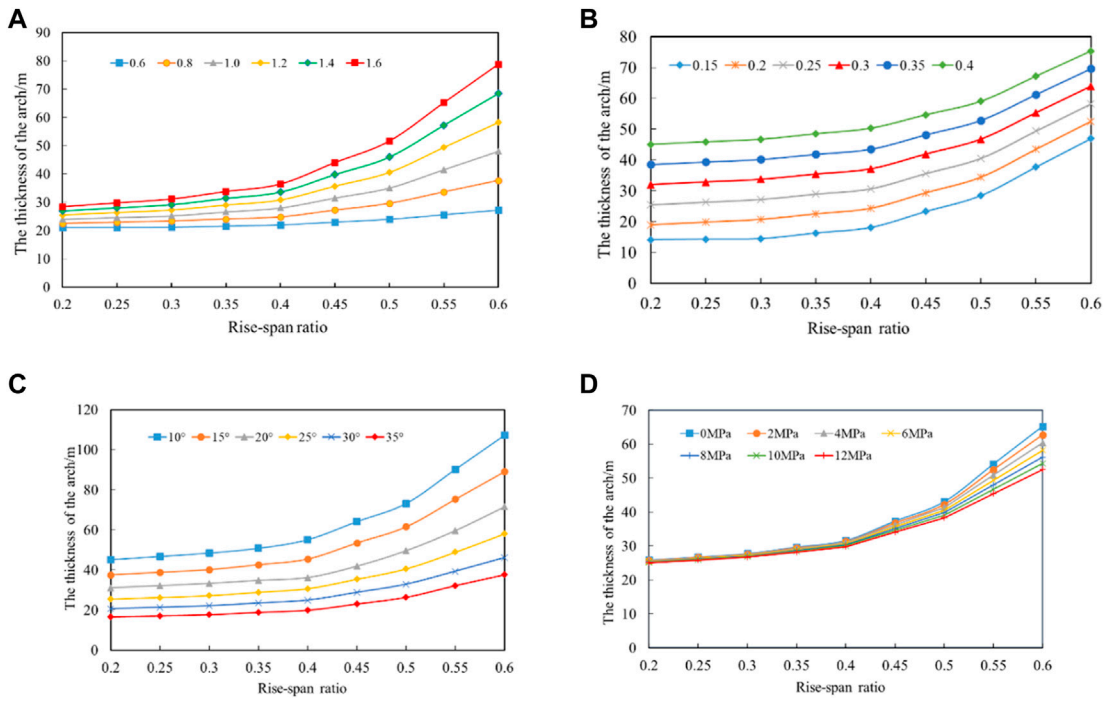

FIGURE 9
The variation law of the arch thickness of the SRPA (Surrounding rock pressure arch) with the rise-span ratio: **(A)** Lateral pressure coefficient, **(B)** Friction factor, **(C)** Angle of internal friction, **(D)** Cohesion.

4.2 Stabilization mechanism

4.2.1 Instability criterion of SRPA

As the working face advances, the overlying stratum fractures continue to evolve and penetrate, and the roof strata periodically produce separation, fracture and collapse. With the self-organization of surrounding rock, the peak area of the advance abutment pressure at the working face moves deeper into the coal wall, and the high stress area of the overlying strata moves deeper into the roof. The SRPA shows a dynamic evolution of equilibrium—expansion—limit—moving. The evolution and stability of the SRPA is non-linear and dynamic. The stress equilibrium state of the pressure arch determines its stability characteristics. In other words, when the maximum stress value at each place exceeds its rock limit bearing capacity, the pressure arch is destabilized at that position, leading to the high stress continuing to transfer to the deeper part and forming a new pressure arch. The SRPA stability is expressed in the form of the relationship between the degree of stress concentration caused by mining disturbances and the strength of the layered rock mass. Due to the large variability of the bearing capacity of the layered rock mass, the different space distributions of the strength envelope and the different degrees of stress concentration in each part of the vault, arch waist and skewback caused by mining disturbance, different strength criteria should be used to judge the stability of each part. Therefore, the dynamic evolution instability modes of the SRPA under insufficient mining conditions are classified into four types: Compression failure instability, tensile failure instability, shear failure instability, and compound failure instability.

$$\begin{cases} \text{Compression failure instability: } \sigma_i \geq \sigma_c \\ \text{Tensile failure instability: } \sigma_i \geq \sigma_t \\ \text{Shear failure instability: } \sigma_i \geq \tau \\ \text{Compound failure instability: } \sigma_i \geq \text{Min}(\sigma_c, \sigma_t, \tau) \end{cases}, \quad (28)$$

where σ_i is the equivalent stress suffered by each part of the vault, arch waist and skewback, MPa, it can be obtained by theoretical calculation, numerical and similar simulations. σ_c, σ_t, and τ are compressive strength, tensile strength and shear strength of the layered rock

mass, respectively, MPa. Where σ_c, σ_t, and τ are obtained by rock mechanics experiments.

4.2.2 Types of instability in the SRPA

According to the bearing characteristics and destabilization criterion of SRPA, its instability is first caused by the concentrated stress in a key position exceeding the ultimate bearing capacity of the surrounding rock, which causes the instability of other parts of the pressure arch under the chain reaction and finally the dynamic instability of the whole pressure arch. Through the distribution law of the internal force of the cross-section shown in Figure 6, and the exploration of the stability of surrounding rock shown in Figure 10, the rock mass in the key part of the SRPA producing mainly the following forms of damage destabilization.

- Tension failure of vault. As shown in Figure 6, the vault location is subject mainly to the joint action of the section bending moment and the section axial force, and the vault is presented as compressive stress under the action of the section axial force. Under the action of the section bending moment, the section bending moment here is greater than 0, and the maximum value of the bending moment of the vault reaches 49 kNm. According to the provisions of the direction of the bending moment in Figure 2 (counterclockwise is positive), the vault position in the section of the bending moment under the action of the performance of the arch inner side of the tension outside the pressure easily undergoes tensile failure. From the analysis of the stability of the surrounding rock, the vault of the SRPA is located in the complete rock layer at the top of the fractured rock mass. The articulated rock block structure formed at its lower part will produce inclined upward support reverse stress on the vault in the process of maintaining stability, which can be decomposed into tensile stress σ_z along the vertical direction Z and compressive stress σ_x along the horizontal direction X. When $\sigma_z \geq \sigma_c$, tensile failure occurs at the vault; when $\sigma_x \geq \sigma_t$, compression failure occurs at the vault. The tensile strength of the rock is much smaller than the compressive strength. Usually, the compressive stress σ_x has not yet reached the compressive strength σ_c, and the tensile stress σ_z has exceeded the tensile strength σ_t of the rock, leading to tensile damage to vault of SRPA. For example, the initial breaking of main roof and key stratum.
- Compression-shear failure of the arch waist. As shown in Figure 6, the location of the arch waist of the pressure arch is affected by the joint influence of the section axial force and shear force. The section shear force in this region is greater than 0, the maximum value is 19 kN, where shear failure is very likely to occur at the maximum location. From the analysis of the stability of the surrounding rock, the arch waist is located in the complete rock layer on both sides of the fractured rock mass. Under the action of overlying strata clamping, the inclined upward compressive stress of the articulated rock block structure acts on the arch waist. Meanwhile, the arch waist is also subjected to vertical compressive stress exerted by the mass of the overlying strata. When the shear stress on the shear surface at this location $\sigma_i \geq \tau$, shear failure occurs at the location of the arch waist of the SRPA. For example, the periodic breaking of main roof and key stratum.

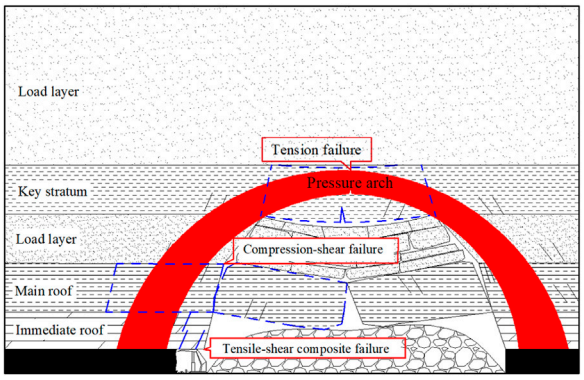

FIGURE 10
Types of instability in the SRPA (Surrounding rock pressure arch).

- Tensile-shear composite failure of skewback. As shown in Figure 6, the skewback of the SRPA will be affected by the joint effect of the section shear force, section bending moment and section axial force, and the internal forces here all reach the maximum value in axis region of arch. The section bending moment at skewback is positive, and the maximum value of 82 kNm, as in the above analysis, showing that this position is very vulnerable to tensile failure. Meanwhile, the section shear force is negative, and the maximum value is −23 kN, where shear failure is easily induced. From the analysis of the stability of surrounding rock, the skewback is located in the peak area of the abutment pressure around the working face. The coal-rock body at the skewback is subjected to the stress $k_0\gamma h$ in the vertical direction, while the coal-rock interlayer thrust T makes the rock layer misalign, leading to the skewback part of the larger mining disturbance stress σ_i, generally having $\sigma_i \geq$ max (σ_c, σ_t, and τ), so tensile and compression-shear compound failure destabilization occurs at the skewback. At the same time, the instability of the skewback is regional and sequential. For example, the periodic breakage of the immediate roof along the coal wall is manifested as compression shear failure of the skewback, and rib spalling at the working face is manifested as tensile failure of the skewback.

In summary, the types of failure instability of the SRPA are as follows: Tension failure at the vault, compression-shear failure at arch waist, and tension-shear composite failure at the skewback. The above types of instability occur independently, not simultaneously but in sequence. According to the instability process of key parts of pressure arch, the instability modes of SRPA can be divided into two categories:

1) “Skewback—vault (arch waist)” instability mode. That is, working face mining results in the gradual shift of skewback to the depth of coal wall, and the instability of the skewback leads to the instability of the vault (arch waist). Verified by similar material simulation experiments, as shown in Figure 11. When the working face advance to 75 m, the state is the stable state after the initial fracture of key stratum I. At this time, the vault of pressure arch develops to the position of key stratum II, as shown in Figure 11A. When the working face continues to advance to 100 m, the key stratum I is periodically broken. The excavation of the working

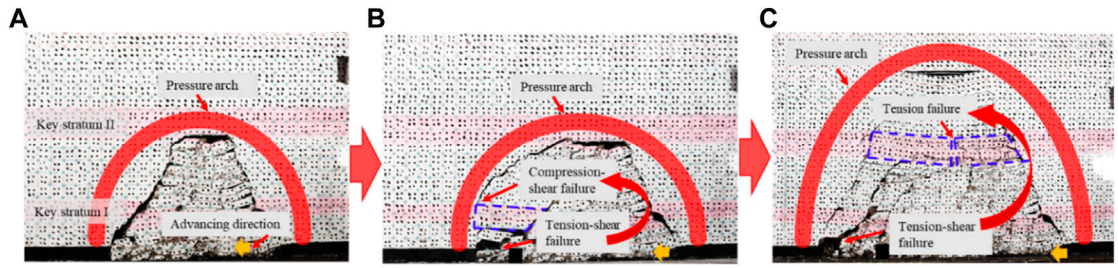

FIGURE 11
"Skewback—vault (arch waist)" instability mode: **(A)** State of key stratum I after initial fracture, **(B)** State of "skewback—arch waist" instability, **(C)** State of "skewback—vault" instability.

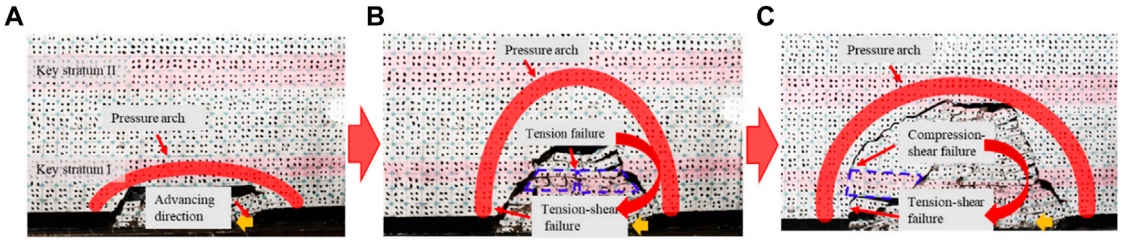

FIGURE 12
"Vault (arch waist)—skewback" instability mode: **(A)** Critical instability state of key stratum I, **(B)** State of "vault - skewback" instability, **(C)** State of "arch waist—skewback" instability.

face leads to the compression-shear failure of the direct roof at the skewback, which leads to the tension and shear fracture of the key stratum I at the arch waist, leading to the instability of the pressure arch. At this time, the pressure arch develops toward the depth of the coal wall, but not upward, as shown in Figure 11B. When the working face continues to advance to 150 m, the key stratum II will be broken for the first time. Similarly, the excavation of the working face will lead to the direct roof breaking at the skewback, which will lead to the tensile failure and instability of the key stratum II at the vault. At this time, the pressure arch will not only develop toward the depth of the coal wall, but also develop upward, as shown in Figure 11C.

2) "Vault (arch waist)—skewback" instability mode. That is, working face mining results in primary and periodic fracture of main roof or key stratum, the mining fissure and high stress zone of surrounding rock gradually transfer to the deep coal and rock mass, and a new pressure arch structure is formed in the depth. The instability of the vault (arch waist) causes the composite instability of the skewback. Verified by similar material simulation experiments, as shown in Figure 12. When the working face advances to 70 m, this state is the critical instability state of key stratum I. At this time, vault of the pressure arch develops to the position of key stratum I, as shown in Figure 12A. During the 30 min interval between the stoping of the working face, the key stratum I is initial fracture at this stage. The vault of the pressure arch is subject to tensile failure and instability, resulting in the skewback position transferring to the depth of the coal wall and the vault growing up to the position of key stratum II, as shown in Figure 12B. When the working face continues to advance to the 100 m position, at this time, the key stratum I is periodically broken, and the tension shear fracture occurs at the arch waist of the pressure arch, causing the skewback to transfer to the depth of the coal wall, as shown in Figure 12C.

5 Conclusion and discussions

This paper aims mainly at the structural characteristics of deep buried giant-thick weakly cemented strata in the western mining area of China. The bearing characteristics and stability mechanism of macroscopic SRPA are studied, and the conclusions are as follows.

(1) The macroscopic SRPA rational arch axis is calculated to be a cubic parabola with the opening downward, and the rise-span ratio is between 0.3 and 0.5. The pressure arch is a flat arch structure along the advancing direction of the working face, and the rise-span ratio increases non-linearly with lateral pressure coefficient and lithology increasing.
(2) According to the morphology of the arch axis, considering the internal and external boundary position of the pressure arch and the arch thickness, the range of the arch area under different stress paths is determined. The SRPA thickness at the full extraction stage is 28–47 m. Increasing the rise-span ratio and lateral pressure coefficient of the pressure arch is conducive to promote the stable bearing of the arch itself; the smaller the cohesion and internal friction angle are, the thicker the arch is needed to be maintain a stable bearing capacity.
(3) Based on arch without articulation theory and the calculated arch axis equation, a two-dimensional mechanical model of

SRPA is established. The axial force distribution of the section of the SRPA is basically consistent with the arch axis, which can have the best bearing capacity. Within the range of [0°, 30°] and [81°, 90°] on both sides of the symmetry axis, tensile failure easily occurs at the vault (49 kN·m) and skewback (82 kN·m). The maximum shear force is 19 kN at the arch waist and −23 kN at the skewback, and the pressure arch is prone to shear failure. According to the instability process of pressure arch key parts, the instability modes of SRPA can be divided into "skewback—vault (arch waist)" and "vault (arch waist)—skewback".

The study of the bearing characteristics and stability mechanism of macroscopic SRPA is used mainly to characterize the strong ground pressure behavior and surface subsidence in the mining process of the working face. In the future, we will focus on actively regulating the dynamic evolution of arches. By adopting the technology of overlying strata separation grouting, the grouting position can be accurately determined to control the surface subsidence and maintain the stability of the arch. Considering that the long-term existence of arches will cause potential safety hazards, the strong ground pressure behavior is controlled by roof hydraulic fracturing arch breaking technology.

Data availability statement

The original contributions presented in the study are included in the article/supplementary material, further inquiries can be directed to the corresponding author.

Author contributions

YY: Conceptualization, Investigation, Data curation, Formal analysis, Writing—Original Draft, Funding acquisition. YZ: Supervision, Resources, Writing—Review and Editing, Project administration. JM: Formal analysis, Investigation. PH: Writing—Review and Editing.

Funding

This work has been supported by the National Natural Science Foundation of China (Grant Nos. 52225402 and U1910206) and the Program of Shanxi Natural Foundation of China (20210302123336).

Conflict of interest

The authors declare that the research was conducted in the absence of any commercial or financial relationships that could be construed as a potential conflict of interest.

Publisher's note

References

Bednarek, L., and Majcherczyk, T. (2020). An analysis of rock mass characteristics which influence the choice of support. *Geomechanics and Engineering* 21 (4), 371–377. doi:10.12989/gae.2020.21.4.371

Cai, M. F. (2013). *Rock mechanics and engineering*. 2nd Edition. Beijing, China: Science press.

Chen, C., and Martin, G. R. (2002). Soil structure interaction for landslide stabilizing piles. *Comput. Geotech* 29 (5), 363–386. doi:10.1016/S0266-352X(01)00035-0

Chen, C. N., Huang, W. Y., and Tseng, C. T. (2011). Stress redistribution and ground arch development during tunneling. *Tunnelling and Underground Space Technology* 26 (1), 228–235. doi:10.1016/j.tust.2010.06.012

Dancygier, A. N., Karinski, Y. S., and Chacha, A. (2016). A model to assess the response of an arched roof of a lined tunnel. *Tunnelling and Underground Space Technology* 56, 211–225. doi:10.1016/j.tust.2016.03.009

Das, S. K. (2000). Observations and classification of roof strata behaviour over longwall coal mining panels in India. *International Journal of Rock Mechanics and Mining Sciences* 37 (4), 585–597. doi:10.1016/S1365-1609(99)00123-9

Du, X. L., Song, H. W., and Chen, J. (2011). Numerical simulation of the evolution of the pressure arch during coal mining. *J. China U. Min. Techno* 40 (6), 863–867.

El Kamash, W., El Naggar, H., and Nagaratnam, S. (2021). Numerical analysis of lateral Earth pressure coefficient in inclined mine stopes. *Geomech. Geophys. Geo-Energy Geo-Resour* 7 (3), 61–24. doi:10.1007/s40948-021-00255-4

Genis, M., Akcin, H., Aydan, O., and Bacak, G. (2018). Investigation of possible causes of sinkhole incident at the Zonguldak Coal Basin, Turkey. *Geomechanics and Engineering* 16 (2), 177–185. doi:10.12989/gae.2018.16.2.177

He, X., Zhao, Y. X., Zhang, C., and Han, P. H. (2020). A model to estimate the height of the water-conducting fracture zone for longwall panels in Western China. *Mine Water Environ* 39 (4), 823–838. doi:10.1007/s10230-020-00726-2

Jaouhar, E. M., Li, L., and Aubertin, M. (2018). An analytical solution for estimating the stresses in vertical backfilled stopes based on a circular arc distribution. *Geomechanics and Engineering* 15 (3), 889–898. doi:10.12989/gae.2018.15.3.889

Jiang, Y., Xu, S., and Hu, Y. (2008). *Structural Mechanics*. Beijing, China: Science Press.

Kong, D. Z., Li, Q., Wu, G. Y., and Song, G. F. (2021). Characteristics and control technology of face-end roof leaks subjected to repeated mining in close-distance coal seams. *Bulletin of Engineering Geology and the Environment* 80 (11), 8363–8383. doi:10.1007/s10064-021-02438-5

Kong, X. X., Liu, Q. S., Zhang, Q. B., Wu, Y. X., and Zhao, J. (2018). A method to estimate the pressure arch formation above underground excavation in rock mass. *Tunnelling and Underground Space Technology* 71, 382–390. doi:10.1016/j.tust.2017.09.004

Kratzsch, H. (1983). *Mining Subsidence Engineering*. New York, NY, USA: Springer-Verlag Berlin Heidelberg.

Li, A., Ma, Q., Lian, Y. Q., Ma, L., Mu, Q., and Chen, J. B. (2020). Numerical simulation and experimental study on floor failure mechanism of typical working face in thick coal seam in Chenghe mining area of Weibei, China. *Environmental Earth Sciences* 79 (5), 118–122. doi:10.1007/s12665-020-8839-2

Li, H. M., Li, H. G., Song, G. J., and Wang, K. L. (2016). Physical and mechanical properties of the coal-bearing strata rock in Shen dong coal field. *Journal of China Coal Society* 41 (11), 2661–2671. doi:10.13225/j.cnki.jccs.2016.1218

Mark, C., Agioutantis, Z., and Agioutantis, Z (2019). Analysis of coal pillar stability (ACPS): A new generation of pillar design software. *International Journal of Mining Science and Technology* 29 (1), 87–91. doi:10.1016/j.ijmst.2018.11.007

Ning, J. G., Wang, J., Tan, Y. L., Zhang, L. S., and Bu, T. T. (2017). *In situ* investigations into mining-induced overburden failures in close multiple-seam longwall mining: A case study. *Geomechanics and Engineering* 12 (4), 657–673. doi:10.12989/gae.2017.12.4.657

Oge, I. F. (2020). Field evaluation of flexible support system with radial gap (FSRG) under a squeezing rock condition in a coal mine development. *Geomech. Geophys. Geo-Energy Geo-Resour* 6 (3), 52–20. doi:10.1007/s40948-020-00175-9

Pardo, G. S., and Saez, E. (2014). Experimental and numerical study of arching soil effect in coarse sand. *Computers and Geotechnics* 57, 75–84. doi:10.1016/j.compgeo.2014.01.005

Poulsen, B. A. (2010). Coal pillar load calculation by pressure arch theory and near field extraction ratio. *International Journal of Rock Mechanics and Mining Sciences* 47 (7), 1158–1165. doi:10.1016/j.ijrmms.2010.06.011

Rezaei, M., Hossaini, M. F., and Majdi, A. (2015). Determination of longwall mining-induced stress using the strain energy method. *Rock Mechanics and Rock Engineering* 48 (6), 2421–2433. doi:10.1007/s00603-014-0704-8

Shabanimashcool, M., and Li, C. C. (2015). Analytical approaches for studying the stability of laminated roof strata. *International Journal of Rock Mechanics and Mining Sciences* 79, 99–108. doi:10.1016/j.ijrmms.2015.06.007

Sun, L. H., Ji, H. G., and Yang, B. S. (2019). Physical and mechanical characteristic of rocks with weakly cemented strata in Western representative mining area. *Journal of China Coal Society* 44 (3), 866–874. doi:10.13225/j.cnki.jccs.2018.6039

Wang, F., Xu, J. L., and Xie, J. L. (2019b). Effects of arch structure in unconsolidated layers on fracture and failure of overlying strata. *International Journal of Rock Mechanics and Mining Sciences* 114, 141–152. doi:10.1016/j.ijrmms.2018.12.016

Wang, S. R., Wu, X. G., Zhao, Y. H., Hagan, P., and Cao, C. (2019a). Evolution characteristics of composite pressure-arch in thin bedrock of overlying strata during shallow coal mining. *International Journal of Applied Mechanics* 11 (3), 1950030. doi:10.1142/S1758825119500303

Wen, Z. J., Rinne, M., Song, Z., Han, Z. Z., and Wen, J. H. (2015). Research on modelling of spatial dynamic structural mechanics and spatio-temporal evolution of coal mine stopes. *Teh. Vjesn* 22 (3), 607–613. doi:10.17559/TV-20150427175109

Xia, B. W., Zhang, X., Yu, B., and Jia, J. L. (2018). Weakening effects of hydraulic fracture in hard roof under the influence of stress arch. *International Journal of Mining Science and Technology* 28 (6), 951–958. doi:10.1016/j.ijmst.2017.12.024

Xie, H. P., Gao, F., Ju, Y., Gao, M. Z., Zhang, R., and Gao, Y. N., (2015). Quantitative definition and investigation of deep mining. *Journal of China Coal Society* 40 (1), 1–10.

Yang, W. B., Jiang, Y. J., Gu, X. X., Wang, Z. X., Shang, Y. C., and Zeng, W. H. (2021). Deformation mechanism and mechanical behavior of tunnel within contact zone: A case study. *Bulletin of Engineering Geology and the Environment* 80 (7), 5657–5673. doi:10.1007/s10064-021-02255-w

Yavuz, H. (2004). An estimation method for cover pressure re-establishment distance and pressure distribution in the goaf of longwall coal mines. *International Journal of Rock Mechanics and Mining Sciences* 41 (2), 193–205. doi:10.1016/S1365-1609(03)00082-0

Zhang, G. J., Guo, G. L., Lv, Y. N., and Gong, Y. Q. (2020). Study on the strata movement rule of the ultrathick and weak cementation overburden in deep mining by similar material simulation: A case study in China. *Mathematical Problems in Engineering* 2020, 1–21. doi:10.1155/2020/7356740

Zhang, J. M., Li, Q. S., Zhang, Y. Z., Cao, G., and Wang, X. Z. (2019). Definition of deep coal mining and response analysis. *Journal of China Coal Society* 44 (5), 1314–1325. doi:10.13225/j.cnki.jccs.2019.6018

Zhang, J., Zhang, Y. S., Du, W. Z., Wang, H. W., and Serati, M. (2021). An analytical approach to estimate the mechanical state of roof strata in underground longwall mining. *Geomechanics and Engineering* 27 (1), 55–62. doi:10.12989/gae.2021.27.1.055

Zhao, Y. H. (2018). *Research On Evolution Characteristics And Instability Mechanism Of Composite Pressure Arch Of Overlying Strata During Shallow Coal Mining*. Jiaozuo, China: Ph.D. Dissertation, Henan Polytechnic University.

Zhao, Y. H., Yu, J., Zhou, C. H., Zhao, K., and Xiao, H. G. (2021). Characterization of pressure arching effect of arch shell surrounding rock considering deviation of principal stress axis. *Chinese Journal of Geotechnical Engineering* 43 (10), 1842–1850.

Zhao, Y. X., and Liu, B. (2021). Deformation field and acoustic emission characteristics of weakly cemented rock under Brazilian splitting test. *Natural Resources Research* 30 (2), 1925–1939. doi:10.1007/s11053-020-09809-x

Zou, X. Z. (1989). New explanation on the hypothesis of pressure arch. *Ground Press. Roof Control* 1989 (01), 67–68+93.

frontiers | Frontiers in Earth Science

TYPE Original Research
PUBLISHED 10 February 2023
DOI 10.3389/feart.2023.1125678

OPEN ACCESS

EDITED BY
Yingfeng Sun,
University of Science and Technology Beijing, China

REVIEWED BY
Jiliang Pan,
University of Science and Technology Beijing, China
Huining Ni,
China University of Mining and Technology, China
Wang Qun,
Taiyuan University of Technology, China

*CORRESPONDENCE
Ke Yang,
keyang2003@163.com

SPECIALTY SECTION
This article was submitted to Environmental Informatics and Remote Sensing, a section of the journal Frontiers in Earth Science

RECEIVED 16 December 2022
ACCEPTED 20 January 2023
PUBLISHED 10 February 2023

CITATION
He X, He S, Cai Y, Xu R and Yang K (2023), Investigation on rational width of coal pillar and roadway support in isolated panel of extra-thick coal seam.
Front. Earth Sci. 11:1125678.
doi: 10.3389/feart.2023.1125678

Investigation on rational width of coal pillar and roadway support in isolated panel of extra-thick coal seam

Xiang He[1,2,3], Shuxin He[1,2,3], Yongbo Cai[1,4], Ruiyang Xu[5] and Ke Yang[2,3]*

[1]Joint National-Local Engineering Research Centre for Safe and Precise Coal Mining, Anhui University of Science and Technology, Huainan, Anhui, China, [2]Hefei Comprehensive National Science Center, Institute of Energy, Hefei, Anhui, China, [3]School of Mining Engineering, Anhui University of Science and Technology, Huainan, Anhui, China, [4]Emergency Science Research Institute, Chinese Institute of Coal Science, Beijing, China, [5]School of Energy and Mining Engineering, China University of Mining and Technology (Beijing), Beijing, China

The methods of numerical simulation and on-site measurement is used to analysis reasonable coal pillar width (CPW) and roadway support in isolated panel of extra-thick coal seam. Numerical modeling shows that a maximum vertical stress in isolated panel is 32.9 MPa, and stress concentration factor reaches 2.99, which is more affected by the mining of adjacent panel, and the peak stress on both sides is higher. By comparing the failure and deformation characteristics of different pillar widths, it is shown that a 6 m pillar can reach the load requirements of overlying strata and ensure that the roadway is in an undamaged and controllable environment. According to the asymmetry of surrounding rock deformation, the final joint control technology of asymmetric anchor cables, high intensity anchor cables, and coal pillar grouting is proposed and get good control effect on site. The research results provide guidance value for surrounding rock control under similar geological condition.

KEYWORDS

coal pillar, stress and displacement, roadway support, isolated panel, extra-thick coal seam

1 Introduction

As the development of modern productive and effective coal mines, extra-thick coal seams have increasingly been the major coal seams in China (Si et al., 2015; Tewari et al., 2018). Recoverable reserves of thick and extra-thick coal seam in China account for approximately 43% of a overall recoverable reserve of coal in China (Poulsen, 2010; Bai et al., 2015). Thick and extra-thick seams have a variety of mining methods due to their large coal seam thickness. At present, the fully mechanized caving mining method is widely promoted and practiced in China, such as Datong mining area, Pingshuo mining area, Shendong mining area, etc (Kang et al., 2009; Shen, 2013; Lisjak and Grasselli, 2014; Gao and Kang, 2016). The fully mechanized caving mining method will produce a certain proportion of coal loss (He et al., 20202020). Reasonable pillar reservation plays a key role in maintaining the stability and safety of the stope and reducing coal waste (Medhurst and Brown, 1998).

Currently, a number of mining experts have performed extensive investigation on the stability and size of yield pillar. According to the integrated pressure and deformation measurement device, Yu et al. (Yu et al., 2016) studied the pressure and displacement variation characteristics of yield pillars. By considering joint fissures, Esterhuizen et al. (Esterhuizen et al., 2011) proposed a

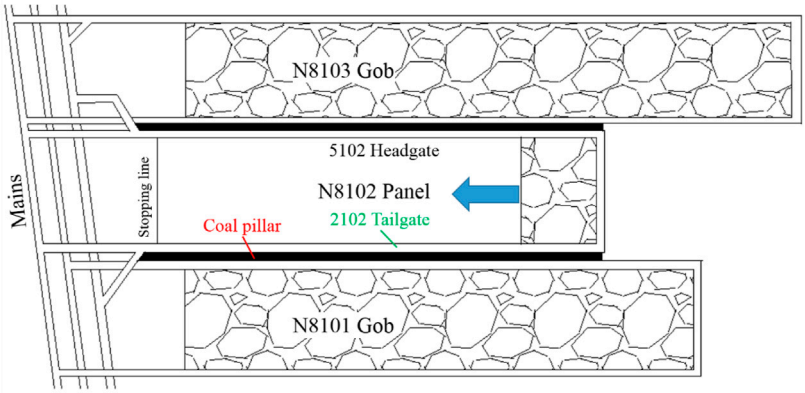

FIGURE 1
The relative position of N8102 panel.

mathematical formula to calculate coal pillar strength. According to method of numerical simulation and field application, Jawed and Sinha (Jawed and Sinha, 2018) studied the coal pillar design and roadway stability under the condition of inclined thin seam. By selecting a reasonable constitutive model for coal pillar, Zhang et al. (Zhang et al., 2017) analyzed the variation of stress and extent of damage. According to field data collected on a coal pillar in underground area, Salamon et al. (Salamon and Munro, 1967; Salamon, 1970; Salamon et al., 1998) developed an equation that considers the pillars strength and size, which is successfully adopted for pillar design. Through writing FISH language and drilling peeps, Wu et al. (Wu et al., 2018) explored distribution characteristics of tension fractures and shear fractures at coal pillars of different sizes, laying a foundation for the study of surrounding rock control. Based on the discrete element numerical simulation method, Gao et al. (Gao et al., 2015) reveals the mechanism of extrusion deformation occurring in coal pillars, which provides guidance basis for gob-side entry support. Through numerical simulation and laboratory experiments, Li et al. (Li et al., 2014) investigated the plastic zone distribution characteristic of yield pillar rib and solid coal rib to guide a pillar design. Wang et al. (Wang et al., 2016) explored the deformation velocity and acceleration of different coal pillar sizes with the effect of dynamic loads. By analyzing overall process of coal pillar deformation and failure, Wagner obtained that the existence of elastic zone is conducive to maintaining the stability of yield pillar. By exploring the evolution characteristics of deviatoric stress in deep large deformation surrounding rock, Wang et al. (Wang and Xie, 2022) proposed to use anchor cable truss for horizontal and vertical displacement control. Yang et al. (Yang et al., 2017) used shotcrete and bolt to control the roadway failure through simulating the law of crack propagation in the roadway under supported and unsupported conditions.

Above research performed a lot of investigation on the stability and size design of coal pillar to ensure the safe production of the panel. However, there are few studies on coal pillar in the isolated panel with the extra-thick coal seam. In view of this, the means of numerical model and on-site test were adopted to explore the evolution law of yield pillar failure and deformation in the isolated panel with extra-thick coal seams, and then clarify the CPW and roadway support scheme.

Stratum	Thickness (m)	Lithology	Columnar
Shanxi Formation of Lower Permian System	22	Medium fine sandstone	
	6	Sandy mudstone	
	4	Siltstone	
	5	Fine sandstone	
	10	Medium coarse grained sandstone	
Upper Carboniferous Taiyuan Formation	5	Carbonaceous mudstone	
	18	Coal seam	
	2	Mudstone	
	6	Sandy mudstone	

FIGURE 2
The comprehensive geological histogram of the N8102 panel.

2 Project overview

The N8102 panel mainly mines coal 3–5#, with the thickness of 18 m and a average dip angle of 1°. The alignment and inclined length is 1,516 m and 251 m, respectively. The buried depth of the panel is 450 m. Surrounding areas of N8102 panel are solid coal area, N8101 gob, three panel main roadways and N8103 gob, as shown in Figure 1.

The roof of 2,102 tailgate is as follows: A main roof is 10 m thick medium coarse-grained sandstone. A immediate roof is 5 m thick carbonaceous and sandy mudstone. A immediate floor is 2 m thick high-collared mudstone and sandy mudstone. A main floor is 6 m thick sandy mudstone. Figure 2 shows a comprehensive geological histogram of N8102 panel.

3 Numerical simulation

3.1 Numerical modeling

Taking practical engineering geological environment of 8,102 panel as the background, the panel and the panel on both

10.3389/feart.2023.1125678

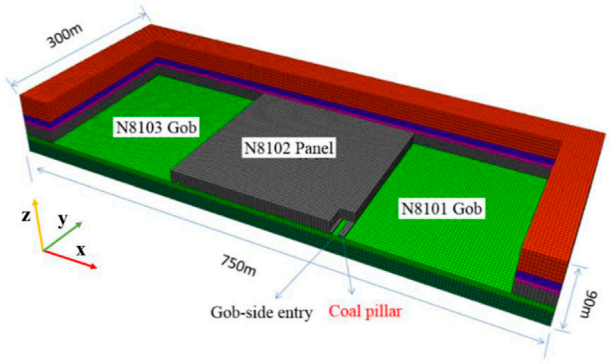

FIGURE 3
Numerical model.

adjacent sides are selected to establish a model (Figure 3). Specific dimension of the model is 750 m × 300 m × 90 m.

Due to the non-homogeneity of a rock mass within a strata, the physico-mechanical parameters obtained in a laboratory are those of intact rock. The mechanical parameters in the laboratory are modified to apply to the actual conditions of a rock mass. Therefore, a rectangular model with dimensions of 12 m × 12 m × 24 m (length × width × height) is created to simulate the compression process of a rock mass, where the mesh size is consistent with the dimensions of the roadway surrounding rock in this paper. By using a trial-and-error approach, parameter modification is considered complete when the macro-mechanical characteristics in a model are consistent with the field. As the mined space on both sides of N8102 isolated panel is huge, double yielding model is used to simulate the filling effect of the gangue, which can reflect the support action of the gangue caving from the goaf. The model adopts the Moore-Coulomb damage criterion with fixed displacements around all sides and bottom of a model, with vertical loads applied to its top. Buried depth of N8102 panel is 450 m. Bulk density of overlying strata is 2,500 kg/m^3. The load applied on the model is 9.922 MPa. Table 1 shows the parameters of each rock stratum when the numerical model is established. Elastic modulus, Poisson's ratio, cohesion and tensile strength are modified in a certain proportion according to the laboratory test results (Itasca, 2007; Cai et al., 2013).

3.2 Stress distribution characteristics of isolated panel

During the simulation of excavation, Tecplot software was used to extract the distribution data and stress nephogram of the vertical stress in N8102 panel after mining on one side and mining on both sides, as shown in Figure 4. Statistical charts were drawn by Origin platform (Figure 5).

The comparative analysis of Figures 4, 5 shows that.

1) After the mining of N8101 panel is completed and the gob collapse is stable, a bearing pressure concentration area is formed at the side of N8102 panel close to the goaf. Peak stress at the roadway middle line can reach 28 MPa, and the stress concentration factor is 2.55. This is because as N8101 panel is mined, the roof is broken, and the bearing stress is transferred to the panel. Vertical stress of the panel reaches more than 25 MPa within the range of 9–20 m, and the peak stress occurs at 14.5 m from the side wall of the gob. As far as 55 m distance to the coal barrier, the vertical stress in N8102 panel should drop to the *in-situ* stress. Because N8101 panel has a large mining space, the effect extent of lateral abutment stress is large.
2) After the mining of N8101 and N8103 panels is completed, and the overlying strata collapse stably, the vertical stress concentration area appears on both sides of N8102 isolated panel. Because the mining space on both sides is roughly equal, and the coal seam thickness and roof lithology are similar, the vertical stress of the isolated panel is symmetrically distributed. Maximum vertical stress is 32.9 MPa, and a stress concentration factor reaches 3.0. Within the change from 0 to 5.2 m on both sides of the panel, minimum vertical stress reaches 6.4 MPa, and then stress increases rapidly to reach the *in-situ* stress at 5.2 m. This is because the shallow solid coal side is greatly affected by mining and is severely damaged. The internal bearing capacity of broken coal body is lower than that of deep coal body, and stress also transfers to the deep solid coal. It indicates that the range 0–5.2 m is the broken area of the coal body. The stress continues to increase, reaching the peak stress at 14.2 m, that is, the elastoplastic junction of coal mass, and then reducing to *in-situ* stress at 70 m, which is called the stress rise zone.
3) It can be seen from the comparison between mining on one side and mining on both sides of N8102 panel that isolated panel is more impacted by the adjacent panels extraction, and maximum stress in the concentration area is higher. The isolated panel is also affected by the lateral abutment pressure in a larger range, and the stress

TABLE 1 Parameter selection of coal and rock.

Roof	Density Kg/m^3	Shear modulus /GPa	Bulk modulus /GPa	Cohesion /MPa	Internal friction angle /(°)
Overburden rock	2500	7.81	11.93	6.9	36
Main roof	2745	8.43	12.31	9.25	34
Immediate roof	2350	7.75	10.21	5.2	32
Coal seam	1,461	0.43	5.1	1.13	16
Immediate floor	2150	2.51	3.70	2.61	31
Main floor	2658	7.84	12.00	7.2	35

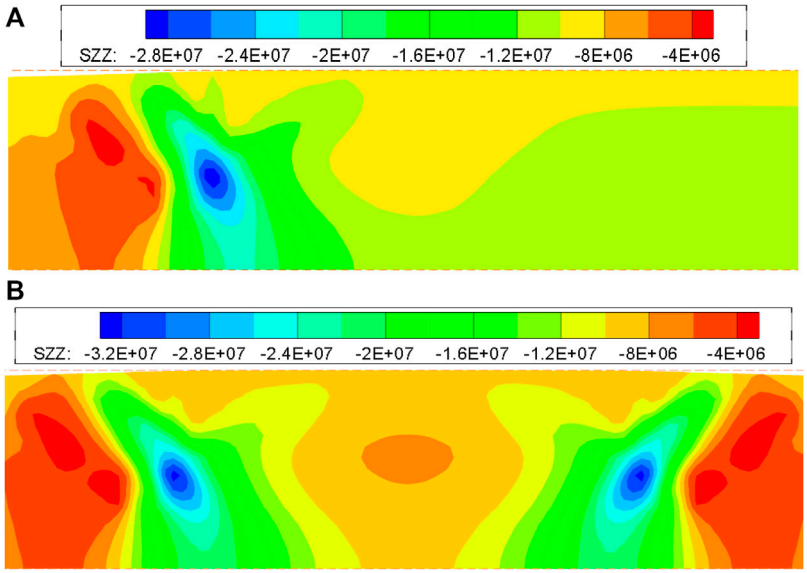

FIGURE 4
Variation characteristics of vertical stress in N8102 panel after mining. **(A)** Mining on one side; **(B)** mining on both sides.

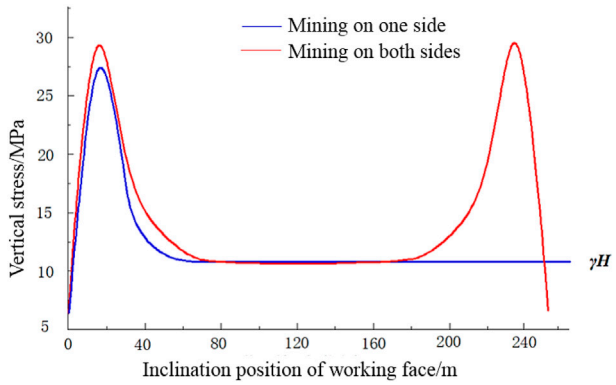

FIGURE 5
Vertical stress distribution curve.

environment is more complex. Therefore, in the process of gob-side entry driving at isolated panel, selecting a scientific and reasonable CPW is more important for the control surrounding rock stability.

3.3 Vertical stress analysis of different CPW during roadway excavation

When the numerical calculation software reaches convergence, vertical stress distribution of the yield pillar in N8102 isolated panel is obtained (Figure 6). Tecplot software is used to set the vertical stress measuring line in the middle of coal pillar simulation schemes. Distribution size of vertical stress in the yield pillar extracted by the monitoring line is obtained (Figure 7). Peak stress distribution curve of virgin rib and pillar rib are obtained (Figure 8).

From the above analysis that a lateral abutment pressure concentration area in N8102 panel is located in the middle of the solid coal rib slightly higher than the roadway. The maximum of the stress concentration area is 32.9 MPa. With the increase of CPW, roadway approaches stress concentration area, and peak value of the lateral abutment pressure decreases from 32.9 MPa to 28.9 MPa. With the increase of CPW, surrounding rock stress becomes larger and larger. When CPW is small, the roadway is generally in a safe and stable environment at the side of the adjacent gob. When CPW is greater than 8 m, vertical stress of surrounding rock increases rapidly. When the CPW is less than 8 m, the roadway is less influenced by the high lateral abutment pressure on the solid coal side. When CPW reaches 12 m, lateral abutment stress begins to transfer to the coal pillar side, the stress concentration begins to appear within the yield pillar and peak stress is greater than *in-situ* stress.

As shown in Figure 7, when CPW increases from 4–22 m, vertical stress of yield pillar presents an obvious unimodal distribution, and presents a pattern of increase followed by decrease from the gob side to the roadway side. Stress concentration occurs in the yield pillar, and stress concentration factor is different, and the factor increases with the increase of CPW. When CPW increases from 4 m–8 m, stress extreme value in the yield pillar is always closer to the gob side. When CPW increases from 8 m–22 m, vertical stress extreme value in the yield pillar is closer to the side of roadway. When CPW is 4 m, maximum of the vertical stress in the narrow yield pillar is lower than the *in-situ* stress at the depth of coal pillar. It indicates that a large area of crushing area appears in the yield pillar and its support capacity is correspondingly reduced due to breaking rotation of rock and high lateral bearing pressure of the panel. In the process of increasing the CPW from 6 m–22 m, extreme value of vertical stress inside the yield pillar is always greater than the *in-situ* stress at the depth of pillar, and the area where the stress inside the yield pillar is greater than *in-situ* stress is closely associated with CPW. After the CPW increases, bearing capacity to the overlying rock is also enhanced.

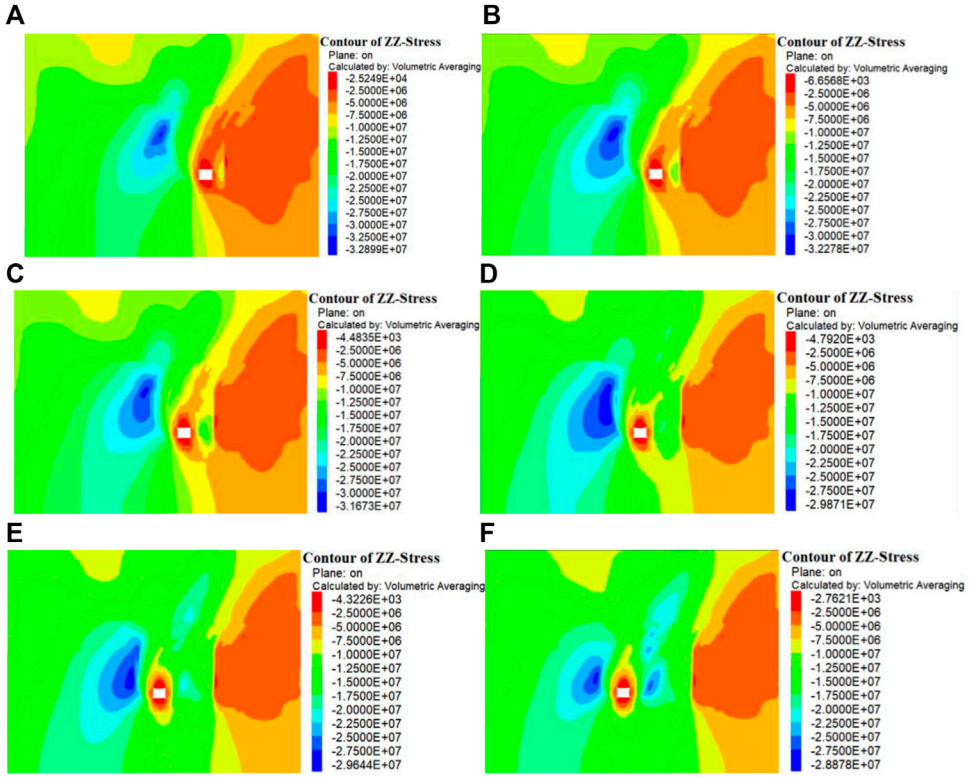

FIGURE 6
Vertical stress distribution characteristics with various CPW. **(A)** 4 m; **(B)** 6 m; **(C)** 8 m; **(D)** 12 m; **(E)** 16 m; **(F)** 22 m.

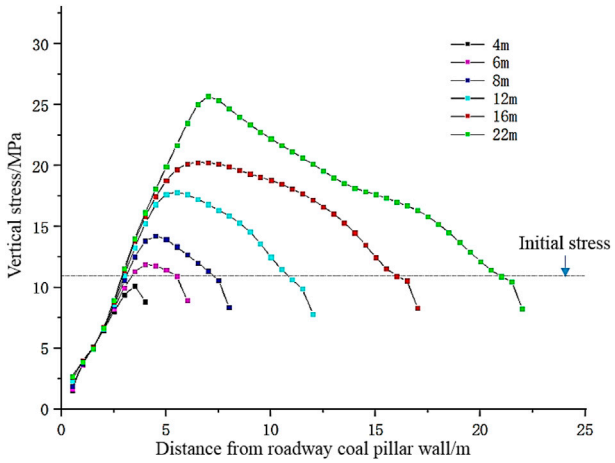

FIGURE 7
Vertical stress distribution curve with different CPW.

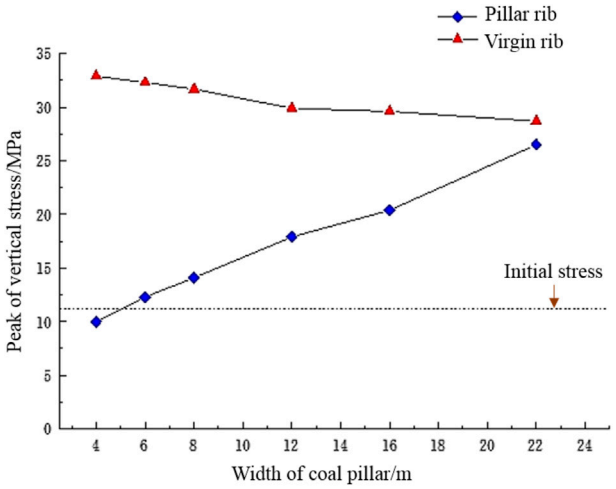

FIGURE 8
Peak of vertical stress distribution curve.

As shown in Figure 8, when CPW increases from 4–22 m, peak stress on the yield pillars continues to increase. When CPW is 4 m, peak stress of the yield pillar is lower than the initial stress at depth of pillar. It shows that the 4 m yield pillar is greatly influenced by panel excavation, and damage enters a broken state. When CPW is 6 m, peak stress of the yield pillar begins to exceed the initial stress, indicating that the 6 m coal pillar has good bearing capacity.

3.4 Effect of CPW on vertical displacement during roadway excavation

From Figures 9, 10, the roof subsidence shows an increasing trend as the CPW increases. When the CPW is less than 8 m, the roof subsidence rises slowly. The maximum roof subsidence for the 6 and

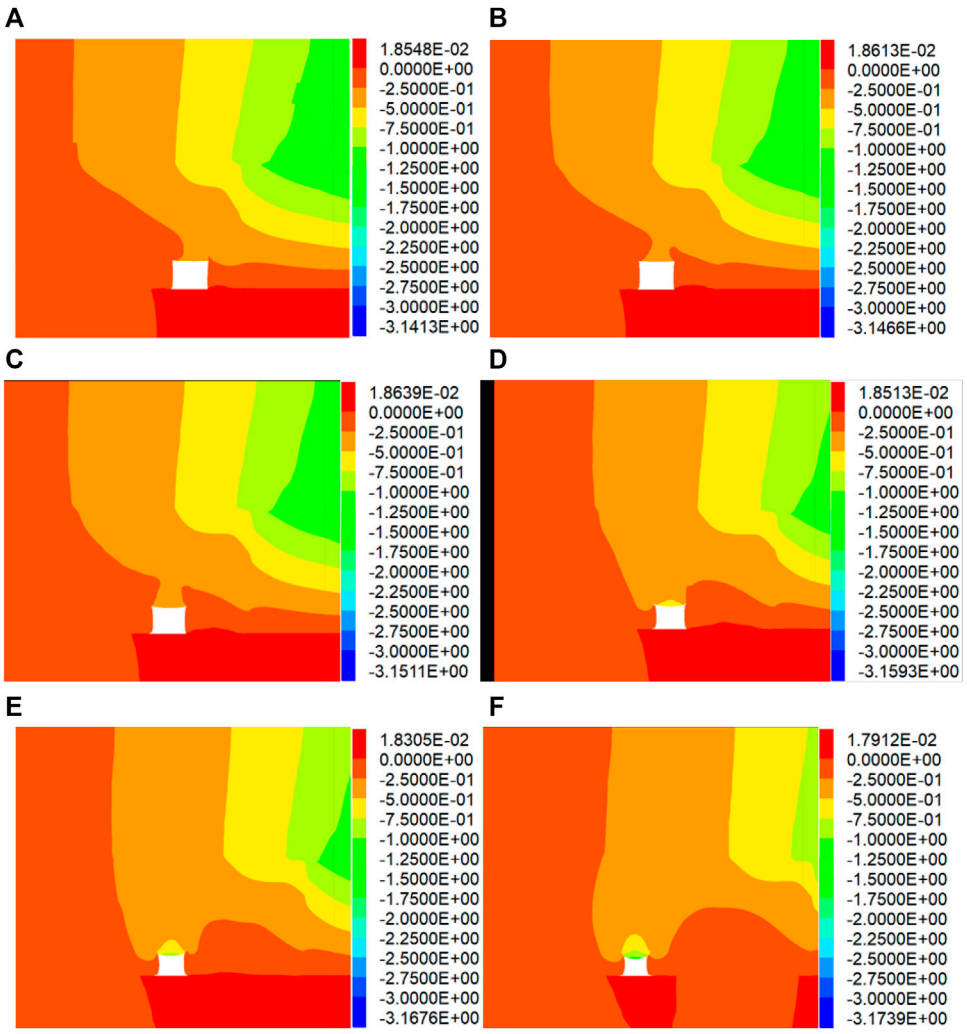

FIGURE 9
Vertical displacement distribution characteristics at various CPW. **(A)** 4 m, **(B)** 6 m, **(C)** 8 m, **(D)** 12 m, **(E)** 16 m, **(F)** 22 m.

8 m CPW is 390 mm and 410 mm respectively, an increase of 24.5% and 33.9% respectively compared to the 4 m pillar width. Meanwhile, as the CPW increases, the position of maximum roof subsidence shifts from the side of pillar towards the centre of roof. When the CPW is greater than 8m, roof subsidence in a roadway begins to rise sharply. The maximum subsidence at 12 m and 20 m CPW increases by 68.1% and 141.6% respectively compared to the 4 m pillar width. Among them, the location of maximum subsidence is distributed in the middle of a roof.

3.5 Effect of CPW on horizontal displacement during roadway excavation

Under the conditions of coal pillar with different widths, the displacement characteristics at pillar ribs and solid coal ribs are that the displacement above the rib is significantly greater than the displacement at the lower end of the rib (Figure 11). It can be seen that the roadway pressure mainly comes from the key block rotary

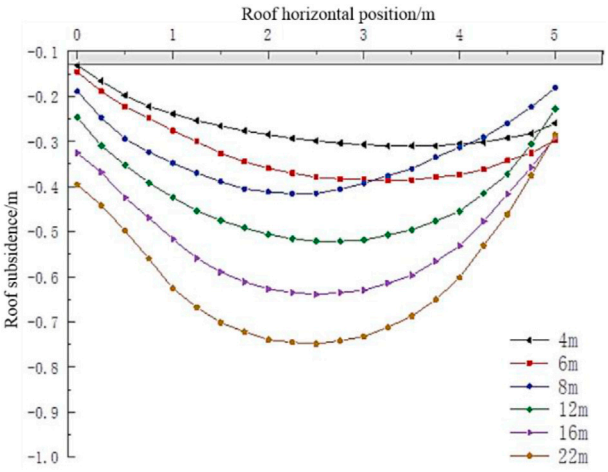

FIGURE 10
Roof subsidence with various CPW.

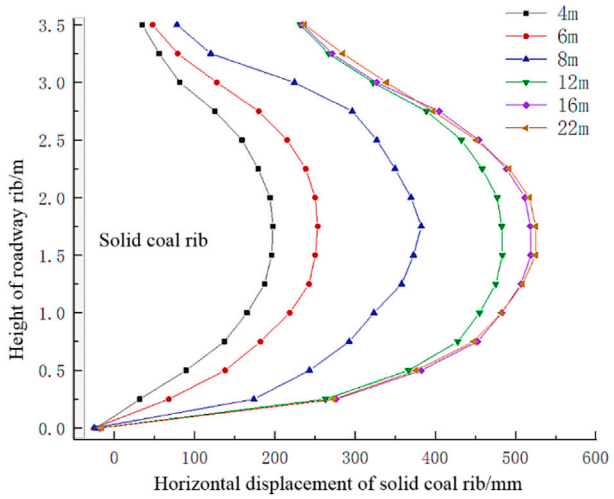

FIGURE 11
Horizontal displacement of solid coal rib at various CPW.

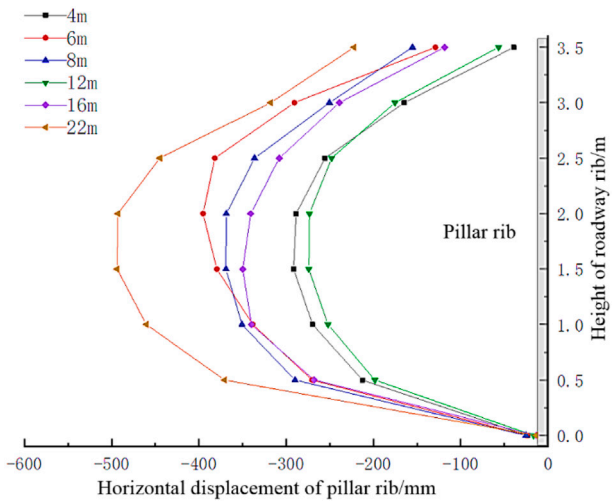

FIGURE 12
Horizontal displacement at coal pillar rib under various CPW condition.

subsidence at the upper part and the high lateral abutment pressure. Because the coal seam of N8102 panel is very thick, the pressure is mainly concentrated in the position inclined to the upper side of a roadway.

As the CPW grows, the solid coal rib is more seriously affected by it, and the horizontal displacement increases (Figure 12). The maximum horizontal displacements on coal pillar ribs and solid coal ribs of 6 m pillar width are 403 mm and 272 mm respectively, an increase of 56.3% and 38% respectively compared to the 4 m pillar. The reason for this is that the 4 m coal pillar is severely fractured, with prominent propagation of plastic characteristics, resulting in a reduction in its load carrying capacity. The 6 m pillar has a good bearing capacity, and the deformation increases with the rise of pressure. As the CPW continues to increase to 12 m, the load bearing capacity of a pillar is rising, resulting in a gradual reduction in the horizontal displacement of pillar rib. When the

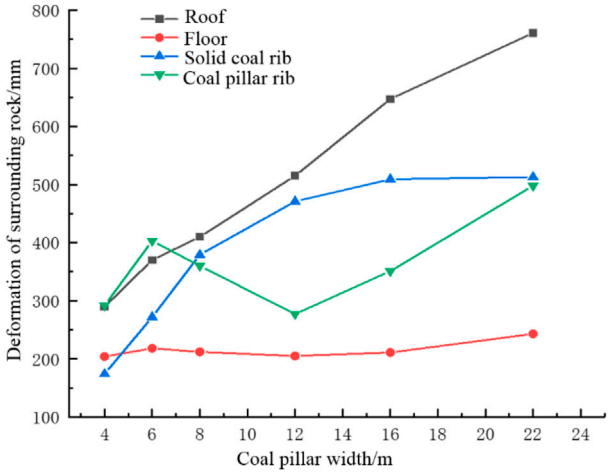

FIGURE 13
Roadway deformation with different CPW.

CPW is greater than 12 m, the horizontal displacement on a pillar rib shows an increasing trend due to the gradual transfer of stresses on solid coal rib into pillar rib.

3.6 Deformation of surrounding rock with different CPW

Figure 13 illustrates a variation curve of the deformation of a roadway and the CPW. The maximum deformation at a roadway with various CPW is obtained in Figure 13.

3.6.1 Roof subsidence

When the CPW is raised to 6 m, the amount of roof subsidence rises by 100 mm compared to a 4 m pillar, resulting in a 34% increase. As width of coal pillar rise to 8 m, the roof subsidence increases by 20 mm, an increment of only 5.1% compared to 6 coal pillars. As the CPW continues to increase to 12, 16, and 22 m, the roof subsidence increases by 32%, 66%, and 95% compared with 6 m coal pillar, respectively.

3.6.2 Floor heave

Floor heave is relatively stable on the whole. Compared with 6 m coal pillar, the floor heave of 4, 8, 12, 16, and 22 m coal pillars has increased by −6.4%, −2.7%, −6%, −3.2%, and 11.5%, respectively and the overall fluctuation is not large.

3.6.3 Displacement of coal pillar ribs

The displacement of coal pillar rib illustrates a trend of increasing, then reducing and finally gradually rising as the CPW increases. When the CPW is 6 m, the deformation of pillar rib increases by 38% compared to a 4 m pillar. When CPW increases to 8 m and 12 m, the displacement of coal pillar rib decreases by 8% and 31% compared with 6 m, respectively. When CPW increases to 16 m and 22 m, the displacement of coal pillar rib increases by −12.9% and 23.5% compared with 6 m pillar, respectively. Among these, stresses within the 22 m coal pillar increase significantly, indicating that the abutment pressure on the solid coal rib are transferred into the pillar ribs.

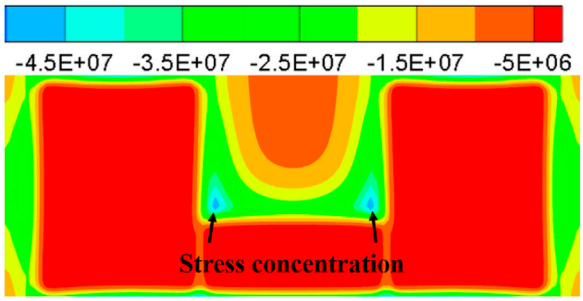

FIGURE 14
Distribution of advance abutment pressure during mining in a panel.

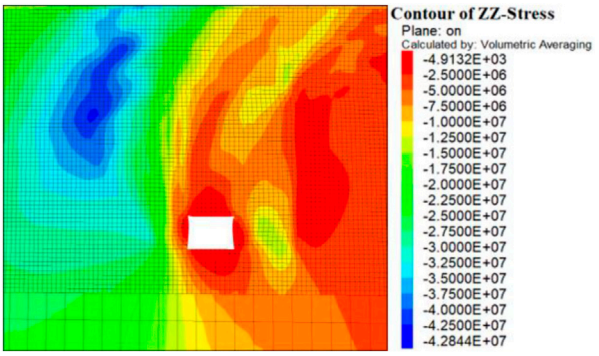

FIGURE 15
Stress distribution of roadway surrounding rock during mining.

3.6.4 Displacement of solid coal ribs

When the CPW grows to 12 m, the deformation of the solid coal rib has been increasing, and the increasing speed is fast. Compared with 6 m coal pillar, when the CPW is only 4 m, the deformation rises by −36%. Compared with 6 m coal pillar, when CPW is increased to 8 m, a solid coal rib has more deformation, and the displacement increase is 39%. With the further rise CPW, the displacement growth slows down, and the displacement increases by 74%, 87%, and 88% respectively compared with the 6 m coal pillar.

To raise the coal recovery rate, the displacement and stress of surrounding rocks are in a better and controllable environment when 6 m coal pillar is reserved. Therefore, it is preliminarily decided to reserve 6 m coal pillar.

3.7 Analysis of stress and displacement during mining in the panel

In order to explain the displacement and advance abutment stress concentration of a roadway under a condition of 6 m width coal pillar, FLAC3D software is employed to analysis of deformation and stress during mining in a panel. Figure 14 illustrates the vertical stress distributions across a panel when a N8102 isolated face is pushed forward by 100 m. The obvious stress concentrating develops in upper corner of a panel, which is 21 m in front of N8102 panel. The peak stress in this region reaches 45 MPa with a stress concentration factor of 4.09. This phenomenon indicates that the excavation of this panel has caused a significant difference in the stress distribution characteristic of a roadway surrounding rock and a more pronounced degree of stress concentration.

Figure 15 illustrates the stress distribution of a roadway for 21 m ahead of the N8102 panel. The peak stress in the 6 m coal pillar increased by 80% from 12.5 MPa to 22.5 MPa under the effect of advance abutment stress, which is greatly affected by the advance abutment stress.

As indicated in Figure 16, under the dual effect of advance abutment pressure and lateral abutment pressure, the roof subsidence of the roadway increases from 390 mm during roadway excavation to 568 mm, an increase of 46%. The maximum displacement of roadway coal pillar rib increases from 403 mm to 642 mm, an increase of 59%. The maximum displacement of the solid coal rib increases by 178 mm. The results display that the displacement of a surrounding rock increases considerably under the influence of advance abutment stress.

Based on the analyses of stresses and displacements in surrounding rocks, 2102 tailgate is greatly affected by the mining of this panel, but the overall stress environment and displacement of surrounding rock can be stabilized within the controllable range through reasonable support. In the process of face mining, it is essential to focus on strengthening the support of the affected section of the advance abutment stress to ensure the roadway stability.

4 Determination of CPW

According to the simulation analyses in Section 3, the results indicate that the variation in CPW leads to stress and deformation

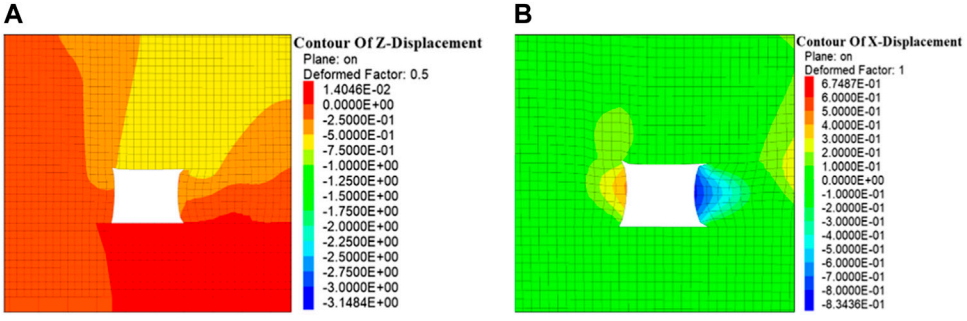

FIGURE 16
Deformation distribution in surrounding rocks during mining. **(A)** Vertical deformation; **(B)** Horizontal deformation.

TABLE 2 Characteristics of surrounding rocks under various CPW.

	4 m Coal pillar	6 m Coal pillar	8–12 m Coal pillar	16–22 m Coal pillar
Coal pillar bearing capacity	Poor	Average	Average	Good
Deformation asymmetry	Obvious	Obvious	Not obvious	Not obvious
Roadway deformation	Small	Medium	Large	Severe
Surrounding rock pressure	Medium	Medium	High	Severe

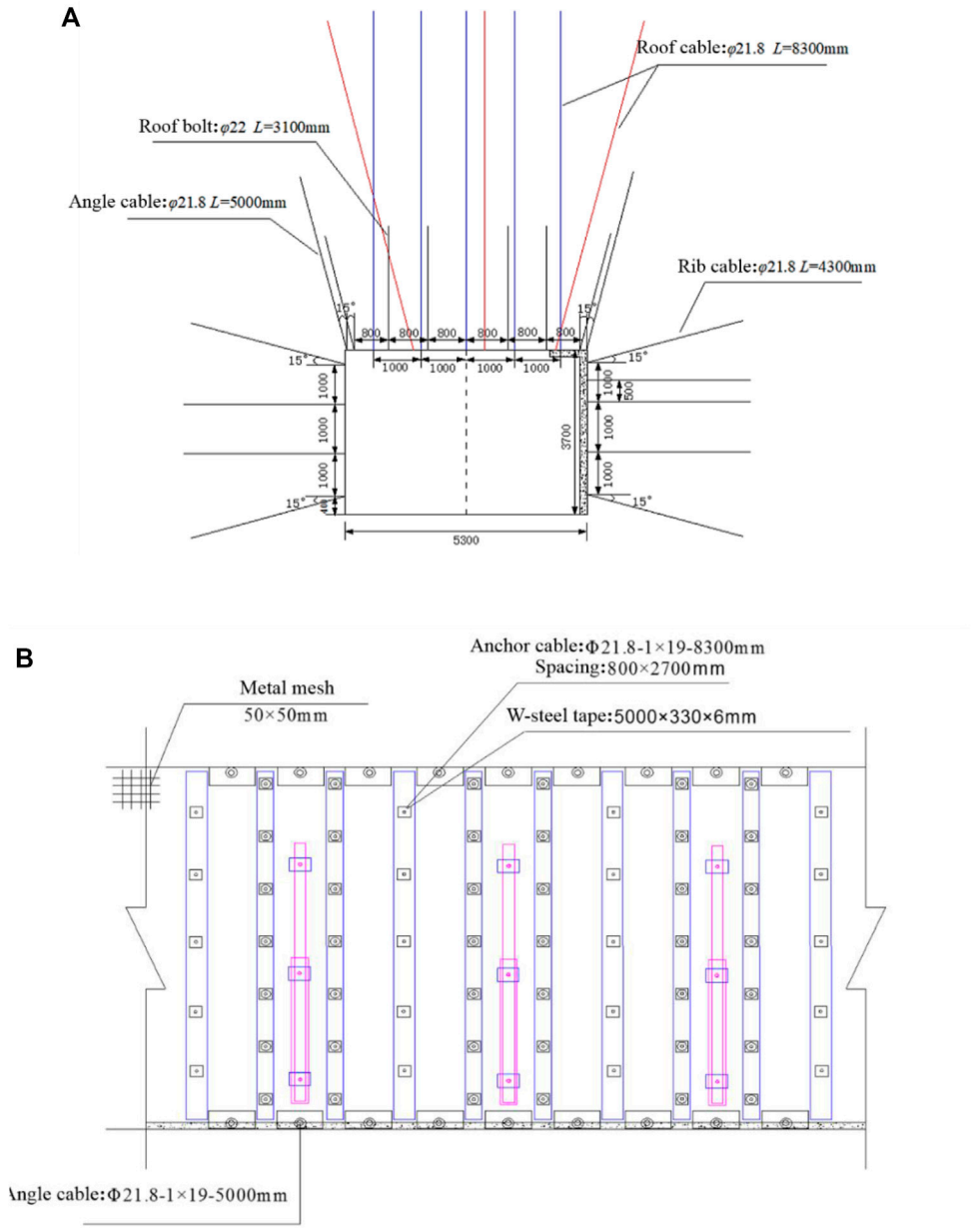

FIGURE 17
Diagrammatic drawing of roadway support. **(A)** Roadway support section; **(B)** Roadway support vertical view.

distribution characteristics of surrounding rocks as shown in Table 2. Considering various influencing factors, although the bearing capacity is average, and surrounding rock has a certain deformation of 6 m coal pillar, the roadway deformation can be controlled in a safe range using a scientific surrounding rock control scheme.

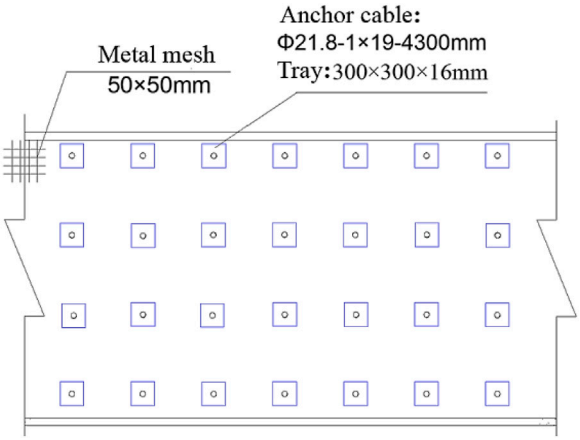

FIGURE 18
Solid coal rib support.

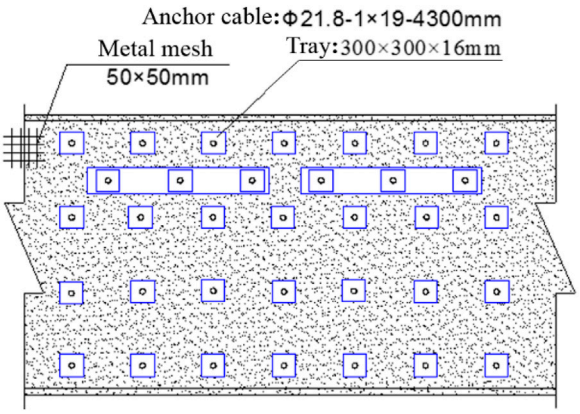

FIGURE 19
Coal pillar rib support.

5 Surrounding rocks control technology and engineering practice of gob-side entry

5.1 Support scheme

Base on the deformation characteristics of 2102 tailgate in N8102 isolated panel and simulation analysis of different CPW, the final asymmetric joint control technology of asymmetric anchor cable truss, high intensity anchor cable, and coal pillar grouting are employed to support a roadway. A diagrammatic drawing of specific roadway support is displayed in Figure 17.

The solid coal rib is supported by anchor cables with a spacing of 1,000 mm x 900 mm. The anchor cables are installed perpendicular to roadway ribs, except for the anchor cables on the upper and lower sides which are installed at 15° to the vertical direction. The anchoring agent is MSZ2360 resin cartridge, with one anchor rope and one anchor rope. The size of the metal mesh used in the rib is 50 × 50 mm. A diagrammatic drawing of the solid coal rib support is shown in Figure 18.

The coal pillar rib is set up with a row of anchor cables more than the solid coal rib. The anchor cables are Φ21.8–1 × 19–4,300 mm steel strand with row spacing of 1,000×900 mm. Each anchor cable adopts an MSZ2360 resin cartridge. To enhance the control of coal pillar ribs, C12 concrete with a thickness of 100 mm is used for grouting and spraying. A diagrammatic drawing of coal pillar rib support is displayed in Figure 19.

5.2 Field verification

As illustrated in Figure 20, a maximum displacement between the roof and floor and between the two ribs during a roadway excavation are 198 mm and 149 mm respectively, which indicates that a roadway is well controlled using asymmetric combined support scheme.

During the mining of N8102 isolated panel, the maximum displacements between two ribs and between roof and floor are

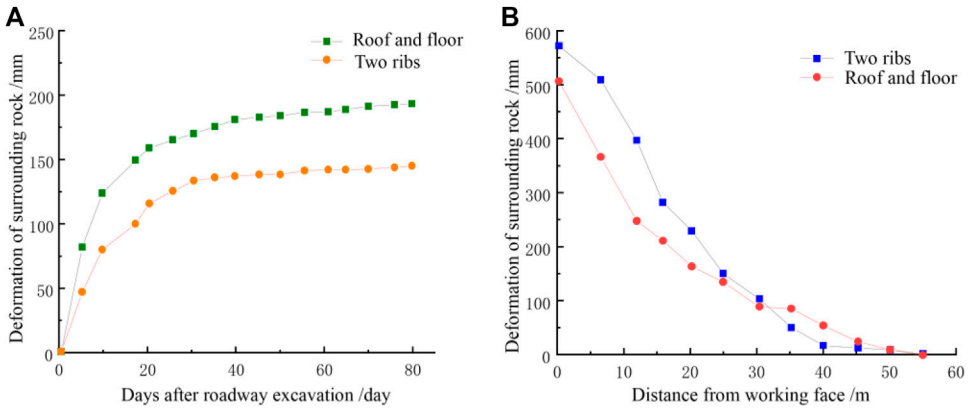

FIGURE 20
Displacement curve of a surrounding rock. **(A)** During roadway excavation; **(B)** During the mining of a panel.

575 mm and 508 mm respectively. The results suggest that the deformation on surrounding rocks during mining is greater than that during roadway excavation. Therefore, the impact of mining on the N8102 panel is more dramatic. However, the support elements in a roadway are still in a stable condition and a whole displacement of surrounding rock of a roadway is in a controllable range.

6 Conclusion

1) The peak stress in N8102 isolated panel is 32.9 MPa, and stress concentration factor is 2.99, which is more affected by the excavation of adjacent panel, and the peak stress on both sides is higher.
2) Through numerical simulation stress and displacement change characteristics of coal pillar ribs and solid coal ribs with different CPW, 6 m pillar width has better bearing characteristics and helps to maintain the durability of surrounding rocks.
3) According to the asymmetry of surrounding rock deformation, the final joint control technology of asymmetric anchor cables, high intensity anchor cables, and coal pillar grouting is proposed and get good control effect on site.

Data availability statement

The original contributions presented in the study are included in the article/supplementary material, further inquiries can be directed to the corresponding author.

Author contributions

XH: Conceptualization, Investigation, Data curation, Formal analysis, Writing—Original Draft. KY: Supervision, Resources, Writing—Review and Editing, Project administration, Funding acquisition. SH: Formal analysis, Investigation. YC: Writing—Review and Editing. RX: Writing—Review and Editing.

Funding

This paper was supported by the Key Projects of Natural Science Research in Anhui Universities (2022AH050839), National Program on Scientific Research Foundation for High-level Talents of Anhui University of Science and Technology (2021yjrc11), Key Basic Research Project of China (2019YFC1904304), Institute of Energy, Hefei Comprehensive National Science Center under Grant No. 21KZS217, National Natural Science Foundation of China (52130402). Independent Research fund of Joint National-Local Engineering Research Centre for Safe and Precise Coal Mining (Anhui University of Science and Technology) (EC2022021).

Conflict of interest

The authors declare that the research was conducted in the absence of any commercial or financial relationships that could be construed as a potential conflict of interest.

Publisher's note

All claims expressed in this article are solely those of the authors and do not necessarily represent those of their affiliated organizations, or those of the publisher, the editors and the reviewers. Any product that may be evaluated in this article, or claim that may be made by its manufacturer, is not guaranteed or endorsed by the publisher.

References

Bai, J. B., Shen, W. L., Guo, G. L., and Yu, Y. (2015). Roof deformation, failure characteristics, and preventive techniques of gob-side entry driving heading adjacent to the advancing working face. *Rock Mech. Rock Eng.* 48 (6), 2447–2458. doi:10.1007/s00603-015-0713-2

Cai, M. F., He, M. C., and Liu, D. Y. (2013). *Rock mechanics and engineering*. 2nd. Beijing, China: Science Press.

Esterhuizen, G. S., Dolinar, D. R., and Ellenberger, J. L. (2011). Pillar strength in underground stone mines in the United States. *Int. J. Rock Mech. Min. Sci.* 48, 42–50. doi:10.1016/j.ijrmms.2010.06.003

Gao, F. Q., and Kang, H. P. (2016). Effects of pre-existing discontinuities on the residual strength of rock mass—Insight from a discrete element method simulation. *J. Struct. Geol.* 85, 40–50. doi:10.1016/j.jsg.2016.02.010

Gao, F. Q., Stead, D., and Kang, H. P. (2015). Numerical simulation of squeezing failure in a coal mine roadway due to mining-induced stresses. *Rock Mech. Rock Eng.* 48 (4), 1635–1645. doi:10.1007/s0060.3-014-0653-2

He, F. L., Li, X. B., He, W. R., Zhao, Y. Q., Xu, Z. H., and Li, Q. S. (2020). The key stratum structure morphology of longwall mechanized top coal caving mining in extra-thick coal seams: A typical case study. *Adv. Civ. Eng.*, 1–13. doi:10.1155/2020/7916729

Itasca (2007). *Fast Lagrangian analysis of continua in 3 dimension*. Minneapolis, MN, USA: User's guide.Version 3.1

Jawed, M., and Sinha, R. K. (2018). Design of rhombus coal pillars and support for roadway stability and mechanizing loading of face coal using SDLs in a steeply inclined thin coal seam—A technical feasibility study. *Arab. J. Geosci.* 11 (15), 1–14. doi:10.1007/s12517-018-3747-4

Kang, H. P., Lin, J., Yan, L. X., Zhang, X., and Wu, Y. Z. (2009). Study on characteristics of underground *in-situ* distribution in Shanxi coal mining fields. *Chin. J. Geophys* 52 (7), 1782–1792. doi:10.3969/j.issn.0001-5733.2009.07.012

Li, W. F., Bai, J. B., Peng, S., Wang, X. Y., and Xu, Y. (2014). Numerical modeling for yield pillar design: A case study. *Rock Mech. Rock Eng.* 48, 305–318. doi:10.1007/s00603-013-0539-8

Lisjak, A., and Grasselli, G. (2014). A review of discrete modeling techniques for fracturing processes in discontinuous rock masses. *J. Rock Mech. Geotech. Eng.* 6 (4), 301–314. doi:10.1016/j.jrmge.2013.12.007

Medhurst, T. P., and Brown, E. T. (1998). A study of the mechanical behaviour of coal for pillar design. *Int. J. Rock Mech. Min. Sci.* 35, 1087–1105. doi:10.1016/S0148-9062(98)00168-5

Poulsen, B. A. (2010). Coal pillar load calculation by pressure arch theory and near field extraction ratio. *Int. J. Rock Mech. Min. Sci.* 47 (7), 1158–1165. doi:10.1016/j.ijrmms.2010.06.011

Salamon, M. D. G., and Munro, A. H. (1967). A study of strength of coal pillars. *J. S Afr. Inst. Min. Metall.* 68, 55–67.

Salamon, M. D. G., Ozbay, M. U., and Madden, B. J. (1998). Life and design of bord-and-pillar workings affected by pillar scaling. *J. S Afr. Inst. Min. Metall.* 98, 135–145. doi:10.1016/S0925-8388(97)00629-4

Salamon, M. D. G. (1970). Stability, instability and design of pillar workings. *Int. J. Rock MechMin Sci. Geomech.* 7, 613–631. doi:10.1016/0148-9062(70)90022-7

Shen, B. T. (2013). Coal mine roadway stability in soft rock: A case study. *Rock Mech. Rock Eng.* 47, 2225–2238. doi:10.1007/s00603-013-0528-y

Si, G. Y., Jamnikar, S., Lazar, J., Shi, J. Q., Durucan, S., Korre, A., et al. (2015). Monitoring and modelling of gas dynamics in multi-level longwall top coal caving of ultra-thick coal seams, part I: Borehole measurements and a conceptual model for gas emission zones. *Int. J. Coal Geol.* 144 (145), 98–110. doi:10.1016/j.coal.2015.04.008

Tewari, S., Kushwaha, A., Bhattacharjee, R., and Porathur, J. L. (2018). Crown pillar design in highly dipping coal seam. *Int. J. Rock Mech. Min. Sci.* 103, 12–19. doi:10.1016/j.ijrmms.2018.01.012

Wang, E., and Xie, S. R. (2022). Determination of coal pillar width for gob-side entry driving in isolated coal face and its control in deep soft-broken coal seam: A case study. *Energy Sci. Eng.* 10 (7), 2305–2316. doi:10.1002/ese3.1139

Wang, S. L., Hao, S. P., Chen, Y., Bai, J. B., Wang, X. Y., and Xu, Y. (2016). Numerical investigation of coal pillar failure under simultaneous static and dynamic loading. *Int. J. Rock Mech. Min. Sci.* 84, 59–68. doi:10.1016/j.ijrmms.2016.01.017

Wu, W. D., Bai, J. B., Wang, X. Y., Yan, S., and Wu, S. X. (2018). Numerical study of failure mechanisms and control techniques for a gob-side yield pillar in the Sijiazhuang coal mine, China. *Rock Mech. Rock Eng.* 52 (4), 1231–1245. doi:10.1007/s00603-018-1654-3

Yang, S. Q., Chen, M., Jing, H. W., Chen, K. F., and Meng, B. (2017). A case study on large deformation failure mechanism of deep soft rock roadway in Xin'An coal mine. *China. Eng. Geol.* 217, 89–101. doi:10.1016/j.enggeo.2016.12.012

Yu, B., Zhang, Z. Y., Kuang, T. J., and Liu, J. R. (2016). Stress changes and deformation monitoring of longwall coal pillars located in weak ground. *Rock Mech. Rock Eng.* 49, 3293–3305.

Zhang, G. C., He, F. L., Jia, H. G., and Lai, Y. H. (2017). Analysis of gateroad stability in relation to yield pillar size: A case study. *Rock Mech. Rock Eng.* 50 (5), 1263–1278. doi:10.1007/s00603-016-1155-1

frontiers | Frontiers in Earth Science

TYPE Original Research
PUBLISHED 11 May 2023
DOI 10.3389/feart.2023.1187864

OPEN ACCESS

EDITED BY
Yingfeng Sun,
University of Science and Technology Beijing, China

REVIEWED BY
Li Ren,
Sichuan University, China
Fei Wu,
Chongqing University, China
Cunbao Li,
Shenzhen University, China

*CORRESPONDENCE
Xin Gui,
gx1994_zj@163.com

RECEIVED 16 March 2023
ACCEPTED 24 April 2023
PUBLISHED 11 May 2023

CITATION
Liu X, Gui X, Qiu X, Wang Y, Xue Y and Zheng Y (2023), Determination method of rock characteristic stresses based on the energy growth rate.
Front. Earth Sci. 11:1187864.
doi: 10.3389/feart.2023.1187864

Determination method of rock characteristic stresses based on the energy growth rate

Xiaohui Liu[1,2], Xin Gui[3]*, Xue Qiu[1], You Wang[1], Yang Xue[4] and Yu Zheng[5]

[1]Key Laboratory of Fluid and Power Machinery, Ministry of Education, Xihua University, Chengdu, China, [2]Key Laboratory of Fluid and Power Machinery of Sichuan Province, Xihua University, Chengdu, China, [3]Sichuan Water Development Investigation, Design & Research Co., LTD., Chengdu, China, [4]CHN Energy Dadu River Hydropower Development Co., Ltd., Chengdu, China, [5]Southwest Municipal Engineering Design & Research Institute of China, Chengdu, China

Introduction: Precisely determining the characteristic stress value of a rock progressive failure process has important theoretical and practical significance for reasonably defining the rock deformation and failure stage, mechanical mechanism, and design parameters.

Methods: Based on the energy characteristics in the process of rock deformation and failure, this paper proposes a new method of rock characteristic stress (EGR) around the index of elastic energy storage capacity, elastic energy growth rate, and dissipative energy growth rate. First, the rationality of the new method is verified by the indoor uniaxial and triaxial loading test data of coal and marble. Second, five different determination methods, namely, lateral strain method, lateral strain difference method, crack strain method, energy dissipation rate method, and volumetric strain method, are compared to further verify the scientific nature of the new method. Finally, the method is applied to the conventional triaxial unloading confining pressure test and true triaxial loading and unloading test of marble, and the new method is fully extended to verify its universality.

Results: The results show that the theoretical basis of the EGR characteristic stress determination method is rigorous and sufficient, and the value process is objective and reasonable. Compared with different methods, the EGR method can accurately define the process of rock asymptotic failure, and its corresponding characteristic stress level is well-consistent and in a reasonable range.

Discussion: The EGR method is applicable to the conventional triaxial unloading confining pressure test and true triaxial loading and unloading test and has good universality.

KEYWORDS

asymptotic failure, characteristic stresses, elastic energy storage capacity index, elastic energy growth rate, dissipative energy growth rate

1 Introduction

In energy exploitation and underground engineering construction, there is often an asymptotic failure process of rock. There are many phenomena such as spalling failure of surrounding rock and formation of a damage zone, which fail to reach the ultimate strength of rock. These phenomena play a vital role in the safety and stability of the project. Therefore, the study of the rock asymptotic failure process and the accurate acquisition of rock characteristic

TABLE 1 Contents, advantages, and disadvantages of common methods for determining characteristic stress.

Method name		Content	Advantage	Disadvantage
Stress–strain correlation method	Crack volume strain	Using the crack volume strain under uniaxial state ε_{vc} to determine σ_{ci}	The stress–strain correlation method was simple and intuitive	The data value had great subjectivity, and different lithologies of rock would cause different degrees of influence, so the characteristic stress value could not be accurately determined
	Transverse strain	The turning point of the first time is used so that the transverse strain changes from non-linear to linear, and the turning point of the second time is used so that the transverse strain changes from linear to non-linear to determine σ_{cc} and σ_{ci}, respectively		
	Moving point regression	The average axial stiffness of rock is calculated and σci is determined through its approximate linear part		
Acoustic emission		The characteristic stress value is determined according to the change characteristics of acoustic emission characteristic parameters such as acoustic emission cumulative impact number, energy count, and b value	Acoustic emission studies the characteristic stress from a microscopic perspective, which was more accurate and realistic	The attenuation effect of crack development on the AE accumulation process made the AE method have certain stress condition limitations
Energy		Determination of the characteristic stress value based on energy theory	Closer to the nature of rock failure	Relatively few studies

stress are the basis for establishing reasonable, scientific and universal rock fracture strength criteria and failure strength criteria. It is a key parameter in predicting the extent and scope of surrounding rock failure (Cai et al., 2004) and has important engineering guiding significance.

In the past 50 years, the progressive failure process of rock has received extensive attention from scholars. Based on the laboratory test research, Bieniawski, (1967); Brown, (1981) divided the progressive failure process of rock into five stages: crack compaction, linear elastic deformation, crack initiation and stable propagation, specimen damage and crack unstable propagation, and specimen failure and post-peak deformation. Cai et al. (2004); Peng et al. (2015); Wang et al. (2011); Peng et al. (2013); Li et al. (2022); Tkalich et al. (2016); Kong et al. (2023); Li et al. (2023) expounded the necessity of dividing the stages of asymptotic failure from the perspective of experiment and theory. The corresponding strength eigenvalues of each stage were compaction stress σ_{cc}, crack initiation stress σ_{ci}, crack damage stress σ_{cd}, peak stress σ_f, and residual stress σ_r, respectively.

Subsequently, scholars discussed how to accurately determine the asymptotic failure characteristic stress. Some research methods with their contents, advantages, and disadvantages are shown in Table 1. The characteristic stress value was usually determined from the stress–strain aspect by volume strain (Brown, 1981), transverse strain (Lajtai et al., 1990), crack strain (Martin and Chandler, 1994), and moving point regression (Eberhardt et al., 1998).However, such methods were generally subjective and cannot accurately determine the compaction stress σ_{cc} and cracking stress σ_{ci}, which would bring hidden dangers to prevent engineering instability.

Therefore, according to the change characteristics of AE characteristic parameters such as AE cumulative impact number, energy count, and b value, it was more advantageous to study different characteristic stresses from a microscopic perspective (Kim et al., 2015; Xie et al., 2023). However, the attenuation effect of crack development on the accumulation process of acoustic emission provided the acoustic emission method with certain limitations of stress conditions.

Therefore, according to the law of energy conversion and conservation, energy conversion is a basic feature in the physical process of matter. As an aggregate of various minerals, rock is also an open system that can receive, store, and release energy (Zhao and Xie, 2008; Xie et al., 2004; Liu et al., 2023). The nature of rock cracking and failure is an energy-driven state instability phenomenon. Energy theory was used to determine that the characteristic stress of rock is bound to be closer to the nature of rock failure (Liu et al., 2022). Griffith (1921) proved the energy theory through a rock tensile test, and Yang et al. (2015) constructed a damage model based on energy dissipation and determined the compaction stress and cracking stress. Jin et al. (2004) calculated the dissipation energy based on cyclic loading, defined the damage variable of materials from the perspective of energy dissipation, and determined the theoretical calculation formula and damage threshold of the damage variable. Xie et al. (2005a) studied the internal relationship between energy dissipation, energy release, rock strength, and overall failure during rock deformation and failure, and based on the strength loss criterion of energy dissipation and the global failure criterion of releasable strain energy, the critical stress of rock global failure was determined. Ning et al. (2018) studied the energy dissipation law of brittle coal and rock under different confining pressures and proposed to determine the crack initiation stress σ_{ci} and damage stress σ_{cd}, based on the elastic strain energy rate and dissipation energy rate. Liu et al. (2020) expressed the energy dissipation process of coal and rock by introducing the dissipation energy rate and proposed a method to determine the fracture closure stress point and damage stress point of coal and rock using the energy dissipation rate curve.

The content, advantages, and disadvantages of commonly used methods for determining characteristic stress are given in Table 1. At present, there are often subjective inaccuracies or limitations in the application of stress–strain correlation methods and acoustic emission methods. Adopting the ability theory method is closer

to the essence of rock failure, providing a more precise and versatile determination of rock characteristic stress. To sum up, a new method is proposed to determine the crack closure stress σ_{cc}, crack initiation stress σ_{ci}, damage stress σ_{cd}, and instability stress σ_{pr}. It comprehensively considers the process of energy transformation, release, and dissipation from the characteristics of energy evolution in the process of rock asymptotic failure. The rationality, scientificity, and universality of the method are discussed and verified. A new approach is proposed to accurately determine the asymptotic failure process of rocks and effectively prevent the instability and failure of underground engineering.

2 Determination method theory and thought

2.1 Elastic energy analysis theory

The failure process of rock under load is essentially a state instability phenomenon driven by energy. Assuming that the rock mechanics test is a thermodynamically closed system, it can be observed from the relationship between work and energy that the work performed by the external to the rock sample W equals the change in the internal energy of the rock sample U_0 during the test process. The energy transformation in marble includes elastic energy, plastic energy, radiation energy, thermal energy, and kinetic energy (Zhao and Xie. 2008; Xie et al., 2005; Xie et al., 2008), among which elastic energy is the energy stored and released by elastic deformation of rock, and plastic energy is the energy consumed by micro-crack propagation and friction between crack surfaces in rock. Radiation energy, heat energy, and kinetic energy are different forms of energy consumption caused by rock fracture propagation, but the proportion is relatively small, the monitoring is complex, and the cost is high. Therefore, in the subsequent analysis, plastic energy, radiation energy, heat energy, and kinetic energy are attributed to dissipative energy, that is, in the transformation of work and energy in marble, the total absorption energy U is composed of the dissipative energy U_d of the released elastic strain energy U_e stored in unit volume. So, the total energy of the rock (Xie et al., 2005) sample is

$$U = U_0 = U_e + U_d. \tag{1}$$

The total absorption energy is

$$U_0 = \int \sigma_1 d\varepsilon_1 + \int \sigma_2 d\varepsilon_2 + \int \sigma_3 d\varepsilon_3. \tag{2}$$

In the aforementioned equation, σ_1, σ_2, and σ_3 are the maximum principal stress, medium principal stress, and minimum principal stress, respectively, and ε_1, ε_2, and ε_3 are the strains in the directions of the maximum principal stress, medium principal stress, and minimum principal stress, respectively.

The elastic energy is calculated as follows:

$$U_e = u_{e1} + u_{e2} + u_{e3}, \tag{3}$$

where u_{ei} is the elastic energy of each principal stress (Xie et al., 2008):

$$u_{ei} = \frac{1}{2}\sigma_i\varepsilon_i = \frac{\sigma_i}{2}\left(\frac{\sigma_i}{\bar{E}i} - \mu_j\frac{\sigma_j}{\bar{E}j} - \mu_k\frac{\sigma_k}{\bar{E}_k}\right), \tag{4}$$

where $\bar{E}$ and $\bar{\mu}$ are the average elastic modulus and Poisson's ratio of marble under load, respectively. Assuming that the rock elastic simulation and Poisson's ratio do not change with rock damage during the rock failure process, the initial elastic modulus E_0 and the initial Poisson's ratio μ_0 of marble can be used instead. It is assumed that marble is an isotropic material, that is,

$$\begin{cases} \overline{E_1} = \overline{E_2} = \overline{E_3} = \bar{E} \\ \overline{\mu_1} = \overline{\mu_2} = \overline{\mu_3} = \bar{\mu} \end{cases}. \tag{5}$$

Substituting Eq. 5 into Eq. 4, replacing $\bar{E}$ with E_0, and replacing $\bar{\mu}$ with μ_0 yield

$$u_{ei} = \sigma_i\varepsilon_i^e = \frac{1}{2E_0}\left[\sigma_i^2 - \mu_0\left(\sigma_i\sigma_j + \sigma_i\sigma_k\right)\right]. \tag{6}$$

By substituting Eq. 6 into Eq. 3, the elastic energy can be obtained:

$$U_e = \frac{1}{2E_0}\left[\sigma_1^2 + \sigma_2^2 + \sigma_3^2 - 2\mu_0\left(\sigma_1\sigma_2 + \sigma_2\sigma_3 + \sigma_1\sigma_3\right)\right]. \tag{7}$$

2.1.1 Elastic energy storage capacity index *Ab*

This paper aimed to explore the accurate determination of the rock characteristic stress value. Considering that both the closure and initiation of rock fractures affect the ability of rock to store elastic energy, this paper will deduce the change trend in the rock's ability to store elastic energy in the process of progressive failure from the perspective of elastic property.

The increase of elastic energy of the rock under load comes from the absorption of elastic energy by the rock during axial contraction. Combining with Eq. 7, it can be seen that elastic energy is essentially a quadratic function of the elastic strain of the rock under load. Assuming that the proportion of axial elastic strain in axial strain at a certain moment is α, then

$$\varepsilon_{1e} = \alpha\varepsilon_1. \tag{8}$$

The elastic modulus and Poisson's ratio in the calculation formula of elastic energy are constant values, which can transform the elastic energy into a quadratic function containing parameters α, ε_1, σ_2, and σ_3 which can transform the elastic energy into a quadratic function containing four parameters:

$$U_e = \frac{1}{2}E_0 \times (\alpha\varepsilon_1)^2 + \frac{1}{2}\left[\frac{\sigma_2^2}{E_0} + \frac{\sigma_3^2}{E_0} - \alpha\varepsilon_1 \cdot \nu_0(\sigma_2 + \sigma_3)\right]. \tag{9}$$

Therefore, the second derivative of elastic energy with respect to axial strain can be defined as the rock elastic energy storage capacity index Ab, which can be expressed as follows:

$$Ab = \frac{\partial^2 U_e}{\partial {\varepsilon_1}^2}. \tag{10}$$

The elastic energy storage capacity index Ab of rock is a function without axial stress and axial strain and represents the elastic energy storage capacity of rock under load after unit strain at a certain time.

2.1.2 Elastic energy growth rate κ_e

The elastic energy storage capacity index *Ab* can be used to analyze the energy storage capacity of marble at each moment for the reasonable and accurate determination of rock characteristic stresses. However, in practice, due to comprehensive factors such as rock anisotropy, heterogeneity, internal defects, and unavoidable test equipment errors in laboratory tests, the data after taking the second derivative of the test data have great volatility, which makes them difficult to observe. Therefore, only the first derivative of axial strain ε_1 is taken in this paper, and the first derivative of elastic energy *Ue* with respect to axial strain ε_1 is defined as the elastic energy growth rate κ_e, expressed as follows:

$$\kappa_e = \frac{\partial Ue}{\partial \varepsilon_1}. \tag{11}$$

The growth rate of the elastic energy κ_e–axial strain ε_1 curve can be used to analyze the elastic energy storage index *Ab* of marble under various axial displacements.

2.2 Dissipated energy growth rate κ_d

It is worth observing that the elastic energy storage capacity curve has obvious changes during the crack closure and initiation. However, both the rock crack expansion and damage stage show a downward trend, which makes it difficult to determine the rock damage stress value. Therefore, considering that the energy dissipation of the loaded rock comes from the development of internal fractures of the rock, the trend of fracture expansion during the progressive failure of the rock will be analyzed from the perspective of energy dissipation.

The stress generated inside the rock under load can be divided into spheric stress *p*, which causes elastic shrinkage, and deviator stress *q*, which causes plastic deformation. By the physical meaning of energy, the marble in the process of gradual damage dissipation mainly comes from rock fracture initiation, development, and expansion caused by plastic deformation produced by energy dissipation. The energy dissipation of rock is closely related to increase in deviatoric stress *q* in the process of loading, so the dissipative energy growth rate κ_d for dissipation can be defined and predominate the U_d derivative of deviatoric stress *q*, and the expression is

$$\kappa_d = \frac{\partial U_d}{\partial q}. \tag{12}$$

According to the variation of dissipated energy κ_d in the process of rock deformation and failure, the fracture damage of the rock under load at each time can be analyzed, and the characteristic stresses of the rock can be determined reasonably and accurately combined with the growth rate of elastic energy.

2.3 Determination method

Assuming that rock deformation and failure is a continuous process, this subsection, which is from the perspective of mathematical analysis and applied mathematics, will combine the elastic energy storage capacity index *Ab*, the growth rate of elastic energy κ_e, and dissipative energy κ_d to determine the threshold (characteristic stresses) of each stage of rock deformation and failure. The process and thinking are as follows:

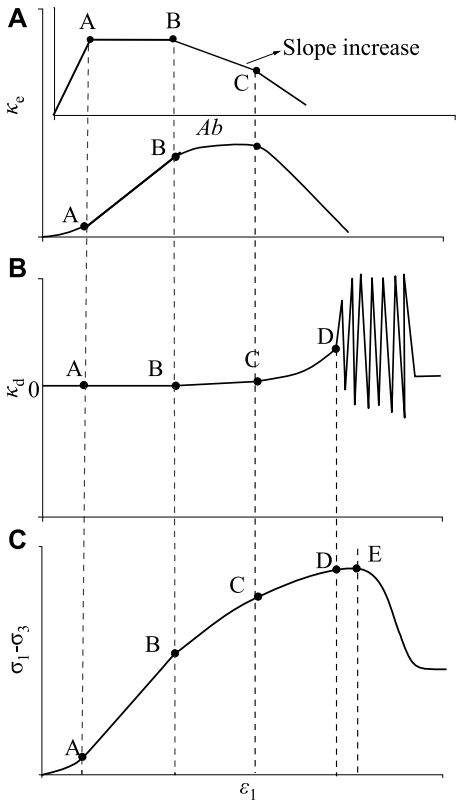

FIGURE 1
Schematic diagram of the determining method of characteristic stresses at each stage: **(A)** elastic energy storage capacity index *Ab* and elastic energy growth rate κ_e curve; **(B)** dissipation energy growth rate κ_e curve; and **(C)** axial stress–strain curve.

1) Compaction stage (crack closure stress σ_{cc})

In this stage, the original pores inside the rock are continuously compressed, the rock performance is improved, and the rock energy storage capacity is strengthened. The growth rate curve of elastic energy is concave, and the elastic energy storage capacity index *Ab* increases. At the same time, the rock has no damage. At this stage, the dissipated energy does not increase from the rock deformation, and the growth rate of dissipated energy is close to "0." At the end of this stage, the growth curve of rock elastic energy follows a linear trend, and the elastic energy storage capacity index *Ab* enters the horizontal stage. The corresponding stress threshold of this stage is the closure stress σ_{cc}.

The crack closure stress is the junction point of the compaction stage and linear elastic stage, which on the left side of elastic energy growth, follows a "concave" shape, elastic energy storage capability index *Ab* shows a growing trend, and on the right side of elastic energy growth for the linear function, the elastic energy storage capability index *Ab* is constant at the same time because the pressure dense phase and the linear elastic stage did not produce rock fracture

damage. Therefore, the growth rate of dissipated energy is close to the "0" line at both ends of the point without any change. The closure stress is the stress value corresponding to point *A* on the curve of the elastic energy growth rate, elastic energy storage capacity index, and dissipative energy growth rate (Figure 1).

2) Linear elastic stage (crack initiation stress σ_{ci})

At this stage, the original pores in the rock have been compressed, and the stress in the rock is not sufficient for pore expansion and generation of new fractures. The rock shows elastic material characteristics, the growth curve of elastic energy increases linearly, and the elastic energy storage capacity index *Ab* shows a horizontal line. The growth rate of dissipated energy is still close to "0," and the corresponding stage stress threshold is the crack initiation stress σ_{ci}.

The crack initiation stress is the boundary point of the linear elastic stage and plastic expansion stage. In the growth curve of elastic energy, it is the point that changes to non-linear growth; in the curve of elastic energy storage capacity index *Ab*, it is the point that deviates from the level; in the growth curve of dissipated energy, it is the point that changes to linear growth, which is marked by point B in Figure 1.

3) Plastic expansion stage (damage stress σ_{cd})

At this stage, due to the heterogeneity of rock, the internal stress of the rock reaches the condition of local crack initiation and expansion, the rock begins to produce plastic deformation, and the elastic energy storage capacity begins to decline. The growth rate curve of elastic energy is "convex," and the elastic energy storage capacity index begins to decline. At the same time, due to the occurrence of crack damage, the rock begins to produce energy dissipation, and the growth rate of dissipated energy begins to increase. The stress threshold at this stage is the damage stress σ_{cd}.

Damage stress is the cutoff point from fracture damage to rapid development, but this point is difficult to be accurately determined by the change in the elastic energy growth rate and elastic energy storage capacity index. However, as the sudden increase of the crack growth rate will change the growth trend of the dissipated energy growth rate, the damage stress can be accurately determined according to the turning point of the dissipated energy growth rate curve that linearly transforms into a "downward convex type," marked by point C in Figure 1.

4) Accelerated crack expansion stage (instability stress σ_{pr})

In this stage, the micro-cracks in the rock accelerate to expand and converge into large cracks, the growth rate of elastic energy and elastic energy storage capacity index decreases, and the energy dissipation of the rock intensifies. The growth rate of dissipative energy accelerates in a "convex" shape, and the corresponding stress threshold is the instability stress σ_{pr}.

Instability stress is the cutoff point between the generation of large cracks and the beginning of the development of large cracks. It cannot be determined in the growth curve of elastic energy and the energy storage capacity index of elastic energy but can be determined by the point with violent fluctuations in the growth curve of dissipated energy, marked by point D in Figure 1.

5) Fracture instability through stage (peak stress σ_f)

At this stage, the large cracks formed in the accelerated fracture expansion stage begin to break through. As the breaking through of large cracks and the development of cracks alternate in this stage, the dissipative energy growth rate curve presents high-amplitude and high-frequency fluctuation. At the end of this stage, the bearing capacity of the sample reaches its maximum.

The peak stress is the end point of this stage. As the energy dissipation of rock continues after the peak stress point, there is no obvious defining feature on the dissipative energy growth rate curve. However, as the maximum point on the stress–strain curve, the peak stress can be easily identified on the stress–strain curve, as shown in point E in Figure 1.

3 Analysis and verification

3.1 Rationality verification

This experiment consists of two kinds of rocks, coal and marble. A uniaxial compression test and conventional triaxial compression test are used to verify this method. The uniaxial compression test and conventional triaxial compression test are based on the MTS815 Flex Test GT rock mechanics test system, Key Laboratory of Deep Earth Science and Engineering of Ministry of Education, Sichuan University, and the test equipment is shown in Figure 2. Coal rock and marble were collected from the Furong Baijiao Coal Mine and Jinping II Hydropower Station auxiliary diversion 1 # construction adit, respectively. The sample taken from Furong Baijiao coal is ash-rich and sulfur-rich anthracite. The Jinping grade II marble sample is thick and extremely thick-layered fine-grained or coarse-grained marble. The physical parameters of the sample are shown in Table 2.

This paper intends to design a uniaxial compression test and triaxial compression test. The uniaxial loading test and conventional triaxial test under 25 MPa confining pressure were carried out on coal and marble, respectively. The tests were all carried out at a $10^{-5}s^{-1}$ strain rate. The strain control loading was realized using a linear variable differential transformer (LVDT) during the test.

According to Eqs 11, 12, the growth rate curve of elastic energy and dissipated energy of single triaxial coal rock and single triaxial marble is plotted as shown in Figure 3. The energy storage capacity curve can be inferred from the elastic energy growth rate curve. According to Figure 3, the growth rate curve of elastic energy shows three stages: 1) upper concave non-linear stage, 2) linear growth stage, and 3) concave non-linear stage; according to the elastic energy growth rate curve, the first-order derivative elastic energy storage capacity index shows a rising–horizontal–downward trend. The growth rate curve of dissipated energy shows four stages: 1) near-straight section, 2) linear rising section, 3) upper concave non-linear stage, and 4) rapid fluctuation section. It follows that the three curve evolution processes are consistent with the determination ideas described in Section 2.2.

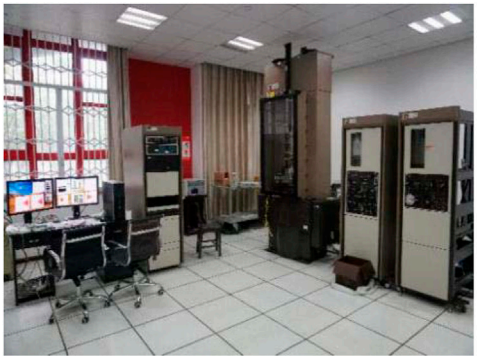

MTS815 rock mechanics test system

Layered coal samples

Complete marble sample

FIGURE 2
Test equipment and rock samples.

TABLE 2 Physical parameters of samples.

Lithology	Stress path	Code	Diameter/ mm	Height/ mm	Volume/ $10^{-4}m^3$	Weight/ g	Density/ g/cm^3	Longitudinal wave velocity (m/s)
Coal	Uniaxial	C0-1	47.55	96.37	17.11	243	1.421	1,046
		C0-2	47.27	99.71	17.50	252	1.444	1,074
		C0-3	47.74	101.10	18.10	264	1.457	1,257
	Conventional triaxial	C25-1	47.33	98.68	17.36	260	1.495	946
		C25-2	47.34	100.15	17.63	288	1.635	747
		C25-3	47.70	93.10	16.64	241	1.446	909
Marble	Uniaxial	M0-1	49.98	100.03	19.63	551	2.807	4,202
		M0-2	49.90	99.93	19.54	549	2.808	4,132
		M0-3	49.89	100.35	19.62	551	2.811	4,202
	Conventional triaxial	M25-1	49.92	100.93	19.75	551	2.791	3,876
		M25-2	49.98	99.96	19.61	551	2.813	4,033
		M25-3	50.16	100.07	19.77	552	2.790	3,876

Many scholars have found that the energy evolution in the process of rock deformation and failure has obvious stage characteristics (Liu et al., 2019; Wang et al., 2019; Zhang et al., 2020). Therefore, this paper chooses to use the first derivative of the energy evolution curve to determine the strength threshold of each stage of rock and find the characteristic stress value of rock. Using energy evolution characteristics to determine characteristic stress, as was first proposed by Ning et al. (2018), helps analyze the evolution law of elastic energy and dissipated energy of coal rock under different confining pressures. It is proposed that the characteristic stress value of coal rock is determined by the ratio of elastic energy and dissipative energy in the total strain energy–elastic energy rate α and dissipative energy rate β. The feasibility of this method is analyzed and verified. According to the law of energy conversion and conservation, energy conversion is a basic feature in the physical process of matter, and the destruction of matter is a state instability phenomenon driven by energy. In the process of rock deformation and failure, the internal energy of rock will inevitably change, leading to continuous evolution of micro-fractures in the rock, from disorderly micro-fractures to macro-cracks that can expand and connect. With the connection and extension of macro-cracks, large cracks will eventually be integrated along a certain direction to cause rock failure. Therefore, it is reasonable and feasible to explain the evolution of fractures and determine the characteristic stress from the perspective of energy growth rate, which has a theoretical background.

In this paper, the energy growth rate curve has certain volatility when determining the strength characteristic value of the sample at each stage

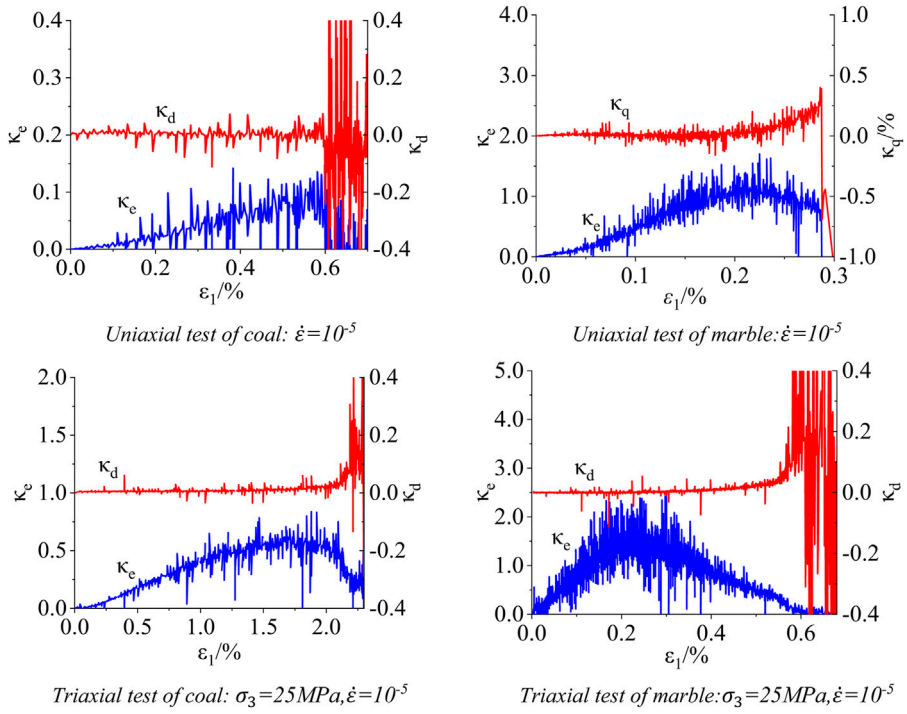

FIGURE 3
Growth rate curve of elastic energy and dissipative energy.

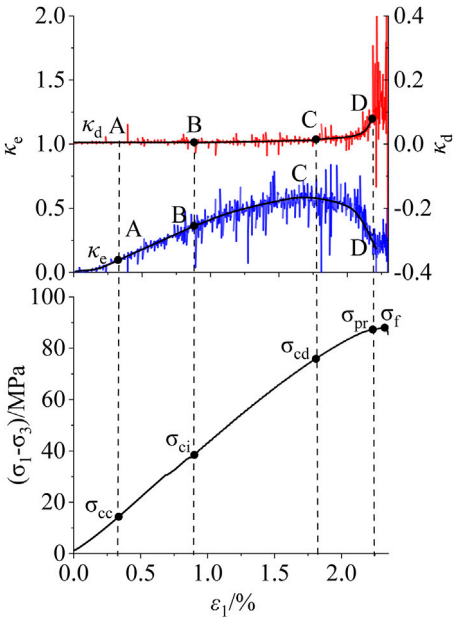

FIGURE 4
Example of the determination of characteristic stress: conventional triaxial compression coal rock, σ_3 =25 MPa, and $\dot{\varepsilon}$ =10^{-5}.

of deformation and failure. On one hand, anisotropy and heterogeneity are caused by random distribution of cracks, cavities, and internal defects in the rock. As a result, rock deformation is irregular and anisotropic, resulting in large and irregular fluctuations in energy growth rate, and this part of the fluctuation is an inevitable, objective existence. On the other hand, system error, test equipment error, and point error will cause fluctuations in the energy growth rate curve. Therefore, it is reasonable for the energy growth rate curve to show certain volatility, and the overall trend and characteristics can reflect the process of crack closure–initiation–propagation–convergence–penetration. Therefore, it is reasonable and feasible to use this method to determine the closure stress σ_{cc}, crack initiation stress σ_{ci}, damage stress σ_{cd}, and instability stress σ_{pr}.

3.2 Scientific verification

The energy growth rate curve of the laboratory test results has certain volatility, but the characteristics are obvious, and it is easy to find the characteristic stress value of each stage. Taking the energy growth rate curve of coal and rock under conventional triaxial compression of 25 MPa confining pressure as an example (as shown in Figure 4), the following characteristic stress values are determined:

1) Closure stress: The elastic energy growth rate at stage I is a concave curve. It can be inferred that the elastic energy storage capacity *Ab* at this stage shows an upward trend and the growth rate of dissipated energy is close to 0, same as the characteristic description of the compaction stage in Section 2.2. Therefore, stage I corresponds to the compaction stage, and the right end point is closure stress.

TABLE 3 Crack closure stress.

Lithology	Code	σ_{cc}/MPa						σ_f	$\frac{\sigma_{cc,EGR}}{\sigma_f}$	$\frac{\overline{\sigma_{cc}}}{\sigma_f}$
		EGR method	Martin method	Lajtai method	DER method	Average value	Standard deviation			
Coal	C0-1	1.84	1.57	0.92	0.68	1.25	0.47	6.77	0.27	0.18
	C0-2	0.92	1.70	1.25	1.63	1.38	0.31	4.01	0.23	0.34
	C0-3	2.21	3.49	2.69	2.26	2.66	0.50	10.89	0.20	0.24
	C25-1	24.76	25.51	25.58	26.17	25.51	0.50	79.20	0.31	0.32
	C25-2	24.99	—	26.83	24.99	25.60	0.61	89.19	0.28	0.29
	C25-3	19.91	20.34	18.20	33.70	23.04	6.21	70.70	0.28	0.33
Marble	M0-1	34.53	50.19	—	12.06	32.26	15.65	163.92	0.21	0.20
	M0-2	34.06	50.56	42.95	16.25	35.96	12.78	179.94	0.19	0.20
	M0-3	38.71	33.52	40.75	14.16	31.79	10.51	168.74	0.23	0.19
	M25-1	51.93	58.01	—	45.54	53.53	5.67	293.02	0.19	0.18
	M25-2	53.29	60.31	—	58.54	57.38	2.98	266.87	0.20	0.22
	M25-3	37.31	54.81	—	21.42	37.85	13.64	291.36	0.13	0.13

1. PDE method: dissipative energy ratio method.
2. DER method: proportion of the dissipated energy method.

10.3389/feart.2023.1187864

TABLE 4 Crack initiation stress.

Lithology	Code	σ_{ci}/MPa						σ_f	$\frac{\sigma_{cc,EGR}}{\sigma_f}$	$\frac{\overline{\sigma_{cc}}}{\sigma_f}$
		EGR method	Martin method	Lajtai method	Zhao XG method	Average value	Standard deviation			
Coal	C0-1	4.04	4.199	3.73	5.34	4.33	0.61	6.77	0.60	0.64
	C0-2	2.16	2.727	2.20	2.14	2.31	0.24	4.01	0.54	0.53
	C0-3	6.62	7.280	4.63	5.90	6.11	0.98	10.89	0.61	0.56
	C25-1	43.51	50.56	39.37	49.30	45.69	4.51	79.20	0.55	0.58
	C25-2	44.20	—	42.53	39.58	42.10	1.91	89.19	0.50	0.47
	C25-3	45.26	50.19	43.33	—	46.26	2.50	70.70	0.64	0.65
Marble	M0-1	93.24	80.26	—	96.66	90.05	7.06	163.92	0.57	0.55
	M0-2	94.14	91.46	84.08	95.98	91.42	4.53	179.94	0.52	0.51
	M0-3	103.04	60.05	78.53	92.83	83.61	16.15	168.74	0.61	0.50
	M25-1	142.83	154.69	—	175.46	156.16	15.19	293.02	0.47	0.53
	M25-2	120.28	139.00	—	151.57	136.95	12.86	266.87	0.45	0.51
	M25-3	140.59	160.82	—	190.22	163.88	20.38	291.36	0.48	0.56

2) Crack initiation stress: The elastic energy growth rate at stage II is linear. It can be inferred that the elastic energy storage capacity *Ab* at this stage shows a horizontal trend and the growth rate of dissipated energy remains 0, which is the same as the characteristic description of the elastic stage. Therefore, stage II corresponds to the elastic stage, and the right end point is crack initiation stress.
3) Damage stress: The elastic energy growth rate at stage III is concave. It can be inferred that the elastic energy storage capacity *Ab* began to decline at this stage and the growth rate of dissipated energy starts to break away from 0, showing a slow linear growth trend, which is the same as the characteristic description of the plastic expansion stage. Therefore, stage III corresponds to the plastic growth stage, and the right end point is the damage stress.
4) Instability stress: In stage IV, the growth rate of elastic energy began to decline. It can be inferred that the elastic energy storage capacity *Ab* at this stage is negative and continues to decline, and the growth rate of dissipated energy shows increases rapidly non-linearly, which is the same as the characteristic description of the rapid expansion stage of fracture. Therefore, stage IV corresponds to the rapid expansion stage of the crack, and the right end point is the instability stress.
5) Peak stress: The fluctuation of the elastic energy growth rate in stage V is intensified and continues to decline. It can be inferred that the elastic energy storage capacity *Ab* will continue to decline at this stage and the growth rate of dissipated energy fluctuates with high amplitude and high frequency, which is the same as the characteristic description of fracture instability and penetration stage. Therefore, stage V corresponds to the rapid expansion stage of the crack, and the right end point is the peak stress.

It can be seen that the closure stress, crack initiation stress, damage stress, and instability stress are determined by using the elastic energy storage capacity index, elastic energy growth rate, and plastic energy growth rate. The accuracy of this determination method will be discussed as follows.

1) Closure stress and crack initiation stress

This study adopts the lateral strain method considering lateral deformation (Lajtai et al., 1990) and the lateral strain difference method (Zhao et al., 2015). The crack strain method (Martin and Chandler, 1994) and the energy dissipation rate method (Liu et al., 2020), which are also based on the energy principle, are used to verify the closure stress and crack initiation stress determined by the energy growth rate method in this study. The closure stress values of coal and marble under different methods is given in Table 3, and the fracture initiation stress value is given in Table 4.

It can be seen from Tables 3, 4 that the crack initiation stress level (ratio of crack initiation stress to ultimate strength) of bedded coal and rock determined by the energy growth rate method is 0.54–0.64, and the reasonable range of the stress level of the crack initiation stress of the bedded rock is 0.5–0.6 (Cai et al., 2004), which basically conforms to the range. At the same time, it can be seen that the crack initiation stress level of this method is also basically consistent with the stress level of 0.47–0.65 of the mean value of the crack initiation stress determined by the four methods.

TABLE 5 Damage stress.

Lithology	σ_{cd}/MPa						σ_f	$\frac{\sigma_{cd,EGR}}{\sigma_f}$	$\frac{\overline{\sigma_{cd}}}{\sigma_f}$
	Code	EGR	Volume strain method	DER	Average value	Standard deviation			
Coal	C0-1	6.08	4.73	6.19	5.67	0.66	6.77	0.90	0.84
	C0-2	3.40	3.07	3.64	3.37	0.23	4.01	0.85	0.84
	C0-3	9.19	6.62	9.47	8.43	1.28	10.89	0.84	0.77
	C25-1	77.60	78.16	80.53	78.76	1.27	89.20	0.87	0.88
	C25-2	73.31	69.16	71.15	71.21	2.04	79.19	0.92	0.90
	C25-3	65.56	—	62.81	64.19	1.37	70.70	0.93	0.91
Marble	M0-1	130.96	119.83	109.78	120.19	8.65	163.92	0.80	0.73
	M0-2	146.30	—	119.34	132.82	13.24	179.94	0.81	0.74
	M0-3	145.92	136.78	114.56	132.42	10.61	168.74	0.86	0.78
	M25-1	250.29	196.30	161.58	203.25	37.19	293.02	0.86	0.69
	M25-2	220.96	184.38	142.46	182.60	32.07	266.87	0.83	0.68
	M25-3	233.98	204.00	180.60	206.19	21.85	291.36	0.80	0.71

TABLE 6 Instability stress.

Lithology	Code	σ_{pr}/MPa	Lithology	Code	σ_{pr}/MPa
Coal	C0-1	6.10	Marble	M0-1	—
	C0-2	3.40		M0-2	—
	C0-3	9.62		M0-3	—
	C25-1	78.76		M25-1	287.66
	C25-2	78.47		M25-2	265.32
	C25-3	70.70		M25-3	274.30

The stress level of marble crack initiation stress is 0.45–0.57, basically in line with the current statistics that the reasonable range of the stress level of complete rock crack initiation stress is 0.4–0.5 (Cai et al., 2004). However, there are some differences which are caused by different lithology, sample conditions, and stress paths. Zhou Hui pointed out that the fracture initiation stress level of marble is 0.47–0.64, through uniaxial and triaxial loading of marble (Zhou et al., 2015), and the value determined by this method is also in this range. At the same time, it can be seen that the crack initiation stress level of this method is also basically consistent with the stress level of 0.51–0.56 of the mean value of the crack initiation stress determined by the four methods, indicating that the determination of the crack initiation stress of this method is more accurate.

The closure stress level of marble determined by this method is 0.13–0.21, which is basically consistent with that obtained by most scholars (Martin and Chandler, 1994; Zhou et al., 2015), and is also consistent with the stress level of 0.13–0.22 of the mean closure stress determined by the four methods. The closure stress level of bedded coal and rock is 0.20–0.31, which is significantly higher than that of marble. This is due to the fact that the bedding coal rock is a heterogeneous sedimentary rock with primary fracture development, and its original pore development degree is far greater than that of marble. Therefore, it is in line with the actual situation that a higher stress level is required for the original crack compaction closure, and this method can accurately reflect the actual size of the closure stress. On the other hand, the closure stress level of bedding coal and rock determined by this method is highly consistent with the mean value of 0.18–0.33 determined by the four methods, which also proves that this method is more accurate in determining the closure stress of coal and rock.

2) Damage stress

The damage stress is compared with the determined value of the energy growth rate method in this paper by the volume strain method, which is widely used at present, and the energy dissipation rate method, which also uses the energy principle. The damage stress level of coal and marble under the three value methods is given in Table 5. It can be seen from Table 5 that the damage stress level of bedded coal and rock determined by the energy growth rate method is 0.84–0.93, and it basically conforms to the reasonable range of 0.9–1.0 for bedded rocks (Cai et al., 2004). At the same time, it can be seen that the damage stress level of this method is basically consistent with the stress level of 0.77–0.91 of the average damage stress determined by the three methods.

The damage stress level of marble is 0.80–0.86, which conforms to the reasonable range of 0.8–0.9 for complete rock (Cai et al., 2004; Zhou et al., 2015). The difference between the stress level of 0.68–0.73 and the mean value of damage stress determined by the three methods is large, mainly due to the large difference between the damage stress values determined by the energy dissipation rate method. Considering that the energy dissipation rate method is proposed for coal and rock, the lithologies of marble and coal and

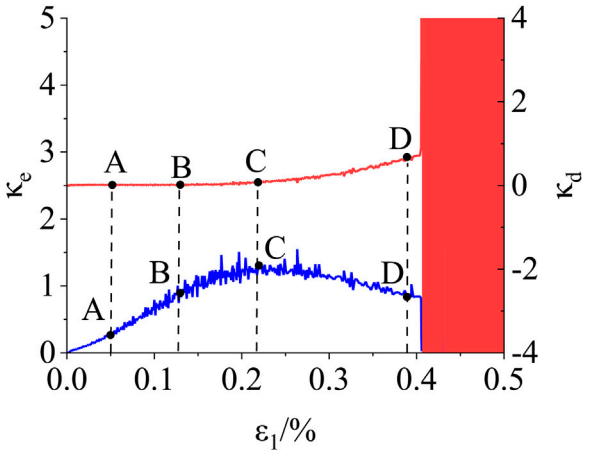

FIGURE 5
Typical elastic energy growth rate curve and dissipated energy growth rate curve of the unloading path.

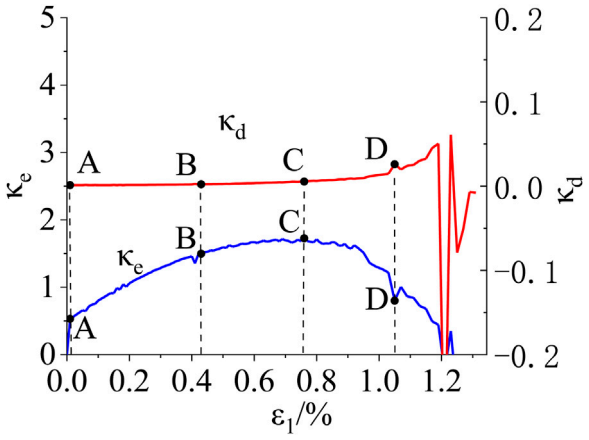

FIGURE 6
Typical elastic energy growth rate curve and dissipative energy growth rate curve of the true triaxial path.

TABLE 7 Characteristic stresses of unloaded marble.

Code	σ_{cc}/MPa	σ_{cc}/σ_f	σ_{ci}/MPa	σ_{ci}/σ_f	σ_{ed}/MPa	σ_{cd}/σ_f	σ_{pr}/MPa	σ_f/MPa
MU25-1	35.49	0.15	105.78	0.45	176.73	0.78	226.94	235.33
MU25-2	29.16	0.12	123.09	0.52	191.59	0.81	222.50	237.88
MU25-3	28.63	0.12	123.32	0.51	181.93	0.76	226.89	240.30

rock are quite different. This method may not be suitable for dense high-confining pressure triaxial marble, and it can be seen that the value difference between the volumetric strain method and this method is small. Moreover, the damage stress level of this method is closer to 0.8–0.9, which indicates that the value of this method is in line with the actual situation. It can be seen that this method is more accurate in determining the damage stress of bedded coal and marble.

3) Instability stress

The instability stress of the rock fracture precursor point determined by the EGR method is shown in Table 6. It can be seen from the table that under the triaxial stress condition, the EGR method can not only determine three traditional characteristic stresses but also find the precursor stress of rock instability failure–instability stress. In addition to three-dimensional stress conditions, the instability stress of coal and rock can also be determined by this method under uniaxial conditions. However, marble is obviously hard and brittle under uniaxial conditions, and under this path, the internal cracks of marble will be directly damaged when they start to connect, and the bearing capacity will decrease suddenly. It is impossible to determine the damage precursor through the point where the cracks penetrate.

The EGR method has good applicability in determining the instability stress under triaxial conditions. However, the applicability under uniaxial conditions is determined by lithology, and it is necessary to determine whether this method can be used to establish through tests.

3.3 Universal verification

It can be seen that the EGR method can accurately determine the compaction, crack initiation, and damage stress at the same time. In addition, this method can find the precursor point of rock fracture, which provides a reference for early warning of rock failure and instability. It can be seen that the EGR method is applicable to the two kinds of rocks with large lithological difference between bedded coal and marble. At the same time, it is also applicable to uniaxial compression and conventional triaxial compression paths, which shows that the EGR method has certain universality. This method is now introduced into the unloading path and the true three-axis loading and unloading path for universal verification.

1) Unloading path

The initial confining pressure of the conventional triaxial unloading confining pressure test is 25 MPa, and the unloading stress level is 80% of the ultimate strength. Test data are from the literature (Gui, 2022). Figure 5 shows the typical elastic energy growth rate curve and dissipation energy growth rate curve under the unloading path. It can be seen that this method can also be used to determine the stress eigenvalue under this path. At the same time,

TABLE 8 Characteristic stresses under the true triaxial path.

Stress path	$(\sigma_{2i}/\sigma_{3i})$/MPa	σ_{cc}/MPa	σ_{cc}/σ_f	σ_{ed}/MPa	σ_{cd}/σ_f	σ_{pr}/MPa	σ_f/MPa
Load	41/25	156.8	0.58	268.3	0.90	297.58	299.45
	56/40	165.1	0.57	288.8	0.87	329.74	333.4
	66/50	180.3	0.6	301.1	0.85	350.20	352.6
Unloaded	41/25	156.8	0.65	241.6	0.96	250.26	250.81
	56/40	165.1	0.65	255.7	0.96	—	267.1
	66/50	180.3	0.68	263.7	0.94	277.67	280.8

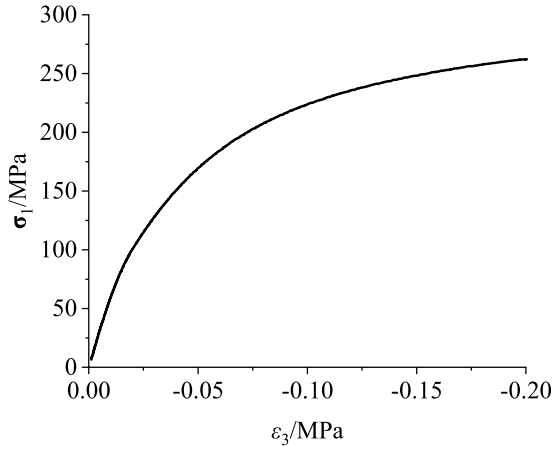

FIGURE 7
Axial stress–transverse strain curve under the failure of the Lajtai method (rock sample: M25-1).

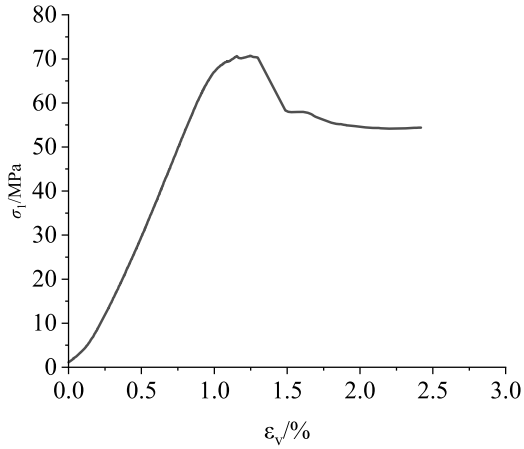

FIGURE 8
Axial stress–volumetric strain curve under the failure of the volume strain method (rock sample: C25-3).

it can be seen that under the conditions of rock unloading and surrounding rock testing, the growth rate curve of dissipated energy during the stage of fracture instability and connection fluctuates significantly, forming a "red block." This indicates that under the condition of unloading confining pressure, the development of fracture connection becomes more intense during the stage of fracture instability and connection in rocks. The characteristic stress values are shown in Table 7. It can be seen that the EGR method is also applicable under the unloading path. The stress level ranges of the crack closure stress, crack initiation stress, and damage stress are 0.12–0.15, 0.45–0.52, and 0.76–0.81, respectively, which are consistent with the reasonable stress level ranges of marble. At the same time, it can be seen that under the condition of triaxial unloading of confining pressure marble, this method is also applicable to the determination of failure precursors.

2) True three-axis loading and unloading paths

Three kinds of initial lateral stresses are designed for the true triaxial loading and unloading test, which are 41/25, 56/40, and 66/50 (initial middle principal stress/initial minimum principal stress). It includes two stress paths: true triaxial loading and true triaxial loading with maximum principal stress simultaneously unloading minimum principal stress. Test data are obtained from the literature (Gui, 2022).

Figure 6 shows the typical elastic energy growth rate curve and dissipation energy growth rate curve of the true triaxial path. It can be seen that under the true triaxial loading and unloading path, the characteristics of the rock energy growth rate curve are also obvious, and only the characteristics of the first stage do not appear. This is because in the numerical test, the marble model has no original micro-defects, so there is no compaction process. Therefore, the EGR determination method is applicable under the true three-axis path. The characteristic stress values under the true triaxial loading and unloading paths are given in Table 8. The stress level range of crack initiation stress and damage stress under the loading path is 0.57–0.6 and 0.85–0.9, respectively, which conforms to the reasonable stress level range of complete marble. The stress level range of crack initiation stress and damage stress under unloading path is 0.65–0.68 and 0.94–0.96, respectively, which is slightly higher than the reasonable stress level range of complete marble. This is because the peak strength of the unloading test is lower than that of the loading path, so it is reasonable to slightly increase the stress level of the characteristic stress. At the same time, it can be

seen that under the condition of true triaxial loading and unloading, this method is also applicable for the determination of instability precursor instability stress.

4 Discussion

The rationality, accuracy, and universality of the EGR method were discussed previously. This section compares this method with the five commonly used methods mentioned in this article and discusses the advantages and disadvantages of this method.

The Martin method determines the crack closure stress and crack initiation stress according to the two turning points of the crack volume strain ε_{vc} before and after the zero value. This method is significantly affected by the value of Poisson's ratio, and the change of Poisson's ratio ±5% will cause a change in crack initiation stress ±40%.

Both the Lajtai method and Zhao XG method consider transverse strain to be more sensitive to crack propagation. Lajtai determined that the turning point of transverse strain from non-linear to linear for the first time is σ_{cc}, and the turning point from linear to non-linear is σ_{ci}. However, the transformation of the transverse strain curve is not obvious in this method, and it is difficult to observe in marble samples. As shown in Figure 7, in the transverse strain curve of the marble sample, there is no linear growth curve. Zhao X G selected the transverse strain data from the beginning of the test to the damage stress point and connected the starting point with the damage stress point determined by the energy dissipation method as the reference line, determined by the maximum value of the transverse strain difference ΔLSR under the same axial stress σ_{ci}. Compared with the Lajtai method, this method has obvious characteristics and is easy to determine. However, due to the influence of damage stress determination, it is necessary to determine the damage stress first with other determination methods.

The volume strain method is the most commonly used method to determine the damage stress at present. The turning point at which the volume strain begins to decrease is the damage stress. However, this method can only determine the damage stress and needs to be combined with other methods to determine the characteristic stress value. On the other hand, the method also fails under certain test conditions, as shown in Figure 8. There is no turning point of volume reduction in triaxial coal and rock during failure.

The DER method is proposed based on the uniaxial coal and rock test. As shown in Table 4 and Table 6, the closure stress and damage stress of marble determined by this method are relatively small, especially the closure stress, which is only 40% of the average value determined by various methods. Obviously, this method is significantly affected by lithology and is more suitable for coal and rock.

The EGR method proposed in this paper is based on further deduction of the rock energy dissipation theory proposed by Xie et al. (2005) and the reasonable explanation of the value process, which has a rigorous and sufficient theoretical basis. Compared with the current determination method, this method can independently determine the three characteristic stresses of closure, crack initiation, and damage and does not need to be combined with other methods. This method can also determine the failure precursor point of the instability stress at the same time, reducing the workload of determining the characteristic stress and the failure precursor point. Combined with the accuracy analysis and universality analysis in this paper, this method is applicable to the uniaxial, conventional triaxial, and true triaxial loading and unloading tests of coal and marble with different lithologies, and the determined characteristic stress is accurate and reasonable. Therefore, it can be considered that this method has certain advantages in determining closure stress, crack initiation stress, damage stress, and instability stress. However, when the method is used to determine the instability stress in the uniaxial test, it will be affected by the lithology. It is necessary to determine whether the method can be used to determine the failure precursor instability stress through the test.

5 Conclusion

Rock failure is a complex process, consisting of different forms of energy conversion and transfer, that is, rock failure is the result of energy conversion, release, and dissipation. Therefore, this paper analyzes the progressive failure process of loaded rock from the perspective of energy, defines the growth rate of elastic energy κ_e and dissipation energy κ_d to analyze the progressive failure process of loaded rock, proposes a new method to determine the stress characteristic value of the energy growth rate (EGR), and uses the conventional loading test of the uniaxial triaxial coal rock and uniaxial triaxial marble to verify. The conclusion is as follows:

1) A method is proposed to determine the crack initiation stress and closure stress by the elastic energy growth rate curve and the elastic energy storage capacity index curve and to determine the damage stress and instability stress by the dissipated energy growth rate curve, which are combined to determine the strength characteristic values of each stage of rock progressive failure
2) The determination method of the EGR characteristic stress value is based on rigorous and sufficient theory, and the evaluation process is objective and reasonable. Meanwhile, the characteristic stress value is determined by a variety of methods. Compared with the reasonable range of stress levels of each characteristic stress, the rationality and accuracy of the determination of characteristic stress values by the EGR method were verified.
3) This method is extended to the conventional triaxial unloading confining pressure test and true triaxial loading and unloading test. This method is also applicable to the aforementioned conditions. It shows that the determination method of the EGR characteristic stress value has good universality, and this method can provide a new idea for the determination of rock strength characteristic values.
4) The rock shows different stress–strain relationships at each stage of progressive failure. Therefore, in the subsequent research, it is necessary to consider how to combine the determination method of characteristic stress with the construction of a rock constitutive model to establish a constitutive model closer to the true stress–strain relationship of rock.

Data availability statement

The original contributions presented in the study are included in the article/Supplementary Material; further inquiries can be directed to the corresponding author.

Author contributions

XL contributed to the conception of the study; XG, YZ, and YX performed the experiment; XL, XG, YW, and XQ contributed significantly to analysis and manuscript preparation; XG performed the data analyses and wrote the manuscript. All authors contributed to the article and approved the submitted version.

Funding

This research was funded by the General Project of the Sichuan Natural Science Foundation (Grant No. 2022NSFSC0279), the Key Scientific Research Fund of Xihua University (Grant No. Z17113), and the Graduate Innovation Fund of Xihua University (Grant No. YCJJ2021056).

Conflict of interest

Author XG was employed by Design & Research Co., LTD. YX was employed by CHN Energy Dadu River Hydropower Development Co. Ltd.

The remaining authors claim that the study was conducted without any commercial or financial relationship, which may be interpreted as a potential conflict of interest.

Publisher's note

References

Bieniawski, Z. T. (1967). Mechanism of brittle fracture of rock: Part I—theory of the fracture process[J]. *Int. J. Rock Mech. Min. Sci. Geomechanics Abstr.* 4 (4), 395–406.

Brown, E. T. (1981). *Rock characterisation, testing and monitoring. ISRM suggested methods[M].* Oxford: Pergamon Press.

Cai, M., Kaiser, P. K., Tasaka, Y., Maejima, T., Morioka, H., and Minami, M. (2004). Generalized crack initiation and crack damage stress thresholds of brittle rock masses near underground excavations. *Int. J. Rock Mech. Min. Sci.* 41 (5), 833–847. doi:10.1016/j.ijrmms.2004.02.001

Eberhardt, E., Stead, D., Stimpson, B., and Read, R. S. (1998). Identifying crack initiation and propagation thresholds in brittle rock. *Can. geotechnical J.* 35 (02), 222–233. doi:10.1139/t97-091

Griffith, A. (1921). The phenomena of rupture and flow in solids [J]. *Philos. Trans. R. Soc. Lond* 221 (A), 163–198. doi:10.1098/rsta.1921.0006

Gui, X. (2022). *Study on energy characteristics and fracture mechanism of deep marble under true triaxial loading and unloading.* Chengdu: Xihua University.

Jin, F. N., Jiang, M. R., and Gao, X. L. (2004). Method of defining damage variable based on energy dissipation [J]. *J. rock Mech. Eng.* 2004 (12), 1976–1980.

Kim, J. S., Lee, K. S., Cho, W. J., Choi, H. J., and Cho, G. C. (2015). A comparative evaluation of stress–strain and acoustic emission methods for quantitative damage assessments of brittle rock. *Rock Mech. Rock Eng.* 48 (2), 495–508. doi:10.1007/s00603-014-0590-0

Kong, L. W., Xie, H. P., and Li, C. B. (2023). Coupled microplane and micromechanics model for describing the damage and plasticity evolution of quasi-brittle material. *Int. J. Plasticity* 162, 103549. doi:10.1016/j.ijplas.2023.103549

Lajtai, E. Z., Carter, B. J., and Ayari, M. L. (1990). Criteria for brittle fracture in compression. *Eng. Fract. Mech.* 37 (1), 59–74. doi:10.1016/0013-7944(90)90331-a

Li, C. B., Yang, D. C., Xie, H. P., Ren, L., and Wang, J. (2023). Size effect of fracture characteristics for anisotropic quasi-brittle geomaterials. *Int. J. Min. Sci. Technol.* 33 (2), 201–213. doi:10.1016/j.ijmst.2022.11.004

Li, S. N., Liu, X. X., and Li, Y. (2022). Study on deformation characteristics and damage evolution of carbonaceous mudstone during progressive failure [J]. *J. China Highw.* 35 (04), 99–107. doi:10.19721/j.cnki.1001-7372.2022.04.007

Liu, W., Zhang, S., and Sun, B. (2019). Energy evolution of rock under different stress paths and establishment of A statistical damage model. *KSCE J. Civ. Eng.* 23 (10), 4274–4287. doi:10.1007/s12205-019-0590-4

Liu, X. H., Hao, Q. J., and Hu, A. K. (2020). Study on determination method of characteristic stress of uniaxial coal and rock under quasi-static strain rate. *JJ J. Rock Mech. Eng.* 39 (10), 2038–2046. doi:10.13722/j.cnki.jrme.2020.0321

Liu, X. H., Xue, Y., and Zheng, Y. (2022). Research on failure precursor based on characteristics of energy dissipation rate for rock[J]. *Front. Earth Sci.* 2022, 812438. doi:10.3389/feart.2021.812438

Liu, Z. X., Meng, X. R., and Zhao, G. M. (2023). Energy and damage analysis of sandstone under true triaxial compression [J]. *J. rock Mech. Eng.* 42 (02), 327–341. doi:10.13722/j.cnki.jrme.2022.0256

Martin, C. D., and Chandler, N. A. (1994). The progressive fracture of Lac du Bonnet granite. *Int. J. Rock Mech. Min. Sci. Geomechanics Abstr.* 31 (6), 643–659. doi:10.1016/0148-9062(94)90005-1

Ning, J., Wang, J., Jiang, J., Hu, S., Jiang, L., and Liu, X. (2018). Estimation of crack initiation and propagation thresholds of confined brittle coal specimens based on energy dissipation theory. *JJ. Rock Mech. Rock Eng.* 51 (1), 119–134. doi:10.1007/s00603-017-1317-9

Peng, J., Rong, G., Cai, M., and Zhou, C. B. (2015). A model for characterizing crack closure effect of rocks. *Eng. Geol.* 189, 48–57. doi:10.1016/j.enggeo.2015.02.004

Peng, J., Rong, G., and Zhou, C. B. (2013). Experimental study on the effect of water pressure on the progressive fracture process of rock [J]. *Geotech. Mech.* 34 (04), 941–946+954. doi:10.16285/j.rsm.2013.04.024

Tkalich, D., Fourmeau, M., Kane, A., and Cailletaud, G. (2016). Experimental and numerical study of Kuru granite under confined compression and indentation. *Int. J. Rock Mech. Min. Sci.* 87, 55–68. doi:10.1016/j.ijrmms.2016.05.012

Wang, C., He, B., Hou, X., Li, J., and Liu, L. (2019). Stress–energy mechanism for rock failure evolution based on damage mechanics in hard rock. *Rock Mech. Rock Eng.* 53 (3), 1021–1037. doi:10.1007/s00603-019-01953-y

Wang, H. L., Fan, P. X., and Wang, M. Y. (2011). Effect of strain rate on progressive failure process and characteristic stress of red sandstone [J]. *Geotech. Mech.* 32 (05), 1340–1346. doi:10.16285/j.rsm.2011.05.008

Xie, H. P., Gu, Y., and Li, L. Y. (2008). Energy mechanism of rock mass deformation and failure process [J]. *J. Rock Mech. Eng.* 2008 (09), 1729–1740. doi:10.3321/j.issn:1000-6915.2008.09.001

Xie, H. P., Ju, Y., and Li, L. Y. (2005b). Rock strength and overall failure criteria based on energy dissipation and release principle [J]. *J. rock Mech. Eng.* 2005 (17), 3003–3010. doi:10.3321/j.issn:1000-6915.2005.17.001

Xie, H. P., Peng, R. D., and Gu, Y. (2005a). Preliminary study on energy analysis of rock failure [J]. *J. Rock Mech. Eng.* 2005 (15), 2603–2608. doi:10.3321/j.issn:1000-6915.2005.15.001

Xie, H. P., Peng, R. D., and Ju, Y. (2004). Analysis of energy dissipation during rock deformation and failure [J]. *J. rock Mech. Eng.* 2004 (21), 3565–3570. doi:10.3321/j.issn:1000-6915.2004.21.001

Xie, Y. C., Michael, Z. H., and Li, C. B. (2023). Anisotropic characteristics of acoustic emission and the corresponding multifractal spectrum during progressive failure of shale under cyclic loading. *Int. J. Rock Mech. Min. Sci.* 165, 105364. doi:10.1016/j.ijrmms.2023.105364

Yang, S., Xu, P., and Ranjith, P. G. (2015). Damage model of coal under creep and triaxial compression. *Int. J. Rock Mech. Min. Sci.* 80, 337–345. doi:10.1016/j.ijrmms.2015.10.006

Zhang, J., Song, Z., and Wang, S. (2020). Experimental investigation on permeability and energy evolution characteristics of deep sandstone along a three-stage loading path [J]. *Bull. Eng. Geol. Environ.* 80. (prepublish).

Zhao, X. G., Cai, M., Wang, J., Li, P. F., and Ma, L. K. (2015). Objective determination of crack initiation stress of brittle rocks under compression using AE measurement. *Rock Mech. Rock Eng.* 48 (6), 2473–2484. doi:10.1007/s00603-014-0703-9

Zhao, Z. H., and Xie, H. P. (2008). Study on energy transfer and dissipation during rock deformation and failure. *J. Sichuan Univ. Eng. Sci. Ed.* 2008 (02), 26–31. doi:10.15961/j.jsuese.2008.02.01

Zhou, H., Meng, F. Z., and Zhang, Z. Q. (2015). Characteristics and generation mechanism of stress-strain threshold of hard rock. *JJ J. Rock Mech. Eng.* 34 (08), 1513–1521. doi:10.13722/j.cnki.jrme.2014.0338

frontiers | Frontiers in Earth Science

TYPE Original Research
PUBLISHED 14 June 2023
DOI 10.3389/feart.2023.1211117

OPEN ACCESS

EDITED BY
Yingfeng Sun,
University of Science and Technology Beijing, China

REVIEWED BY
Tengteng Li,
Jiangsu University, China
Feng Du,
China University of Mining and Technology, China
Kedi Wang,
Tsinghua University, China

*CORRESPONDENCE
Zuo Sun,
sunzuo@mail.ccri.ccteg.cn

RECEIVED 24 April 2023
ACCEPTED 05 June 2023
PUBLISHED 14 June 2023

CITATION
Jia L, Sun Z, Lu J and Gu B (2023), Coal breaking characteristics of high pressure water jet and the law of coordinated pressure relief of slits.
Front. Earth Sci. 11:1211117.
doi: 10.3389/feart.2023.1211117

Coal breaking characteristics of high pressure water jet and the law of coordinated pressure relief of slits

Lianxin Jia[1], Zuo Sun[2]*, Junshuai Lu[1] and Beifang Gu[3]

[1]Guoneng Shendong Coal Group Co, Ltd, Ordos, China, [2]Emergency Science Research Institute, Chinese Institute of Coal Science, Beijing, China, [3]School of Environmental and Municipal Engineering, North China University of Water Resources and Electric Power, Zhengzhou, China

Hydraulic fracturing creates slots on the coal surface through the impact of high-pressure water jets, resulting in stress gradients in the surrounding coal, thereby inducing stress release and increasing gas extraction efficiency. It is an effective measure to prevent coal and gas outbursts. Numerical simulations demonstrate that high-pressure water jets generate slots in the coal, leading to stress gradients in the surrounding coal. These stress gradients drive the coal to move gradually towards the slots, thereby releasing stress. The stress unloading degree in the *Y* direction is greater than that in the *X* and *Z* directions. Damage occurs in the coal near the slots, causing a significant increase in the number of fractures within the coal, which improves gas extraction efficiency. The study reveals the variation in stress unloading of coal between hydraulic fracturing boreholes and extraction boreholes in adjacent positions. By cross-referencing various factors in numerical simulations, the extent of damage in different directions caused by slot formation under different factor combinations is determined. A mathematical model for the range of coal damage surrounding the slots is obtained through MATLAB fitting. The research findings provide references for on-site testing and applications of high-pressure water jet technology.

KEYWORDS

water jet, hydraulic slitting, coal breaking characteristics, coordinated pressure relief, numerical simulation

1 Introduction

The mechanism of coal and gas outbursts has been extensively studied in the academic community, leading to a comprehensive and widely accepted explanation known as the integrated action hypothesis (Taylor, 1852; Halbaum, 1899; Jou, 2000; Li and Lin, 2010). Conducting research and applications on the intensified unloading and permeability enhancement of low-permeability coal seams contributes to finding solutions and preventive measures for coal and gas outburst accidents (Liu et al., 2014; Zarrouk and Moore, 2009; Liu et al., 2011; Soliman, 1999).

Hydraulic fracturing exhibits significant effects on relatively hard coal formations. By subjecting the coal to high-pressure water jet impacts, slots are formed, leading to unloading and permeability enhancement in the surrounding coal, thereby increasing gas extraction efficiency. Therefore, hydraulic fracturing is an effective measure for preventing outbursts. Zheng et al. (2014) proposed two hydraulic fracturing methods, namely, "strong water rapid cutting" and "fine water slow cutting." They investigated the effects of different fracturing

methods on borehole jets through numerical simulations and field experiments. Li et al. (2014) conducted multiple experiments to explore the characteristics of pressure-flow during the transition process, clarifying the systemic energy characteristics and energy dissipation rules in this process. Yuan et al. (2013) addressed the difficulty of controlling transient pressure and flow during the operational transition of hydraulic fracturing systems. They tested the transient pressure and flow for different nozzle and valve core structural parameters, studying the impact of nozzle and valve core structural parameters on transient pressure and flow. Tang et al. (2012) conducted theoretical and numerical simulation studies on the effectiveness of hydraulic fracturing. Song et al. (2011) analyzed the stress changes induced by hydraulic fracturing in terms of stress variation angles. They employed theoretical analysis and numerical simulation methods, based on the permeation mechanics theory of planar radial flow, to conduct in-depth analysis and exploration of the permeability enhancement principles of hydraulic fracturing. Feng et al. (2001) conducted large-scale coal sample experiments to study the phenomenon of coal and gas outbursts during hydraulic fracturing. They investigated the outburst mechanism of coal and gas during hydraulic fracturing using a combination of experimental and simulation approaches. Zhang et al. (2013) studied the hydraulic fracturing process, proposing that slots formed through hydraulic fracturing in the coal release gas from the outburst coal seam, leading to the release of geological stress. Li et al. (2015) studied the permeability enhancement principle of the combined hydraulic fracturing and hydraulic fracturing techniques used during pre-drainage of coal seam gas. They conducted comparative experiments in the field. Duan et al. (2002) demonstrated that fracturing can increase gas extraction through experiments on the permeability enhancement of coal using large-scale hydraulic fracturing. Wu et al. (2009) analyzed the "bottleneck effect" caused by stress concentration around boreholes and investigated the influence of stress perpendicular to the slot plane, maximum principal stress, and the angle between the slot and stress on unloading through numerical simulations. Zhao and Feng, 2001 studied the methods to enhance the permeability of low-permeability coal seams under the solid-gas coupling effect through experiments. Wang et al. (2015) studied the spatial relationship between coal galleries and bottom drawing galleries, determined the reasonable layout area for bottom drawing galleries, and established a mathematical model for calculating the length of boreholes. Huang et al. (2011) investigated the generation of coal fractures during the hydraulic fracturing process through theoretical research. Long et al. (2011) developed a rapid coal cutting technique using combined deep hole pre-split blasting and high-pressure hydraulic fracturing. They optimized the borehole layout and hydraulic parameters of high-pressure hydraulic fracturing. Fu et al. (2014) studied a water hydraulic integrated technology based on regional gas control, including drilling, fracturing, pressurization, unloading, and injection processes.

Due to the complexity of the coal fracturing process, there are research gaps in understanding the unloading and destructive effects of slots formed by hydraulic fracturing on surrounding coal, as well as the range of damage in different directions. In this study, based on rock mechanics and elastoplastic mechanics, FLAC3D numerical simulation software was employed to investigate the stress-strain and fracture characteristics of the coal surrounding the slots formed by high-pressure water jets. Numerical simulations were conducted to analyze the mutual influence of unloading effects among multiple fracturing boreholes, and the synergistic unloading effects between slots were studied under different borehole arrangement scenarios. Finally, a mathematical model was established to describe the range of coal fracturing caused by hydraulic fracturing.

2 Influence law of slitting on the pressure relief of coal around the slit

2.1 Numerical model construction

The parameters of the numerical calculation model were set based on the actual conditions of Coal Seam No. 6 in Tanjiachong. A rectangular model was established, with a cylindrical outer layer surrounding the surrounding rock in a radial grid. Due to the far distance from the borehole and the predominance of stress effects, it is less prone to deformation and failure, thus a larger grid size was set. The numerical model units were set to 1 m in the *X* and *Z*-axes, and 0.05 m in the *Y*-axis. The inner surrounding rock was modeled as a cylindrical shell, considering its proximity to the borehole and the likelihood of deformation and failure. Therefore, a smaller grid size was used, with unit dimensions of 0.5 m in the *X*-axis, 0.05 m in the *Y*-axis, and 0.5 m in the *Z*-axis. The core part of the model was the borehole model, which had a cylindrical shape. The unit dimensions were set to 0.25 m in the *X*-axis, 0.05 m in the *Y*-axis, and 0.25 m in the *Z*-axis. The model was established with dimensions of 17 m in strike, 10 m in dip, and 17 m in height, and considering the hardware limitations, the slot depth was set to 1 m. The numerical calculation model consisted of a total of 53,600 elements. According to the site conditions, the strike direction of the working face was set as the *X*-axis, and the dip direction was set as the *Y*-axis. The material assignment parameters for the numerical model are shown in Table 1.

The model materials were treated as elastic, and the numerical simulation adopted the Mohr-Coulomb constitutive model. The calculation precision was set to 10^{-5}. The shear modulus and bulk modulus in the material parameters were assigned with large values to prevent plastic failure during stress initialization. Finally, an initial stress field was applied to the model after stress initialization. The stress distribution after stress initialization is shown in Figure 1.

2.2 Stress variation law of coal mass around the slot

The basic parameters of the numerical model were set as follows: slot depth of 1m, slot width of 0.2m, and water jetting pressure of 30 MPa. For observation convenience, the model was sliced after the simulation, as shown in Figure 2. Panel a represents a slice perpendicular to the *Y*-axis, panel b represents a slice perpendicular to the *Z*-axis, and panel c represents a slice perpendicular to the *X*-axis. Panels a, b, and c show the stress distribution cloud maps in the respective directions. Panels d, e, and f are enlarged views of the research area, with the left side of the

TABLE 1 The mechanical parameters in numerical simulation.

Shear modulus *S*	Internal friction angle *F*	Bulk modulus *B*	Density *D*	Tensile strength *T*	Cohesion *C*
(Pa)	(°)	(Pa)	(kg/m^3)	(Pa)	(Pa)
0.19×10^9	20	0.36×10^9	1,400	0.03×10^6	1×10^6

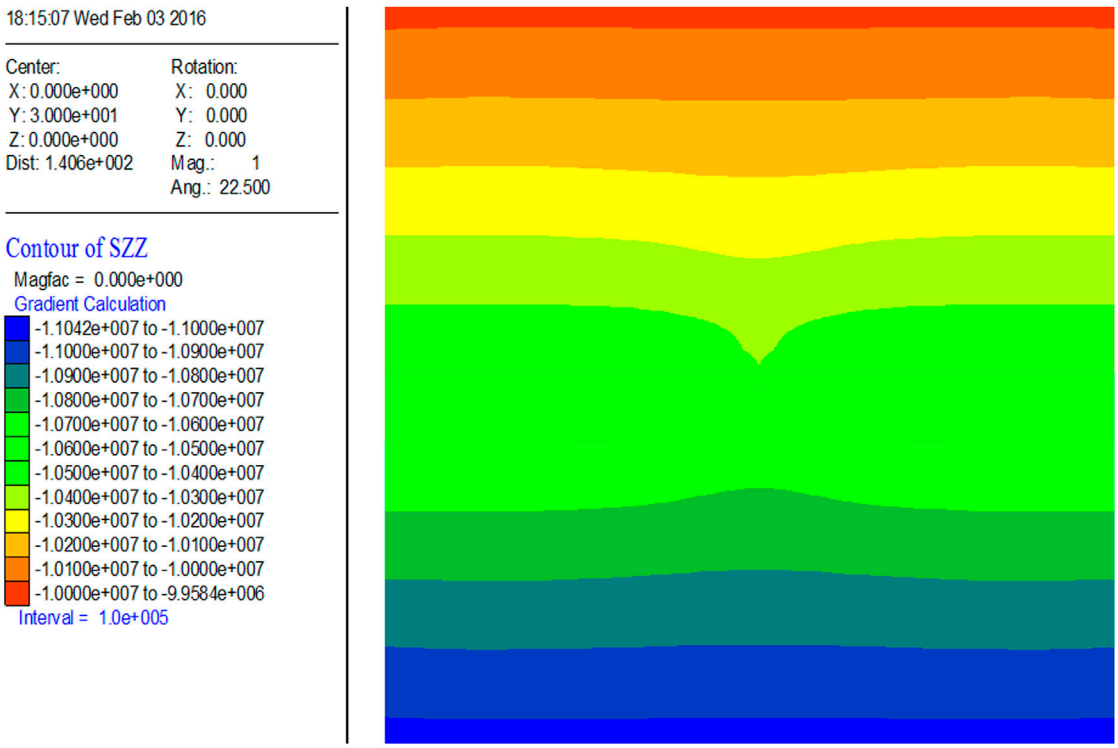

FIGURE 1
Initial stress field vertical stress state.

cloud maps removed. From the stress cloud maps, it can be observed that the stress distribution around the coal mass near the slot follows a trend of gradually decreasing stress in the *X* and *Y* directions. Additionally, a symmetric distribution can be observed, with the symmetry center located at the midpoint of the slot. The stress distribution around the slot shows a decreasing trend in the *Y* direction. Furthermore, a symmetric distribution can be observed, with the symmetry center also located at the midpoint of the slot. The difference from the stress distribution in the *X* direction is that it exhibits a "butterfly" shape on the cross-section. The stress distribution in the *Z* direction is similar to that in the *X* direction. It decreases gradually from near the slot towards the outside and exhibits a symmetric distribution centered at the midpoint of the slot. Outside the influence area of the slot until the model boundary, the coal mass remains unaffected by the slot. Additionally, from the stress cloud maps in panels d to f of Figure 2, it can be seen that the coal mass around the slot experiences positive stress, indicating that it is subjected to tensile stress. Furthermore, the decreasing trend of tensile stress is significant. This trend is attributed to the slot depth being much greater than its width due to hydraulic slot cutting, resulting in a higher degree of stress relief in the *Y* direction compared to the *X* and *Z* directions.

For quantitative analysis, observation points were set at different distances from the center of the slot within the model to obtain the stress values at these points after numerical simulation. The corresponding stress concentration factors were calculated, as shown in Table 2. The table also reflects the same stress variation pattern as the cloud maps, that is, for the same distance from the center of the slot, the stress relief in the *Y* direction is much greater than in the *X* and *Z* directions.

The volumetric stress unloading variation of the coal mass in the X, Y, and Z directions corresponding to different stress concentration factors is shown in Figure 3. Within the entire range of stress concentration factors, for larger stress concentration factors, the corresponding volumetric stress unloading is smaller, consistent with the previously studied stress distribution patterns. Furthermore, when the stress concentration factor is relatively large, it can be observed from the graph that the stress concentration factor in the *Y* direction is greater than in the other two directions. This is due to the slot depth being much larger

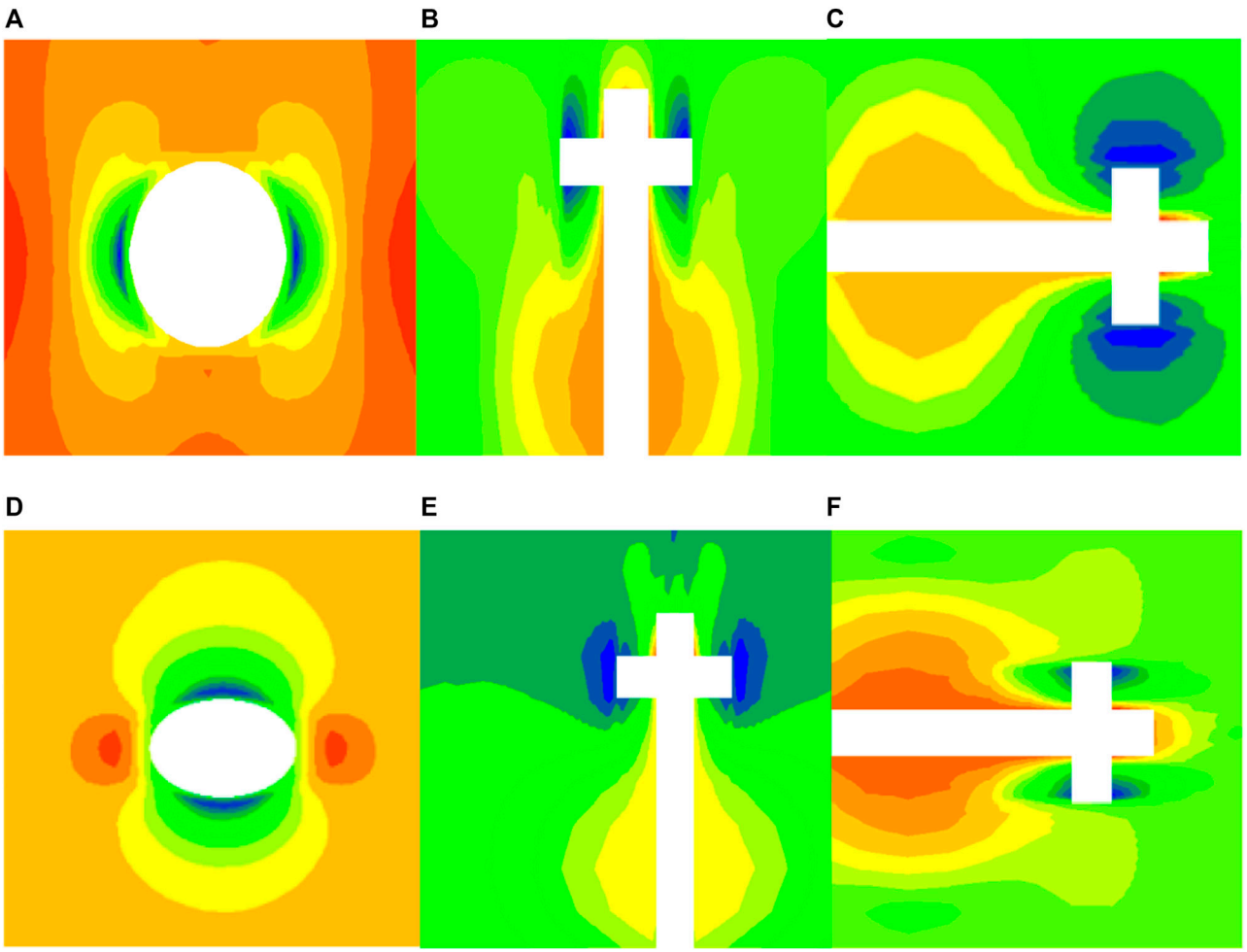

FIGURE 2
Stress distribution cloud of the single slotting: **(A,D)** Slice perpendicular to the *Y*-axis; **(B,E)** Slice perpendicular to the *Z*-axis; **(C,F)** Slice perpendicular to the *X*-axis.

TABLE 2 Stress concentration factor of different center distance.

X-directi-on position(m)	Stress unloadi-ng value (MPa)	Stress concent-ration factor (%)	Y direction-n position (m)	Stress unloadi-ng value (MPa)	Stress concentr-ation factor (%)	*Z* direction position (m)	Stress unload-ing value (MPa)	Stress concent-ration factor (%)
1.3	4.8	60	0.5	0.5	95	1.3	5.0	50
1.5	6.5	50	1.0	2.0	80	1.5	6.7	40
1.8	8.5	30	1.5	4.3	70	1.8	8.0	20
2.0	9.0	30	2.0	11.0	20	2.0	9.2	10
2.2	11.0	20	2.5	11.0	10	2.2	9.7	10

than the slot width, resulting in greater stress relief in the *Y* direction. Conversely, when the stress concentration factor is relatively small, the stress relief in the *Y* direction is smaller than in the *X* direction. This is because the hydraulic slot cutting produces a much larger slot depth in the *X* direction compared to the *Y* direction, leading to better stress relief in the *X* direction. From Figure 3, it can be seen that the rate of increase in volumetric stress unloading varies for each direction. As the stress concentration factor increases, the rate of decrease in volumetric stress unloading accelerates for each direction. When the stress concentration factor is large, the rate

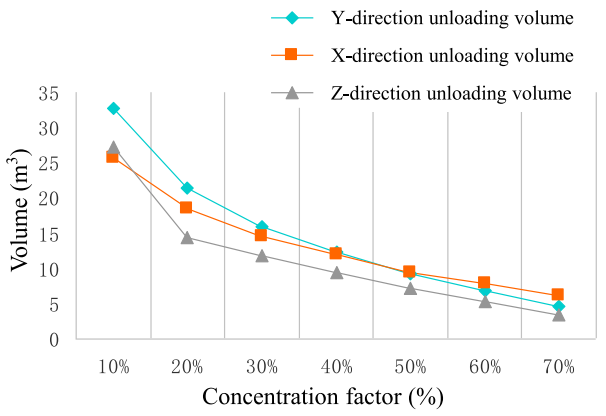

FIGURE 3
Relationship between concentration factor and unloading volume.

of decrease in volumetric stress unloading is slower in the *Y* direction compared to the other directions, indicating that the stress relief effect is better in the *Y* direction when the hydraulic slot width is much smaller than its depth.

After the implementation of hydraulic slotting measures, the stress at the edge of the slot where coal has been ejected is zero. From the edge to the deep part of the coal mass, the pressure gradient forces the coal to move. When the distance from the slot is far, the stress concentration factor is low, indicating that for coal closer to the slot, the slot plays a crucial role in stress relief, although the stress relief effect diminishes rapidly with increasing distance. Additionally, as analyzed earlier, due to the geometric characteristics of the slot, the stress concentration factor in the *Y* direction is greater than in the other directions, indicating that the stress relief effect in the *Y* direction is better.

2.3 Destruction law of coal mass around slots

After hydraulic slotting, based on the previous research, different stress distributions exist at different distances from the slot, resulting in varying stress concentration factors. When the stress exceeds the ultimate strength limit of the coal mass, the coal will be crushed and enter a plastic state. Coal in a plastic state is highly unstable and forms numerous cracks internally, while its strength rapidly decreases. The development and extension of internal cracks in the coal mass lead to a sharp increase in permeability, enabling gas migration channels within the coal mass to connect. As a result, the gas moves more quickly towards the slot space, and when gas drainage is conducted, it significantly improves the efficiency of gas extraction, ultimately eliminating the risk of outbursts. Compared to other areas, coal mass in a plastic state has minimal outburst risk because it possesses very little elastic potential energy and gas kinetic energy, lacking the conditions for dynamic phenomena to occur. The range of coal mass around the slot in the plastic state is shown in Figure 4.

For observation convenience, the model was sliced after the simulation, as shown in Figure 4. Panel a represents a slice perpendicular to the *Y*-axis, panel b represents a slice perpendicular to the *Z*-axis, and panel c represents a slice perpendicular to the *X*-axis. From Figure 4A, it can be observed that the plastic zone distribution in the vertical direction (*Y*-axis) presents an elliptical shape, with a larger horizontal extent of plastic damage compared to the vertical extent. This is because the horizontal stress applied to the borehole is greater than the vertical stress, making the coal mass more susceptible to horizontal damage. From Figure 4B, it can be seen that the impact of the slot on the surrounding coal mass is much greater than that of the hydraulic slotting borehole, indicating that hydraulic slot cutting is more effective in gas extraction compared to solely drilling holes. Due to the much greater depth of the slot compared to its width, the area of the coal mass in the plastic failure zone is much

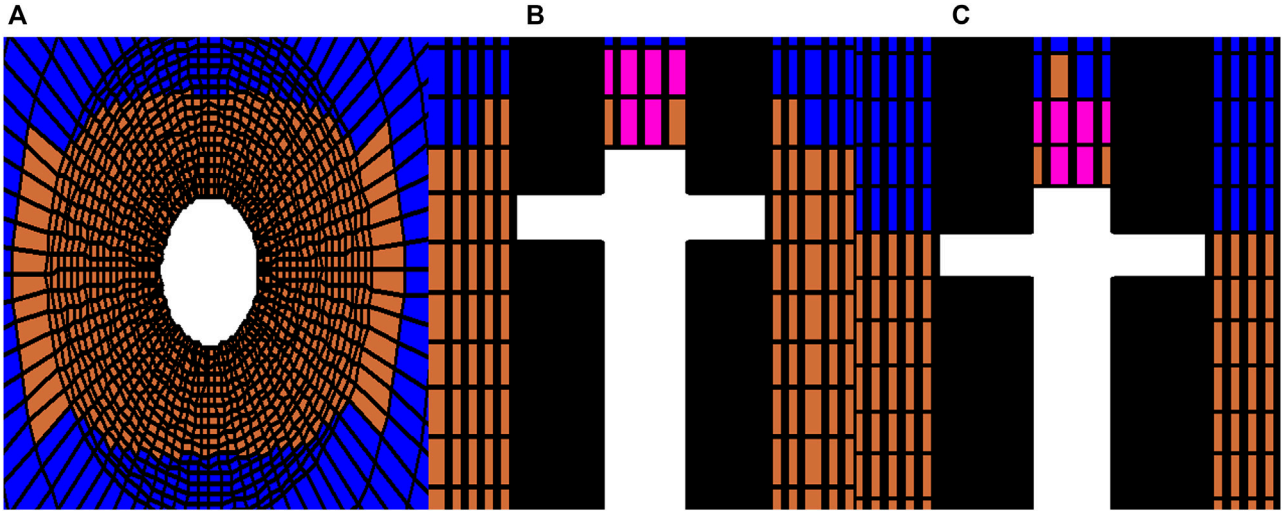

FIGURE 4
The map of plastic zone: **(A)** Slice perpendicular to the *Y*-axis; **(B)** Slice perpendicular to the *Z*-axis; **(C)** Slice perpendicular to the *X*-axis.

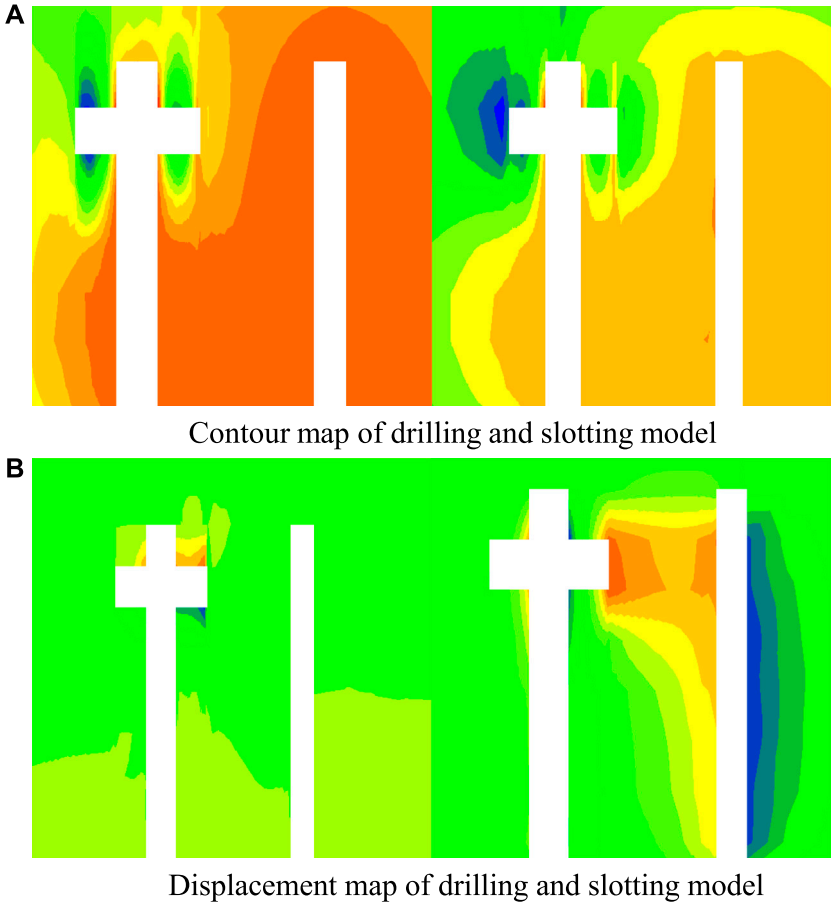

FIGURE 5
Contour and displacement map of drilling and slotting model: **(A)** Contour map of drilling and slotting model; **(B)** Displacement map of drilling and slotting model.

larger in the direction parallel to the borehole than in the direction perpendicular to the borehole. From a three-dimensional perspective, the distribution of coal mass in the plastic zone is similar to that of the slot model, but with a larger diameter. As concluded earlier, the stress unloading in the *Y* direction is greater than in the other directions, and this can also be observed from the plastic zone diagram. The plastic zone in the *Y* direction is larger than in the other directions. By examining the stress unloading level at the boundary of the plastic zone, observation points were set at different distances from the center of the slot to determine the stress unloading at the boundary of the plastic zone. It can be concluded that the stress unloading is significant at the boundary of the plastic zone for all coal masses within the plastic zone. For practical application, the range of the slot's influence can be determined by the radius of the plastic zone, avoiding blind areas in gas extraction and thus preventing outbursts.

3 The law of synergistic pressure relief between slits

This section investigates the mutual influence of stress relief under three different arrangements: parallel placement of slot cutting and gas extraction boreholes, parallel placement of slot cutting boreholes, and intersecting placement of slot cutting boreholes. The stress relief mutual interaction patterns in the case of multiple slot cutting boreholes are summarized. The numerical model parameters were set as follows: coal seam depth of 400 m, water jet pressure of 30 MPa, slot depth of 1 m, slot width of 0.2 m, and slot spacing of 3 m.

3.1 Influence of slotted drilling on gas drainage drilling

A new model was established with a distance of 3 m between the slot cutting boreholes and the gas extraction boreholes. Figure 5 shows the stress-strain cloud map of the coal mass between the slot cutting boreholes and the gas extraction boreholes, and Figure 6 shows the plastic zone distribution.

The distance between the center of the slot cutting borehole and the center of the gas extraction borehole was set to 3 m. As revealed by the previous numerical simulation, the gas extraction borehole falls within the effective range of hydraulic slot cutting. From the stress distribution cloud map, it can be observed that there is a small stress relief area around the gas extraction borehole after its

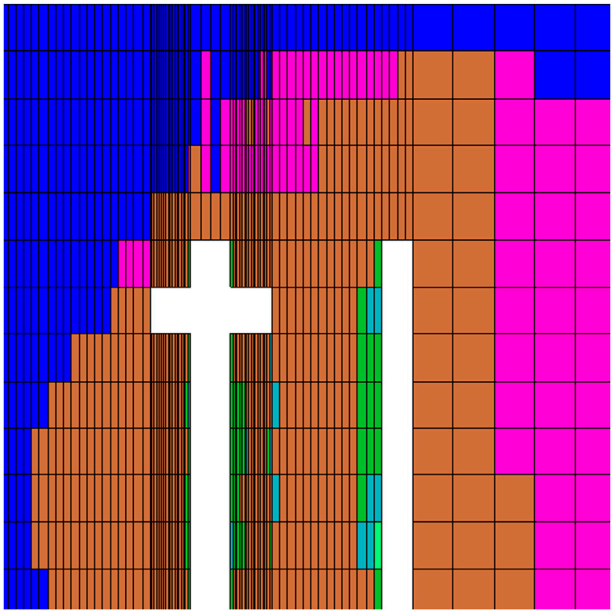

FIGURE 6
Block state of drilling and slotting model.

construction. After hydraulic slot cutting, the coal mass on the left side of the gas extraction borehole falls within the effective range of hydraulic slot cutting, resulting in significant deformation and noticeable stress relief. The influence of hydraulic slot cutting gradually reduces the stress relief range in the *X* direction on the left side of the gas extraction borehole, while the changes in stress relief range in other directions are not significant. The comparison of stress relief effects on both sides of the gas extraction borehole is evident. The plastic damage zone map shows that the coal mass between the slot cutting borehole and the gas extraction borehole has undergone complete plastic deformation due to the effect of slot cutting. Therefore, when arranging slot cutting boreholes, if the distance between two boreholes is smaller than the effective stress relief range of hydraulic slot cutting, it is possible to construct only one hydraulic slot cutting borehole to effectively reduce the workload.

3.2 Influence of parallel arrangement between kerf boreholes for pressure relief

The previous section examined the influence of hydraulic slot cutting boreholes on the stress relief of adjacent gas extraction boreholes. This section simulates the mutual influence of stress relief in the coal seam when two hydraulic slot cutting boreholes are placed in parallel. A new model was established with a distance of 5 m between adjacent slot cutting boreholes. The stress variation cloud map of the coal mass is shown in Figure 7, and the plastic zone distribution is shown in Figure 8.

From the stress distribution cloud map, it can be observed that when two hydraulic slot cutting boreholes are placed horizontally with a distance of 5 m, the stress relief range gradually increases from the start of hydraulic slot cutting, and the displacement range of the coal mass also expands. The coal mass in the middle is affected by the deformation of the coal masses on both sides due to the synergistic stress relief effects. The stress relief range in the middle is greater than that of a single hydraulic slot cutting measure. The simulation was conducted for 5,000 steps, and after the numerical

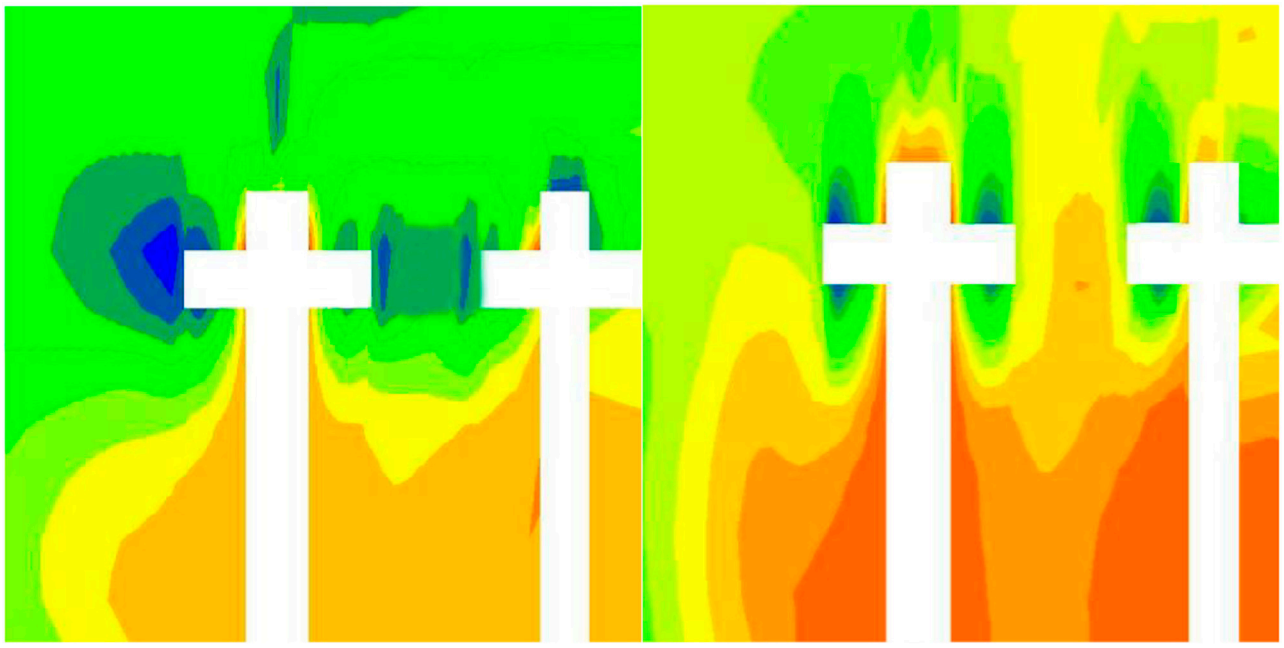

FIGURE 7
Contour map of parallel slotting model.

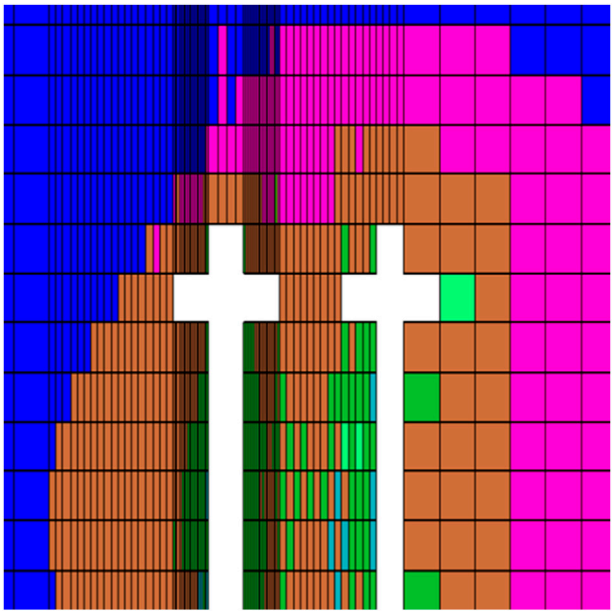

FIGURE 8
Block state of slotting model.

simulation, the coal mass between the horizontally adjacent hydraulic slot cutting boreholes has undergone complete stress relief.

From the plastic damage zone map, it can be observed that the coal mass is significantly affected by the hydraulic slot cutting measures on both sides, resulting in greater plastic damage compared to a single hydraulic slot cutting borehole. After the numerical simulation, the coal mass between the horizontally adjacent hydraulic slot cutting boreholes has completely undergone plastic deformation, confirming the synergistic stress relief effects when slot cutting boreholes are arranged in parallel.

3.3 Influence of pressure relief on cross-arrangement of kerf drilling

This section focuses on the mutual stress relief effects of intersecting hydraulic slot cutting boreholes. Two slot cutting boreholes were placed with a center-to-center distance of 5 m in the *X*-axis direction and 2 m in the *Y*-axis direction. The coal mass between the two boreholes is affected by the intersecting placement of the slot cutting boreholes. The stress cloud map is shown in Figure 9, and the plastic zone is shown in Figure 10.

From the stress distribution cloud map, it can be observed that when two hydraulic slot cutting boreholes are placed in an intersecting pattern, the coal mass between the two slots is subjected to stress relief not only in the *X* direction but also in the *Y* direction. When affected by stress relief from two different directions, the stress relief is greater than that of a single hydraulic slot cutting borehole. After the numerical simulation, the coal mass between the two hydraulic slot cutting boreholes has undergone complete stress relief.

From the plastic damage zone map, it can be seen that the coal mass is significantly affected by the two intersecting slots, resulting in greater plastic damage compared to a single hydraulic slot cutting borehole. After the numerical simulation, the coal mass between the two hydraulic slot cutting boreholes has completely undergone

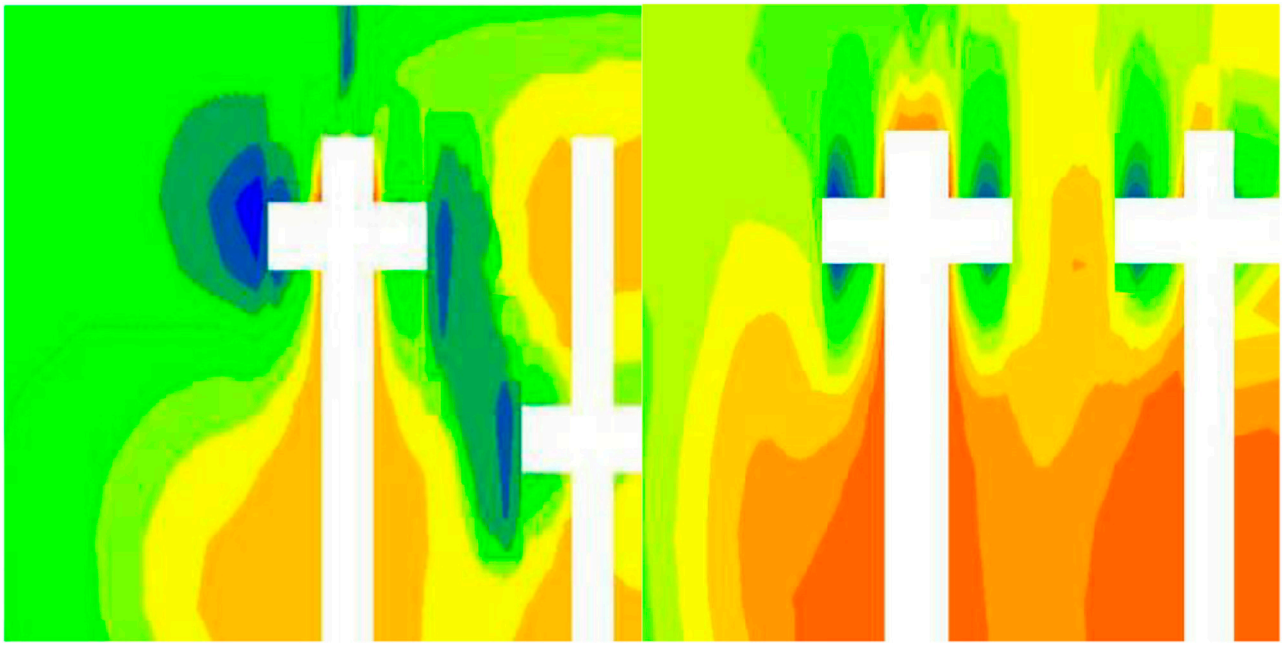

FIGURE 9
Contour map of parallel slotting model.

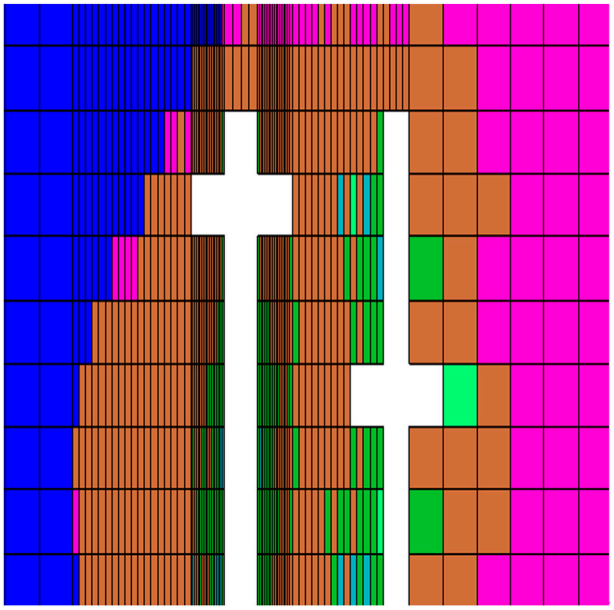

FIGURE 10
Block state of slotting model.

plastic damage due to the effects of the intersecting slot cutting measures. Therefore, the implementation of intersecting slot cutting boreholes can effectively increase the stress relief range and reduce the engineering workload.

4 Research on mathematical model of coal damage radius

The depth of the slot cutting has a greater influence on the plastic zone in the Y direction, while its impact on the X and Z directions is smaller. The width of the slot cutting has a greater influence on the plastic zone in the X and Z directions, while its effect on the Y direction is smaller. Therefore, a simplified mathematical model is derived based on the geometric characteristics of the slot. The failure radius of the disc-shaped slot cutting in each direction is given by:

$$\begin{cases} X = r + \Delta(X) \\ Y = d + \Delta(Y) \\ Z = r + \Delta(Z) \end{cases} \tag{1}$$

Here, r is the slot depth, d is the slot width, F is the *in-situ* stress, $\Delta(X)$, $\Delta(Y)$ and $\Delta(Z)$ represent the plastic zone range in the respective directions.

TABLE 3 The relationship between the parameters of plastic area.

Buried deep(m)	Kerf width(m)	Kerf depth(m)	*X*-direction plastic zone range(m)	*Y*-direction plastic zone range(m)	Plastic zone in *Z* direction(m)
400	0.1	1.0	1.188	3.105	0.875
400	0.2	1.0	2.932	3.105	2.412
400	0.3	1.0	4.488	3.105	3.989
600	0.1	1.0	3.785	4.688	1.322
600	0.2	1.0	5.522	4.688	2.867
600	0.3	1.0	6.988	4.688	4.442
800	0.1	1.0	4.665	6.255	2.734
800	0.2	1.0	6.291	6.255	4.292
800	0.3	1.0	7.921	6.255	5.861
400	0.2	0.5	2.932	1.876	2.412
400	0.2	1.0	2.932	3.105	2.412
400	0.2	1.5	2.932	4.341	2.412
600	0.2	0.5	5.522	3.465	2.867
600	0.2	1.0	5.522	4.688	2.867
600	0.2	1.5	5.522	5.920	2.867
800	0.2	0.5	6.291	5.036	4.292
800	0.2	1.0	6.291	6.255	4.292
800	0.2	1.5	6.291	7.395	4.292

Using MATLAB, for curve fitting, the plastic zone range is obtained as follows.

The *in-situ* stress is represented by the coal seam depth $F = \gamma H$. To determine $\Delta(X)$, $\Delta(Y)$, $\Delta(Z)$, a numerical simulation plan is designed with the parameters arranged in a cross-combination, as shown in Table 3.

$$\begin{cases} \Delta(X) = 0.00433H + 16.46d - 2.192 \\ \Delta(Y) = 0.0079H + 2.462r - 2.517 \\ \Delta(Z) = 0.00468H + 15.58d - 2.588 \end{cases} \quad (2)$$

Substituting Eq. 2 into Eq. 1, the failure radius of the slot cutting in each direction can be determined as:

$$\begin{cases} X = r + 0.00433H + 16.46d - 2.192 \\ Y = d + 0.0079H + 2.462r - 2.517 \\ Z = r + 0.00468H + 15.58d - 2.588 \end{cases} \quad (3)$$

With the aid of this mathematical model, the failure range of the slot cutting in each direction can be quickly determined based on the slot parameters, providing reference for the layout of hydraulic slot cutting boreholes in practical applications.

5 Conclusion

A numerical model of coal mass subjected to high-pressure water jet slot cutting was established using FLAC3D software. The model parameters were determined based on the analysis of the regional coal seam conditions. The stress-strain behavior and failure characteristics of the surrounding coal mass after slot cutting were investigated, as well as the synergistic stress relief effects under different slot cutting layouts. The main conclusions are as follows.

(1) Numerical simulations of the stress variation in the coal mass surrounding the slot cutting revealed that the construction of hydraulic slot cutting in the coal seam resulted in the formation of slots through the impact of high-pressure water jets. This created stress gradients in the surrounding coal mass, driving the coal mass to gradually move towards the slots and release stress. Due to the significantly greater depth of the slots compared to their width, the stress relief in the Y direction was greater than in the X and Z directions. Plastic deformation zones were observed in the coal mass near the slots, indicating damage to the coal mass and an increase in the number of cracks, thereby enhancing gas extraction efficiency.

(2) The stress relief variations in the coal mass between adjacent hydraulic slot cutting boreholes and gas extraction boreholes were obtained. The synergistic stress relief effects between the slots can enhance the stress relief in the coal mass between them. When hydraulic slot cutting boreholes were arranged in a crossed pattern, the stress relief in the coal mass between the slots was more significant compared to parallel arrangements. Therefore, the use of crossed arrangements can appropriately increase the spacing between slots to improve engineering efficiency.

(3) The failure range of the coal mass surrounding the slots under different combination conditions was determined through simulation studies. Based on the simulation results, a mathematical model for the failure range of the coal mass surrounding the slots was obtained by curve fitting using MATLAB. This model can provide a reference for practical applications in the field.

Data availability statement

The original contributions presented in the study are included in the article/supplementary material, further inquiries can be directed to the corresponding author.

Author contributions

All authors listed have made a substantial, direct, and intellectual contribution to the work and approved it for publication.

Funding

The authors gratefully acknowledge the support provided by the National Natural Science Foundation of China (52204220, 52174188), and the China Coal Technology and Engineering Group Co., Ltd. (2022-QN001).

Conflict of interest

Authors LJ and JL were employed by the company Guoneng Shendong Coal Group Co, Ltd.

The authors declare that this study received funding from the China Coal Technology and Engineering Group Co., Ltd. The funder had the following involvement in the study: provide the numerical simulation software.

Publisher's note

References

Duan, K. L., Feng, Z. C., Zhao, Y. S., Zhao, Y. Q., and Yang, D. (2002). Testing study of methane drainage by bore and hydraulic-cutting seam from low permeability coal seam. *J. China Coal Soc.* 1, 50–53. doi:10.3321/j.issn:0253-9993.2002.01.011

Feng, Z. C., Kang, J., and Duan, K. L. (2001). Experimental and mechanism study of coal and gas burst in the process of hydraulic cutting seam. *J. Liaoning Tech. Univ. Nat. Sci.* 4, 443–445.

Fu, J. W., Fu, X. H., Sun, M. C., and Guo, Q. W. (2014). Gas control technology based on the hydraulic measures of "drilling cutting pressuring releasing and injecting. *Saf. Coal Mines* 5, 47–51. doi:10.13347/j.cnki.mkaq.2014.05.013

Halbaum, W. H. (1899). Discussion of J Gerrard's paper Instantaneous outbursts of fire-damp and coal. *Broad Oak Colliery. Inst. Min. Eng.* 10522, 258–265.

Huang, B. X., Cheng, Q. Y., and Liu, C. Y. (2011). Hydraulic fracturing theory of coal-rock mass and its technical framework. *J. Min. Saf. Eng.* 2, 167–173. doi:10.3969/j.issn.1673-3363.2011.02.001

Jou, M. (2000). Analysis of the stability of water-jet cutting with linear theory. *J. Mater. Process. Technol.* 104, 17–20. doi:10.1016/S0924-0136(00)00583-5

Li, X. H., Wang, X. C., and Kang, Y. (2014). Energy characteristic and dissipation in transient process of hydraulic cutting seams system in coal seam. *J. China Coal Soc.* 39, 1404–1408. doi:10.13225/j.cnki.jccs.2014.9014

Li, X. J., and Lin, B. Q. (2010). Status of research and analysis on coal and gas outburst mechanism. *Coal Geol. Explor.* 1, 7–13. doi:10.3969/j.issn.1001-1986.2010.01.002

Li, Z. F., Sun, D. F., Chen, J. F., Lei, H. B., and Xiao, S. Q. (2015). Application of permeability improving technology combined with hydraulic pressure fracturing and hydraulic slotting. *Coal Sci. Technol.* 10, 72–76. doi:10.13199/j.cnki.cst.2015.10.014

Liu, F. F., Huang, Y. Y., Xu, Q., Xie, G. M., Sun, J. l., and Wu, B. (2014). Influence of advance and retreat high-pressure water jet slotting on coal seam depressurization antireflection effect. *Saf. Coal Mines* 9, 165–168. doi:10.13347/j.cnki.mkaq.2014.09.049

Liu, J., Wang, H., Yuan, Z., and Xiaogang, F. (2011). Experimental study of pre-splitting blasting enhancing pre-drainage rate of low permeability heading face. *Procedia Eng.* 26, 818–823. doi:10.1016/j.proeng.2011.11.2242

Long, J. M., Li, W. S., Chen, J. F., Zhou, S. C., and Li, Z. F. (2011). Research on rapid seam opening of cross-cut technology in songzao mine. *Coal Sci. Technol.* 7, 35–38. doi:10.13199/j.cst.2011.07.41.longjm.013

Soliman, M. (1999). *Use of oriented perforation and new gun system optimizes fracturing of high permeability, unconsolidated formations*. Latin American and Caribbean Petroleum Engineering Conference. doi:10.2523/53793-MS

Song, W. Y., Wang, Z. F., and Tang, J. P. (2011). Principle of gas extraction by increasing permeability of coal seam with hydraulic cutting and its application. *China Saf. Sci. J.* 4, 78–82. doi:10.16265/j.cnki.issn1003-3033.2011.04.014

Tang, J. P., Yang, S. L., and Li, L. P. (2012). Numerical simulation of effects of different hydraulic cutting arrangement on pressure relief and gas outburst prevention. *Chin. J. Geol. Hazard Control* 1, 61–66. doi:10.16031/j.cnki.issn.1003-8035.2012.01.011

Taylor, T. J. (1852). Proofs of subsistence of the firedamp of coal mines in a state of high tension *in situ*. *North Engl. Inst. Min. Mech. Eng.* 1, 275–299.

Wang, N. B., Lin, B. Q., and Gao, Y. B. (2015). Optimized design and application of borehole slotting drilling through floor of high outburst seam. *Coal Sci. Technol.* 5, 62–66. doi:10.13199/j.cnki.cst.2015.05.016

Wu, H. J., Lin, B. Q., Yang, W., Yao, J., and Di, C. (2009). Numerical analysis of the pressure relief effect on slot at different initial stresses. *J. Min. Saf. Eng.* 2, 194–197.

Yuan, B., Kang, Y., and Li, X. H. (2013). Experimental study on transient characteristics of hydraulic cutting seams system in coal seam. *J. China Coal Soc.* 12, 2153–2157. doi:10.13225/j.cnki.jccs.2013.12.020

Zarrouk, S. J., and Moore, T. A. (2009). Preliminary reservoir model of enhanced coalbed methane (ECBM) in a subbituminous coal seam, Huntly Coalfield, New Zealand. *Int. J. Coal Geol.* 77, 153–161. doi:10.1016/j.coal.2008.08.007

Zhang, L. J., Lin, B. Q., and Gao, Y. M. (2013). Quick eliminating outburst technology of coal mine based on high-pressure hydraulic slotting process. *Saf. Coal Mines* 3, 64–66. doi:10.13347/j.cnki.mkaq.2013.03.014

Zhao, L., and Feng, Z. C. (2001). Testing study of improving seepage flow laws of low seepage coalbed by hydatic-cutting seams. *J. TaiYuan Univ. Technol.* 2, 109–111.

Zheng, C. S., Lin, B. Q., Yang, W., and Zou, Q. L. (2014). Hole-spraying mechanism of hydraulic slotting drilling and the influence of slotting mode. *Saf. Coal Mines* 1, 5–8. doi:10.13347/j.cnki.mkaq.2014.01.002

frontiers | Frontiers in Earth Science

TYPE Original Research
PUBLISHED 26 October 2023
DOI 10.3389/feart.2023.1270662

OPEN ACCESS

EDITED BY
Jianwei Tian,
Technical University of Denmark, Denmark

REVIEWED BY
Xin Du,
University of Science and Technology of China, China
Xiaochen Wei,
Southwest Petroleum University, China

*CORRESPONDENCE
Shuangshuang Zhang,
waiwai1515@163.com

RECEIVED 01 August 2023
ACCEPTED 16 October 2023
PUBLISHED 26 October 2023

CITATION
Zhang S, Guo K, Yang H and Gao X (2023), The productivity segmented calculation model of perforated horizontal wells considering whether to penetrate the contaminated zone.
Front. Earth Sci. 11:1270662.
doi: 10.3389/feart.2023.1270662

The productivity segmented calculation model of perforated horizontal wells considering whether to penetrate the contaminated zone

Shuangshuang Zhang*, Kangliang Guo, Haoran Yang and Xinchen Gao

College of Earth Sciences, Yangtze University, Wuhan, China

Perforation technology is often used to improve the productivity of horizontal wells in oilfield exploitation. During the perforation process, the formation seepage mode and productivity will change accordingly whether the contaminated zone is shot through. If we continue to use the previous productivity formula, it will cause a large calculation error and bring economic loss to the development of oil and gas fields. Firstly, based on the principle of equivalent seepage resistance, the reservoir-hole inflow profile in these two cases is analyzed in detail, and the reservoir-hole seepage model is constructed in different regions. The perforated horizontal well section is divided into N micro-unit sections, and the pressure drop model in the wellbore is constructed using the fluid mechanics theory. A new perforated horizontal well productivity prediction model is then created by coupling the reservoir-hole seepage model with the pressure drop model in the wellbore as a whole to accurately reflect the production performance of the perforated horizontal well. Through comparison and verification, it is concluded that the calculation results of the model are more precise, which can greatly reduce the productivity error. This method is reasonable and practical. When the oilfield's actual well data is substituted into this model, it is discussed and analyzed that the reservoir's physical characteristics, contamination level, and perforation completion parameters all have an impact on the productivity of horizontal wells, with the original formation's permeability and reservoir contamination thickness having the most pronounced effects. These findings may effectively direct the design of technological processes and performance impact prediction.

KEYWORDS

perforated horizontal well productivity, contaminated zone of strata, equivalent seepage resistance method, flow pressure drop, coupling model, segmented numerical calculation, sensitivity analysis

1 Introduction

During the production of oil and gas wells, the pollution caused by drilling and completion of the formation around the wellbore will lead to a decrease in the permeability of the formation fluid, which will lead to a decrease in formation pressure and reduce the productivity of perforated wells (Hawkins, 1956). The

formation of the formation pollution zone around the wellbore is mainly due to the penetration and diffusion of pollutants (Patel and Singh, 2016). The chemical agents and additives used in the drilling and completion process may penetrate the formation and cause formation pollution. During perforation operation, the formation around the well may be impacted and vibrated, resulting in formation fracture and fracture propagation, which in turn causes pollutants to penetrate the formation. In the process of oil and gas exploitation, the strata around the wellbore may be affected by pressure changes and fluid migration, resulting in the diffusion of oil and gas and other pollutants into the surrounding strata. The characteristics of the formation pollution zone are mainly manifested in the changes in formation physical properties and formation fluid (Burton and Hodge, 1998; Patel and Singh, 2016). The formation pollution zone may lead to a change in formation permeability, which reduces the permeability of the formation. The formation pollution zone may cause the pollution of the formation pore water, which makes the chemical composition of the formation pore water change, such as the change of pH value and the change of ion concentration. The formation of pollution zones may have adverse effects on oil and gas exploitation, such as reducing oil recovery and increasing mining costs.

To improve the production effect of horizontal wells, perforation completion technology is often used to improve its productivity. The perforation horizontal completion method has seen significant improvements throughout this time to increase the fluid channel's smoothness between the production layer and the wellbore and lessen production layer damage (McDowell and Muskat, 1950; Xiaochen et al., 2023) used an electrolytic simulation model to study the effect of perforation parameters on productivity and concluded that if the perforation is long enough, the productivity of perforated wells may be higher than that of open-hole wells. [Harris (1966)] used the finite difference technique to analyze the influence of perforation parameters on productivity but did not consider the influence of the compaction zone. [Klotz et al. (1974)] used the finite element method to evaluate the perforation productivity with a compacted zone. (McLeod, 1983) gave the skin of the compaction zone and pollution zone and deduced the productivity formula of a perforated horizontal well. [Karakas and Tarlq (1991)] constructed a semi-analytical model that proposed the empirical equation of perforation skin and analyzed the influence of formation pollution and perforation on well productivity. [Marett et al. (1993)] established a parameter optimization model for perforated horizontal wells, which considered the interaction of comprehensive factors such as formation pollution, perforation compaction, and well deviation angle in detail, and achieved good optimization results.

In the productivity prediction model of perforated horizontal wells, to improve the development effect and ultimate recovery rate, scholars (Giger et al., 1984; Joshi, 1986) carried out a lot of research work and obtained the productivity prediction formula for perforated horizontal wells, as well as the distribution law of seepage field and pressure drop. Among them, the Joshi model is the most widely used. Aiming at the problem of uneven inflow profile in the horizontal wellbore (Sq, 1994), established a single-phase flow model for perforated horizontal wells, but the final production was reduced [Su and Gudmundsson, 1994; Ouyang (1998)]. Proposed that the pressure drop in the wellbore cannot be ignored, and the pressure drop in the perforated horizontal wellbore is divided into four parts: wall friction pressure drop, acceleration pressure drop, hole roughness pressure drop, and mixed pressure drop. According to the theory and experiment, the corresponding pressure distribution and flow distribution formulas of variable mass flow in horizontal wellbore are obtained (Tong et al., 2023). The coupling model established by (Holmes et al., 1998) in the case of wellbore friction pressure drop is also applicable to multiphase flow [Kabir and Sanchez (2009)]. Considered the coupling of reservoir and wellbore, established a three-dimensional coupling model, used Newton's iterative algorithm to solve the numerical simulation, and gave the prediction of flow rate and flow pressure in horizontal wellbore. Aiming at the problem of large errors in productivity prediction (Luo et al., 2015), established a flow relationship model and analyzed the influence of near-well heterogeneity, wellbore flow pressure drops, and completion parameters on the inflow profile of horizontal wells [Wang et al. (2021)]. Transformed the three-dimensional seepage problem into a two-dimensional seepage problem and deduced the horizontal well productivity formula considering the fluid rheological properties and reservoir heterogeneity [Zhang et al. (2022)]. Used simulation software to simulate the multiphase flow pattern and pressure change of the wellbore after gas invasion [Wang et al. (202)]. Established a multiphase flow model of multi-component fluid in a wellbore and analyzed the variation of bottom hole pressure and temperature [Ma et al. (2022)]. Proposed a parameter optimization method for horizontal well sections to improve oil well productivity [Li and Wang (2022)]. Considered the horizontal well flow model of formation pollution and concluded that the smaller the pollution radius, the closer the horizontal well is to the external area, and the faster the oil production rate.

The application of perforating horizontal well completion technology is becoming increasingly widespread. Scholars have studied the productivity prediction and productivity influence law of perforating horizontal wells through a large number of experiments and methods. Different reservoir parameters and perforating parameters have different effects on the selection of perforating technology and the size of productivity release, but there are also some problems. For example, during the perforation process, in the case of not penetrating the pollution zone and penetrating the pollution zone, the formation seepage mode will change accordingly, and the productivity prediction results will also change. The current productivity approach will result in significant calculation errors and financial losses for the exploitation of oil and gas resources if we continue to utilize it. Therefore, it is urgent to study the inflow profile state and productivity prediction of perforated horizontal wells under these two different conditions.

The model proposed in this paper is a segmented calculation model for the productivity of perforated horizontal wells considering whether to penetrate the contaminated zone. It can accurately simulate the formation seepage law and predict productivity. This is a method that has not been involved in all previous models. Based on the equivalent seepage resistance method, the reservoir-hole inflow profile under the two

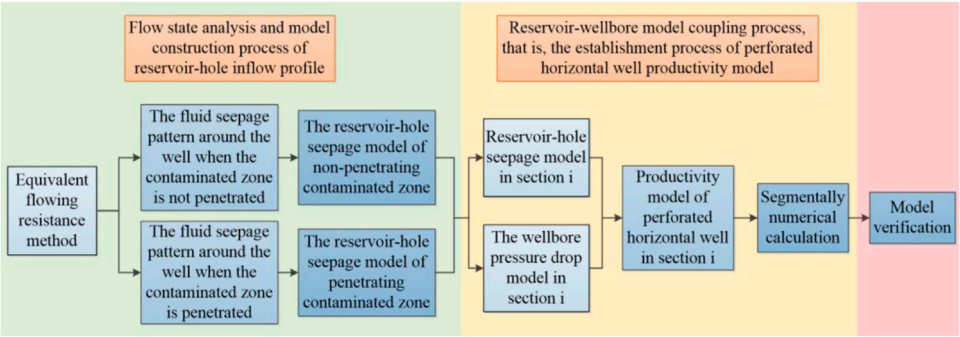

FIGURE 1
Flow chart of model construction.

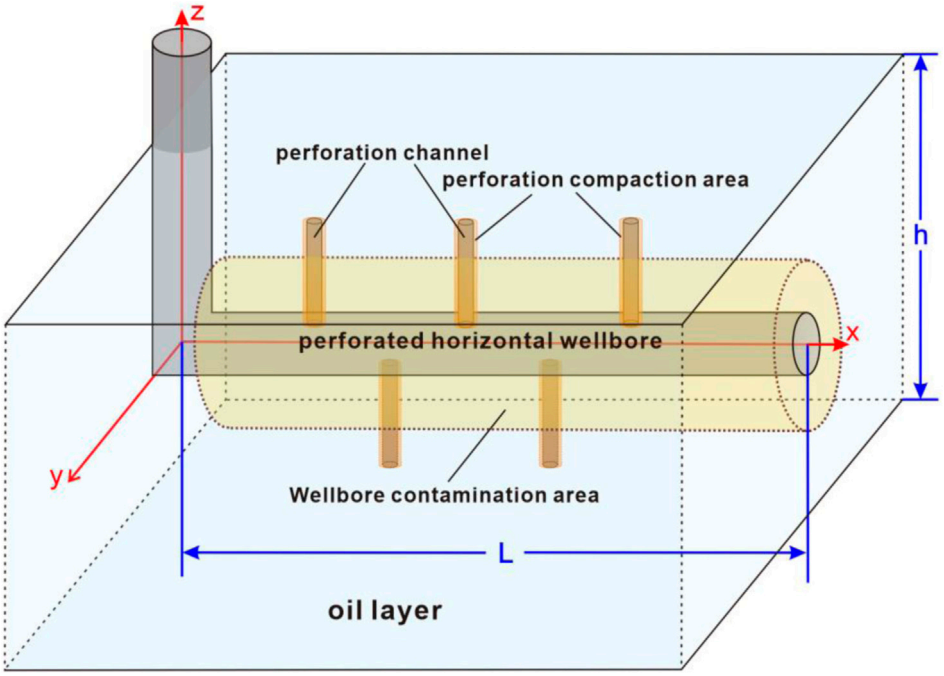

FIGURE 2
Geometric model of perforated horizontal well.

conditions of whether to penetrate the contaminated zone is thoroughly examined, and the reservoir-hole seepage resistance model is constructed in different regions. This model is more accurate than the previous one and can significantly lower the calculation error for production capacity. The wellbore pressure drops model and the reservoir-hole seepage model are coupled, and a segmented numerical calculation is performed. According to the actual situation of the reservoir, the inflow profile along the horizontal wellbore can be adjusted to optimize the production performance of the entire horizontal well. The model comparison proves that the model in this paper is reasonable and practical, which can effectively guide the technical process design and effect prediction of perforated horizontal wells, and provide economic benefits for oilfield development.

2 Model establishment

Oilfield exploitation typically uses near-well stimulation techniques to increase oil well productivity, while perforation completion technology is utilized to increase the productivity of horizontal wells. The fluid flow pattern in the reservoir has changed as a result of perforation (Doan et al., 1990). Three different flow patterns have been observed during the process: reservoir radial flow, three-dimensional flow in the perforation area, and pipe flow in the horizontal wellbore. The fluid flows in these three parts are mutually boundary conditions and interact with each other. We suggest a new productivity calculation model that aims to accurately simulate the productivity dynamic law of perforated horizontal wells when penetrating and not penetrating the contaminated zone, and

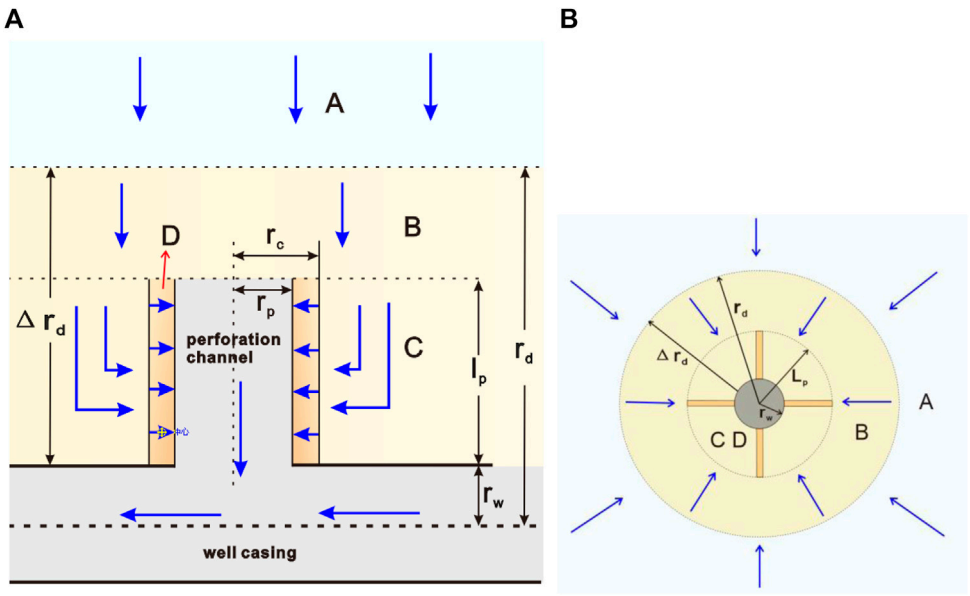

FIGURE 3
Three-radial flow model of non-penetrating contamination zone.

how to effectively evaluate the productivity of perforated horizontal wells. This chapter mainly describes the construction and verification of the model, and the whole flow chart is shown in Figure 1.

Firstly, the geometric model of the perforated horizontal well is constructed as illustrated in Figure 2, with the reservoir, fluid, and perforation assuming the following characteristics:

(1) There is a perforated horizontal well parallel to the top and bottom of the oil layer sealed by horizontal, equal thickness, top and bottom impermeable interlayers. The thickness of the oil layer is h (m), and the length of the horizontal well section is L (m);
(2) There is a contamination area around the horizontal wellbore and a compaction area around the perforation;
(3) The fluid in the reservoir is a single-phase isothermal steady seepage flow, the fluid is incompressible, and the boundary pressure of the liquid supply is constant;
(4) The fluid in the horizontal wellbore is a single-phase isothermal flow, and there are frictional resistance pressure drops, acceleration pressure drops, and mixing pressure drops in the horizontal wellbore.

2.1 Reservoir-hole seepage model

The fluid flow capacity in the real reservoir will be impacted by the permeability of the reservoir along the horizontal section, drilling and completion contamination, and perforation compaction, resulting in a fluctuation of the inflow profile along the horizontal section. The seepage pattern will also change differently when the contaminated zone is not penetrated and penetrated. At this point, the fluid flow pattern around the horizontal well section should be analyzed separately, and then based on the equivalent seepage resistance method (Zhang et al., 1998), the reservoir-hole seepage resistance calculation model is constructed in different regions.

(1) Non-penetrating the contaminated zone

The flow surrounding the wellbore in this model is separated into four areas when the perforation depth l_p is smaller than the formation contamination thickness Δr_d (Figures 3A and 3B).

Area A is the original formation area, without formation contamination and perforation, and the fluid flow pattern is a plane radial flow around the horizontal wellbore. The outer boundary radius of the area is the drainage radius r_e, the inner boundary radius is the formation contamination radius r_d, the reservoir thickness is the length L of the horizontal well section, and the permeability is the original permeability K of the formation.

Using the equivalent seepage resistance method (Zhang et al., 1998), the formula representing the relationship between seepage resistance, pressure difference, and productivity can be written as:

$$Q = \frac{p_e - p_w}{R_A}$$

According to the productivity formula of ideal open-hole wells:

$$Q = \frac{2\pi KL(P_e - P_w)}{\mu B[\ln(r_e/r_d)]}$$

The seepage resistance of area A can be obtained (the productivity formula in this paper is based on the practical unit of SI mineral production):

$$R_A = \frac{\mu B}{2\pi KL} \ln \frac{r_e}{r_d} \quad (1)$$

There is formation contamination but no perforation in the B area, and the fluid flow pattern is a plane radial flow around the

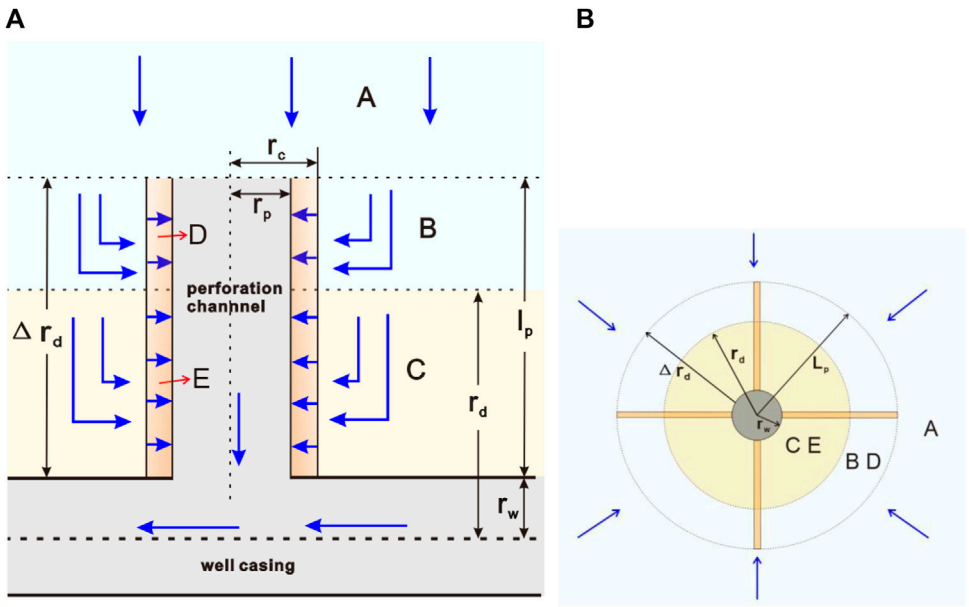

FIGURE 4
Three-radial flow model of penetrating contamination zone.

horizontal wellbore. The outer boundary radius of the area is the formation contamination radius r_d, the inner boundary radius is the sum of the wellbore radius and the perforation depth $r_w + l_p$, the reservoir thickness is the length L of the horizontal well section, and the permeability is the formation contamination permeability K_d caused by the influence of drilling and completion. The seepage resistance of area B is (The reasoning process is the same as the derivation of seepage resistance in Area A, and the derivation of Formula 3, 4, 6–10 in the following is also the same as the derivation of seepage resistance in Area A):

$$R_B = \frac{\mu B}{2\pi K_d L} \ln \frac{r_d}{r_w + l_p} \tag{2}$$

Area C has both formation contamination and perforation, and the fluid flow pattern is different from that of areas A and B. The fluid is a radial flow perpendicular to the perforation hole with the perforation hole as the central axis. The outer boundary is half h_p of the distance between the two perforation holes, the inner boundary is the perforation compaction radius r_c, the reservoir thickness is the perforation depth l_p, and the permeability is the formation contamination permeability K_d. The seepage resistance of the C area is:

$$R_C = \frac{\mu B}{2\pi K_d l_p} \ln \frac{h_p}{r_c} \tag{3}$$

The D area is the perforation compaction area, and the fluid is also a radial flow perpendicular to the perforation hole with the perforation hole as the central axis. The outer boundary is the perforation compaction radius r_c, the inner boundary is the perforation radius r_p, the reservoir thickness is the perforation depth l_p, and the permeability is the permeability of the compaction zone K_c. Generally, the permeability of the perforation compaction zone is 20%–25% of the original formation permeability (Bell et al., 1972). The seepage resistance of zone D is:

$$R_D = \frac{\mu B}{2\pi K_c l_p} \ln \frac{r_c}{r_p} \tag{4}$$

The fluid flow is identical in the perforation areas C and D, which are connected by a series. According to the series formula of equivalent seepage resistance (Zhang et al., 1998):

$$R = R_{\mathrm{I}} + R_{\mathrm{II}}$$

The fluid seepage resistance around a single perforation hole can be obtained as follows:

$$R_{\mathrm{I}} = R_C + R_D \tag{5}$$

(2) Penetrating the contaminated zone

The flow surrounding the wellbore in this model is separated into five areas when the perforation depth l_p is larger than the formation contamination thickness Δr_d (Figures 4A and 4B).

Area A is the original formation area, without formation contamination and perforation. The flow mode and parameters of area A are the same as those of area A without perforation. The only difference is that the inner boundary radius is the sum of the wellbore radius and perforation depth $r_w + l_p$. Using the equivalent seepage resistance method, the seepage resistance of Area A can be obtained as follows:

$$R_A = \frac{\mu B}{2\pi K L} \ln \frac{r_e}{r_w + l_p} \tag{6}$$

There is no formation contamination but perforation in the B area, and the fluid is radial flow around the perforation hole. The

outer boundary radius of this area is half h_p of the distance between two perforations, the inner boundary is the perforation compaction radius r_c, the reservoir thickness is $r_e + l_p - r_d$, and the permeability is the original permeability K of the formation. The seepage resistance of area B is:

$$R_B = \frac{\mu B}{2\pi K\left(r_w + l_p - r_d\right)} \ln \frac{h_p}{r_c} \tag{7}$$

Area C has both formation contamination and perforation. The flow mode and internal and external boundary parameters are the same as those in area B. The difference is that the reservoir thickness is $r_d - r_w$, and the permeability is the formation contamination permeability K_d. The seepage resistance of area C is:

$$R_C = \frac{\mu B}{2\pi K_d\left(r_d - r_w\right)} \ln \frac{h_p}{r_c} \tag{8}$$

The D area is the perforation compaction area, and the fluid is also the radial flow around the perforation hole. The outer boundary is the perforation compaction radius r_c, the inner boundary is the perforation radius r_p, the reservoir thickness is $r_w + l_p - r_d$, and the permeability is the compaction zone permeability K_{c1}. The seepage resistance of zone D is:

$$R_D = \frac{\mu B}{2\pi K_{c1}\left(r_w + l_p - r_d\right)} \ln \frac{r_c}{r_p} \tag{9}$$

The E area is the perforation compaction area. The flow mode and internal and external boundary parameters are the same as those in the D area. The difference is that the thickness of the oil layer is $r_d - r_w$, and the permeability is K_{c2}. The seepage resistance of zone D is:

$$R_E = \frac{\mu B}{2\pi K_{c2}\left(r_d - r_w\right)} \ln \frac{r_c}{r_p} \tag{10}$$

The two regions of B and D are connected in series as a region without contamination and perforation, and the two regions of C and E are connected in series as a region with contamination and perforation. According to the series formula of equivalent seepage resistance (Zhang et al., 1998), the seepage resistance in these two large areas is:

$$R_{BD} = R_B + R_D, R_{CE} = R_C + R_E$$

However, there is a parallel relationship between these two large regions. According to the parallel formula of equivalent seepage resistance (Zhang et al., 1998), as follows:

$$\frac{1}{R} = \frac{1}{R_{\mathrm{I}}} + \frac{1}{R_{\mathrm{II}}}$$

The fluid seepage resistance around a single perforation hole can be obtained as follows:

$$\frac{1}{R_1} = \frac{1}{R_B + R_D} + \frac{1}{R_C + R_E} \tag{11}$$

2.2 Reservoir-wellbore coupling model

Fluid constantly enters the wellbore from the reservoir during perforating horizontal well production, and the flow rate of this part affects the distribution of pressure drop in the horizontal wellbore. At the same time, the pressure drop in the horizontal wellbore in turn affects the flow into the wellbore (Landman et al., 1991). Therefore, it is necessary to combine the reservoir-hole seepage model in Section 2.1 with the influence of flow pressure drop in the wellbore to examine it as a whole to accurately reflect the production performance of perforated horizontal wells. As seen in Figure 5, the entire perforated horizontal wellbore has been divided into N wellbore unit segments.

Suppose: 1) The crude oil in the reservoir flows into the horizontal wellbore from the perforation hole, and the flow in the wellbore is turbulent flow; 2) The fluid is single-phase, incompressible, Newtonian viscous fluid; 3) And in the same wellbore section, the inflow of each perforation is the same, and the flow rate is perpendicular to the wall; 4) Ignore the volume force.

Assuming that the number of perforation holes on the ith infinitesimal segment is M, then:

$$M = \frac{nL}{N} \tag{12}$$

2.2.1 Section ith reservoir-hole seepage model

According to the reservoir-hole seepage model in Section 2.1 of this paper, the seepage resistance in the whole reservoir area of Section ith can be obtained as follows:

(1) Non-penetrating the contaminated zone:

For the entire perforation area, the fluid flow between the hole and the hole is parallel. Combined with Formula 5, 12, the flow resistance of the ith perforation area is:

$$R_{pi} = \frac{R_{1i}}{M} = \frac{N\left(R_{Ci} + R_{Di}\right)}{nL} \tag{13}$$

The seepage resistance in the whole reservoir area of the ith section is the sum of the seepage resistance of the perforated area and the unperforated area of the ith section. Combined with Formula 1ormula –Formula 4, 13, it is obtained that:

$$R_i = R_{Ai} + R_{Bi} + R_{pi}$$

That is:

$$R_i = \frac{\mu B}{2\pi L}\left(\frac{1}{K_i}\ln\frac{r_{ei}}{r_{di}} + \frac{1}{K_{di}}\ln\frac{r_{di}}{r_{wi} + l_{pi}}\right) + \frac{\mu BN}{2\pi l_{pi} n_i L}\left(\frac{1}{K_{di}}\ln\frac{h_{pi}}{r_{ci}} + \frac{1}{K_{ci}}\ln\frac{r_{ci}}{r_{pi}}\right) \tag{14}$$

(2) Penetrating the contaminated zone:

Combined with the Formula 11, 12, the flow resistance of the ith perforation area is:

$$R_{pi} = \frac{R_{1i}}{M} = \frac{N}{nL\left(\frac{1}{R_{Bi}+R_{Di}} + \frac{1}{R_{Ci}+R_{Ei}}\right)} \tag{15}$$

The seepage resistance in the whole reservoir area of the ith section is the sum of the seepage resistance of the perforated area and the unperforated area of the ith section. Combined with Formula 6 – 10, 15, it is obtained that:

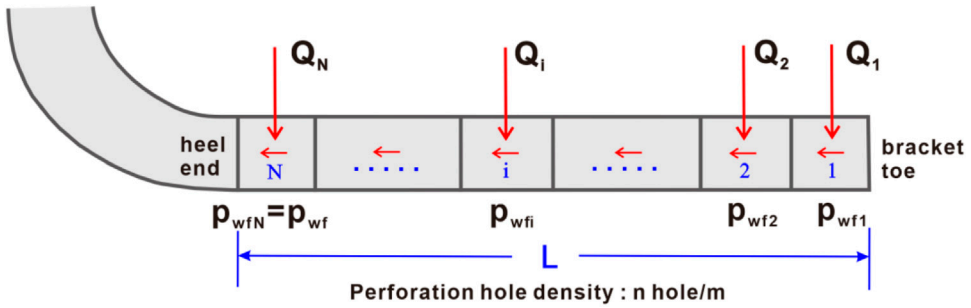

FIGURE 5
Sectional section of the horizontal wellbore.

$$R_i = R_{Ai} + R_{pi} \tag{15}$$

That is:

$$R_i = \frac{\mu B}{2\pi L}\left[\frac{N}{n_i x_i} + \frac{1}{K}\ln\frac{r_{ei}}{r_{wi}+l_{pi}}\right] \tag{16}$$

Where: $x_i = \frac{r_{wi}+l_{pi}-r_{di}}{\frac{1}{K_i}\ln\frac{h_{pi}}{r_{ci}}+\frac{1}{K_{c1i}}\ln\frac{r_{ci}}{r_{pi}}} + \frac{r_{di}-r_{wi}}{\frac{1}{K_{di}}\ln\frac{h_{pi}}{r_{ci}}+\frac{1}{K_{c2i}}\ln\frac{r_{ci}}{r_{pi}}}$

2.2.2 Section *i*th wellbore pressure drop model

The fluid in the reservoir flows into the wellbore through the hole after the casing perforation operation of the horizontal well section. The fluid flow in the horizontal wellbore is complicated by the fluid flow along the horizontal portion in addition to the fluid flow along the axial direction, resulting in a variable mass flow with an increasing flow rate along the flow direction (Su and Gudmundsson, 1994). According to the theory of fluid mechanics, the injection flow from the perforation hole has a certain influence on the main flow in the wellbore. The pressure drop of the wellbore pipe flow includes the friction loss of the pipe wall, the acceleration loss, and the mixing pressure loss (Ouyang, 1998). The flow pressure drop model in the wellbore can be expressed as:

$$\Delta p = \Delta p_f + \Delta p_a + \Delta p_h \tag{17}$$

According to the Formula 17, the calculation formula of the pressure drop of the pipe flow in the *i*th section can be obtained as follows:

$$\Delta p_i = \Delta p_{f\,i} + \Delta p_{ai} + \Delta p_{hi} \tag{18}$$

Where: $\Delta p_{f\,i} = \frac{\lambda_i \rho v_{1i}^2 d_i}{4 r_w}\left[1 + \frac{Q_i}{\sum_{j=1}^{i-1} Q_i} + \left(\frac{1}{3} + \frac{1}{6M_i^2}\right)\left(\frac{Q_i}{\sum_{j=1}^{i-1} Q_i}\right)^2\right]$

$$\Delta p_{ai} = \rho v_{1i}^2\left[M_i^2\left(\frac{r_{pi}}{r_w}\right)^4\left(\frac{v_{pi}}{v_{1i}}\right)^2 + 2M_i\left(\frac{r_{pi}}{r_w}\right)^2\left(\frac{v_{pi}}{v_{1i}}\right)\right]$$

$$\Delta p_{hi} = \rho\frac{Q_i^2 + 2Q_i\sum_{j=1}^{i-1} Q_j}{2(\pi r_w)^2}$$

$$v_{1i} = \frac{\sum_{j=1}^{i-1} Q_j}{\pi r_w^2},\ v_{pi} = \frac{Q_i}{\pi r_{pi}^2 M}$$

Then the flow pressure of section *i*th of the perforated horizontal well is:

$$p_{wfi+1} = p_{wfi} - \Delta p_i \tag{19}$$

2.2.3 Section *i*th productivity model of perforated horizontal well

Due to the small length of each section, the flow parameters change little, and each micro-element section can be regarded as a homogeneous formation. According to the equivalent seepage resistance method, the production equation of the *i*th section of the horizontal well is obtained as follows:

$$Q_i = \frac{p_{ei} - p_{wfi}}{R_i} \tag{20}$$

In summary, the *i*th yield equation is:

(1) Non-penetrating the contaminated zone $(l_p \le \Delta r_d)$

$$Q_i = \frac{2\pi L\left(p_{ei} - p_{wfi}\right)}{\mu B\left(\frac{1}{K_i}\ln\frac{r_{ei}}{r_{di}} + \frac{1}{K_{di}}\ln\frac{r_{di}}{r_{wi}+l_{pi}}\right) + \frac{\mu B N}{l_{pi} n_i}\left(\frac{1}{K_{di}}\ln\frac{h_{pi}}{r_{ci}} + \frac{1}{K_{ci}}\ln\frac{r_{ci}}{r_{pi}}\right)} \tag{21}$$

(2) Penetrating the contaminated zone $(l_p > \Delta r_d)$

$$Q_i = \frac{2\pi L\left(p_{ei} - p_{wfi}\right)}{\mu B\left[\frac{N}{n_i x_i} + \frac{1}{K}\ln\frac{r_{ei}}{r_{wi}+l_{pi}}\right]} \tag{22}$$

Where: $x_i = \frac{r_{wi}+l_{pi}-r_{di}}{\frac{1}{K_i}\ln\frac{h_{pi}}{r_{ci}}+\frac{1}{K_{c1i}}\ln\frac{r_{ci}}{r_{pi}}} + \frac{r_{di}-r_{wi}}{\frac{1}{K_{di}}\ln\frac{h_{pi}}{r_{ci}}+\frac{1}{K_{c2i}}\ln\frac{r_{ci}}{r_{pi}}}$

2.3 Perforated horizontal well productivity segmentation numerical calculation

When the oil well is produced, the pressure at the heel end of the horizontal wellbore is known, that is p_{wf}. Therefore, the unknown quantities to be solved are the wellbore inflow $Q_1, Q_2 \cdots Q_i \cdots Q_N$ on each wellbore unit section and the pressure $p_{wf1}, p_{wf2} \cdots p_{wf_i} \cdots p_{wfN}$ on each wellbore unit section. These unknowns can be determined by the flow Eqs 21, 22 and the flow pressure Eq. 19 in the wellbore established above. The specific calculation steps are as follows (see Figure 6):

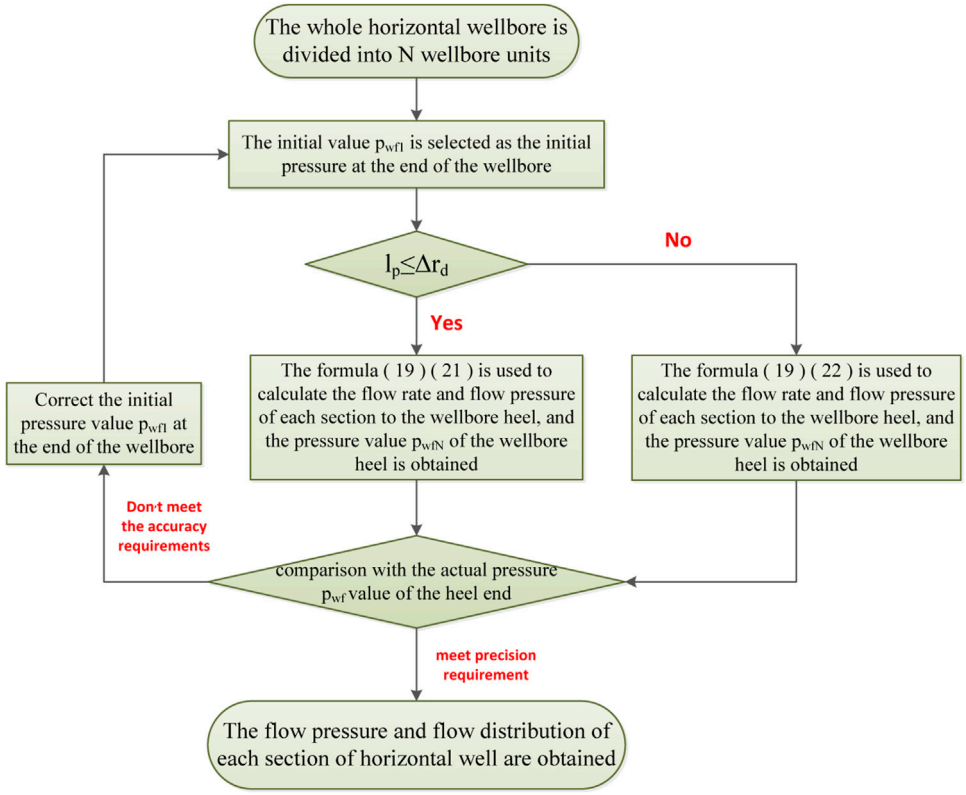

FIGURE 6
Block diagram of numerical calculation steps for productivity segmentation.

(1) The total length of the horizontal wellbore is L, and the whole horizontal wellbore is divided into N wellbore unit sections. According to the completion scenario, each wellbore unit section's perforation depth, density, pore size, and other characteristics are calculated;

(2) Starting from the toe end of the horizontal wellbore, the initial value p_{wf1} is set as the initial pressure value of the toe end of the wellbore, and the wellbore inflow Q_1 on the first wellbore unit section is calculated according to the Formula 21 or 22;

(3) At this time, the main flow rate of the wellbore $Q = Q_1$, according to the wellbore flow pressure loss calculation Eq. 18, and the total pressure drop $\Delta p_1 = \Delta p_{f1} + \Delta p_{a1} + \Delta p_{h1}$ on the first wellbore unit section are obtained. According to the flow pressure Formula 19, the flow pressure $p_{wf2} = p_{wf1} - \Delta p_1$ on the next wellbore unit section is obtained;

(4) According to the seepage pressure-productivity Formula 21 or 22 of the reservoir on the wellbore unit section, the wellbore inflow Q_2 on the second unit section is calculated. At this time, $Q = Q_1 + Q_2$. Then according to the Formula 18, 19, the pressure drops ΔP_2 in this section and the flow pressure p_{wf3} in the next section are calculated.

(5) Similarly, for the third to N wellbore unit segments, the calculation is carried out following the above steps, and the main flow rate $Q = \sum_{j=1}^{i} Q_j$ of the wellbore is calculated for the ith segment, Therefore, $Q_3, Q_4 \cdots Q_i \cdots Q_N$ and $p_{wf3}, p_{wf4} \cdots p_{wfi} \cdots p_{wfN}$ is obtained sequentially.

(6) The calculation is terminated and the oil well production is Q if the computed heel flow pressure p_{wfN} meets the accuracy requirement compared with the given heel end flow pressure p_{wf}. If the accuracy requirement is not met or if $p_{wfi} < 0$ occurs during the calculation, p_{wf1} is reset and the calculation is transferred to step (2) until the iterative error is within the control accuracy range. After the above calculation is completed, the flow pressure and flow rate distribution of each section of the horizontal well can be obtained.

3 Model validation

Five horizontal wells in the J Oilfield are estimated as examples using the segmented calculation model of perforated horizontal well productivity described above. Table 1 displays the essential information.

The productivity calculation approach presented in this study may be used to display the horizontal wells' wellbore inflow profile. Using well A as an example, Figure 7 illustrates the wellbore inflow profile of the perforated horizontal well. The figure truly reflects that the inflow profile along the horizontal wellbore is indeed uneven during horizontal well mining. The rate of wellbore injection increases gradually from the toe of the horizontal wellbore to its heel due to the influence of the flow pressure drop in the horizontal

TABLE 1 Basic data of five horizontal wells in J oilfield.

Well number	Well A	Well B	Well C	Well D	Well E
Drainage area (km^2)	0.85	0.132	0.124	0.124	0.85
Vertical depth (m)	1,526.34	1,648.19	2,497.61	1825.65	1785.96
Horizontal section length (m)	358.5	142	207.4	150	300
Reservoir thickness (m)	10	6	18	6.5	12
Average permeability (mD)	380	620	490	586	450
Crude oil density (kg/m^3)	958	900.4	891.3	906	900.4
Crude oil viscosity (mPa.s)	9	6	5	6	8
Wellbore radius (m)	0.178	0.124	0.124	124.5	178.5
Supply pressure (MPa)	13	18	25.5	17.6	16
Wellhead pressure (MPa)	0.22	0.55	0.29	0.5	0.29
Perforating gun type	120	102	102	102	120

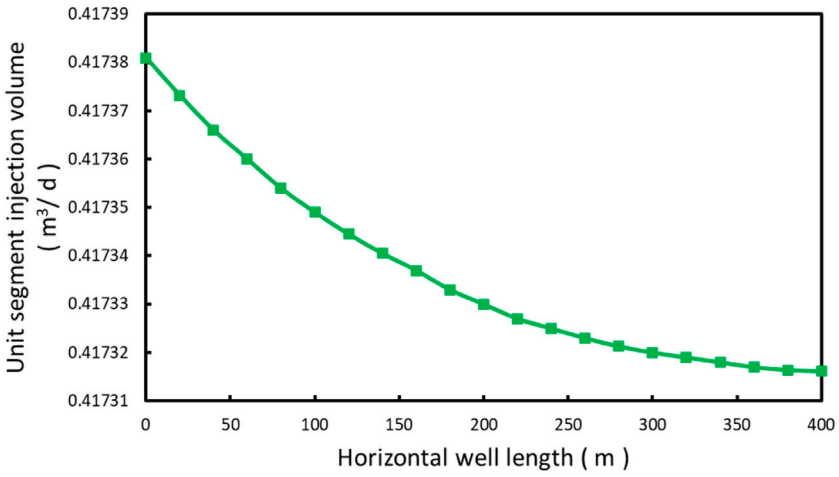

FIGURE 7
Inflow profile of the perforated horizontal well wall.

wellbore. The calculation results of this model and the Joshi model are compared with the actual production in the field, see Table 2.

The productivity formula of horizontal wells proposed by Joshi is widely used. Joshi believes that the flow of horizontal wells is composed of horizontal plane flows and vertical plane flows. The calculation formula does not consider various wellbore parameters and wellbore pressure drop, so the calculation results generally seriously overestimate the productivity of horizontal wells. It can be seen from Table 2 that the average error value of the productivity results predicted by the Joshi method is 37.18%, which is larger than the actual yield.

The calculation results of the productivity model of perforated horizontal wells built in this paper are close to the actual production of oil wells, and the average error is 10.15%, which indirectly indicates the rationality and practicability of the model in this paper. The reasons for the small error value are: 1) The two different inflow profile seepage modes of non-penetrating and penetrating contaminated zones are analyzed in detail for the establishment of reservoir-hole seepage models, and the model is generated in different regions, which significantly minimizes the productivity calculation error. 2) Considering the influence of horizontal wellbore pressure drop, through model coupling and segmented numerical computation, the findings of the final productivity calculation are very accurate and practicable.

Among them, the production calculation results of well A, well C, and well E are slightly lower than the actual results, because the horizontal section distance of these three wells is relatively long, and the pressure drop in the wellbore is also large, resulting in a decrease in the hole flow. The model proposed in this paper is used to predict the influence of wellbore pressure drop, so the final productivity result is slightly lower than the actual result. The average error of the three wells of well A, well C, and well E is −12.06%. The distance between the horizontal sections of Well B and Well D is relatively short, and there is a small wellbore pressure drop. However, it can be seen from the data in Table 1 that the average permeability of these

TABLE 2 Comparison of calculation results of horizontal well productivity.

		Actual production	This paper model	Joshi model
Well A	Productivity (m^3/d)	65.5	55.84	88.5
	Error magnitude (%)	—	14.75	35.1
Well B	Productivity (m^3/d)	58.4	62.97	81.3
	Error magnitude (%)	—	7.83	39.2
Well C	Productivity (m^3/d)	62.5	57.45	92
	Error magnitude (%)	—	8.08	47.2
Well D	Productivity (m^3/d)	60.19	64.24	79.2
	Error magnitude (%)	—	6.73	31.6
Well E	Productivity (m^3/d)	67.52	59.57	89.7
	Error magnitude (%)	—	13.35	32.8
Average magnitude of error (%)		—	10.15	37.18

TABLE 3 Basic data of well H in Oil field J.

Parameters	Value	Parameters	Value
Boundary supply pressure, p_e (MPa)	12	Boundary supply radius, r_e (m)	300
Reservoir thickness, h (m)	20	Original formation permeability, K (mD)	350
Contaminated zone permeability, K_d (mD)	60	Crude oil conversion coefficient, B	1.084
Horizontal section length, L (m)	200	Fluid density, ρ (kg/m^3)	900
Wellbore radius, r_w (m)	0.098	Fluid viscosity,μ (mPa.s)	5
Absolute wellbore roughness, (mm)	0.19	Contamination thickness,Δr_d (m)	0.4
Perforation density, n (hole/m)	16	Perforation phase angle, Θ (°)	90
Perforation diameter, r_p (m)	0.02	Flow pressure at the heel end of the wellbore, p_{wf} (MPa)	10
Perforation depth, l_p (m)	0.5	Pressure iteration accuracy	0.01

two wells is slightly higher. When using the model in this paper, the results will be slightly higher than the actual results. The average error of production in Well B and Well D is +7.28%.

4 Capacity sensitivity analysis

According to the above model, for a certain length of perforated horizontal wells, the reservoir's physical characteristics (permeability), contamination status (contamination thickness, contamination degree), completion parameters (pore density, pore diameter, and pore depth) are the main factors affecting the flow pressure and flow distribution of each section of horizontal wells. H Well in J Oilfield is used as an example to examine the degree of influence that different factors have. The basic data of the well are shown in Table 3. The hole depth is 0.35 m when the contaminated zone is not penetrated, and the hole depth is 0.55 m when the contaminated zone is penetrated. The change curve of the productivity index of horizontal wells under the influence of different parameters is calculated (see Figure 8).

The diagram shows that reservoir physical properties, contamination status, and perforation completion parameters all affect horizontal well productivity, with the influence of original formation permeability and reservoir contamination thickness being the most obvious. Under certain other conditions, the productivity index of horizontal wells without penetrating the contaminated zone and penetrating the contaminated zone increases linearly with the increase of formation permeability (see Figure 8A). Figure 8B demonstrates that as contamination thickness increases, the productivity index declines rapidly, owing to a decrease in the permeability of the contaminated zone and an increase in flow resistance. Simultaneously, when the contamination thickness exceeds the perforation depth (the contaminated zone is not penetrated), the productivity index decreases significantly. The production index decreases with increasing contamination degree, as shown in Figure 8C, and the influence degree of the non-penetrating contaminated zone is more than that of the penetrating contaminated zone.

The graphic indicates the productivity index of horizontal wells increases with the increase of the perforation depth, and perforation depth is an essential factor affecting horizontal well productivity. It can be seen from Figures 8D–F that the impact of pore density on the productivity index is more obvious than that of pore diameter and phase angle. In Figure 8D, when the hole density is small, the

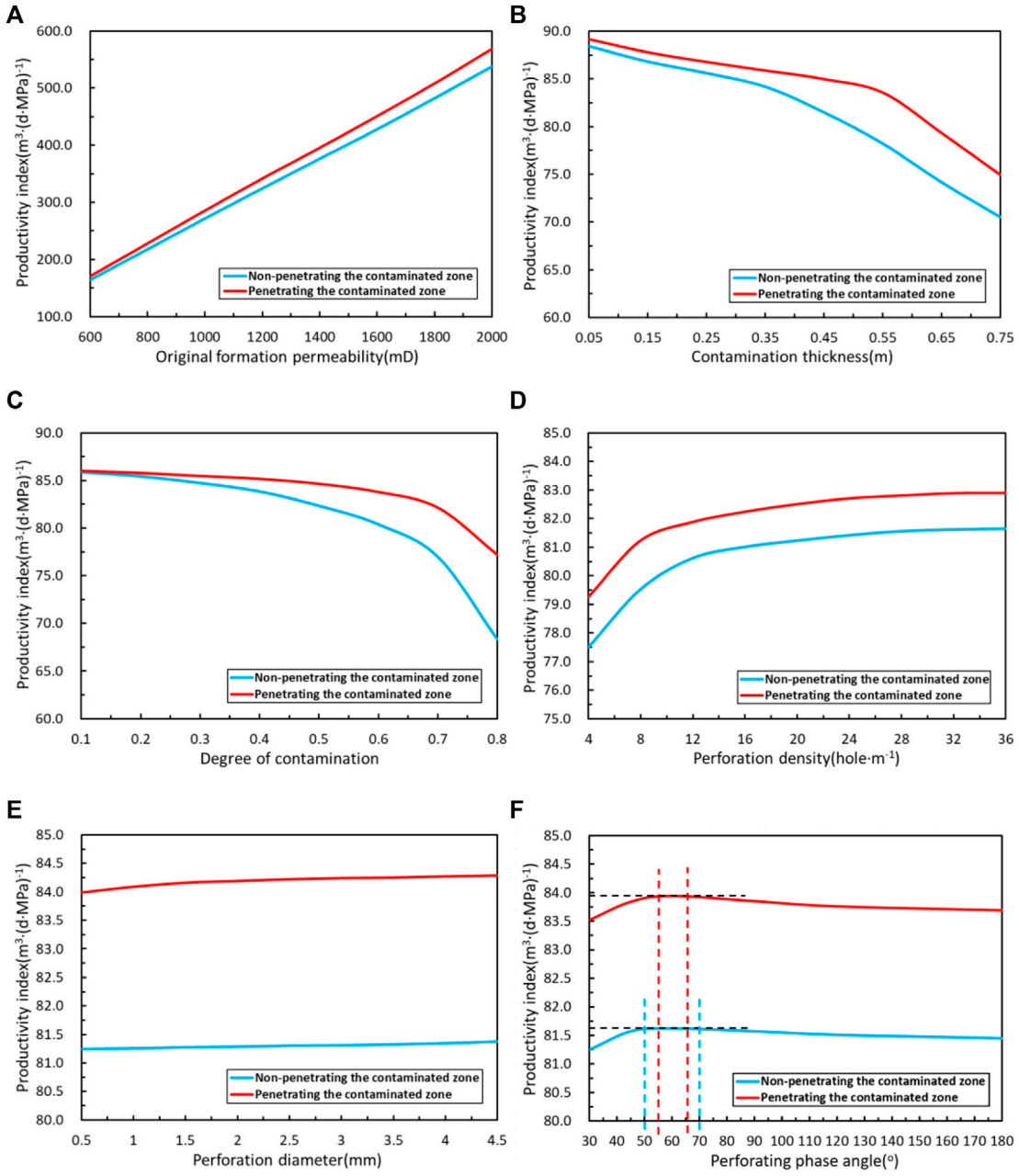

FIGURE 8
Variation diagram of productivity index and completion parameters.

productivity index increases rapidly with the increase of the hole density, but the change in the productivity index is not obvious after the hole density increases to a certain number of holes. Combined with field experience, it is apparent that high hole density may degrade casing strength and potentially cause serious downhole accidents. In the case of the shaped charge, increased hole density means decreasing perforation depth. In the field, it is commonly used to improve perforation depth by sacrificing hole density to attain a better perforation effect. In Figure 8E, the productivity index exhibits a sluggish upward trend as pore size increases, and its influence is minimal. With the change in perforation phase angle shown in Figure 8F, the overall change in the horizontal well productivity index is not immediately apparent. The productivity index increases first and subsequently drops as the phase angle is gradually increased. In the case of not penetrating the contaminated zone, the productivity reaches the maximum when the perforation phase angle is between 50–70°; in the case of penetrating the contaminated zone, the productivity reaches the maximum when the perforation phase angle is between 55–65°.

5 Summary and conclusion

When the perforation passes through the contaminated zone, the formation seepage mode and productivity will change accordingly.

Continuing to use the previous productivity formula will cause large errors. Based on the principle of equivalent seepage resistance, this paper proposes a segmented calculation model for the productivity of perforated horizontal wells considering whether to penetrate the contaminated zone, which can accurately simulate the formation seepage law and predict productivity. This is a method that has not been involved in previous models. The main conclusions are as follows:

(1) The seepage model of the reservoir-hole inflow profile is analyzed in detail when the perforation process is not penetrating the contaminated zone, and the dynamic law of the productivity of the perforated horizontal well is accurately simulated. A new productivity calculation model for perforated horizontal wells is produced through model coupling;
(2) The calculation results of the productivity model of perforated horizontal wells in this paper are close to the actual production of oil wells, and the average error is 10.15%. It is concluded that the model is reasonable and practical. It can adjust the inflow profile along the horizontal wellbore, to optimize the production performance of the whole horizontal well, which can effectively guide the technical process design and effect prediction of a perforated horizontal well, and provide economic benefits for oilfield development;
(3) Sensitivity analysis shows that reservoir physical properties, contamination status, and perforation completion parameters have a certain influence on the productivity of horizontal wells, among which the influence of original permeability and reservoir contamination thickness is the most obvious.

Data availability statement

The original contributions presented in the study are included in the article/Supplementary material, further inquiries can be directed to the corresponding author.

Author contributions

SZ: Formal Analysis, Investigation, Methodology, Writing–original draft, Writing–review and editing. KG: Conceptualization, Writing–original draft. HY: Data curation, Writing–original draft. XG: Formal Analysis, Writing–original draft.

Funding

The author(s) declare that no financial support was received for the research, authorship, and/or publication of this article.

Acknowledgments

The authors are very grateful for the support of Yangtze University for this article. The authors wish to acknowledge KG for interpreting the significance of the results of this study.

Conflict of interest

The authors declare that the research was conducted in the absence of any commercial or financial relationships that could be construed as a potential conflict of interest.

Publisher's note

All claims expressed in this article are solely those of the authors and do not necessarily represent those of their affiliated organizations, or those of the publisher, the editors and the reviewers. Any product that may be evaluated in this article, or claim that may be made by its manufacturer, is not guaranteed or endorsed by the publisher.

References

Bell, W. T., Brieger, E. F., and Harrigan, J. W. (1972). Laboratory flow characteristics of gun perforations. *J. Petroleum Technol.* 24, 1095–1103. doi:10.2118/3444-PA

Burton, R. C., and Hodge, R. M. (1998). "The impact of formation damage and completion impairment on horizontal well productivity," in Proceedings of the Paper presented at the SPE Annual Technical Conference and Exhibition, New Orleans, Louisiana, September 1998 (OnePetro). doi:10.2118/49097-MS

Doan, Q., Farouq Ali, S. M., and George, A. E. (1990). "SCALING CRITERIA AND MODEL EXPERIEMENTS FOR HORIZONTAL WELLS," in Proceedings of the Paper presented at the Annual Technical Meeting, Calgary, Alberta, June 1990.

Giger, F. M., Reiss, L. H., and Jourdan, A. P. (1984). "The reservoir engineering aspects of horizontal drilling," in Proceedings of the Paper presented at the SPE Annual Technical Conference and Exhibition, Houston, Texas, September 1984.

Harris, M. H. (1966). The effect of perforating oil well productivity. *J. PETROLEUM Technol.* 18, 518–528. doi:10.2118/1236-pa

Hawkins, M. F. (1956). A note on the skin effect. *J. Petroleum Technol.* 8, 65–66. doi:10.2118/732-G

Holmes, J. A., Barkve, T., and Lund, Ø. (1998). "Application of a multisegment well model to simulate flow in advanced wells," in Proceedings of the Paper presented at the European Petroleum Conference, The Hague, Netherlands, October 1998.

Joshi, S. D. (1986). "A review of horizontal well and drainhole technology," in Proceedings of the Paper presented at the SPE Annual Technical Conference and Exhibition, Dallas, Texas, September 1987.

Kabir, A., and Sanchez, G. (2009). "Accurate inflow profile prediction of horizontal wells through coupling of a reservoir and a wellbore simulator," in Proceedings of the Paper presented at the SPE Reservoir Simulation Symposium, The Woodlands, Texas, February 2009. doi:10.2118/119095-MS

Karakas, M., and Tarlq, S. M. (1991). Semianalytical productivity models for perforated completions. *SPE Prod. Eng.* 6, 73–82. doi:10.2118/18247-PA

Klotz, J. A., Krueger, R. F., and Pye, D. S. (1974). Effect of perforation damage on well productivity. *J. Petroleum Technol.* 26, 1303–1314. doi:10.2118/4654-PA

Landman, M. J., Laboratories, B. R. M., and Goldthorpe, W. H. (1991). *Optimization of perforation distribution for horizontal wells.*

Li, J., and Wang, T. (2022). Production analysis of horizontal wells in a two-region composite reservoir considering formation damage. *Front. Energy Res.* 10, 818284. doi:10.3389/fenrg.2022.818284

Luo, X., Jiang, L., Su, Y., and Huang, K. (2015). The productivity calculation model of perforated horizontal well and optimization of inflow profile. *Petroleum* 1, 154–157. doi:10.1016/j.petlm.2015.04.002

Ma, C., Xing, Y., Qu, Y., Cheng, X., Wu, H., Luo, P., et al. (2022). A new fracture parameter optimization method for the horizontal well section of shale oil. *Front. Earth Sci.* 10, 895382. doi:10.3389/feart.2022.895382

Marett, B. P., Landman, M. J., and Research, B. (1993). "Optimal perforation design for horizontal wells in reservoirs with boundaries," in Proceedings of the Paper presented at the SPE Asia Pacific Oil and Gas Conference, Singapore, February 1993.

McDowell, J. M., and Muskat, M. (1950). The effect on well productivity of formation penetration beyond perforated casing. *J. Petroleum Technol.* 2, 309–312. doi:10.2118/950309-G

McLeod, H. O. (1983). The effect of perforating conditions on well performance. *J. Petroleum Technol.* 35, 31–39. doi:10.2118/10649-PA

Ouyang, L.-B. (1998). "A simplified approach to couple wellbore flow and reservoir inflow for arbitrary well configurations," in Proceedings of the Paper presented at the SPE Annual Technical Conference and Exhibition, New Orleans, Louisiana, September 1998.

Patel, M. C., and Singh, A. (2016). "Near wellbore damage and types of skin depending on mechanism of damage," in Proceedings of the Paper presented at the SPE International Conference and Exhibition on Formation Damage Control, Lafayette, Louisiana, USA, February 2016. doi:10.2118/179011-MS

Sq, S. (1994). *Use of partial perforations in oseberg horizontal wells*.

Su, Z., and Gudmundsson, J. S. (1994). "Pressure drop in perforated pipes: experiments and analysis," in Proceedings of the Paper presented at the SPE Asia Pacific Oil and Gas Conference, Melbourne, Australia, November 1994 (OnePetro). doi:10.2118/28800-MS

Tong, L., Xiaochen, W., Xiangjun, L., Lixi, L., Xuancheng, W., Jin, C., et al. (2023). A criterion for a hydraulic fracture crossing a natural fracture in toughness dominant regime and viscosity dominant regime. *Eng. Fract. Mech.* 289, 109421. doi:10.1016/j.engfracmech.2023.109421

Wang, G., Liu, Y., and Liu, Z. (2021). Research and application of cold productivity formula of horizontal well in the power-law fluid heavy oil reservoir. *Front. Energy Res.* 9, 792427. doi:10.3389/fenrg.2021.792427

Wang, X., Huang, L., Li, X., Bi, S., Li, H., Zhang, J., et al. (2022). Wellbore multiphase flow behaviors of gas kick in deep water horizontal drilling. *Front. Phys.* 10, 1049547. doi:10.3389/fphy.2022.1049547

Xiaochen, W., Jin, C., Xiangjun, L., Lixi, L., Tong, L., Xuancheng, W., et al. (2023). Statistical damage constitutive model considering water-weakening effect based on the Hoek–Brown criterion. *Environ. Earth Sci.* 82, 408. doi:10.1007/s12665-023-11093-w

Zhang, J., Lei, G., and Zhang, Y. (1998). *Seepage flow in porous media*. Dongying: University of Petroleum Press.

Zhang, W., Xue, X., Zhang, C., Qu, Y., Ke, K., Pan, S., et al. (2022). A drilling wellbore pressure calculation model considering the effect of gas dissolution and suspension. *Front. Earth Sci.* 10, 993876. doi:10.3389/feart.2022.993876

10.3389/feart.2023.1270662

Glossary

Designation

L– Horizontal section length, m

r_e– Reservoir drainage radius, m

r_w– Wellbore radius, m

r_p– Perforation radius, m

r_d– Contamination radius around perforated horizontal well, m

r_c– Compaction radius around perforation hole, m

l_p– Perforation depth, m

h_p– Half of the distance between two adjacent perforations, m

Δr_d– Perforation compaction thickness, m

K– Original formation permeability, mD

K_d– Formation contamination permeability, mD

K_c– Perforation compaction permeability, mD

μ– Formation crude oil viscosity, mPa·s

B– Crude oil conversion coefficient, underground/ground tons

n– perforation density, hole/m

N– Perforating horizontal section

M– Number of perforation holes on the ith infinitesimal segment

p_e– Reservoir boundary pressure, MPa

p_{wf}– Wellbore heel pressure, MPa

Δp– Flow pressure drop in the horizontal wellbore, MPa

Δp_f– Pressure drops caused by friction loss of wellbore wall, MPa

Δp_a– Pressure drops caused by acceleration loss, MPa

Δp_h– Pressure drops caused by mixing pressure loss, MPa

R_1– Fluid seepage resistance around a single perforation hole, Pa

R_{pi}– Flow resistance of the ith perforation zone, Pa

R_i– The seepage resistance in the whole reservoir area of section i, Pa

Q_i– Horizontal well i section production, m^3/d

p_{ei}– Boundary pressure of the ith reservoir, MPa

p_{wfi}– Horizontal well flow pressure of section i, MPa

λ_i– Section i frictional resistance coefficient, Dimensionless

ρ– Fluid density, kg/m^3

v_{1i}– The fluid velocity in the i-1 section wellbore (calculated as 0 in the first section), m/s

v_{pi}– The flow velocity of each hole in the i section, m/s

d_i– Section i length, m

r_{ei}– Oil discharge radius of the ith reservoir, m

r_{pi}– Section i perforation hole radius, m

r_{di}– The radius of wellbore contamination in section i, m

r_{ci}– Section i perforation compaction radius, m

l_{pi}– Perforation radius of section i, m

h_{pi}– Half of the distance between two adjacent holes in the i-section, m

n_i– Section i perforation density, hole/m

K_i– Section i original formation permeability, mD

K_{di}– Contaminated permeability around the ith wellbore, mD

K_{ci}– Compacted permeability around the ith perforation hole, mD

Δp_i– Flow pressure drop in i section wellbore, MPa

Δp_{fi}– Pressure drops caused by friction loss of i section wellbore wall, MPa

Δp_{ai}– The pressure drop caused by the ith acceleration loss, MPa

Δp_{hi}– Pressure drops caused by mixing pressure loss in section i, MPa

frontiers | Frontiers in Earth Science

TYPE Original Research
PUBLISHED 01 November 2023
DOI 10.3389/feart.2023.1274369

OPEN ACCESS

EDITED BY
Yanan Gao,
China University of Mining and Technology, China

REVIEWED BY
Chun Zhu,
Hohai University, China
Huining Ni,
China University of Mining and Technology, China
Wang Qun,
Taiyuan University of Technology, China
Jiliang Pan,
University of Science and Technology Beijing, China

*CORRESPONDENCE
Chen Li,
leesin0225@163.com

RECEIVED 08 August 2023
ACCEPTED 17 October 2023
PUBLISHED 01 November 2023

CITATION
Xin D, Li C, Chen T, Fang X, Zhao Q and Chen H (2023), Research on top-level planning for sustainable high-quality development of China's largest scale deep coal mining area.
Front. Earth Sci. 11:1274369.
doi: 10.3389/feart.2023.1274369

Research on top-level planning for sustainable high-quality development of China's largest scale deep coal mining area

Delin Xin[1], Chen Li[1]*, Tuantuan Chen[1], Xinying Fang[2], Qiang Zhao[1] and Hu Chen[1]

[1]CCTEG Wuhan Engineering Company, Wuhan, China, [2]School of Marxism, China University of Geosciences, Wuhan, China

Coal is the dominant energy source in China, as it has an advantageous position in terms of resource distribution. Against the backdrop of China's high-quality economic development and the global energy crisis, after nearly a decade of preparation, the Xinjie Taigemiao Mine Area (XTMA) has entered the substantial planning and design stage. Based on the resource development conditions and the background of the times of XTMA, the paper provides an in-depth analysis of the connotation and characteristics of XTMA's high-quality development. Subsequently, the overall development concept of "1358" for XTMA is proposed, which includes one strategic objective, three new models, five attribute goals, and eight assessment indicators. Based on this, a top-level planning and design for the implementation of high-quality development in XTMA is carried out comprehensively from aspects such as spatial layout, intelligent safety, integrated zero-carbon, ecological green, technological innovation, cluster management, and harmonious happiness. Finally, we look forward to the long-term blueprint for high-quality development of the XTMA and put forward urgent recommendations for current construction. The research on the high-quality development plan of XTMA will promote the development of China's coal industry and is of great significance.

KEYWORDS

Xinjie Taigemiao Mine Area, high quality development, planning and design, development philosophy, implementation path

1 Introduction

China's resource conditions have the characteristics of "rich coal, poor oil, and little gas," which leads to a significant proportion of coal in China's primary energy consumption. In 2022, it still accounted for approximately 56% (Kang et al., 2019; Xie et al., 2021a). Therefore, coal bears an important responsibility in ensuring national energy security and stable supply (Wu et al., 2019; Hou et al., 2022). The 20th National People's Congress of the Communist Party of China proposed that "actively and steadily promote carbon peak carbon neutrality, and further promote the energy revolution..." In the new era, China's energy development needs to actively adapt to the new development requirements of the domestic and international situation. It is of great significance to firmly adhere to a new path of high-quality development and focus on the present and the long term (Fu and Xiao, 2021).

Many experts and scholars have put forward constructive views on the high-quality development of the coal industry. Wang (2018) summarizes and reviews the achievements of the coal industry over the past 40 years since the reform and opening up, objectively analyzes the current situation and trends of the coal economy, and plans the next work requirements for the coal industry. Wang et al. (2019a), Wang et al. (2020a), and Wang (2022) put forward the overall requirements and construction goals of coal mine intellectualization for high-quality development of coal industry, and carried out the top-level design of coal mine intellectualization. Niu (2019) and Niu (2021) studied the focus of high-quality development in the industry from six dimensions based on current forms and policies, and discussed the practical significance of high-quality development in coal enterprises. Li (2019) and Kang et al. (2021) have planned key tasks for high-quality development of the industry in response to three imbalanced and six insufficient issues in industry development, combined with the new requirements of energy development in the new situation. Jin et al. (2020) analyzed the stress characteristics of regional industrial development on the ecological environment background, atmospheric environment, water resources and water environment, and ecological functions, and summarized the main contradictions and relationships that need to be grasped between regional industrial development and ecological environment protection. Liu et al. (2021) and Liu et al. (2022) summarized the main achievements of China's coal technology since the 13th Five Year Plan and clarified the main tasks of "31110" scientific and technological innovation, which has guiding value for the high-quality development of coal technology during the 14th Five Year Plan. Li et al. (2021) proposed 29 specific paths from 5 dimensions to achieve high-quality development of the coal industry. Liu et al. (2021) and Jia et al. (2022) defines the connotation of high-quality development of coal industry, constructs the evaluation index system of basic capacity of high-quality development of coal industry. Lin (2022) based on China's national conditions analyzes the scenario of carbon peak in 2030. Yuan (2023) systematically summarized significant technological innovation achievements in six aspects and clarified four future innovation directions for high-quality development, pointing out the direction for high-quality coal development.

The development of XTMA is a key project of the country and is fully equipped to be developed by the China Energy Investment Corporation (CHN Energy). The exploration, planning, design, and development of the mining area are carried out by the Shenhua Xinjie Energy Co., Ltd. (Xinjie Energy) of the CHN Energy (Xin et al., 2020). How can we implement the concept of high-quality development, transform the allocation of coal resources, and develop coal resources intensively and efficiently through comprehensive planning, top-level design, and early layout? This is a major practical problem that urgently needs to be solved (Li, 2019; Kang et al., 2021; Li et al., 2021). Therefore, it is urgent to combine the characteristics of the mining area and the requirements of the times to clarify the development connotation, overall development concept, and construction route of the mining area. This is crucial to the high-quality development of XTMA and even China's coal industry.

Based on extensive literature reviews, we found that previous research has mostly focused on individual insights of expert scholars or, in other words, macro-level outlooks on future prospects. This paper is set against the backdrop of an actual mining area under construction, and its research results will directly guide the development and construction of the mining area. Compared to macro-level planning, it is more feasible, and compared to design, it is more exploratory. This paper is an organic integration of planning, research, and design, which makes it more practically significant in comparison.

2 XTMA high quality development background

2.1 Overview of XTMA basic conditions

XTMA is located in Ordos City, Inner Mongolia Autonomous Region, and its resources belong to the Dongsheng Coalfield. The total planned area of XTMA is 681.03 km^2, with a coal resource of approximately 12.298 billion tons. There are 15 minable coal seams with a burial depth of 520–920 m. XTMA coal seam has stable occurrence, excellent coal quality, simple mining technology conditions, and is suitable for large-scale mechanized mining. XTMA plans to construct eight coal mines with a total production capacity of 56.00 Mt/a. The construction timeline of XTMA planning is shown in Figure 1.

Ordos, where XTMA is located, is located at the northern end of the national "two horizontal and three vertical" urbanization strategy pattern, with a complete transportation network and supporting industrial system. The spatial location is shown in Figure 2. As the world's largest coal production company, thermal power generation company, wind power generation company, and coal-to-oil and coal-to-chemicals company, CHN, who is responsible for implementing the development of XTMA, has strong technological and financial advantages. At the same time, XTMA also faces unfavorable factors such as deep strong strata behaviors (Yin et al., 2021; Zhu et al., 2021), overlapping mining rights (coal and natural gas), rock burst (Tang and Tang, 2012; Qin et al., 2023; Ren et al., 2023), and ecological fragility (Zhang et al., 2019; Wang et al., 2020b; Cai et al., 2020).

2.2 The connotation and characteristics of XTMA high quality development

XTMA's high-quality development needs to be based on a new stage of development, implement new development concepts, and construct a new development pattern. Therefore, based on the actual situation of the XTMA, we have defined its connotation of high-quality development, as described below (Fu and Xiao, 2021; Jia et al., 2022).

Starting from the perspective of the full life cycle of the mining area, we must adhere to the principle of ecological priority and green development. We must adhere to the people-centered approach and insist on high-start planning, high-standard construction, and high-quality development. We will stimulate endogenous motivation through technological innovation, promote production-sales balance through intensive and efficient measures, enhance quality and efficiency through safety and intelligence, enhance development vitality through zero-carbon and green initiatives, and achieve open sharing through

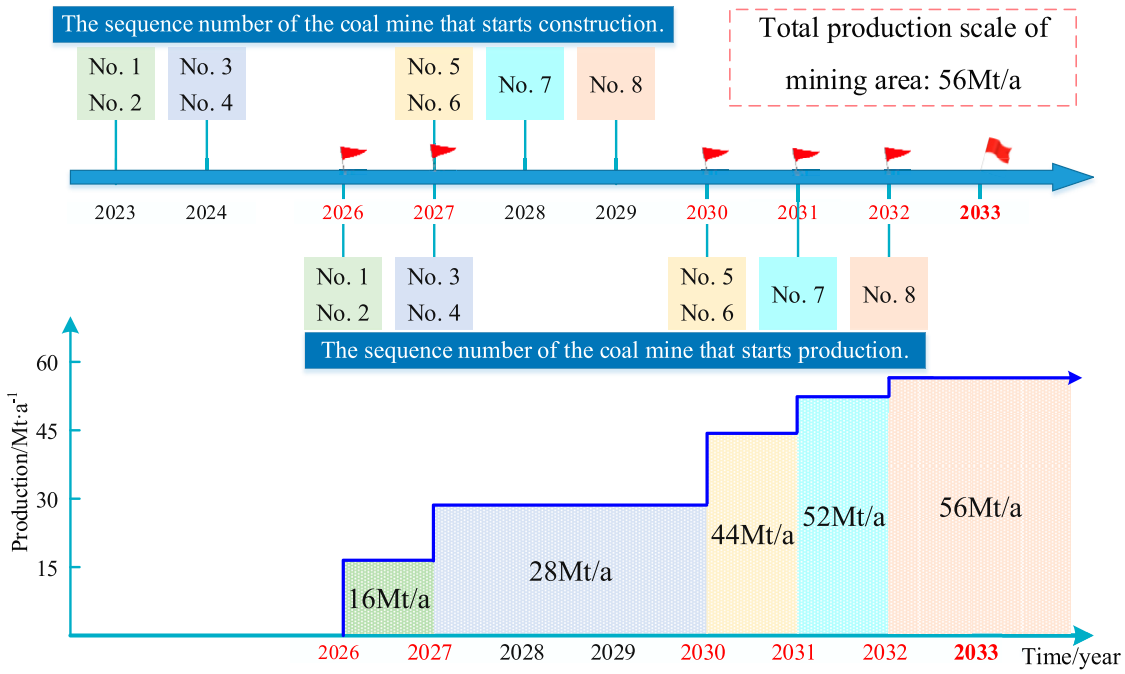

FIGURE 1
Construction timeline of XTMA planning.

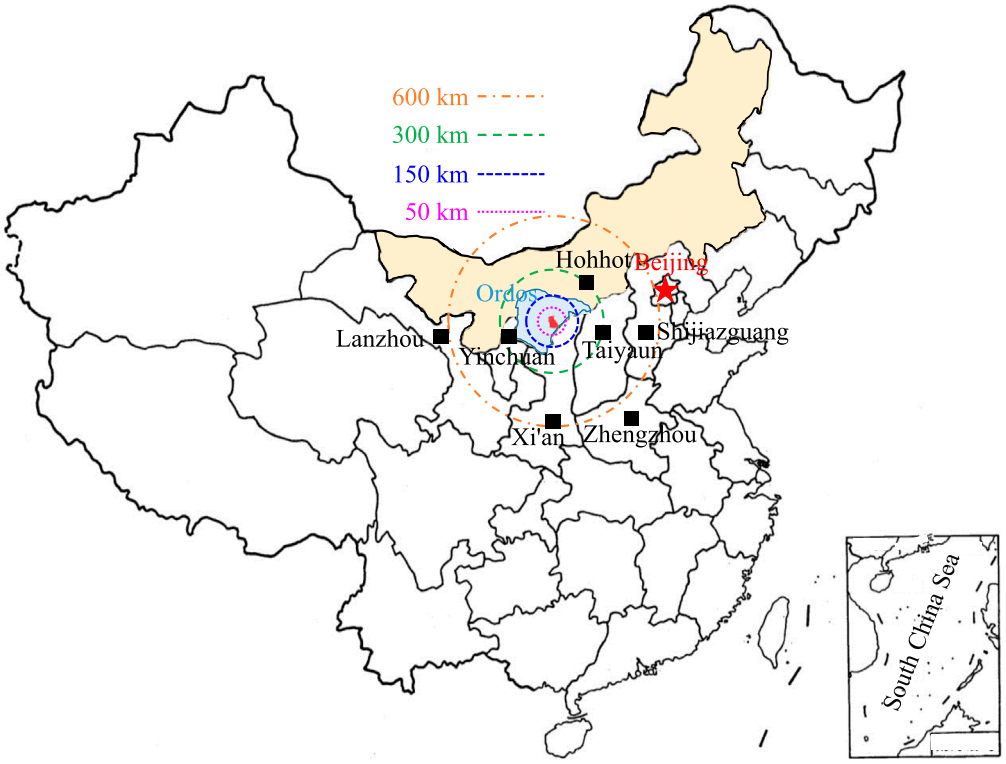

FIGURE 2
Geographical location map of the XTMA

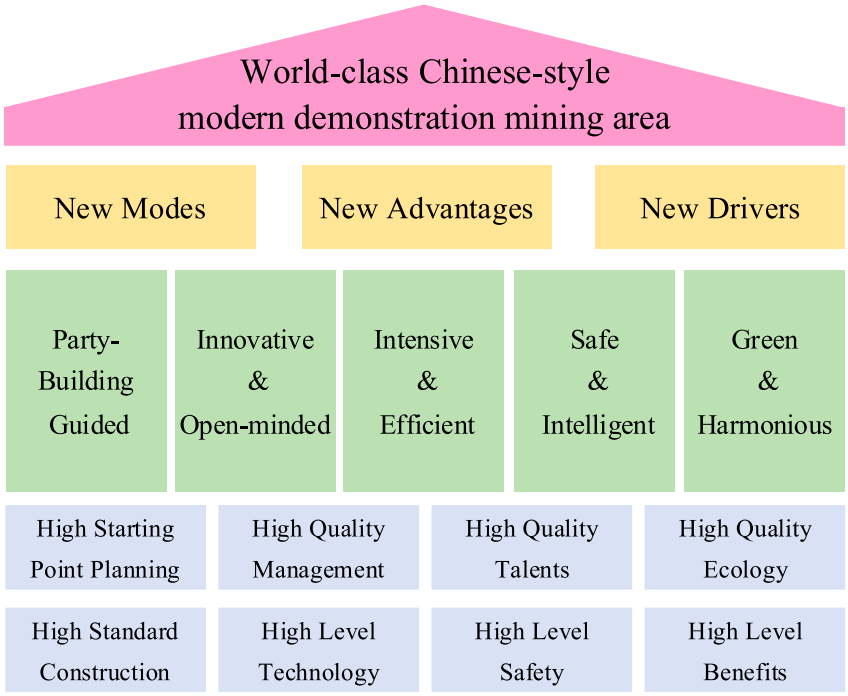

FIGURE 3
XTMA "1358" development strategy diagram.

harmony and happiness. We will promote the deep integration and coordinated development of mining areas with new energy, new technologies, and new industries, thereby enhancing the competitiveness of corporate responsibility. We strive to create the maximum economic, environmental, and social value for stakeholders.

Based on the above requirements and objectives, XTMA can ultimately achieve comprehensive, coordinated and sustainable development. Therefore, the high-quality development of XTMA features a full life cycle, comprehensive elements, overall harmony, ecological priority, technological leadership, and market demand orientation.

3 Overall development concept of XTMA high quality development

From the perspective of the entire life cycle of mining areas, we carry out the national five development concepts, implement the new energy security strategy of "four revolutions, one cooperation," and the overall development strategy of the China Energy Investment Corporation's "one goal, three types and five modernizations, seven first-class" enterprises. Based on the external development environment and internal development conditions of the enterprise, as well as the actual situation of the mining area, the overall development strategy of the mining area has been planned, which can be summarized as the "1358" development strategy, as shown in Figure 3.

"1358" development strategy is elaborated as follows.

"1" represents the ultimate goal of high-quality planning in this mining area, which is to build a world-class demonstration mining area with Chinese modernization. This is the mission layer of our strategic development thinking. At the same time, this goal is also the implementation of the "1357" strategic target of the China Energy Investment Corporation.

"3" represents new models (integrated coal fields, one development company, one-time planning, step-by-step implementation), new advantages (resource advantage, location advantage, latecomer advantage, local enterprise advantage), and new driving forces (leading technology, leading talents, refined management, coordinated development). By gathering new driving forces to create new models and better leverage new advantages, this is the power layer of our planning thinking. This is also a profound implementation of the spirit of the 20th National Congress of the Communist Party of China, that is, to explore new areas and new tracks for development, and continuously create new momentum and new advantages for growth.

"5" represents the specific target attributes that the mining area will achieve in the future, including a party-building guided mining area, an innovative & open mining area, an intensive & efficient mining area, a safe & intelligent mining area, and a green & harmonious mining area. In other words, under the absolute leadership of the Chinese Communist Party, the "Five Types" construction of XTMA corresponds to the "Five Transformations" development of the group company, directly depicting and promoting the long-term blueprint of XTMA and advancing its high-quality construction.

"8" represents the assessment indicators for whether the predetermined goals have been achieved in the planning and construction process of the mining area. They are high starting point planning, high quality management, high quality talents, high quality ecology, high standard construction, high level technology, high level safety, and high level benefits. At the same time, "8 High" is also the

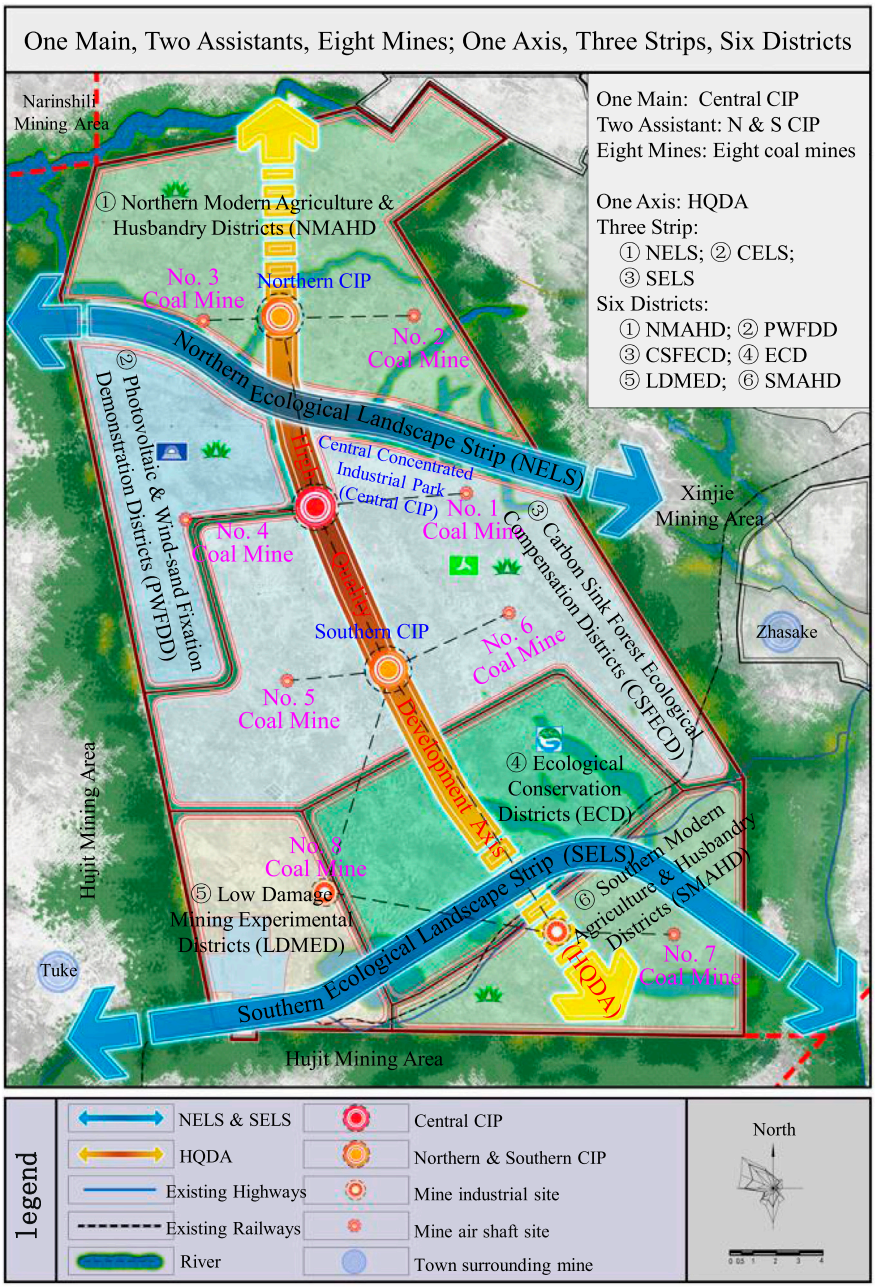

FIGURE 4
Spatial structure planning diagram of the XTMA.

guarantee for the high-quality development of the mining area, and it is a highly condensed execution layer of this plan.

4 Implementation path of XTMA high quality development

4.1 Reasonable development layout planning

Space planning should coordinate the three major spaces of production, living, and ecology, following the planning principle of "favorable production and convenient living." We should coordinate the new energy industry, build a green development layout, develop modern agriculture and husbandry, promote a community of interests between industry and agriculture, and build an innovative model of mining area development that integrates regional development. As a result, a cluster style industrial park with livable and suitable industries, beautiful environment, and complete functions will be formed (Wang, 2019b; Niu, 2019). The spatial development layout of the intensive and efficient cluster demonstration area for planning the integration of cluster mining is shown in Figure 4.

Taking into account the positioning, development goals, and current conditions of the mining area, we adhere to coordinating

local government planning and enterprise development to build a high-quality mining area that is livable and suitable for balanced development. Therefore, we have planned and formed a spatial development layout of the mining area with "One main, Two Assistant, Eight Mines; One Axis, Three Strip, Six Districts."

"One main, Two Assistant, Eight Mines" is a concise summary of the spatial structure layout of core production ground facilities in mining areas such as planned mines and coal preparation plants.

"One main", i.e., Central Concentrated Industrial Park in the XTMA (Central CIP), includes the joint industrial site of No. 1–No. 4 Coal Mine, installation stations, main auxiliary facilities (water supply, power supply, communication, heating), affiliated enterprises, roads, etc. "Two Assistant", i.e., Concentrated industrial parks in the north and south of the XTMA (N & S CIP) , includes the industrial sites of No. 2–No. 3 Coal Mine (located in the North CIP) and No. 5–No. 6 Coal Mine (located in the South CIP), some auxiliary facilities (water supply, power supply, communication, heating), affiliated enterprises, installation stations, roads, etc. "Eight Mines", i.e., eight large coal mines (No. 1–No. 8 Coal Mine) planned in the mining area, with a planned production capacity of 56.0 Mt/a.

"One Axis, Three Strip, Six Districts" is a unified planning and summary of the development axis of mining area planning, green electricity, photovoltaic wind energy, ecological agriculture and husbandry, and other related industries.

"One Axis" is a high-quality development axis that runs through the central part of the mining area from north to south. "Three Strip" are the Northern Ecological Landscape Strip (NELS), the Central Ecological Landscape Strip (CELS), and the Southern Ecological Landscape Strip (SELS). "Six Districts" are the Northern Modern Agriculture & Husbandry Districts (NMAHD), the Photovoltaic & Wind-sand Fixation Demonstration Districts (PWFDD), the Carbon Sink Forest Ecological Compensation Districts (CSFECD), the Ecological Conservation Districts (ECD), the Low damage mining experimental Districts (LDMED), and the Southern Modern Agriculture & Husbandry Districts (SMAHD).

4.2 Construction of intelligent and safe mining area

We will deploy an integrated management and control platform in accordance with the "Six Unifications, Large Concentration" construction model of the group company. Plan to build a three-dimensional transparent geological guarantee system with high standards and actively apply digital twin technology. In this planning path, it is planned to comprehensively build an intelligent network system of coal industry with intelligent perception, intelligent decision-making and automatic execution. Continuously promote the deep integration of advanced information technologies such as 5G, big data, cloud computing, and artificial intelligence into coal mining production scenarios. Based on this, we will achieve remote control and intelligent management of production systems in coal mines and coal preparation plants, assisting in the development of "reducing personnel, increasing safety, and improving efficiency" in mining areas (Wang et al., 2019a; Wang et al., 2020a; Hou et al., 2022; Kang et al., 2023). The planning ideas and goals for intelligent and safe mining areas are shown in Figure 5.

Following the phased implementation and step-by-step improvement approach, the timing planning for intelligent and safe mining areas is as follows.

Short-term goal (2023–2026): In the plan, it is planned to build a "One Cloud Computing" of intelligent mining for Xinjie Energy, and to build a high-speed transmission network and network management for the mining area. We plan to build a company data center, a spatiotemporal intelligent GIS multi-dimensional geographic information platform, an intelligent integrated control platform, and a mining area intelligent decision-making center to achieve intelligent mining.

Mid-term goal (2027–2033): The intelligent construction, backbone transmission network and other information infrastructure of the company and mining area, the intelligent integrated control platform of the mining area, and the spatiotemporal intelligent GIS multi-dimensional geographic information platform are expanded and improved according to the mine construction sequence. Based on this, XTMA is gradually achieving intelligence across the entire mining area.

Long-term goal (2034-): The XTMA will complete the construction of a smart and safe mining area based on the overall architecture of "One Cloud Computing, Multiple Edge Computing, One Backbone Network, Multiple Professional Networks, Three Platforms (Intelligent Integrated Control Platform of Xinjie Energy, Intelligent Coal Mine Comprehensive Control Application Platform, and Intelligent coal selection comprehensive control application platform), Five Centers (safety decision-making, production decision-making, business decision-making, smart people's livelihood, and smart ecology), and N Intelligent Application Scenarios." Through the above planning, the establishment of a digital asset system for Xinjie Energy can achieve digital empowerment and achieve advanced intelligent mining area construction of "intelligence, personnel reduction, efficiency improvement, and increased safety."

4.3 Construction of integrated zero carbon mining area

This path plan will benchmark the dual carbon target to build a diversified clean energy supply system. The long-term expectation is to form a zero carbon demonstration zone that covers zero carbon management, zero carbon supporting facilities, zero carbon mining life, and diversified collaborative development (wind, solar, electricity, and heating). The ultimate goal of the planning is to achieve "positive and negative offset zero emissions" in the mining area (Liu et al., 2019b; Lin, 2022), as shown in Figure 6. There are three stages in the construction timeline.

Phase 1 (2023–2032): Energy conservation and emission reduction, reaching peak as soon as possible.

The 8 coal mines in the mining area are planned to be completed and put into operation by the end of 2032, with a production capacity of 56Mt/a. The node of the first phase construction of a zero

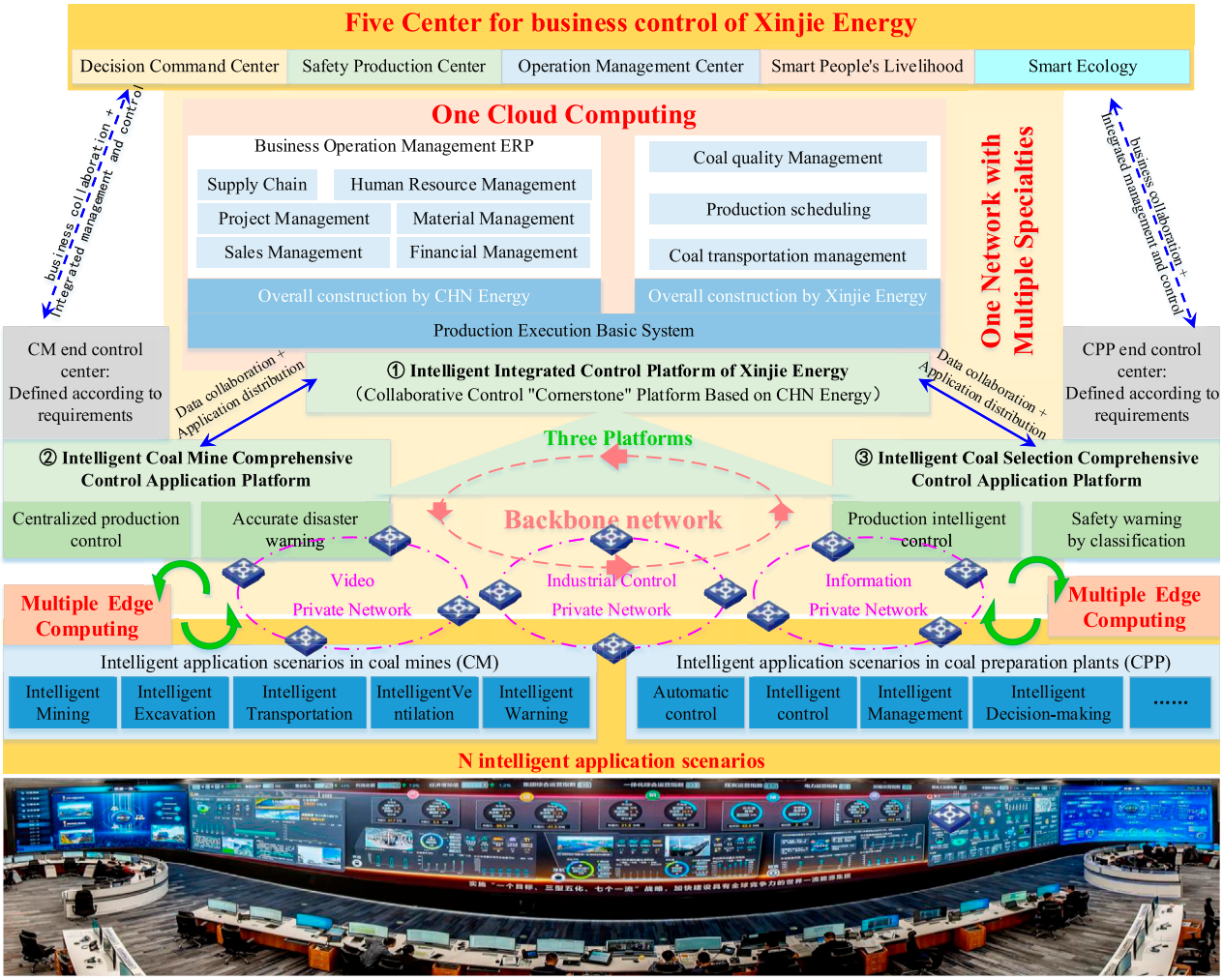

FIGURE 5
Overall planning blueprint for the construction of the intelligent and safe mining area.

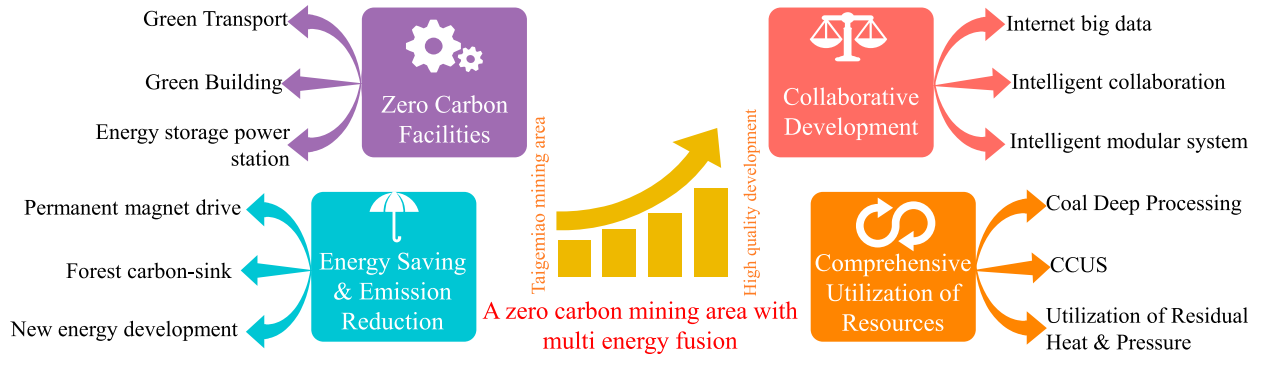

FIGURE 6
Implementation path diagram of zero-carbon mining area.

carbon mining area is the official production of all coal mines in the mining area. During this period, the mining area plans to build zero carbon building infrastructure (electrification, photovoltaic, and recycling of building construction and operation; installation of photovoltaic equipment on building surfaces; and the use of new energy vehicles to form a “decarbonization” transportation energy

system). These technologies and solutions will enable the mining area to achieve carbon peak once all coal mines are fully put into operation.

The recent quantifiable planning goals are as follows: invest in electric vehicles and 30 hydrogen-powered vehicles; construct 2 integrated hydrogen refueling and battery charging/exchanging stations; build a 100,000 kW/400,000 kWh energy storage station; achieve a 44% forest land coverage and 40% grassland coverage in the mining area; construct 42.4 km^2 (2.07 million kW) of photovoltaic and 83 km^2 (200,000 kW) of wind power facilities.

Phase 2 (2032–2035): Deep decarbonization and low-carbon transformation.

After continuous construction, XTMA has basically built a first-class high-quality mining area by 2035. At this stage, the established functions of the mining area are equipped, the technology is advanced, and the conditions are mature. The construction of new energy infrastructure such as solar energy, wind energy, and energy storage in the mining area is complete. Therefore, we plan to integrate and coordinate the energy demand and supply of the mining area. By combining new energy substitution projects with green facilities and green buildings to achieve decarbonization, we will further achieve the transformation and progress from low-carbon mining areas to zero carbon mining areas.

Phase 3 (2035-): Comprehensive neutralization and zero carbon mining area.

Looking ahead to the year 2035, all planned mines in the mining area have been completed and put into operation, and are expected to perform well. Through natural carbon sink, CCUS, comprehensive utilization of residual pressure and waste heat and other technologies, low-carbon mining areas have been successfully transformed and upgraded to zero carbon mining areas, realizing comprehensive carbon neutrality of the mining area and be-coming world-class benchmark mining areas.

4.4 Construction of ecological green mining area

The planning of this section follows the principles of overall layout, zero carbon efficiency, people-oriented, and ecological priority. We plan for the entire life cycle of the mining area, including preparation for construction, production after completion, and future transformation. The planning content is divided into six parts, including environmental requirements for mining areas, resource development methods, ecological protection and restoration, comprehensive utilization of resources, and green innovation drive, covering all aspects of green development in mining areas, as shown in Figure 7. The planning approach ensures a green development model for mining areas based on coal, centered on high-quality development, taking diversified and efficient development as measures, constrained by ecological environment protection, driven by resource recycling, and guaranteed by green innovation (Jin et al., 2020; Wang et al., 2020b; Liu et al., 2022).

We adhere to the "three simultaneities" of mining, protection, and governance, with a people-oriented approach of first relocating, then mining. During the production period of the mining area, it is necessary to standardize the treatment and resource utilization of industrial waste, and pay attention to achieving full cycle protection of the environmental ecology. During the construction period of the mining area, it is necessary to meet the requirements of green mining construction, such as greening and beautification of the mining area, as well as the standardization and efficiency of building layout. The construction of green mines also needs to ensure the scientific and reliable production layout and process technology, and plan and implement low-loss mining in advance (such as water conservation, filling sedimentation reduction, gas coal coordination, etc.). During the development period of the mining area, new energy sources such as photovoltaic, wind power, geothermal, and biomass energy should be reasonably developed. It is necessary to strengthen the monitoring and protection of regional ecological environment in mining area development, such as geological disaster prevention and control, aquifer damage repair, air pollution, mining subsidence, etc. We plan to utilize advanced technology and equipment for efficient resource recovery (intelligent high mining face, underground coal liquefaction, etc.), clean coal utilization (coal washing, coal to oil, coal to gas, etc.), and co associated resource utilization (mine water, coal slurry, waste heat, etc.). In addition, it is necessary to implement measures for energy conservation, emission reduction, and clean energy substitution (green electricity, hydrogen energy), develop a circular economy, and integrate green technological innovation and green development culture throughout the development of mining areas.

4.5 Construction of technological innovation highlands

The planning of this section is guided by the actual needs of the mining area, with the aim of promoting the agglomeration of innovative resources and improving the scientific and technological innovation system (Liu et al., 2021). Based on the major key technological needs and social responsibilities of different periods, the construction of technological highlands is divided into three stages (construction period, pioneering period, and integration period). In addition, we plan to build a collaborative innovation three-level technology research and development platform, hoping to solve the key problems that restrict the high-quality development of mining areas through this platform's technology research and development. At the same time, this platform can further break through the common key technical challenges that constrain the development of the coal industry. The construction concept of technological innovation highlands is shown in Figure 8.

During the construction period, in response to the complex mining technology conditions in the mining area, we will focus on conducting basic research on disaster prevention and control and well construction technology research from four dimensions: safety, ecology, efficiency, and benefits. The key technologies during the construction period mainly focus on the mining technology of rock burst mines, the protection and utilization technology of mine water resources, the protection and comprehensive management technology of the ecological environment above and below the

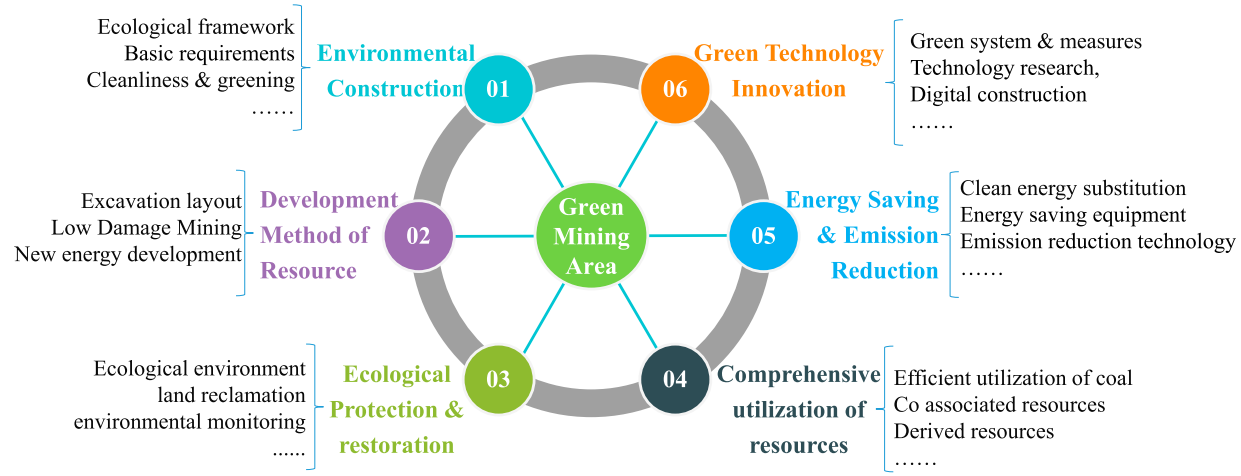

FIGURE 7
Implementation path diagram of green mining area.

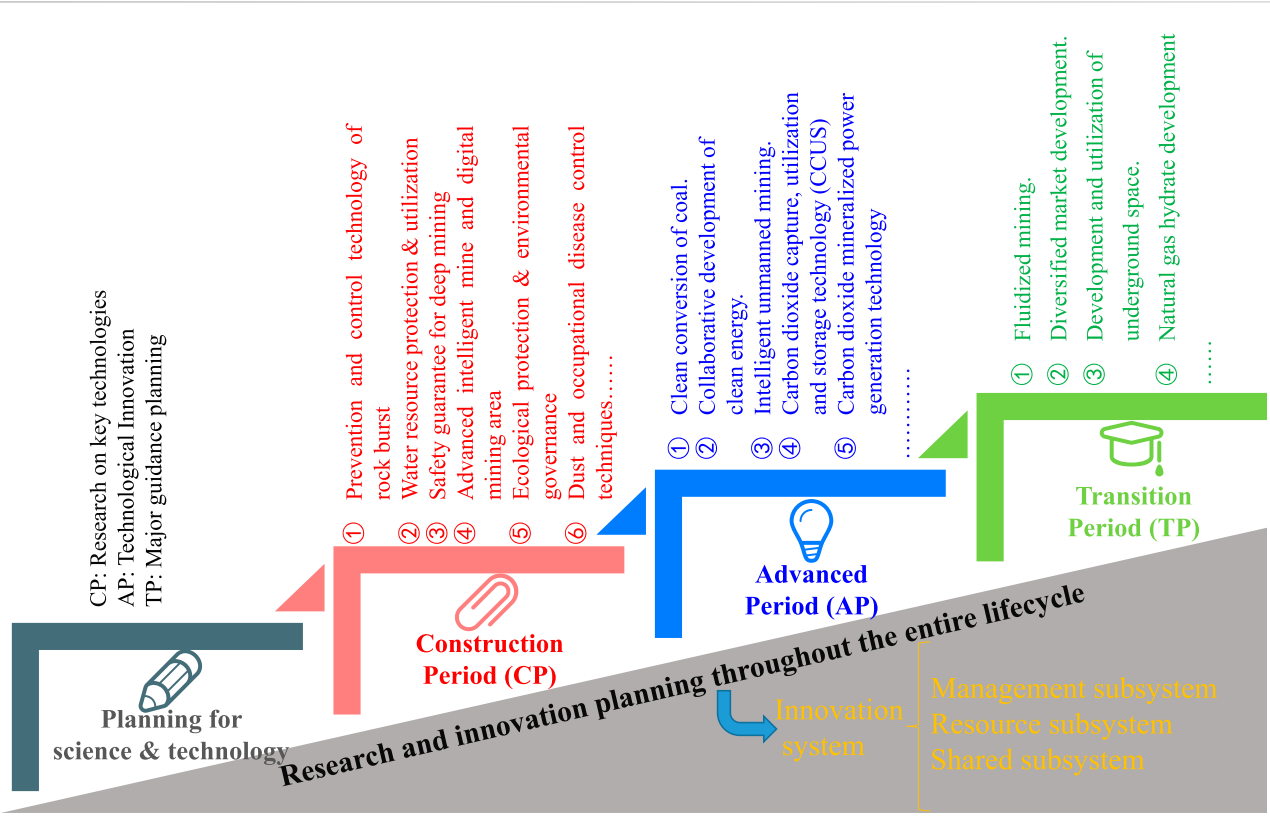

FIGURE 8
Concept of science and technology innovation.

mine, the strategic planning of coordinated mining of coal and natural gas resources, the safety and digital construction technology of mines, and so on (Fan et al., 2021; Jiang et al., 2023; Li et al., 2023; Lyu et al., 2023; Xiong et al., 2023).

The pioneering period mainly focuses on the key technical research directions during the construction and retirement stages of high-quality mining areas, as well as the important technical guidance to lead the development of the coal industry from an industrial perspective. Key technologies to focus on include unmanned mining, fluidized mining, comprehensive development and utilization of underground space, integrated development and utilization of resources, UCG, CCUS, etc.

The construction system of the collaborative innovation three-level technology research and development platform includes a technology management subsystem, a technology resource subsystem, and a research sharing subsystem. The three-level platforms are composed of a basic practice base rooted in coal mines (First level R&D platform: exploring engineering experience, implementing innovative technologies, and implementing safety production), a technology innovation platform based on mining areas (Second level R&D platform: Intensify the common challenges and development needs of various mines, and establish a technology innovation R&D center to serve this mining area), and a collaborative innovation community serving the industry (Third level R&D platform: based on the XTMA and relying on CHN Energy Corporation, solving key scientific problems in mining development, serving CHN Energy Corporation and leading the industry). The establishment of this platform will greatly promote the implementation of industry, academia, research and application.

4.6 Construction of cluster management mode

Combining the positioning and specificity of XTMA, we have constructed a "cluster management" paradigm (The XTMA plans to build eight large coal mines, the unified management of eight coal mines constitutes a cluster management mode) and formed a new "1337" mining area development and management model. "1" is a strategic policy, which is to promote XTMA's strategic vision of building a world-class high-quality demonstration mining area. "3" refers to three goals and three driving forces, respectively. The meaning of the three goals is that the management during the high-quality development of mining areas should always revolve around the three goals of safety, efficiency, and green. The three driving forces mean that technological innovation, management innovation and cultural innovation promote the realization of goals. "7" represents the seven paths to implement this management mode, namely, flattening, specialization, marketization, refinement, standardization, intellectualization, and cleanliness. Under the guidance of the "1337" new mining area development and management model, the mining area cluster management model has formed an orderly, stable, hierarchical, and diversified system connotation.

Establish a framework for the "cluster mining" management innovation system based on the innovation of cluster management mode, as shown in Figure 9. The system framework specifically includes 10 aspects, including Coal Mine Safety Risk Pre Control Management System, Benchmarking Management System, Comprehensive Cost Refinement Management System, Integration System of Industry & Finance, Enterprise Standard System, Professional Management System, Flat Organizational Structure Management System, Green & Low-Carbon Management System, Internal Market-Oriented Management System, and Human Resource Management System. The system framework clarifies management objectives, approaches, and main methods and modes. The application of this management system can enhance the scientific management level of enterprises. In addition, the management system also clarifies the future development direction and will provide strong support for building world-class high-quality demonstration mining areas.

4.7 Construction of harmonious and eudemonic mining area

Xijinping pointed out that "only enterprises that actively undertake social responsibility are the most competitive and viable enterprises." The construction of XTMA should be based on the "RISE" brand strategy of CHN Energy Corporation, and deeply integrate the concept of "Heaven-Earth-Human" responsibility culture. In the process of high-quality development of XTMA, enterprises must take up social responsibility, do their own work and positioning well, and achieve coordination and balance in the following four aspects:

(1) Coordination and balance between mining areas and industrial structure: the development of mining areas must be coordinated and balanced with the local industrial structure, to ensure that its development will not have a negative impact on other industries in the local area, but will promote sustainable economic development in the local area. For example, the formation of coal-based coal development, coal washing, coal chemical industry, coal power plant, professional team, life service supply and other industries.
(2) Coordination and balance between mining areas and natural environment: the development of mining areas needs to consider the impact on the local natural environment, protect the ecological environment, protect biodiversity, and achieve sustainable development. For example, the green area in the mining area has been further improved, environmental pollution has been controlled, and the village appearance has been improved.
(3) Coordination and balance between mining areas and urban and rural areas: the development of XTMA needs to consider the coordination and balance with local urban and rural areas, promote the economic development of the local society and improve the living standards of the people. For example, people in and around mining areas have more diverse types of work and higher incomes.
(4) Coordination and balance between mining areas and employee happiness: the development of the enterprise must be coordinated and balanced with the realization of employee happiness, guarantee the rights and welfare of employees, improve their job satisfaction and happiness, and promote harmonious labor relations. The contents closely related to people's lives in the working environment, housing, education, medical care, and elderly care have been improved, and the economic material has been greatly satisfied.

To achieve a humanistic and harmonious eudemonic mining area, we need to start from three aspects. Firstly, enterprises must establish a concept of social responsibility work, which not only creates better economic benefits internally but also fulfills its own social responsibility externally. Secondly, it is necessary to establish a mechanism of cooperation and development between mining areas and local enterprises. In the process of mining area development, enterprises should participate in local construction in multiple dimensions and give full play to their social responsibility. Finally, it is necessary to focus on the happy life of employees. While creating a safe and low-intensity work environment, provide

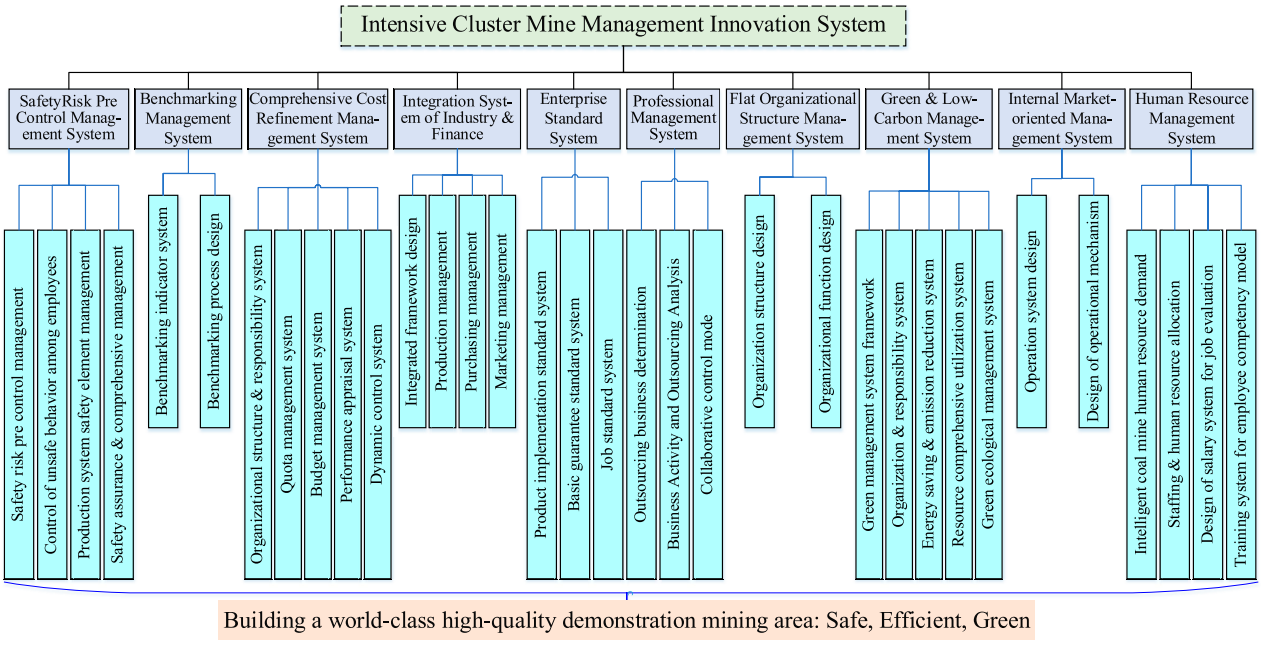

FIGURE 9
"Cluster mine" management innovation system framework.

better salary and comprehensive welfare protection for employees, constantly improve their sense of acquisition, happiness and security, thus achieving a humanistic and harmonious eudemonic mining area.

5 Objectives and significance of mining area phase construction

5.1 Stage goals for high-quality development of mining areas

① Short-term goal (2023–2030): Preliminary first-class

The period from 2023 to 2030 is our short-term goal, and we aim to achieve a preliminary first-class level. Specifically, we plan to complete the construction and operation of the four wells in the northern part, reaching a scale of 28.0Mt/a, and improve the functions of the mining area. We also plan to establish an intensive and efficient industrial park that integrates innovation, intelligence, safety, efficiency, greenness, and happiness, providing a better environment and conditions for our production. In addition, we will strive to create a beautiful and livable happy mining area and provide better living conditions and welfare guarantees for our employees.

② Mid-term goal (2030–2035): Basically first-class

The period from 2030 to 2035 is the achievement of the mid-term goal construction, during which all eight coal mines in the mining area will be in full operation, with a total production capacity of 56.0 Mt/a. Specifically, we have built an intensive and efficient mining cluster demonstration zone, innovation-driven smart safety leading zone, multi-energy integration zero-carbon advanced zone, and beautiful and eudemonic green model zone. The basic completion of these different modules in the mining area has also promoted the basic construction of a world-class high-quality development demonstration mining area.

③ Long-term goal (2035-): Comprehensively first-class

During this period, we will consider relocating water sources and developing the northern exploration area; we are committed to building the mining area into a national coal reserve base with a capacity of billions of tons. At the same time, we will also build and put into good use the green electricity industry, agriculture and husbandry, carbon sequestration forest ecological compensation area, and low-loss mining experimental area. This will allow relevant parties to fully benefit from the dividends of high-quality development. Ultimately, we will fully build a world-class high-quality development demonstration mining area.

5.2 The significance of XTMA's high-quality development

XTMA is a national coal strategic reserve base. In the context of the world undergoing unprecedented changes, China is shifting its economy towards high-quality development (Liu et al., 2019a; Kang et al., 2023), deepening its new energy security strategy (Li et al., 2022; Li et al., 2023), pursuing the dual-carbon goals (Xie et al., 2021b; Miao et al., 2022), protecting the ecological environment of the Yellow River Basin (Wang, 2019b; Yu and Zhang, 2022), and facing the growing global energy crisis (Hao, 2022). Against this

FIGURE 10
The central industrial Park of the XTMA.

backdrop, the high-quality development of XTMA is particularly critical and urgent.

Building XTMA into a green, safe, efficient and intelligent international first-class modern benchmark mining area can not only fully leverage the role of CHN Energy Corporation as a "national team" and "main force" in energy supply, but also effectively embody its function as a "voltage regulator" and "ballast" in energy supply. It can also guide the scientific development of the mining area in the next 30–50 years and form a replicable and promotable experience. In addition, the high-quality development of XTMA will play a leading role, which is of great significance for the high-quality development and transformation of the coal industry, supporting the development of CHN Energy Corporation and local economic growth, and is also a necessary condition for building a world-class modern benchmark mining area. The surface planning of the central industrial park in the XTMA (serving No. 1 Coal Mine to No. 4 Coal Mine) is shown in Figure 10.

6 Summary and suggestions

6.1 Summary

China's resource endowment determines that coal development plays a fundamental role in ensuring energy security, and mining area development is the most basic and important link in the coal industry. The high-quality development of mining areas is the cornerstone of the continuous implementation of high-quality development of the coal industry in the new era.

Based on the research of high-quality development planning in this article, XTMA can be developed into a "smart and safe leading area, cluster management demonstration area, zero-carbon advanced area, and green model area." Our vision is to ultimately achieve the "Five-Zero Goals" in XTMA, which are: zero fatalities in safety, zero injuries in health, zero damage in mining, zero emissions in environmental protection, and carbon neutrality in carbon reduction (zero carbon). The high-quality development of XTMA will promote the open sharing of new concepts, new strategies, new technologies, and new models in the coal industry, and then form the "Xinjie model" that leads the development of the coal industry in a new paradigm. At the same time, the high-quality development of XTMA will also promote the upgrading of this mining area into a carrier of upgrading the Chinese coal industry and a world-class modern benchmark mining area, leading the high-quality development of the coal industry.

6.2 Prospect

The high-quality development of XTMA will exert a strong driving force on the high-quality development of China's coal industry, and the coal industry will undergo changes in coal production, supply, utilization, and other aspects in the future.

For example, coal production will achieve highly intelligent automation, realizing the vision of "drilling without going down the well, mining without seeing the coal" and "underground robots, surface technology personnel." Another example is that coal supply will form a model of "flexible production and customized

marketing." Moreover, coal utilization will achieve a trend of "clean, low-carbon, high-end, and diversified."

6.3 Suggestions

To strengthen the implementation path of this plan, we have put forward the following five suggestions for Xinjie Energy.

① Designating XTMA as a leading area for high-quality development of coal industry.
② Establishing a national-level energy technology R&D and technology collaborative innovation center.
③ Developing ecological construction standards for mining areas and scientifically delineating ecological conservation redlines.
④ Exploring safety supervision models that are compatible with efficient management models.
⑤ Give full play to the role of local government in overall planning and coordination.

Data availability statement

The original contributions presented in the study are included in the article/supplementary material, further inquiries can be directed to the corresponding author.

Author contributions

DX: Conceptualization, Funding acquisition, Project administration, Resources, Writing–review and editing. CL: Conceptualization, Visualization, Writing–original draft. TC: Data curation, Formal analysis, Writing–original draft. XF: Resources, Writing–review and editing. QZ: Investigation, Writing–original draft. HC: Investigation, Writing–original draft.

Funding

The authors declare financial support was received for the research, authorship, and/or publication of this article. This work is supported by the Innovation Project of CCTEG Wuhan Engineering Company (ZZYF202318 and ZZYF202321) and CHN Energy Technology Project (GJNY-21-129). The funders were not involved in the study design, collection, analysis, interpretation of data, the writing of this article, or the decision to submit it for publication.

Acknowledgments

Thanks to the guidance and suggestions provided by experts and scholars from the China Energy Investment Corporation (CHN Energy), China Coal Technology & Engineering Group (CCTEG), Shaanxi Coal and Chemical Industry Group Co., Ltd., Shandong Energy Group Co., Ltd. (SDE), China University of Mining and Technology, China University of Mining and Technology (Beijing), and other organizations for the planning of Xinjie Taigemiao Mining Area.

Conflict of interest

Authors DX, CL, TC, QZ, and HC were employed by CCTEG Wuhan Engineering Company.

The remaining author declares that the research was conducted in the absence of any commercial or financial relationships that could be construed as a potential conflict of interest.

Publisher's note

All claims expressed in this article are solely those of the authors and do not necessarily represent those of their affiliated organizations, or those of the publisher, the editors and the reviewers. Any product that may be evaluated in this article, or claim that may be made by its manufacturer, is not guaranteed or endorsed by the publisher.

References

Cai, Y., Li, X., Deng, W., Xiao, W., and Zhang, W. (2020). Simulation of surface movement and deformation rules and detriment key parameters in high-strength mining. *J. Min. Strat. Control Eng.* 2 (4), 46–54. doi:10.13532/j.jmsce.cn10-1638/td.20200622.001

Fan, J., Guo, Z., Tao, Z., and Wang, F. (2021). Method of equivalent core diameter of actual fracture section for the determination of point load strength index of rocks. *B. Eng. Geol. Environ.* 80 (6), 4575–4585. doi:10.1007/s10064-021-02236-z

Fu, J., and Xiao, X. (2021). Supporting economic and social progress with high quality energy development. *People's Trib.* 2021 (4), 56–57. doi:10.3969/j.issn.1004-3381.2021.04.015

Hao, Y. (2022). The source and influence of energy crisis in Europe. *People's Trib.* 2022 (7), 102–105. doi:10.3969/j.issn.1004-3381.2022.07.025

Hou, G., Wang, G., Xue, Z., Ren, H., Ouyang, M., Wang, F., et al. (2022). Key technologies and equipment for automatic driving of coal mine auxiliary transportation. *J. Min. Strat. Control Eng.* 4 (3), 5–17. doi:10.13532/j.jmsce.cn10-1638/td.20220310.001

Jia, X., Wang, L., and Zhai, Z. (2022). Connotation, evaluation and development path of high-quality development of coal industry from the perspective of carbon peak. *J. Xi'An Univ. Sci. Technol.* 42 (3), 589–599. doi:10.13800/j.cnki.xakjdxxb.2022.0323

Jiang, B., Xin, Z., Zhang, X., Deng, Y., Wang, M., Li, S., et al. (2023). Mechanical properties and influence mechanism of confined concrete arches in high-stress tunnels. *Int. J. Min. Sci. Techno.* 33 (7), 829–841. doi:10.1016/j.ijmst.2023.03.008

Jin, F., Ma, L., and Xu, D. (2020). Environmental stress and optimized path of industrial development in the Yellow River Basin. *Resour. Sci.* 42 (1), 127–136. doi:10.18402/resci.2020.01.13

Kang, H., Jiang, P., and Liu, C. (2023). Development of intelligent rapid excavation technology and equipment for coal mine roadways. *J. Min. Strat. Control Eng.* 5 (2), 5–7. doi:10.13532/j.jmsce.cn10-1638/td.20230403.001

Kang, H., Wang, G., Wang, S., Liu, J., Ren, S., Chen, P., et al. (2021). High-quality development of China's coal industry. *Strategic Study CAE* 23 (5), 130–138. doi:10.15302/J-SSCAE-2021.05.016

Kang, H., Xu, G., Wang, B., Wu, Y., Jiang, P., Pan, J., et al. (2019). Forty years development and prospects of underground coal mining and strata control technologies in China. *J. Min. Strat. Control Eng.* 1 (2), 7–39. doi:10.13532/j.jmsce.cn10-1638/td.2019.02.002

Li, G., Zhu, C., He, M., Zuo, Y., Gong, F., Xue, Y., et al. (2023). Intelligent method for parameters optimization of cable in soft rock tunnel base on longitudinal wave velocity. *Tunn. Undergr. Sp. Tech.* 133 (3), 104905–104913. doi:10.1016/j.tust.2022.104905

Li, H. (2019). Discussion on the high quality development path of coal industry in new times. *China coal.* 45 (10), 22–26. doi:10.3969/j.issn.1006-530X.2019.10.006

Li, H., Zhao, Y., You, W., and Ding, Z. (2021). Research on high-quality development of the coal industry in China Energy Investment Group under the new development pattern. *China coal.* 47 (1), 46–51. doi:10.19880/j.cnki.ccm.2021.01.006

Li, K. (2023). Global energy revolution and new features of energy security. *Int. Petrol. Econ.* 31 (1), 42–48. doi:10.3969/j.issn.1004-7298.2023.01.015

Li, X., Li, Q., Han, P., and Xu, X. (2022). Identification of surface damage degree in high-intensity mining and control technologies. *J. Min. Strat. Control Eng.* 4 (03), 90–99. doi:10.13532/j.jmsce.cn10-1638/td.20220223.001

Lin, B. (2022). China's high-quality economic growth in the process of carbon neutrality. *China Finance Econ. Rev.* 11 (4), 3–22. doi:10.1515/CFER-2022-0020

Liu, F., Cao, W., Zhang, J., Cao, G., Guo, L., Liu, Y. L., et al. (2021). Current technological innovation and development direction of the 14th Five-Year Plan period in China coal industry. *J. China Coal Soc.* 46 (1), 1–8. doi:10.12047/j.cjap.0099.2021.098

Liu, F., Guo, L., and Zhao, L. (2022). Research on coal safety range and green low-carbon technology path under the dual-carbon background. *J. China Coal Soc.* 47 (1), 1–15. doi:10.13225/j.cnki.jccs.yg22.0016

Liu, Q., Gao, J., and Xu, X. (2019a). Pattern optimization and carbon emissions of coal supply in China. *J. Nat. Resour.* 34 (3), 473–486. doi:10.31497/zrzyxb.20190303

Liu, X., Cui, L., Li, B., and Du, X. (2019b). The combined effects of omitting confounders and measurement error on statistical inference of mediation and a new tool for sensitivity analysis. *J. Beijing Inst. Technol. Soc. Sci. Ed.* 23 (3), 1–2. doi:10.1080/00273171.2019.1694478

Lyu, B., Zhao, X., Zhang, T., Han, M., and Cao, C. (2023). Design of yielding device and optimization of support scheme of anchoring system in large deformation roadway. *J. Min. Strat. Control Eng.* 5 (4), 1–10. doi:10.13532/j.jmsce.cn10-1638/td.2023.04.001

Miao, Y., Cheng, L., Zheng, X., Chen, X., Wang, Z., and Xu, B. (2022). Study on dynamic response characteristics of mining stress in shallow deep mining roadway. *J. Min. Strat. Control Eng.* 4 (6), 60–68. doi:10.13532/j.jmsce.cn10-1638/td.2022.06.001

Niu, K. (2019). Research on eight new orientations of coal industry development in the new era. *Coal Econ. Res.* 39 (5), 61–64. doi:10.13202/j.cnki.cer.2019.05.011

Niu, K. (2021). The discussion on strategic direction of coal enterprises development in the 14th Five-Year Plan Period. *China coal.* 47 (1), 41–45. doi:10.19880/j.cnki.ccm.2021.01.005

Qin, Z., Gao, J., and Zheng, X. (2023). Impact of R&D investment and network penetration on human development: evidence from China. *J. Min. Strat. Control Eng.* 5 (2), 1–25. doi:10.1007/s11205-023-03091-z

Ren, F., Zhu, C., He, M., Shang, J., Feng, G., and Bai, J. (2023). Characteristics and precursor of static and dynamic triggered rock burst: insight from multifractal. *Rock Mech. Rock Eng.* 56 (3), 1945–1967. doi:10.1007/s00603-022-03173-3

Tang, S., and Tang, C. (2012). Numerical studies on tunnel floor heave in swelling ground under humid conditions. *Int. J. Rock Mech. Min.* 55 (2), 139–150. doi:10.1016/j.ijrmms.2012.07.007

Wang, G. (2022). New technological progress of coal mine intelligence and its problems. *Coal Sci. Technol.* 50 (1), 1–27. doi:10.13199/j.cnki.cst.2022.01.001

Wang, G., Liu, F., Pang, Y., Ren, H., and Ma, Y. (2019a). Coal mine intellectualization: the core technology of high quality development. *J. China Coal Soc.* 44 (2), 349–357. doi:10.13225/j.cnki.jccs.2018.2041

Wang, G., Pang, Y., and Ren, H. (2020a). Intelligent coal mining pattern and technological path. *J. Min. Strat. Control Eng.* 2 (1), 5–19. doi:10.13532/j.jmsce.cn10-1638/td.2020.01.001

Wang, J. (2019b). Sustainable coal mining based on mining ground control. *J. Min. Strat. Control Eng.* 1 (2), 40–47. doi:10.13532/j.jmsce.cn10-1638/td.2019.02.003

Wang, S., Shen, Y., Sun, Q., and Hou, E. (2020b). Scientific issues of coal detraction mining geological assurance and their technology expectations in ecologically fragile mining areas of Western China. *J. Min. Strat. Control Eng.* 2 (4), 5–19. doi:10.13532/j.jmsce.cn10-1638/td.20200817.001

Wang, X. (2018). Build a modern coal economic system to promote the high-quality development of coal industry. *China Coal Ind.* 34 (8), 1–6. CNKI:SUN:MTQG.0.2018-08-005.

Wu, Q., Tu, K., Zeng, Y., and Liu, S. (2019). Discussion on the main problems and countermeasures for building an upgrade version of main energy (coal) industry in China. *J. China Coal Soc.* 44 (6), 1625–1636. doi:10.13225/j.cnki.jccs.2019.0387

Xie, H., Miao, H., and Zhou, H. (2021a). Research on the "14th five-year" development strategy of Chinese mining. *Sci. Bull. Natl. Nat. Sci. Found. China* 35 (6), 856–863. doi:10.16262/j.cnki.1000-8217.2021.06.002

Xie, H., Ren, S., Xie, Y., and Jiao, X. (2021b). Development opportunities of the coal industry towards the goal of carbon neutrality. *J. China Coal Soc.* 46 (7), 2197–2211. doi:10.13225/j.cnki.jccs.2021.0973

Xin, D., Fang, X., and Zhang, Y. (2020). Master plan of Xinjie Taigemiao Mining Area based on the five development principles. *Coal Eng.* 52 (12), 1–6. doi:10.11799/ce202012001

Xiong, F., Zhu, C., Feng, G., Zheng, J., and Sun, H. (2023). A three-dimensional coupled thermo-hydro model for geothermal development in discrete fracture networks of hot dry rock reservoirs. *Gondwana Res.* 122 (12), 331–347. doi:10.1016/j.gr.2022.12.002

Yin, Q., Wu, J., Zhu, C., He, M., Meng, Q., and Jing, H. (2021). Shear mechanical responses of sandstone exposed to high temperature under constant normal stiffness boundary conditions. *Geomech. Geophy.s Geo.* 7 (2), 35–17. doi:10.1007/s40948-021-00234-9

Yu, W., and Zhang, Z. (2022). Theoretical logic and path selection of ecological protection and high quality development in the Yellow River Basin in the New era. *Price Theory & Pract.* 2022 (9), 89–92. doi:10.19851/j.cnki.cn11-1010/f.2022.09.367

Yuan, L. (2023). Theory and technology considerations on high-quality development of coal main energy security in China. *Bull. Chin. Acad. Sci.* 38 (1), 11–22. doi:10.16418/j.issn.1000-3045.20220819002

Zhang, J., Ju, Y., Zhang, Q., Ju, F., Xiao, X., Zhang, W., et al. (2019). Low ecological environment damage technology and method in coal mines. *J. Min. Strat. Control Eng.* 1 (2), 56–68. doi:10.13532/j.jmsce.cn10-1638/td.2019.02.005

Zhu, C., He, M., Jiang, B., Qin, X., Yin, Q., and Zhou, Y. (2021). Numerical investigation on the fatigue failure characteristics of water-bearing sandstone under cyclic loading. *J. Mt. Sci-Engl.* 18 (12), 3348–3365. doi:10.1007/s11629-021-6914-0

frontiers | Frontiers in Earth Science

TYPE Original Research
PUBLISHED 22 November 2023
DOI 10.3389/feart.2023.1212064

OPEN ACCESS

EDITED BY
Jianwei Tian,
Technical University of Denmark, Denmark

REVIEWED BY
Richeng Liu,
China University of Mining and Technology, China
Kun Tu,
China University of Mining and Technology, China
Tianran Ma,
China University of Mining and Technology, China

*CORRESPONDENCE
Milovan Fustic,
milovan.fustic@nu.edu.kz

RECEIVED 25 April 2023
ACCEPTED 06 November 2023
PUBLISHED 22 November 2023

CITATION
Kozhagulova A, Yapiyev V, Karabayanova L, Dillinger A, Zavaley V, Kalitova A, Bayramov E, Holbrook J, Grasby SE and Fustic M (2023), Geological controls on the geothermal system and hydrogeochemistry of the deep low-salinity Upper Cretaceous aquifers in the Zharkent (eastern Ily) Basin, south-eastern Kazakhstan.
Front. Earth Sci. 11:1212064.
doi: 10.3389/feart.2023.1212064

Geological controls on the geothermal system and hydrogeochemistry of the deep low-salinity Upper Cretaceous aquifers in the Zharkent (eastern Ily) Basin, south-eastern Kazakhstan

Ashirgul Kozhagulova[1,2], Vadim Yapiyev[1,3], Leila Karabayanova[1], Antoine Dillinger[1], Vyacheslav Zavaley[4,5], Aisulu Kalitova[4,5], Emil Bayramov[1], John Holbrook[6], Stephen E. Grasby[7] and Milovan Fustic[1,8]*

[1]School of Mining and Geosciences, Nazarbayev University, Astana, Kazakhstan, [2]Oil and Gas Faculty, Atyrau Oil and Gas University, Atyrau, Kazakhstan, [3]The Environment and Resource Efficiency Cluster (EREC), Nazarbayev University, Astana, Kazakhstan, [4]Department of Hydrogeology, Engineering and Oil and Gas Geology, Satbayev University, Almaty, Kazakhstan, [5]Geoterm Production Company LLP, Almaty, Kazakhstan, [6]Department of Geological Sciences, Texas Christian University, Fort Worth, TX, United States, [7]Geological Survey of Canada, Calgary, AB, Canada, [8]Department of Geosciences, University of Calgary, Calgary, AB, Canada

The Zharkent (eastern Ily) Basin is renowned for its low-salinity natural hot springs and geothermal wells, primarily utilized for recreational purposes. Despite the growing commercial interest, the geothermal system in this area is very poorly documented or understood. Accordingly, we conducted a multi-disciplinary study, focusing on the advanced characterization of waters from productive Cretaceous strata, along with the interpretation of geothermal gradients and reservoir recharge in a geological context. Conventional wisdom asserts that Ily is an intracratonic basin characterized by high geothermal heat in its central part and by geothermal aquifers that are rapidly replenished by meteoric water recharge via porous strata exposed on the basin margin. Our results argue for an alternative and expanded interpretation of these systems. Elevated geothermal gradients (with average of up to 40°C/km in the southern part of the basin and locally possibly up to 55°C/km) are likely associated with crustal thinning owing to the development of a pull-apart basin. Anomalously fresh water (<1 g/L) in the deep (up to 2850 m depth) Upper Cretaceous reservoir is charged laterally, predominantly by snowmelt waters from basin bounding mountains. Recharge includes both mountain-front recharge (MFR), where water infiltrates into outcrops of reservoir rock near the mountain fronts, and mountain-block recharge (MBR), characterized by deep groundwater flow through fractured, predominantly rhyolite basement rocks (as evidenced from their solutes in reservoir waters). The combination of elevated geothermal gradients, low salinity water chemistry, and excellent reservoir properties makes the studied

reservoir horizon an attractive target for geothermal development. Our results are applicable to other geothermal systems in strike-slip settings across Central Asia, and potentially worldwide.

KEYWORDS

geothermal energy, Zharkent Basin, hydrogeochemistry, pull apart basin, groundwater

1 Introduction

New alternative energy resources and methods for enhancing their efficiency are imperative to mitigating the growing dangers from climate change. The global strategy to reduce CO_2 emissions includes capture and sequestration of CO_2, alongside the development of cleaner energy production options. Geothermal energy production is recognized as a promising alternative source of clean energy, particularly in regions with elevated geothermal gradients, with growth of up to 150 GWe by 2050 predicted (Jolie et al., 2021).

Conventional geothermal resources are found in areas with active magmatism or in warm sedimentary basins (Dipippo, 2016; Jolie et al., 2021). The latter typically exhibit moderately high temperatures (~150°C–200°C) in basins with extensional or transtensional (i.e. pull apart basins) tectonic conditions, as observed in locations such as Salton Sea and Cerro Prietto in the Gulf of California, USA (Sutrisno et al., 2019). These geothermal fields commonly have highly permeable zones in porous sedimentary strata and/or natural fracture systems (Sutrisno et al., 2019), and they may manifest hot springs or fumaroles on the surface (Jolie et al., 2021). However, there are also blind geothermal resources that lack surface manifestations, such as in the Great Basin, western USA (Faulds et al., 2016).

The Zharkent (eastern Ily) Basin (Figure 1) is known for its natural hot springs, and hosts elevated geothermal gradients (up to 40°C/km; Jóhannesson et al., 2019). During petroleum exploration drilling in the 1950s (Filipyev, 1957; Filipyev and Rabkin, 1959) hot water (wellhead temperature ~96°C) was discovered from Upper Cretaceous reservoirs at depths of 2682–2730 m. Similarly, the same interval in a recently drilled well (5539; depth of ~2850 m; Figure 2A; Kalitov, 2016) produces 103°C hot water. The thickness of this highly permeable (up to eight Darcies) and productive water-bearing horizon ranges from ~30 to 50 m across the basin (Kalitov, 2016). Cretaceous strata mainly comprise conglomerate and sandstone interlayered with minor claystone and siltstone (Figure 2B), both interpreted as fluvial and shoreface deposits of an endorheic system (Dillinger, 2021). Conglomerates comprise extraformational pebbles and gravels bonded by clay-carbonate cement, whereas sandstone is quartz-rich, medium-to coarse-grained, and weakly cemented. The Mesozoic-Cenozoic section is thickest in the central and northeastern parts of the basin (Figure 3).

Based on observed geothermal shows and gradients, the Zharkent Basin is identified as a promising candidate for geothermal energy production (Boguslavsky et al., 1999; Jóhannesson et al., 2019). However, these authors have not documented the subsurface geological conditions adequately to develop a geothermal play-type model that explains the origin and magnitude of the thermal resource. Moreover, recent studies by Campbell et al. (2013), Mackenzie et al. (2018), Grützner et al. (2019), and Wu et al. (2021) reveal the existence of strike-slip faults that are not included in the existing basin models, despite their crucial control on geothermal resources (Sutrisno et al., 2019).

Tectonic and sedimentary features observed in basin bounding mountains and ridges (Figure 1) are linked to sedimentation in the adjacent basin (details in Section 2.1; Huang et al., 2018; Wang et al., 2006; Kober et al., 2013; Macaulay et al., 2014; Sobel et al., 2006; Burtman, 2012; Han et al., 2004; Verestek et al., 2018; Grützner et al., 2019; Frisch et al., 2019; Hellwig et al., 2017; Lucas et al., 2000; Voigt et al., 2017). However, geothermal development is hampered by a lack of constraint on tectonic processes occurring within the basin (beneath the present-day sedimentary cover; Figures 1–3) and their potential role in: i) forming and shaping accommodation for sediments; ii) controlling the increased geothermal gradients documented by various researchers e.g. Boguslavsky et al. (1999) and Jóhannesson et al. (2019); and iii) influencing fluid flow in the basin. Additionally, structural styles described in mountains and ridges (summarized in Section 2.1) are challenging to reconcile with generalized and widely accepted basin models generated from a correlation between sparcely drilled wells (Figure 3; Kalitov, 2016), and a need for developing more modern basin tectono-stratigraphic models that integrate a wider range of data types.

The present study integrates data from geochemical, geophysical, and stratigraphic sources to present an integrated tectono-stratigraphic model for the Upper Cretaceous Zharkent geothermal trend. We utilize new hydrogeochemistry and stable water isotope results from 18 samples taken from a range of localities across the basin to gain a better understanding of the Zharkent Basin geothermal system. Furthermore, numerous previously published subsurface temperature, water chemistry data, stratigraphy, geological cross-sections and maps, gravimetry surveys, as well as recent works on the regional structural setting, have been reprocessed. Data including temperature profiles, water chemistry, stable water isotopes, tectonic history, and stratigraphy were integrated to generate a comprehensive conceptual basin model for a sediment-hosted geothermal system.

2 Geological settings

2.1 Tectono-stratigraphic framework and basin evolution

The Zharkent Basin is bordered by the Kalkan, Katutau, and Dzhungarian Alatau mountains to the north; the Ketmen Ridge to the south; and transitions to the Almaty Basin to the west (Figure 1). To the east, it extends into China as the Yili Basin (Wang et al., 2006; Huang et al., 2018). The central part of the Zharkent Basin is mainly covered by Quaternary sediments, while older Cenozoic and Mesozoic sediments crop out along the basin's periphery (Figures 2A, 3). The sedimentary succession non-conformably overlies an extensive upper Paleozoic volcanic series characterized by an abundance of rhyolites

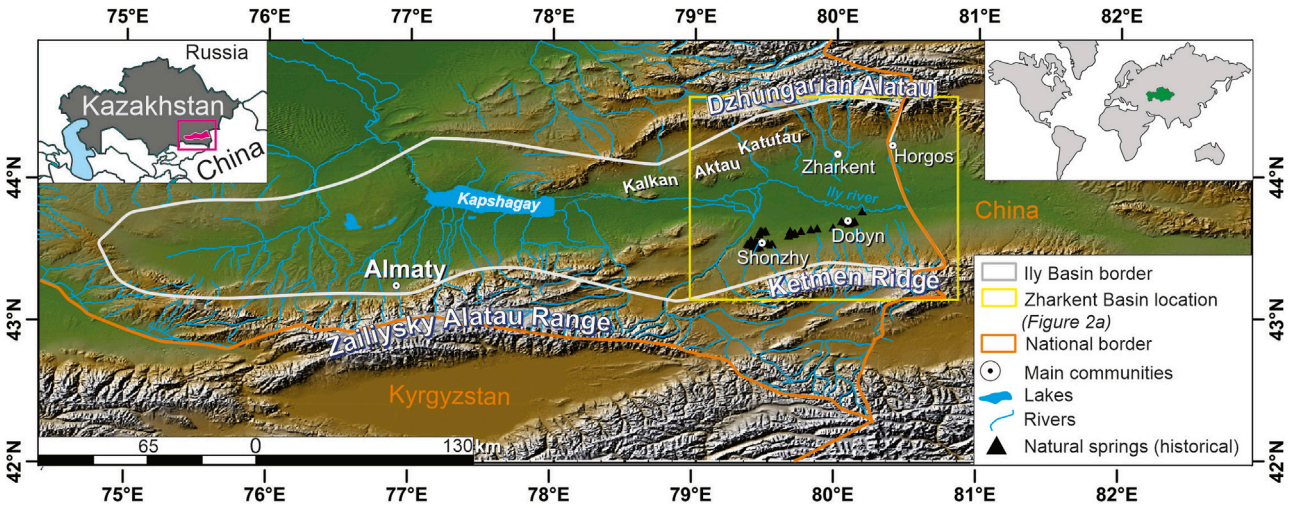

FIGURE 1
Ily Basin overview map made with GeoMapApp (www.geomapapp.org)/CC BY (Ryan et al., 2009) showing the main mountain ranges and ridges (grey colored high relief); intermountain depressions (brown and green), and drainage system. Juxtaposed are locations of main communities and natural thermal springs (historical) in the Zharkent area. Inset on the left-side shows the location of Ily Basin (magenta rectangular) within Kazakhstan, and the inset on the right-side shows the location of Kazakhstan on the world map. The yellow rectangle shows the location of Figure 2A.

(Mukhamedzhanov, 1989; Figure 2B). This volcanic series also largely constitutes the Dzhungarian Alatau Mountains and Ketmen Ridge on the northern and southern parts of the basin, respectively (Figure 2A).

Sedimentation in the Zharkent Basin commenced in the Middle Triassic in response to local subsidence and associated formation of an intermontane depression (Daukeev et al., 2002). Triassic to recent basin fill comprises sandstone, conglomerate, as well as lacustrine mudstones derived from locally sourced siliciclastics (Figure 2B). Extensional and/or strike-slip fault displacement in the Middle-Late Triassic, subsequent thermal subsidence and downward flexure, and a warm, humid climate in the Early Jurassic, triggered the accumulation of thick Lower Jurassic coals within otherwise clay-rich siliciclastic successions (Allen et al., 1991).

In the Late Jurassic, basin uplift associated with the development of the Ketmen Ridge (Figure 1) to the south led to local erosion of older Mesozoic deposits. Sedimentation resumed in the Early Cretaceous across much of the broader intermontane Ily Basin, including the Zharkent Basin, with sediments mostly sourced from the uplifted Ketmen Ridge to the south and the emerging Dzhungarian Alatau Mountains to the north (Figure 2B). Thermal history modeling and fission track analysis demonstrate a phase of uplift and erosion over the Chinese part of the Ketmen Ridge and Dzhungarian Alatau Mountains in the Late Cretaceous–early Paleogene time that likely affected deposition in the Ily Basin (Jolivet et al., 2010). This phase was followed by tectonic quiescence towards the middle of the Paleogene, and the Zharkent Basin became a peneplained intracratonic sag that filled with thick paleosol successions (Lucas et al., 1997).

From the Oligocene through the early Miocene, sedimentation was largely controlled by compression and left-lateral shear in response to the uplift of the Tien Shan Mountains to the south of the basin that was triggered by the collision between India and Asia (Sobel et al., 2006; Kober et al., 2013; Macaulay et al., 2014). Tectonic strain chiefly manifests as a succession of E-W-striking faults producing uplifts from basement-cored anticlines (Kober et al., 2013) and basin bounding thrust faults (flower structures), resulting in N-S shortening and basin closure in the middle-late Miocene (Han et al., 2004; Burtman, 2012; Verestek et al., 2018). Contemporaneous phases of extension in response to strike-slip displacement in a transfer zone also linked two slightly diverging thrusts in the Katutau region (Figure 1; Kober et al., 2013).

Continued NNW-directed compression led to folding, thrusting, and uplifting in the west-east oriented Kalkan and Aktau mountains from the late Miocene to the Pleistocene (Figure 1; Kober et al., 2013). More recently, Grützner et al. (2019) highlighted the importance of displacement on left-lateral strike-slip faults in the Ily basin-bounding mountain ranges, and right-lateral oblique thrust faults in the basin interior for accommodating regional N-S shortening and large-scale NE-SW shear. Throughout the Cenozoic, the central basin was filled with alluvial-lacustrine and fluvial deposits, and coarse alluvial-fan deposits and paleosols formed at the margins in dominantly hot and arid conditions (Lucas et al., 2000; Hellwig et al., 2017; Voigt et al., 2017; Frisch et al., 2019).

2.2 Hydrogeological background

The Zharkent Basin aquifers include Neogene, Paleogene, Cretaceous, Jurassic, and Triassic rocks (Figures 2A, 3; Kalitov, 2016); however, the geothermal water is thus far produced only from the Upper Cretaceous aquifer. Paleozoic formations mostly comprise porphyritic rhyolites (Figures 2A,B) (Akchulakov, 2012; Kalitov, 2016), and have been tested in some wells. Because of low flowrates (<0.3 L/s), Paleozoic rocks are considered non-productive (Table 1). Water data from both Jurassic and Triassic formations are highly variable both in terms of flow rates (from nil to about 55 L/s) and salinity (from <1 g/L to up to 15.2 g/L; Table 1; Kalitov, 2016). The tested Miocene and Pliocene formations also had low flowrates (<2 L/s).

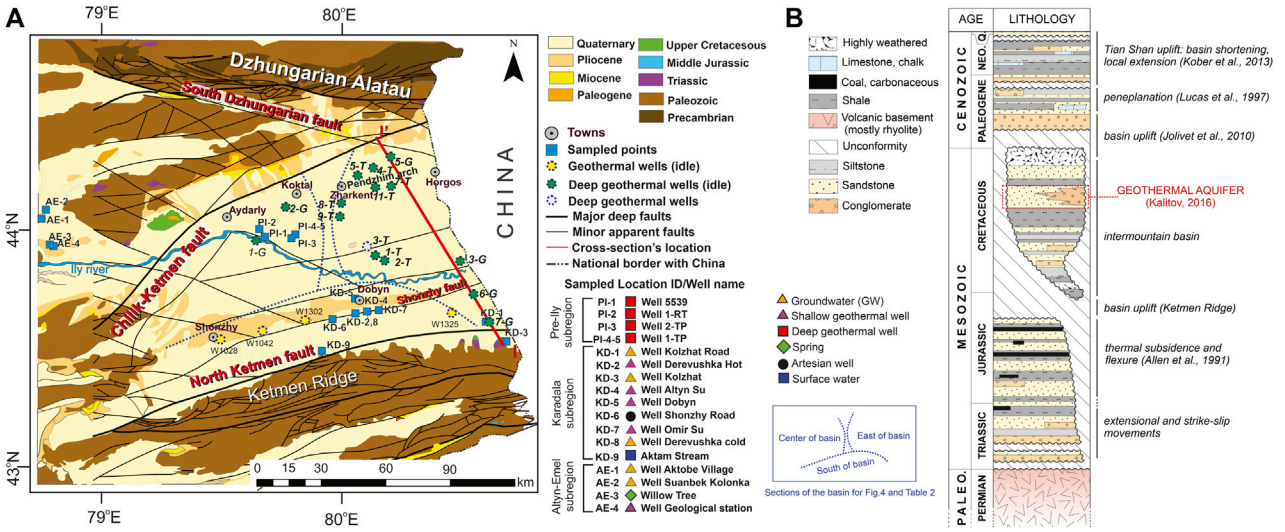

FIGURE 2
(A) Geological map of Zharkent Basin (digitized "Geological map of Kazakh SSR," 1979) with juxtaposed locations of geothermal wells, main towns, and major faults (Line I–I′ represents the cross-section depicted in Figure 3); Note: elongated Pliocene exposures between Shonzhy and Dobyn are attributed to inferred south-dipping reverse Shonzhy fault(s) (Grützner et al., 2019); **(B)** Simplified Permian-to-Quaternary litho-stratigraphy along with major tectonic phases. For thickness and depths please see Figure 3.

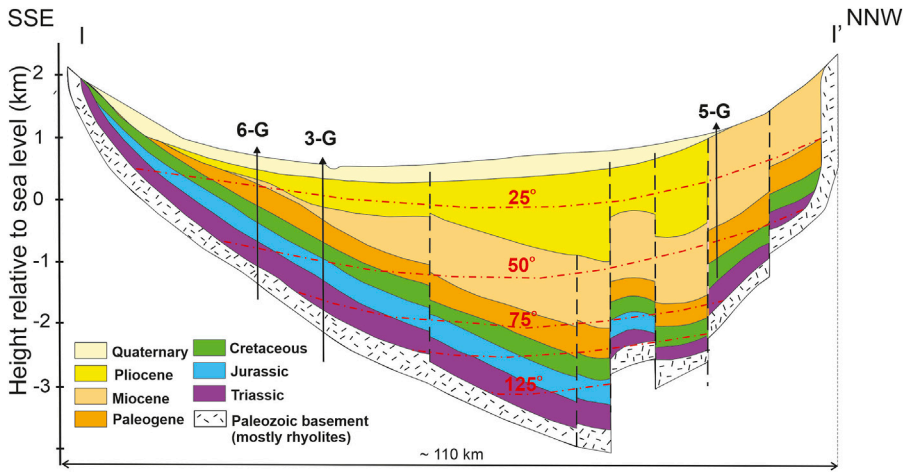

FIGURE 3
Geological cross-section I–I′ through the Zharkent Basin (please see location in Figure 2A) depicting the major stratigraphic subdivisions, inferred faults, and estimated isotherms (red dashed lines labeled 25°, 50°, 75°, 100°, and 125°C; modified after Kalitov et al., 2016). Note 1: The extent (preservation) of Triassic and Jurassic strata in other parts of the basin is limited, resulting in direct contact of Cretaceous and Cenozoic rocks with Paleozoic volcanics (Dillinger, 2021). Note 2: The shape of the basin resembles an intracratonic sag, (see Lucas et al., 1997). The limited number of faults expected in sag basins is in line with Middleton (1989); however, previous authors did not interpret faults in the context of modern plate tectonic terminology. Furthermore, locations of most faults in the basin are inferred to explain differences in depths and/or stratigraphic thicknesses between sparsely drilled well locations. The potential role of basin-bounding mountains (Figures 1, 2A) on basin formation and intra-basinal faults was also not considered in the inference of faults. This study attempts to address the above gaps.

Furthermore, their high Total Dissolved Solids (TDS) content (up to 22 g/L) makes them unfavorable for geothermal water production. Waters are produced from Paleogene aquifers at both low and highly varying flowrates (ranging from 6 L/s in the basin center to 0.01 L/s in the northern part of the basin), which implies that the Paleogene layers are either not extensive or that permeability decreases northward (Mukhamedzhanov, 1989).

Produced geothermal water is characterized by low TDS values (less than 1 g/L), initial natural flowrates of up to 75.2 L/s, and wellhead measured water temperature as high as 96°C–102°C (Kalitov, 2016). Geothermal water has a narrow range (0.3–0.9 g/L; Table 1) of salinity variation across the basin, but natural flowrates vary up to a factor of three, and no flow is reported from well testing for the wells located in the north part of the basin.

10.3389/feart.2023.1212064

TABLE 1 Summary of water properties (historical data after Kalitov, 2016)[a].

Data from well[a] #	TDS, g/L	Natural flowrate at the start of production, L/s	Sample depth, m	Water type
Miocene				
?	6–22	<0.1	?	Mixed Na + Cl dominated
Pliocene				
1-G	0.6–18.8	0.25–2.4	968–2070	Mixed Na + CO_3 + SO_4 dominated
Paleogene				
1-G	5	6.1	2475–2509	Mixed Na + Cl + SO_4 dominated
4-G	6.4	0.2	376–385	
7-T	15.9	0.01	2664–2670; 2685–2693	
Cretaceous				
1-G	0.9	46.3	2693–2732	Mixed Na + CO_3 + SO_4 dominated
3-G	0.26	60.2	1377–1448	
6-G	0.35	75.2	715–755; 745–765; 780–790	
3-T	0.33	30	2278–2344	
1-TP	0.5	50	2800–2900	
2-TP	0.5	22	2718–2790	
1-RT	0.6	24.5	2737–2817	
5539	0.8	54.5	2763–2793	
4-T	-	no inflow		
5-G	-	no inflow	2380	
Middle Jurassic				Mixed Na + SO_4 + Cl dominated
3-T	0.99	15	2292–2376	
1-T		20	2450–2550	
7-T		0.8	?	
Lower Jurassic				
3-T	2.45	17.4	2612–2670	
Upper Triassic				
6-G	low salinity	28.9	1273–1330	?
1-T	-	tested, but no flow	2670–2902	
3-T	-	tested, but no flow	2835–2995	
Lower Triassic				
2-T	15.2	1	2620–2830	?
3-G	?	55.6	2215–2275	
7-G	0.85	0.2	1132–1150	
Paleozoic				
3-G	8.45–8.53	0.03–0.34	2550–2790; 2815–2980	Mixed Na + Ca + Cl dominated
6-G	?	0.2	2268–2295; 2220–2252	
7-G	20.8	0.5	1208–1231	

[a]For lithology refer to Figure 2B.

3 Data and methods

3.1 Geothermal gradient calculations and mapping

Depth-temperature profiles were based on the temperature measurements collected directly from the geochemical sampling points as well as published temperature data (Table 2; Figure 2; Kalitov, 2016; Mukhamedzhanov, 1989). Water temperature was measured at a tap-off of the well with a portable thermometer. Inputs for calculating geothermal gradients included the measured water temperatures T_{bottom} (^oC), the depth of the screened production intervals $Depth\ (m)$, and average surface temperature of 12°C $T_{surface}$ (^oC) (Mukhamedzhanov, 1990). The gradients were estimated as approximate $\frac{T_{bottom}-T_{surf.}}{Depth}$ ($^oC/m$), which does not account for changes in lithology, and therefore presented as a min-max range in depth-temperature profiles. These calculated values and previously published geothermal gradients (Mukhamedzhanov, 1989) formed a database (Supplementary Table S1) that was used for generating a geothermal gradient distribution map across the basin. The Spline interpolation technique was selected as optimal for the present research to derive gently varying surfaces through the interpolation of the sparsely distributed geothermal gradient points. The technique is based on the mathematical function that minimizes overall surface curvature, contributing to the smoothness (continuous and differentiable) of the function and exact passing through the limited number of source points (Franke, 1982; Mitáš and Mitášová, 1988; ESRI, 2011) gridded with a 100 m cell size. The greater count of points leads to a smoother surface in the 2-D minimum curvature spline technique. The spline algorithm is based on the following equation for the surface interpolation (ESRI, 2011):

$$S(x,y) = T(x,y) + \sum_{j=1}^{N} \lambda_j R(r_j), \quad (1)$$

where j=1,2,.,N; N is the count of input points; λ_j represents the coefficients from the solution of linear equations; r_j is the distance from point (x,y) to the jth point; and T (x,y) and R(r) are defined as per the selected option. Moreover, to minimize extrapolation artifacts, the extent of the map is restricted to areas with reasonable well and data coverage. Generated isolines were then manually locally adjusted to account for known geologic features (i.e. the Shonzhy fault). The software-generated geothermal gradients' divisions remained unchanged but redistributed in the NEE direction along the Shonzhy fault (c.f. Mukhamedzhanov, 1989).

3.2 Hydrogeochemistry sampling and analysis

Water samples were collected during field campaigns in May-June 2021 and May-June 2022. The sampling period was constrained by weather conditions (cold and arid climate) and the associated accessibility of remote sites. The samples included water from well-heads of four deep (>2.5 km deep) geothermal wells (PI-1–4), five shallow (600–700 m deep) geothermal wells (AE-4, KD-2, KD-4, KD-5, and KD-7), four shallow (~200 m deep) groundwater wells (AE-1, AE-2, KD-1, KD-3, and KD-8), as well as one spring (AE-3) and one artesian warm well (KD-6) (Figure 2; Table 3). We also collected one streamwater sample (KD-9) in Karadala region (Table 3; Figure 2). All deep and shallow geothermal wells produce hot water from the Upper Cretaceous aquifer(s). The depth difference is because strata are tilted toward the basin axis (Figure 3). The samples PI-4 and PI-5 (collected in 2021 and 2022 respectively, Supplementary Table S2) are sourced from the same well (1-TP at 2830 m) depth. For easier spatial referencing, sample identification numbers (ID's) are assigned based on geographic sub-regions and distinguished in Table 3 as AE for Altyn-Emel sub-region, KD for Karadala sub-region, and PI for the deep geothermal in Pre-Ily region.

TABLE 2 Data on bottomhole temperatures vs. depths in Upper Cretaceous formations grouped in three main sections: South, Central, and East. For lithology, please refer to Figure 2B.

Section of the basin	Well	Temperature, °C	Depth, m
South basin	1028	28	367
	1042	28	475
	1302	29	467
	1046	42	540
	1325	22	443
Central basin	2-TP	84	2993
	1-TP	84	3013
	1-G	96	2800
	1-RT	98	2885
	5539	103	2850
East basin	6-G	32	746
	3-G	49	1379
	1-T	85	2888
	3-T	63	2410
	2-T	93	3073
	5-T	127	4031
	7-T	87	2750
	8-T	71.3	2750

All samples were collected in 250 mL HDPE bottles. The bottles were sealed with scotch tape or parafilm M (Bemis Company, USA, Part no. PM-992) to prevent evaporation. The pH and electrical conductivity (EC) were measured by a multiparameter benchtop meter (inoLab Multi 9310 IDS with conductivity cell and pH electrode). TDS was determined by measuring EC and multiplying by a coefficient (0.55 for low salinity samples and 0.64 for the brackish sample (after Hubert and Wolkersdorfer, 2015) (AE-4; Table 3). The conductivity over the sum of major ions method is used because of missing carbonates content data (not measured) in some of the samples. Before analysis, the samples were filtered using standard 0.45 µm PTFE syringe filters. The major cations (Ca, Mg, Na, K), trace elements (Fe, Al, Fi, Zn, Cu, Mn, B, Ba, Sn, Sr, Cd, Co, Ni, Sb, Se, As, Pb) and silicon (Si) analysis was performed on ICP-OES (Thermo Fisher Icap 6300 DUO) with the samples spiked with nitric acid beforehand (analytical grade). The anions (Cl, SO_4, and NO_3) were determined by ion chromatography (Dionex ICS 6000 and Metrohm 930 Compact IC Flex) at Nazarbayev University Core

TABLE 3 Water sample locations including measured temperatures. Note: cold water refers to temperature of 30°C and less.

Sample ID	Subregion	Location name	Source type/Depth, m	T, °C
AE-1	Altyn Emel	Aktobe village	Groundwater (GW)/~150–200 m	<30
AE-2		Suanbek Kolonka	Groundwater (GW)/no data	<30
AE-3		Willow Tree	Spring	no data
AE-4		Geological station	Shallow geothermal well/no data	<30
KD-1	Karadala	Kolzhat Road	Groundwater (GW)	<30
KD-2		Derevushka (hot)	Shallow geothermal well/~650 m	47
KD-3		Kolzhat	Groundwater (GW)	no data
KD-4		Altyn Su	Shallow geothermal well/~650 m	47
KD-5		Dobyn	Shallow geothermal well/~650 m	42
KD-6		Shonzhy Road	Artesian warm well	no data
KD-7		Omir su	Shallow geothermal well/~650 m	39
KD-8		Derevushka cold	Groundwater (GW)/~150–200 m	<30
KD-9		Aktam Stream	Surface water	no data
PI-1	Pre-Ily	5539	Deep geothermal well/2850 m	103
PI-2		1-RT	Deep geothermal well/2885 m	90
PI-3		2-TP	Deep geothermal well/2953 m	87
PI-4		1-TP	Deep geothermal well/2830 m	89
PI-5		Keremagash 1-TP	Deep geothermal well/2830 m	~89

Facilities. The bicarbonate ions (HCO3) were measured by titration with hydrochloric acid 0.1 mol/L with methyl red/bromcresol and phenolphthalein indicators (ISO 9963–1:1994) by a third-party laboratory. The sum of (major) ions was calculated by summing concentrations of Ca, Mg, Na, K, HCO_3, Cl, SO_4, and NO_3 ions. In case of the absence of EC measurements, the sum of ions was also used as a TDS estimate. Silicon measurements were converted to SiO_2 by dividing the concentration Si by 0.4674. Piper and mixing diagrams are constructed in Geochemist Workbench Community Edition (version 16). The trace-element compositions are presented in Supplementary Table S2.

Stable water isotope analyses were conducted on a Liquid Water Isotope analyzer (Los Gatos Research, model IWA-912) at Nazarbayev University. The samples were normalized to Vienna Standard Mean Ocean Water (VSMOW2) and Standard Light Antarctic Precipitation (SLAP2) scales, and are reported in parts per thousand (‰ or permille) (Kendall and Doctor, 2003). The analysis was conducted with two to three replicate runs to obtain reproducible results with seven measured injections using primary and secondary standards with bracketing normalization. Measurement uncertainties are ≤±0.8‰ for δ^2H and ± 0.2‰ for $\delta^{18}O$. We also calculated the deuterium-excess:

$$d - excess = \delta^2H - 8\delta^{18}O \quad (2)$$

Additionally, monthly stable water isotope data for precipitation were downloaded from waterisotopes.org (Bowen, 2022) for Ketmen Ridge (latitude 43.3109°, longitude 80.0983°, altitude 2000 m) and Dzhungar Alatau (latitude 44.5531°, longitude 79.9013°, altitude 2000 m) to distinguish the relative contribution of cold (October to March) vs. warm (April to September) seasonal precipitation to recharge. The mean values for both oxygen and hydrogen of arithmetic averages for cold and warm seasons were used for both mountain ranges.

4 Results and interpretation

4.1 Depth-temperature profiles (geothermal gradients) and map

4.1.1 Results

Geothermal gradients are in the range of 21.1°C–30.3°C/km (East of basin), 25.1°C–32.9°C/km (Center of basin), and 27.3°C–53.5°C/km (South of basin) (Figure 4). The geothermal gradient distribution is also highly variable locally across the basin with a strong positive anomaly (40°C–60°C/km) near the towns of Dobyn and Shonzhy (Figure 5). The geothermal gradients are moderately elevated (~29.8°C/km) in the central part of the basin where wells are currently producing geothermal waters for balneology purposes at sanatorium Keremagash (well 1-TP), and greenhouse and fish-farming (wells 5539, 1-RT, 2-TP; Figures 2, 5). Data from wells 3-G and 6-G support slightly lower geothermal gradients in the eastern part of the basin is indicated by.

4.1.2 Interpretation

The observed variations in geothermal gradient (Figures 4, 5) are consistent with abrupt variations in crustal thickness and/or localized vertical flow of heated water along faults and fracture systems. Prior interpretations alternatively did not capture this high

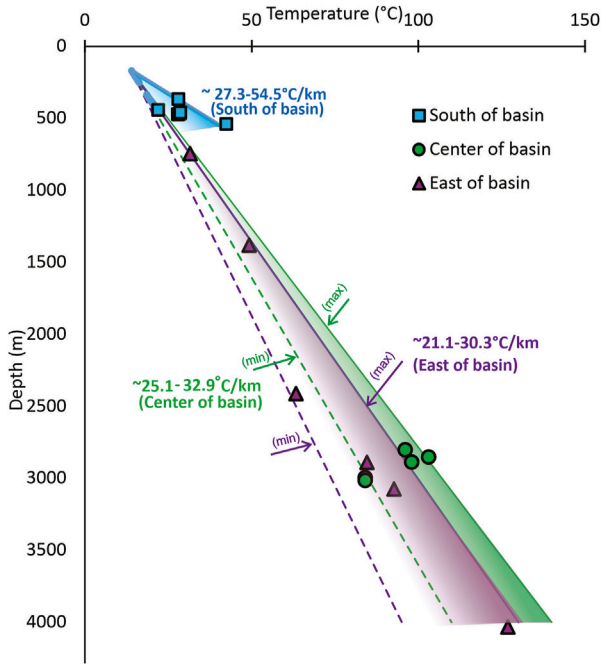

FIGURE 4
Average depth-temperature profiles and geothermal gradients of the South, Central, and East parts of the Zharkent Basin (Table 2; Figure 2A), calculated based on data from 18 wells shown in Figure 2A.

variability, and argued for linear alike depth-temperature gradients within a relatively uniform intracratonic sag basin (Figure 3). Potential evidence for this variability includes temperature anomalies along the Shonzhy fault trend between the towns of Shonzhy and Dobyn (Figure 5). The displacement geometry of the Shonzhy fault (Figure 3) is debatable. Most maps show it as a normal fault with the formation of an inferred graben on the South side (Figures 2, 3). However, Grützner et al. (2019) have classified the Shonzhy as an active south-dipping reverse fault characterized by about 20 m of recent vertical displacement, and an unknown amount of lateral displacement (Figure 9C in Grützner et al., 2019). The overall context of Grützner et al. (2019) thrust and strike-slip faults in the Ily Basin, argues the term "south dipping reverse fault", and imply the fault is a part of a steeply dipping flower structured thrust fault system, where some faults are reactivated as reverse faults by compression. Yet another possibility is that the Shonzhy fault is a more discrete strike-slip fault oriented parallel to those documented in the mountains to the south and the north (Figure 2). Its location >20 km north of the North Ketmen Fault (Figure 2), and thick sedimentary cover south of it (Grützner et al., 2019), suggests possible subsidence caused by strike-slip transtentional forces, genetically related to transpression that contributed to flanking mountains, which would also result in an array of en echelon faults and together create a network of grabens, step overs, and/or relay ramps that formed pull-apart depressions (Faulds and Hinz, 2015).

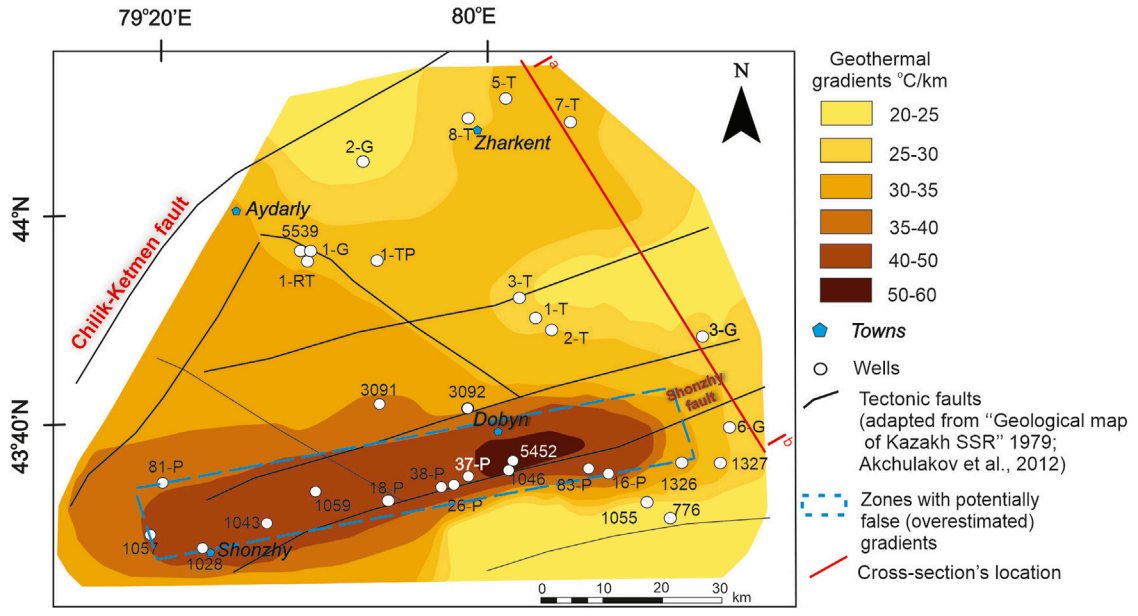

FIGURE 5
Geothermal gradient distribution with juxtaposed locations of main communities, geothermal wells and major faults. Cross-section I^a-I^b (a part of I-I′ in Figure 2A) is generated based on the data summarized in Supplementary Table S1. To minimize extrapolation artifacts, the extent of the map is restricted to areas with reasonable well and data coverage. Generated isolines were then manually adjusted locally to account for known geologic features (i.e. the Shonzhy fault). The software-generated geothermal gradient divisions remained unchanged but redistributed in NEE direction along the Shonzhy fault (c.f. Mukhamedzhanov, 1989). Note: Rectangle (blue dashed lines) indicates the area with high temperature anomaly of enigmatic origin. Scenarios proposed in this study include: i) localized gradient anomolies crustal thinning underneath a poorly defined tectonic block or structural element such as step over or relay ramp; and/or ii) false temperature gradients caused by upward flow of hot water, along faults and/or fractures, from deeper seated aquifers.

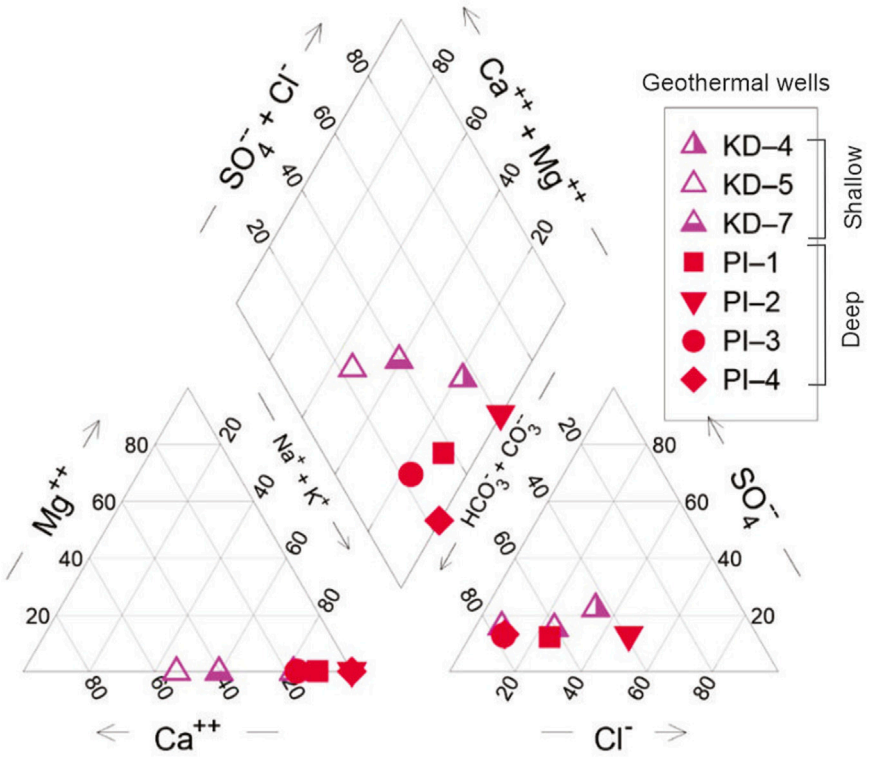

FIGURE 6
Piper diagram showing measured anion-cation ratios in samples collected from geothermal wells (Tables 3 and 4; Figure 2). Note: The data is limited to only seven samples out of 18, due to missing HCO_3 and/or below detection limit of Mg data in remaining samples.

The proximity of the temperature anomaly to the Shonzy fault (Figure 5) argues for a genetic relationship between the two. Potential scenarios include:

i) The normal-fault scenario inferred from Kalitov 2016 (Figure 3) implies extensional stresses generating a graben or similar depression from crustal stretching, which further implies local crustal thinning. This would force higher temperature gradients beneath the tectonically stretched block (graben). Similarly, a pull-apart depression caused by transtensional forces would cause similar crustal thinning and an analogous temperature anomaly.
ii) The flower structure scenario implies that the Pliocene exposure north of the Shonzhy fault (characterized by the absence of Quaternary sediments due to erosion or depositional hiatus (Figure 2A), is a thrust sheet which is uplifted more than the overlying thrust sheet south of the Shonzhy fault. In this context, the depressed tectonic block south of the Shonzhy fault is a localized piggyback basin. This scenario does not produce crustal thinning and thus cannot account directly for increased temperature gradient (Figures 4, 5). Increased temperature gradients instead would reflect localized and preferential fluid movement along this fault-fracture system.

Either of the above scenarios implies extensive networks of faulting and fracturing which would promote upward migration of deeper sourced hot water and its potential accumulation in highly permeable Upper Cretaceous strata in the Shonzhy-Dobyn area. This would imply that although temperature measurements are correct, the anomaly shown on the map (Figure 5) does not represent the actual gradient and is overestimated. Additional structural information coupled with geothermometry (*sensu* Ferguson et al., 2009) is needed to prove or rule out this scenario. Similar water chemistry of Upper Cretaceous aquifers across the basin argues against challenges to the mixing of their waters with deeper sourced brines, the evidence of thermal springs along the fault line (Figure 1) suggests that the Shonzhy fault(s) might be at least locally open to the surface. Importantly, the localized nature of Shonzhy–Dobyn anomaly suggests the potential presence of more, still undiscovered anomalies in the basin. Section 5.1 provides a detailed review and supporting evidence for intra-basinal strike-slip tectonic setting including the formation of a transtentional pull-apart basin and associated crustal thinning, faults, and fractures.

4.2 Hydrogeochemistry and stable water isotopes

Chemical and stable water isotope analyses (n=18) include samples from shallow groundwater (n=5), a natural spring (n=1), an artesian well (n=1), surface water (n=1), geothermal wells (with depth down to 650 m, n=5), and deep geothermal wells (with the depth of about 2800–3000 m, n=5) (Figures 6–8 and Tables 3, 4; see also Supplementary Table S2 for the trace elements concentrations). All waters collected from deep and shallow geothermal wells (Table 3) sample the Upper Cretaceous

TABLE 4 The results of chemical and stable water isotope analyses.

Sample ID	$\delta^{18}O$, ‰	$\delta^{2}H$, ‰	d-excess, ‰	pH	EC, µS/cm	TDS, mg/L	∑ions, mg/L	Ca	Mg	Na	K	HCO_3	Cl	SO_4	NO_3	Si	SiO_2
								ppm [mg/l]									
AE-1	-12.91	-90.56	12.74	n/a[a]	590	325	219	69.3	13.6	43.4	1.2	n/a[a]	21.5	65.2	4.9	0.5	1.0
AE-2	-13.81	-99.00	11.50	n/a[a]	765	421	368	54.0	5.5	99.0	0.9	n/a[a]	49.3	155.5	3.8	0.0	0.0
AE-3	-13.04	-91.06	13.22	n/a[a]	543	299	238	72.7	14.8	38.6	1.4	n/a[a]	28.2	69.2	13.4	6.1	13.0
AE-4	-14.03	-105.62	6.58	n/a[a]	7080	4531	4519	95.4	10.0	1485.0	10.1	n/a[a]	1197.5	1721.2	0.0	5.7	12.2
KD-1	-13.86	-102.09	8.83	n/a[a]	1107	609	532	85.9	21.4	124.0	4.2	n/a[a]	77.9	216.0	2.9	5.3	11.3
KD-2	-14.44	-104.85	10.66	n/a[a]	1532	843	710	15.7	1.7	300.9	4.0	n/a[a]	208.9	177.5	1.1	9.8	20.9
KD-3	-12.49	-86.45	13.49	n/a[a]	623	343	270	67.8	11.7	56.1	1.3	n/a[a]	10.8	115.1	6.7	5.1	10.8
KD-4	-14.09	-100.87	11.84	7.2	n/a[a]	n/a[a]	1503	70.0	bdl[b]	365.1	9.7	573.4	252.9	228.6	3.2	n/a[a]	n/a[a]
KD-5	-13.5	-102.4	5.60	n/a[a]	n/a[a]	n/a[a]	719	73.2	bdl[b]	71.9	3.1	463.6	28.8	76.2	2.6	n/a[a]	n/a[a]
KD-6	-14.07	-98.44	14.15	n/a[a]	572	315	238	10.1	1.0	113.7	1.3	n/a[a]	52.7	56.5	2.2	8.2	17.4
KD-7	-13.3	-100.6	5.80	7.55	n/a[a]	n/a[a]	888	75.1	bdl[b]	125.1	3.9	475.8	111.8	94.9	1.1	n/a[a]	n/a[a]
KD-8	-13.50	-94.49	13.55	n/a[a]	873	480	404	47.6	7.5	129.4	2.0	n/a[a]	66.3	147.4	4.2	6.4	13.8
KD-9	-11.93	-82.96	12.47	n/a[a]	545	300	185	67.0	14.5	30.5	2.5	n/a[a]	9.2	56.0	5.7	5.2	11.2
PI-1	-14.3	-108.7	5.70	8.19	n/a[a]	n/a[a]	1165	27.8	bdl[b]	269.3	7.0	622.2	140.7	92.6	5.4	n/a[a]	n/a[a]
PI-2	-13.8	-107.6	2.80	8.12	n/a[a]	n/a[a]	1190	bdl[b]	bdl[b]	387.7	6.2	402.6	288.6	102.6	2.5	n/a[a]	n/a[a]
PI-3	-13	-103.8	0.20	8.56	n/a[a]	n/a[a]	1006	32.2	bdl[b]	177.4	11.1	646.6	50.1	83.6	5.4	n/a[a]	n/a[a]
PI-4	-14.6	-110.7	6.10	8.15	n/a[a]	n/a[a]	835[c]	bdl[b]	bdl[b]	159.5	4.5	549	43.3	73.9	4.5	n/a[a]	n/a[a]
PI-5	-14.46	-104.21	11.48	n/a[a]	640	352	256[c]	0.4	0.0	146.0	1.7	n/a[a]	37.9	65.3	4.9	25.5	54.6

[a]n/a is missing data (some major ions were not measured due to delay in collection and analysis (bicarbonates) and the absent portable meters (pH, TDS) at the time of sampling.
[b]bdl is below the detection limit. The detection limit for individual major ions and silica is 0.1 mg/L. The trace elements detection limit is 10 µg/L.
[c]A large difference between the samples of similar origin (PI-4, and PI-5) is due to missing measurement similar to *.

10.3389/feart.2023.1212064

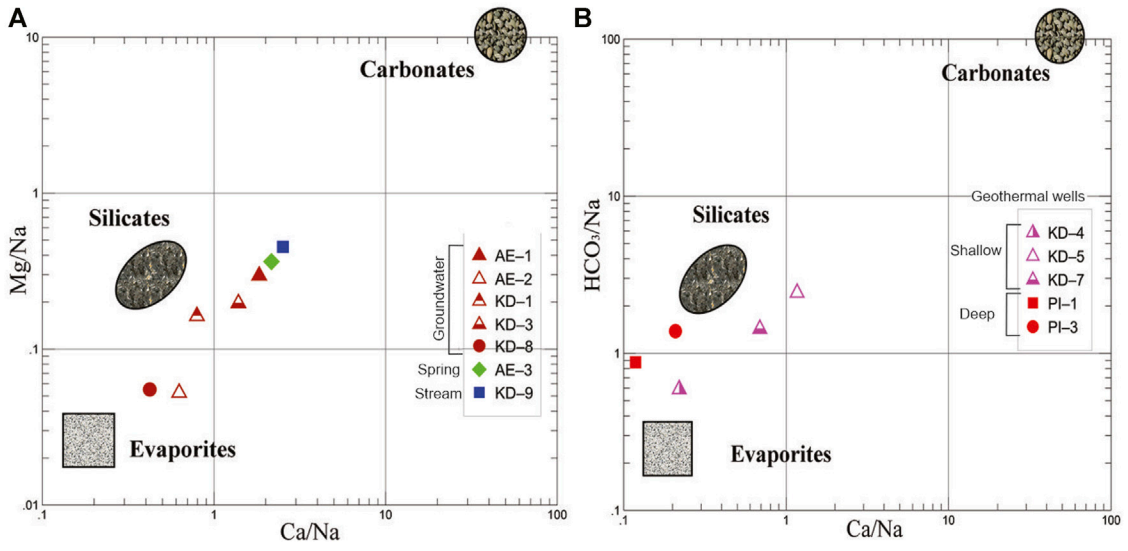

FIGURE 7
Mixing diagrams of Na-normalized log-scaled molar ratios **(A)** Ca/Na versus Mg/Na for stream water, a spring, and shallow GW wells, **(B)** Ca/Na versus HCO_3/Na for sampled deep and shallow geothermal wells (Upper Cretaceous Aquifer). The color code for deep and shallow geothermal as well as shallow groundwater samples is the same as in Figure 8. The end members of carbonates, silicate and evaporate are from Gaillardet et al. (1999). The values are in mmol/L. The diagrams are limited to the samples with a full suite of measured available anions and cations (ratios).

aquifer only, while samples from groundwater wells and Willow Tree spring (AE-3) are from undefined shallower Cenozoic strata.

4.2.1 Hydrogeochemistry

4.2.1.1 Results

The sum of major ions ranges from 185 to 4519 mg/L (average 847 mg/L) showing an overall low dissolved solids content (generally <1 g/L, Table 4). The highest TDS value (4531 mg/L) was measured in the warm geothermal well in Altyn Emel Park (AE-4, Table 4). Chemical analysis shows formation waters from deep geothermal wells (PI-1, PI-3, PI-4) predominantly belong to Na-HCO_3 type and water from shallow geothermal wells (KD-5 and KD-7) primarily belong to Ca-Na-HCO_3 type. A shallow (KD-4) and a deep (PI-2; well 1-RT) sample are characterized by Na-Cl type water (Figure 6; Table 2), with sum of ions of 1.5 and 1.2 g/L, respectively. Overall, the order of dominance (for absolute concentrations) for all samples for anions is HCO_3 > Cl ≥SO_4, and for cations is Na > Ca >> Mg >> K (Table 4). SiO_2 concentrations range from 1 to 54.6 mg/L (Table 4) and are the highest in the deep geothermal well (sample PI-5; well 1-TP), which is also characterized by low salinity (circa 300 mg/L without HCO_3). Sample PI-4 (well 1-TP) was sourced from the same depth interval (2830 m) 1 year apart, and has TDS of about 800 mg/L. PI-4 has a similar major ion speciation as PI-5 (Table 4), but silica was not measured in this sample.

4.2.1.2 Interpretation

The mixing diagrams of Na-normalized ratios of dissolved Ca, Mg, and HCO_3 (Figure 7) show evidence of water-rock interaction. The natural spring (AE-3), the stream water (KD-9), several shallow groundwater wells (AE-1, KD-1, KD-3), and shallow geothermal wells (KD-5, KD-7) are characterized by Ca/Na ratios ranging from 0.69 to 1.83, pointing to silicates as the main source of dissolved ions in waters with salinity <1 g/L (Figure 7; Table 4). In contrast, two shallow groundwater wells (AE-2, KD-8), a shallow geothermal (KD-4) and a deep geothermal well 5539 (sample PI-1) have Ca/Na ratios ranging from 0.12 to 0.63 (Figure 7), which is close to the evaporate end member. Depleted Ca, Mg, and HCO_3 relative to Na (Figure 7) in samples KD-4 and PI-2 (well 1-RT) are indicative of chemistry influenced by evaporite dissolution. This is corroborated by very low Mg content (<10 mg/L) in all analyzed shallow and deep geothermal wells (Table 4) compared to groundwater samples which consistently contain >10 mg/L of Mg. These magnesium ranges suggest that shallow groundwaters (AE-2, KD-8) are likely affected by evapo-concentration sourced from the surface, while deeper geothermal wells (KD-4, PI-1) derive salts most likely from the dissolution of secondary evaporites buried in the overlaying Cenozoic formations of Zharkent depression (*sensu* Hellwig et al., 2017).

The main dissolved silicate mineral is probably sodium feldspar (albite, $NaAlSi_3O_8$), which is present both in the mountain block (rhyolites) and rock fragments included in sandstone of the Upper Cretaceous aquifer (unpublished BSc report, Umralin, 2022). The anomalously high concentration of silica in a deep well (sample PI-5/well 1-TP) strongly suggests interdependence of burial temperatures and enhanced silica dissolution in the deep subsurface.

Two geothermal wells (AE-4, PI-5) and a warm artesian well (KD-6; Supplementary Table S2) have elevated (exceeding World Health Organization (WHO) threshold of 10 μg/L) concentrations of arsenic (As), with the highest recorded level of almost 60 μg/L (well TP-1, sample PI-5; Supplementary Table S2). Three shallow groundwater wells (AE-2, KD-1, KD-3), the stream water (KD-9), and a deep geothermal well sample have Pb concentrations over 10 μg/L (WHO threshold). Further interpretation of these findings within the drinking water standards is beyond the scope of this

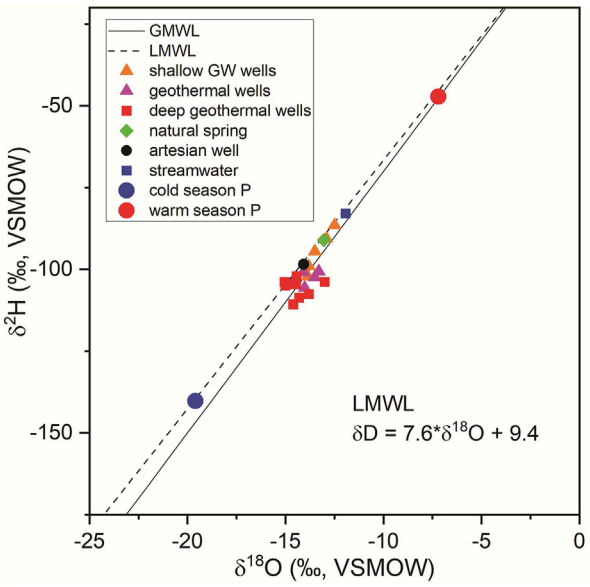

FIGURE 8
The cross plot of oxygen-hydrogen stable isotope results (in ‰ VSMOW) of all water samples collected in the Zharkent Basin (shallow groundwater wells, geothermal wells, natural spring, artesian well, streamwater; Table 3). The Global Meteoric Water Line (GMWL, black line) from Craig (1961) was chosen over the more recent one by Rozanski et al. (1993) as it is more general and less linked to specific locations of the world. The Local Meteoric Water Line (LMWL; dashed black line) for Central Asia $\delta^2H = 7.6\delta^{18}O+9.4$ is based on Saidaliyeva et al. (2021). The cold season (blue point, 140.25‰ for δ^2H and 19.6‰ for $\delta^{18}O$) and warm season (red point, 47.2‰ for δ^2H and 7.2‰ for $\delta^{18}O$) are based on data from Bowen et al. (2005), see section 3.2.

study; however, these should be carefully considered in future studies and are therefore included informationally in the Supplemental Material (Supplementary Table S2).

4.2.2 Stable water isotopes

4.2.2.1 Results

The mean values of stable water isotopes of all samples are -99.9‰ ± 7.61‰ for δ^2H and -13.7‰ ± 0.76‰ for $\delta^{18}O$ (Figure 8; Table 4). The mean *d-excess* is 9.52‰ ± 4.21‰, which is close to that of global precipitation (10‰) and almost identical to the reported intercept of the Local Meteoric Water Line (LMWL of 9.4‰; Figure 8). The deep geothermal wells (n=6) have lower isotope values of -106.56‰ ± 2.85‰ δ^2H and 14.17‰ ± 0.67‰ for $\delta^{18}O$ compared to the other water sources (Figure 8; Table 4). The isotope composition of shallower geothermal water (n=5) is -102.87‰ ± 2.28‰ for δ^2H and -13.87‰ ± 0.46‰ for $\delta^{18}O$. The surface water sample has values of δ^2H = -82.96‰, $\delta^{18}O$ = -11.94‰ (Figure 8; Table 4). The shallow groundwater samples (n=6) are slightly more enriched than geothermal water samples for δ^2H (-94.52‰ ± 6.29‰) and for $\delta^{18}O$ (-13.32‰ ± 0.6‰), and are characterized by a higher variability for deuterium (Figure 8).

4.2.2.2 Interpretation

The predominance of negative water stable isotope data (Figure 8) indicates that the geothermal water is largely a mixture of mountain snow and/or glacial ice melt (based on precipitation data from Saidaliyeva et al., 2021; Figure 8).

5 Discussion

5.1 Source of heat

5.1.1 The origin of geothermal waters in zharkent basin—a critical review

The data presented in this study challenge and improve prior interpretations for the origin of geothermal gradients and waters in the Zharkent basin because of added observations, some of which include:

i) Historically, the occurrence of geothermal waters in the Zharkent Basin are interpreted to be associated with the basin-scale increased geothermal gradients (Boguslavsky et al., 1999; Jóhannesson et al., 2019) and/or upflow along interconnected fault systems (Mukhamedzhanov, 1989; Kalitov, 2016). However, the source of heat and the plate-tectonic drivers of basin growth, faults, and fluid flow patterns remain speculative.
ii) The distribution of geothermal gradients is believed to be symmetric and highly predictable across the basin (i.e. curvi-linear isotherms; Figure 3) with the highest temperatures in the central part of the basin (Figure 3). The literature does not provide explanations.
iii) The actual surface evidence of faults within the basin is very limited as they appear blind, and are most likely covered by Quaternary sediments (Figure 2). The presence of currently mapped faults is mostly inferred from subsurface data to explain abrupt changes in depths of stratigraphic units and/or stratigraphic thicknesses between sparsely drilled well locations (Figure 3). Furthermore, all faults are graphically presented as normal faults inferring extensional setting, but neither modern plate tectonic terminology nor integration with recent structural studies in basin bounding ranges and ridges (Jolivet et al., 2010; Kober et al., 2013; Grützner et al., 2019; Jia et al., 2020) was integrated into this interpretation.
iv) Vertical fluid flow (Mukhamedzhanov, 1989; Kalitov, 2016) is interpreted based on the linear occurrence of natural thermal springs close to and parallel to the interpreted Shonzhy fault (Figure 1), and the linear shape of closely spaced geothermal wells along the main highway, which uncoinsidentaly runs parallel to the fault as well (Figure 2).

Below we provide and discuss alternative interpretations for the source of heat and water in the context of presented results, recent literature, and modern tectonic principles.

5.1.2 Refined basin tectonics, accommodation space, and crustal thinning

Recent interpretations of the tectonic history of south-eastern Kazakhstan suggest that the area is in a structural domain dominated by compression and right-lateral shear which is still active today (Kober et al., 2013; Grützner et al., 2019). These

processes result in simultaneous mountain building South and North of the Yili basin (eastern extension of the Ily basin in China, Figures 1, 2), and the formation of basinal accommodation for sediments between mountain chains. The post- Late Cretaceous depositional tectonic history summarized below suggests that accommodation for sediments is by basin subsidence, most likely provided by transtentional forces ("Cenozoic phase of east–west extension"; Kober et al., 2013) and formation of a localized pull-apart basin.

Prior thermochronology and tectonostratigraphic studies indicate five stages of Late Cretaceous and Cenozoic tectonic activity in the Ily Basin area (Han et al., 2004; Burtman, 2012; Jia et al., 2020) that significantly shaped the basin. These serve as a foundation for additional interpretations and include:

i) Late Cretaceous-early Paleocene: rapid and localized uplift of the Narat and Borohoro ranges, i.e. the Chinese extensions of the Ketmen Ridge and Dzhungarian Alatau, respectively. Compressional movements reactivated preexisting basin-bounding, south-dipping thrust faults, and were driven by far-field deformation of the Central Asian lithosphere (Jolivet et al., 2010; Jia et al., 2020).
ii) Late Eocene-Oligocene: the northern part of the Zharkent Basin started to uplift due to E-W low magnitude extension and N-S shortening (Kober et al., 2013), which initiated subsidence of a basinal depocenter south of the Pendzhim arch within coordinates 44°–44°15′ N and 80°–80°15′ E (Hellwig et al., 2018).
iii) Miocene: the main north and south Paleozoic strike-slip (Altyn-Emel, Southern Dzhungarian) and mega-flower-structure-related thrust (Ketmen, Shonzhy) faults (Figure 9), which define the natural boundaries of the Zharkent depression, reactivated and led to the further deepening of the basin (Grützner et al., 2019).
iv) Late Pliocene - early Pleistocene: the highest tectonic activity including extensive N-S shortening, which led to a significant uplift in the E-W thrust faults (Grützner et al., 2019).
v) Middle Pleistocene to present: characterized by a continued N-S-directed shortening trend, but at a slower pace compared to the early Pleistocene (Han et al., 2004).

The North Tian Shan orogen trends toward pure-shear crustal shortening, which is absorbed by N-S thrust faults and N-W and N-E sinistral and dextral strike-slip faults (Wu et al., 2021). Moreover, the Zharkent Basin is simultaneously subject to overall N-S shortening and E-W extension (Grützner et al., 2019). Ongoing shear strain is expressed by numerous examples of surface expressions including dextral (Figure 1 in Grützner et al., 2019) and sinistral movements (Figures 5, 6, 9C in Grützner et al., 2019) as well as up to 500 m long, sinistral offset of streams observed on satellite images along the northern flanks of Ketmen Ridge (Figures 1, 2), between Nazgur Cavern (43°28′54.0″ N and 80°15′89.0″ E) and Sukam Village (43°29′12.10″ N and 80°10′48.52″ E) and elsewhere on the flanks of the basin. Intensive shearing observed in basin bounding ranges and ridges extends into neighboring intermontane basins in the North Tien Shan (e.g. E-W elongated depressions in Kyrgyzstan and China; Figure 1), that are defined by E-W-striking flower structures and associated thrust faults trending parallel to the mountain fronts (Kober et al., 2013; Cording et al., 2014; Grützner et al., 2019).

Simple-shear 'bookshelf' faulting expresses in the area between the Junggar Basin and the Kazakh Platform, within the area of geothermal interest. The clockwise rotation of the Tarim Basin relative to the stable Kazakh Plate caused a regional N-S shortening that decreases from west to east (Grützner et al., 2019). This is reflected by the left-lateral slip rate from 6.2 ± 1.8 mm/yr range in the Ili Basin to no more than 2.0 mm/yr in the Southern Dzhungarian Alatau fault (Yu et al., 2021).

We note that although thrust faults have locally formed minor (<1 km wide) micro-foreland basins (e.g. Charyn Canyon; Kober et al., 2013; their Figure 11), the geological maps (Figure 2), cross-sections (Figure 3; Kalitov, 2016), gravimetry survey (Gravimetric map of the USSR, 1971), and our field observations show a larger superimposed trend for all exposed sedimentary strata dipping towards the basin center. This implies that flower structure thrust faults illustrated by Jolivet et al. (2010) and Jia et al. (2020) are at most secondary elements in generating the accommodation for an up to 3 km thick Cenozoic sediment pile accumulated between opposing Dzhungarian Alatau and Ketmen ridge thrusts (Figures 1–3, 11). Additionally, the basin is progressively deepening towards its center, which contradicts the generation of a foreland basin by peripheral thrust loading, whereby a wedge-shaped basin geometry is expected with the thickest sediments near basin-marginal thrust loads (Figure 3). The intracratonic sag basin (Lucas et al., 1997) implies no genetic relationship with high basin bounding mountain (Figures 2, 3) which seems very unlikely. Thus, the co-occurrence of a major depocenter in the basin center between the bounding mountain belts (Figures 2, 3), but still far away from the influence of flanking flower structures, requires an alternative interpretation that favors common cause, but not cause and effect between these two structural trends.

The main strike-slip, thrust, and other undifferentiated faults overlain on a gravity map (Figure 9) show a correlation of trends. The NE-oriented gravity anomaly isolines align with the orientation of the strike-slip faults, implying that the faults play a role in the formation of the transtensional Zharkent Basin, which provided accommodation space for sediments. Crustal thinning can be inferred from large negative gravity anomalies (Figure 9), induced by the attenuation of cooler dense crust and the introduction of a hotter mantle near the surface that heated the plate and the sedimentary cover. Negative anomalies are consistent with the advent of transtensional structural trends observed and inferred within the basin. The major strike-slip faults and associated mega-flower structures are traced on the surface along the edges of Zharkent Basin (Figure 9; Grützner et al., 2019). However, most likely, there is a significant number of local strike-slip and associated en-echelon faults of Cenozoic age, which are covered by Quaternary deposits (Figure 2) and are typically difficult to localize in the subsurface (Muraoka et al., 2010).

We propose that the Zharkent Basin is regionally a transtensional pull-apart basin filled by up to 3 km of sediments (Figures 3, 9) This is consistent with substantial evidence of shallower basement and transpressional movements in Ily Basin bounding ranges that took place throughout the Cenozoic (Kober et al., 2013; Grützner et al., 2019) as additional components of this regional shearing trend. We further suggest that the proposed tectonic attenuation has significantly contributed to basin-scale crustal thinning, which in

return has caused elevated geothermal gradients of up to 55.4°C/km (Figures 4, 5). The variations in temperature gradients (Figures 4, 5) suggests that crustal thinning is uneven across the basin. This phenomena is typical for pull-apart basins, such as the Salton Sea where higher temperatures were attributed to superimposed subregions of extensional to transtensional strain (Faulds and Hinz, 2015). These authors highlighted that grabens and step overs or relay ramps, typical of larger extensional and transtensional systems, are the most favorable intrabasinal areas for locally increased heat. Local heat anomalies like those observed in the Zharkent Basin are thus expected in regional transtensional systems.

Considering the sparsity of well data and the absence of seismic data, a constraint of discrete tectonic elements within the Zharkent Basin is challenging. However, the proposed pull-apart model is consistent with available structural, stratigraphic, and geophysical observations, and offers a conceptual model for assessing intrabasinal grabens and relay ramps as targets for elevated heat flow. The pull-apart interpretation offers a platform for revisiting interpretations of previously mapped faults (Figure 3). The evidence of Shonzhy-Dobyn temperature anomaly characterized by a geothermal gradient as high as 55°C/km (Figures 4, 5), and the argument that it is most likely one of perhaps many intrabasinal grabens (*sensu* Alexeiev et al., 2009); Section 4.1), suggests the potential for more similar thermal anomalies in the basin which have not been drilled yet. Finding such anomalies in areas where the Upper Cretaceous sandstone is buried deeper (in the Shonzhy-Dobyn area it is ~50°C at a depth of only 600–700 m) and potentially reaching temperatures of >120°C would mean the discovery of a geothermal play suitable for direct electricity production (Lee, 2001; Dickson and Fanelli, 2003).

5.2 Basin recharge and water-rock interactions

5.2.1 The upper cretaceous aquifer

Prior workers argue that Upper Cretaceous aquifers in the Zharkent basin are charged by meteoric water sourced from the Ketmen Ridge and Dzhungarian Alatau Mountain (Figure 1) drainage system (Mukhamedzhanov, 1989; Kalitov, 2016) and partially via deep groundwater flow through fractured rocks (Kim et al., 1971). These processes are known as mountain-front recharge (MFR) and mountain-block recharge (MBR), respectively. These interpretations (Kim et al., 1971; Mukhamedzhanov, 1989; Kalitov, 2016) are based on basin configuration (e.g. enclosed basin) and analogous hydrogeological systems. We use new evidence from hydrogeochemistry and water isotopes to test these proposed recharge mechanisms.

The geothermal waters produced from the Upper Cretaceous aquifer in the Zharkent Basin are characterized by extremely low salinities ranging from about 0.3 to 0.8 g/L (Table 4) when compared to the more saline waters more typically observed at their production depths (Mcintosh, 2021) and standards for using it for agriculture and geothermal productions (Yapiyev et al., 2021). Results from a single shallow geothermal well (AE-4) indicates slightly brackish water (~4.5 g/L), perhaps because of the localized influence of saline surface processes on water chemistry. The very low TDS values and the presence of Si, HCO_3, and Na ions (Table 4) indicate that rock-water interactions are dominated by the dissolution of silicate-rich rocks such as rhyolites and feldspars which are abundant in Paleozoic rocks and derived Mesozoic fragments in the Zharkent Basin (Figures 2, 3). The source of Na and Si is commonly attributed to sodium feldspar and/or rhyolite hydrolysis by hydrogen ions donated by bicarbonate dissociation (Sharp and Tranter, 2017; Absametov et al., 2023). Such silicate dissolution is also documented elsewhere in hydrothermal systems (Shoedarto et al., 2022; Xing et al., 2022). Shoedarto et al. (2022) showed silicate weathering dominates water-rock interaction in hot springs in Southern Bandung, West Java, Indonesia. Chemical dissolution of silicate rocks is positively correlated with temperature (Gaillardet et al., 1999) and is usually low in cold climate regions (Anderson, 2007) compared to higher dissolution in the deep subsurface (Kharaka and Hanor, 2003). The high Si content, high temperature, low salinity, and predominantly quartz lithology of the Upper Cretaceous aquifer (Umralin, 2022; unpublished BSc report) suggests that the solutes in water are likely derived from silicate dissolution in deeper strata. While mixing diagrams (Figure 7) point to the potential presence of evaporates, their actual quantity is probably minimal as evidenced by low TDS (Table 4) and two to three times lower concentrations of Cl compared to Na (Table 4).

The progressive depletion in heavier isotopes with depth (Figure 8) suggests that the primary source of water in the Upper Cretaceous aquifers is the cryosphere (snow, glaciers, and permafrost) of the Tien Shan Mountains (Hoelzle et al., 2019) with snowmelt by far being the largest contributor (Kraaijenbrink et al., 2021). Snowmelt is the most isotopically depleted known water source (Beria et al., 2018), which suggests that winter precipitation in the mountains is the primary source for studied Upper Cretaceous geothermal waters (Figure 8; Table 4). The median values of $\delta^{18}O$ in winter precipitation (December-January-February) in Central Asia are reported to be around -15 to -21‰ (Saidaliyeva et al., 2021), similar to that measured here in geothermal wells of around -14‰ (Figure 8). Summer (June-July-August) precipitation values, by contrast, are isotopically much heavier, with median values of around—5‰ (Saidaliyeva et al., 2021). The data from the global dataset of stable water isotopes in precipitation (Bowen et al., 2005) shows a higher contribution of cold-season precipitation to geothermal groundwater recharge (Figure 8). Recently, Hellwig et al. (2018) reported $\delta^{18}O$ values of water from springs collected in eastern Ily (Altyn-Emel location) to be in the range of -12.8 to -13.6‰ which is very close to our measurements (e.g. -13.04‰ for AE-3; Figure 8). These isotope values contrast with much more enriched values more typical of rainfall signatures (-8.6 to −3.09‰, Hellwig et al., 2018).

The deviation of the isotopic composition of water in geothermal wells right of the LMWL (Figure 8), also known as the 'oxygen isotope shift' (Kharaka and Hanor, 2003) is commonly observed in geothermal systems (Kong et al., 2020; Mcintosh, 2021). This enrichment of $\delta^{18}O$ is commonly caused by high-temperature exchange of formation-water with silicate minerals. This interpretation is also supported by our water chemistry data presented herein (Table 4; Section 5.2.1).

Water sample KD-9 (Figure 8), collected from a stream draining from the nival zone in Ketmen Ridge (Figure 2), is more isotopically enriched relative to subsurface samples (the springs, the artesian well

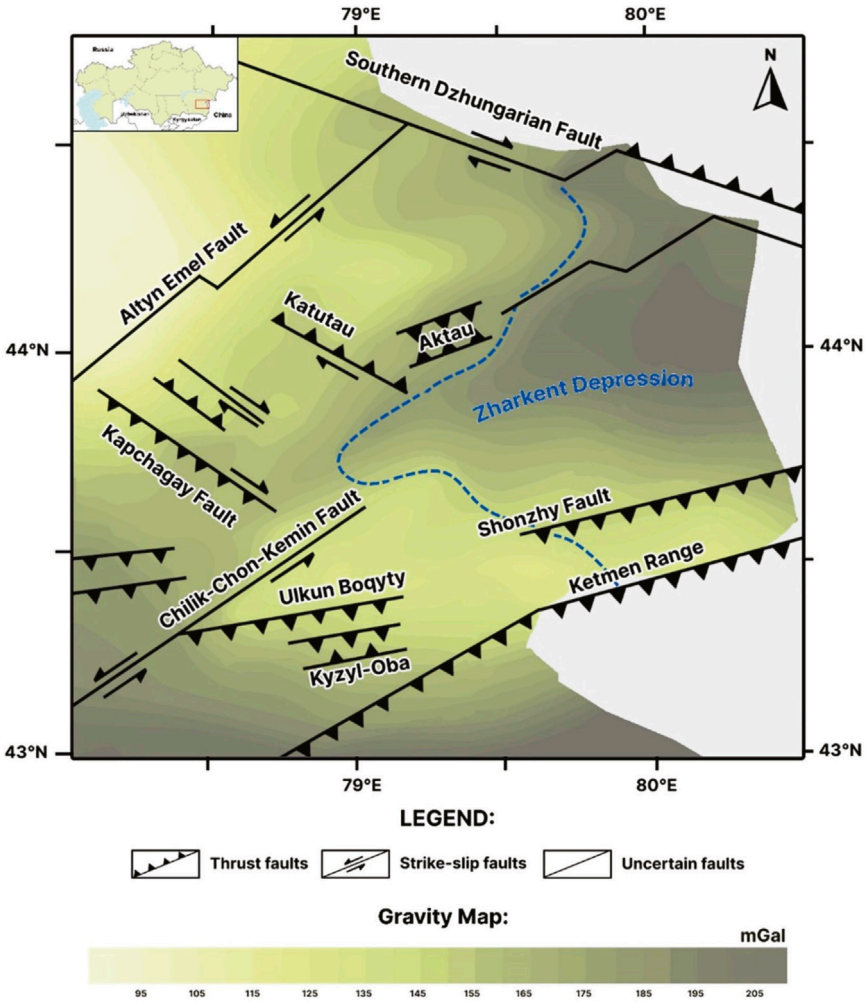

FIGURE 9
Location of main regional faults juxtaposed on the gravity map. The gravity map is modified from the Gravimetric map of the Stepanov and Yanushevich 1971. Map of tectonic faults is modified from (Campbell et al., 2013), Mackenzie et al. (2018), Grützner et al. (2019), and Wu et al. (2021). Note: Altyn-Emel and Chilik-Chon-Kemin faults are Paleozoic age strike-slip faults.

shallow GW, deep and shallower geothermal wells (Figure 8; Table 3). This further demonstrates the larger influence of meltwater recharge with deeper aquifers via deeper flow paths from the mountain block. Recently (Mcintosh, 2021), used stable water isotopes to show that maximum meteoric water circulation depths vary from 1 to 5 km in North America. The deeper circulation is expected to occur in areas of greater topographic relief, like that of the Zharkent area. Jasechko et al. (2017) suggested that globally water at wells deeper than 250 m is mostly (42%–85%) 'fossil' groundwater, recharged by precipitation more than ~12 000 years ago. Though, the previous preliminary results of groundwater residence time in the Zharkent basin, based on the absence of tritium detection (Kozhagulova et al., 2022) should be treated as a potential over-interpretation as the samples were analyzed without prior enrichment. A very low salinity (Figure 10) and isotopically depleted signal in deep geothermal wells (Figure 8), cumulatively points to long-duration deep groundwater flow paths from the mountain cryosphere to the Cretaceous aquifer.

Despite having relatively low variability in salinity across the basin, natural flowrates vary up to 3 times, even for the wells that are drilled in close vicinity to each other (e.g. wells 1-RT and 5539 producing 24.5 and 54.5 L/s respectively (Mukhamedzhanov, 1989). This clearly suggests variable reservoir properties controlled by depositional heterogeneity, which are a subject of ongoing research and beyond the scope of this study.

5.2.2 Cenozoic aquifers

Cenozoic aquifer lithologies are characterized by poor permeability (Figure 10) and low flow rates (Kalitov, 2016), and are not used for geothermal production. However, the integration of their water chemistry (Chakabayev, 1960 and this study) promotes a better understanding of basin recharge.

Vertical salinity variation of Cenozoic formation waters is significant (Figure 10). Water samples taken from Pliocene aquifers have low ion content (around 1 g/L), and show an abrupt rise in Miocene aquifers (with TDS values up to 19 g/L), implying that underlying sedimentary units would be characterized

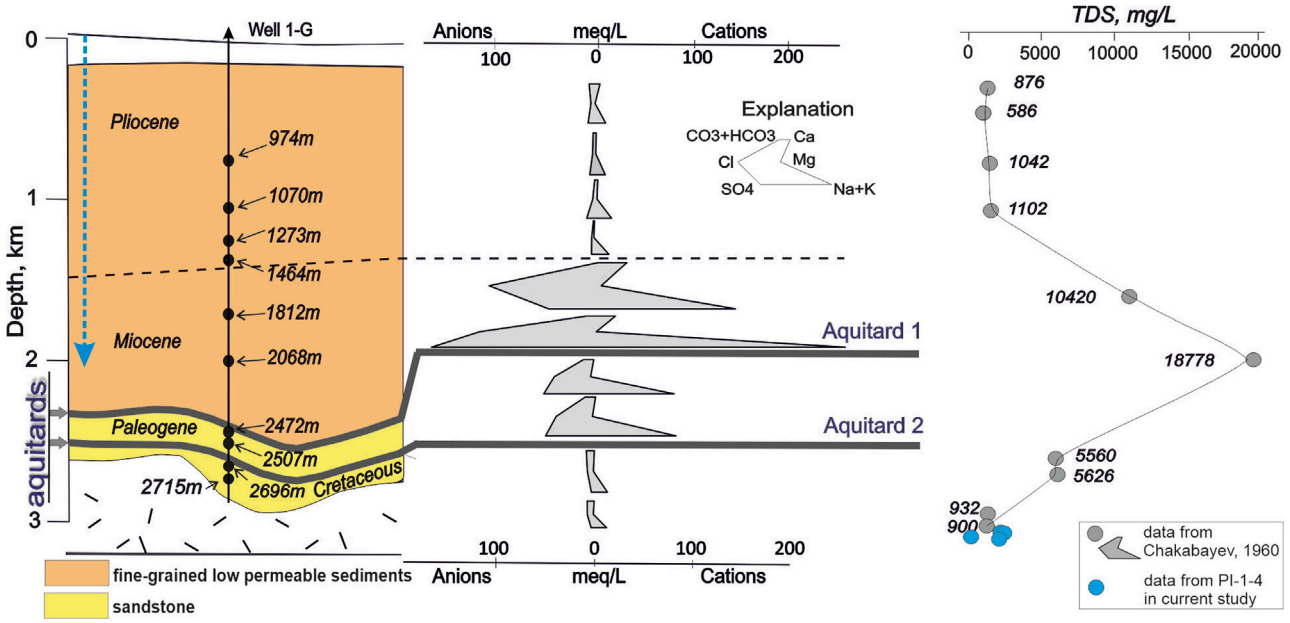

FIGURE 10
Stiff diagram of major ion composition and vertical salinity profile of the deep geothermal well 1-G (see location in Figure 2A). Input data for the TDS depth profile are from Chakabayev (1960) and from this study (blue dots). Both data sources confirm the low salinity of Cretaceous aquifer waters as well as presence of major aquitards in the overlying strata. Blue dashed arrow indicates proposed dominant recharge mechanism for non-productive and more saline Miocene and Pliocene horizons. Cretaceous groundwater is most likely charged by mountain-front and/or mountain-block recharge mechanisms (Figure 11).

by even higher salinity. However, this is not the case as water gets less saline in underlying Paleogene aquifers, and becomes virtually fresh in deeper buried Upper Cretaceous aquifers (Table 4; Figure 10). These abrupt salinity shifts point to the presence of aquitards between Miocene and Paleogene, and Paleogene and Cretaceous aquifers, respectively (Figure 10). The chemical profile (Figure 10) suggests that dissolved salts (from secondary evaporates such as halite and gypsum) are mostly likely percolating from the modern-day surface (i.e. Ily River floodplains and evaporate ponds) to accumulate at the bottom of the Miocene (depth=2068 m, Na-SO_4 water type, TDS ~19 g/L; Figure 10). In contrast, the underlying less saline Paleogene formation waters (depths at 2500–2700 m, Na-SO_4 water type, TDS ~5.6 g/L; Figure 10), and essentially fresh waters in the Cretaceous layers (Na-HCO_3 water type, TDS ~0.9 g/L) implies that both the Paleogene and Cretaceous aquifers are recharged primarily by lateral groundwater flow (Figure 11), and are not in strong connectivity with the overlying more saline layers. Higher salinities in the Paleogene than in the Upper Cretaceous strata suggest a mixing of laterally charged fresh waters and saline waters that over geological time scale have percolated or diffused through the proposed aquitard 1 (Figure 10). The water chemistry of well 1G based on Chakabayev (1960) is in line with recent data (Kalitov, 2016; Table 1) as well as TDS of the recently acquired water samples presented in this study (Table 4; Figure 10). The similarity of Upper Cretaceous waters obtained from well 1G and more recent deep wells including 5539 (PI-1), 1-RT (PI-2), 2-TP (PI-3), 1-TP (PI-4 and PI-5) implies that our interpretation of historical water chemistry data presented above and proposed recharge mechanisms are likely valid across the basin.

In summary, Miocene and Pliocene strata are recharged from percolation down from the overlying basin floor, and Cretaceous waters are recharged laterally from winter precipitation in the Tien Shan Mountains. Paleogene strata are likely a mixture of the two.

5.3 Revised conceptual model of the Zharkent Basin

The integration of the tectonic history of the basin coupled with stratigraphy (Figures 2, 3, 9) and interpretations based on the studied waters' hydrogeochemistry and stable isotope data (Figures 6–8, 10) as well as geothermal gradients (Figures 4, 5) allowed for generating an integrated conceptual three-dimensional model of the Zharkent geothermal system highlighting its recharge system in the context of stratigraphy and regional structures (Figure 11).

We propose that the Upper Cretaceous aquifer is recharged primarily by deep groundwater flow in which old cryosphere water is pushed by a high hydrostatic head from the mountains by the process known as mountain-block recharge (MBR) mechanism (Manning and Solomon, 2005; Markovich et al., 2019; Somers and McKenzie, 2020). The MBR is possibly coupled with mountain-front recharge (MFR) with stream water infiltrating through the basin fill in piedmont areas of Ketmen Range and Dzhungarian Alatau (*sensu* Hellwig et al. (2018) and particularly through sub-cropping and outcropping Upper Cretaceous sandstone strata (Figures 2, 3, 11). This MBR component is similar to other intermontane basin aquifers recharged primarily by adjacent mountains (Manning and Solomon, 2005; Dar et al.,

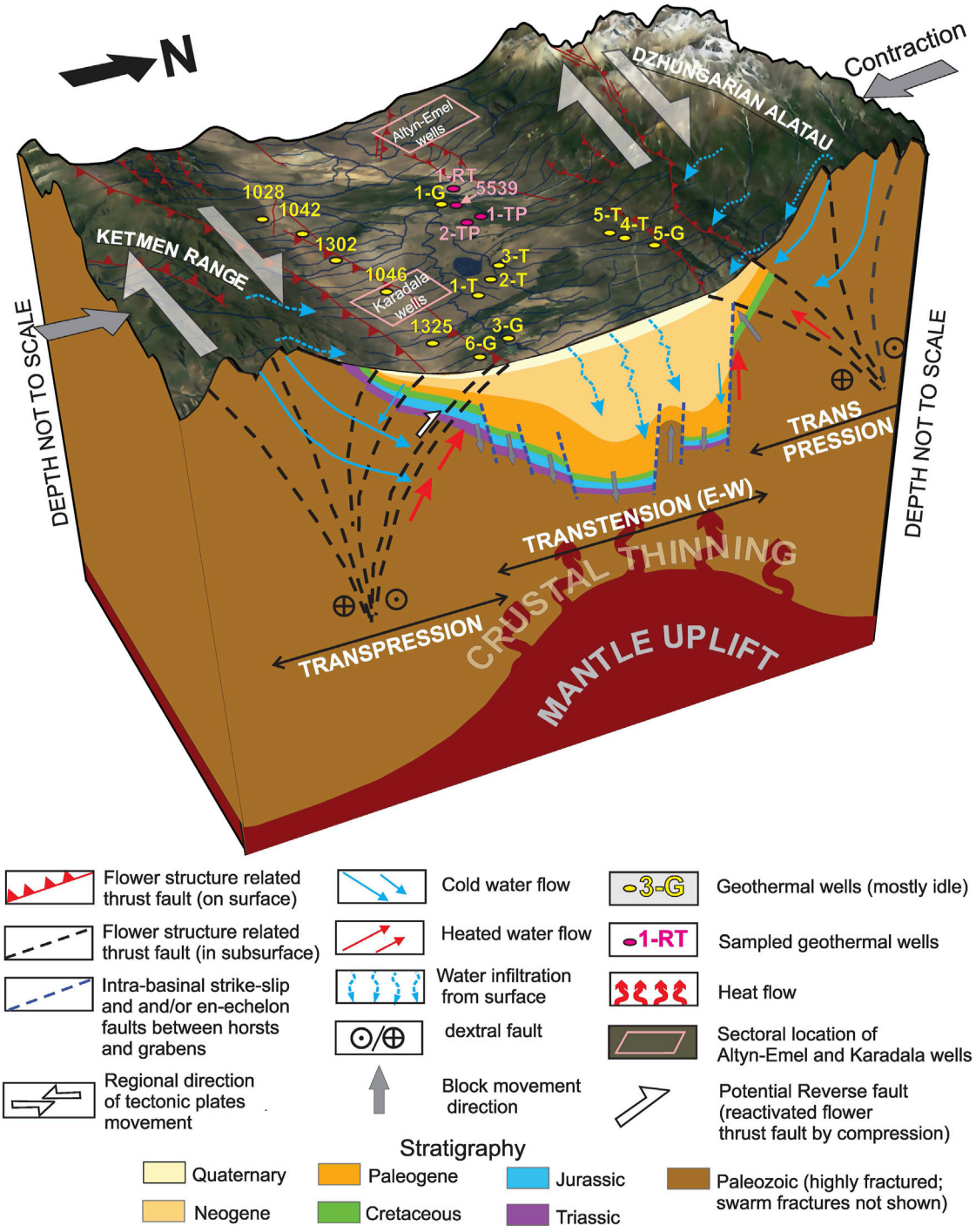

FIGURE 11
Integrated conceptual three-dimensional tectono-stratigraphic, heat, and hydrogeological model of the Zharkent Basin highlighting new evidence relevant to the geothermal system analysis proposed in this study, including: i) crustal thinning caused by recent and/or ongoing regional strike-slip faulting and formation of localized tectonic depression interpreted as a pull-apart basin (the most likely reason for basin-wide increased temperature gradients); Flower structures (steeply dipping thrust faults) on the edges of the basin are produced by transpression while intrabasinal faults are likely produced by transtension, and may include a range of features including an en-echelon network of faults and fractures and associated grabens, horsts, and relay ramps whose presence and geometries cannot be precisely recognized and mapped with available datasets; ii) complex recharge system in the context of stratigraphy and regional structures which includes the interplay of **(A)** gravity driven vertical water infiltration (percolation) from surface (blue wavy dashed arrows), **(B)** water from streams near mountain fronts directly charging porous Cretaceous aquifers (blue dashed arrows), referred as mountain-front recharge (MFR) and **(C)** deep groundwater flow (blue arrows) known as mountain-block recharge (MBR) mechanisms; iii) possible localized heated water upflow along the faults (red arrows). Note 1: geospatial illustration of scenarios proposed to explain geothermal gradient variations across the basin (Figures 4, 5) would require additional surveys and datasets which are currently not available. Note 2: although strike-slip arrows suggest dextral movements numerous pieces of evidence show both sinistral and dextral strike-slip faults (Grützner et al., 2019; Wu et al., 2021).

2022). In contrast, the shallower, Cenozoic groundwater systems are recharged from mountain front and meteoric precipitations. The infiltration velocity of groundwater is very low (Mcintosh, 2021), but the current study does not reveal the age of the water currently produced, and thus not the recharge rate. Sustainable development likely requires ongoing re-injection of produced water into the producing reservoir, which is not the current practice (Kozhagulova et al., 2022).

The complex deformation history of the Zharkent Basin during the multiple phases of major strike-slip faulting led to the formation of a regional pull-apart basin and associated localized weakening and thinning of the crust allowing for heat being transferred via conduction. Transtension and crustal thinning related to pull-apart basin development caused rapid subsidence and formed accommodation for a thick sedimentary succession as well contributed to elevated geothermal gradients (Figure 11). Some heated water might have moved towards the surface and/or accumulated in shallower reservoirs along fracture fault systems (e.g. Shonzhy–Dobyn anomaly) and therefore heat is transferred through the convection mechanism as well. However, the consistent low salinity argues it is more likely that variable geothermal gradients (Figures 4, 5) are the results of complex distribution of tectonic blocks within the larger pull-apart basin.

6 Conclusions and future work

The results of this study promote a novel interpretation of the Zharkent (Eastern Ily) basin's tectonic setting and recharge system through a 3D model that integrates stratigraphic, structural, and geochemical data. These findings differ from prior interpretations and are of significant interest for a better understanding of the overall geothermal system. Our model argues for the following conclusions:

1) Highly variable (from ~25.1°C up to °54.5 C) geothermal gradients are a product of strike-slip faulting which caused the formation of a pull-apart basin characterized by spatially variable crustal thinning. This conclusion is based on the integration of recent tectonic studies and gravimetric mapping as well as consideration of modern plate tectonic principles, along with well control and temperature data. Heat transfer is dominantly, if not exclusively, conductive. However, the localized contribution of convective transfer by water circulation across potentially open faults cannot be excluded.
2) Stable water isotope results from the Upper Cretaceous reservoir point to snow-melt as a predominant groundwater recharge source.
3) While water chemistry results in this study collaborate previous reports suggesting very low TDS [<1 g/L] in the Upper Cretaceous aquifer, recognition of ions indicative of silica dissolution also argues for lateral recharge by a combination of mountain block recharge (MBR; perhaps via fractured porphyritic rhyolite basement) and mountain-front recharge (MFR) by gravity-driven infiltration of surface water via outcropping reservoirs.
4) Up to 20 times higher salinity in the Paleogene and Neogene formations overlaying the Cretaceous reservoir originates from downward water percolation from the surface, including origin from modern evaporative ponds. The mixing of surface and laterally charged waters with Upper Cretaceous water is prevented by at least two major aquitards.

Further steps for testing and refining the proposed model should focus on a better understanding of the local high-temperature anomalies and their association with the faulting network in the Zharkent Basin. A more precise localization of the pull-apart features of the basin will potentially lead to a better comprehension of the spatial heat distribution, and allow for constraining more constraints for resolving heat maps. Ongoing detailed sedimentological studies focused on interpreting the depositional environments and architecture of the Upper Cretaceous reservoir will advance knowledge about reservoir connectivity and associated risks for commercial geothermal developments. Subsequent common-risk segment maps are expected to identify the most attractive areas for commercial geothermal developments. Moreover, further water sampling for groundwater age (residence time) and chemistry will aid reservoir modeling in the region and will help to refine models for the recharge source of the geothermal aquifers.

Data availability statement

The original contributions presented in the study are included in the article/Supplementary Material, further inquiries can be directed to the corresponding author.

Author contributions

AsK: Conceptualization, Methodology, Original draft preparation; VY: Methodology, Original draft preparation; LK: Conceptualization, Original draft preparation; AD: Visualization, Writing–Draft preparation, Editing; VZ: Data acquisition, Supervision; AiK: Experimental work, Data acquisition; EB: Software, Validation; SG: Supervision, Reviewing; JH: Supervision, Reviewing; MF: Conceptualization, Supervision, Writing–Reviewing and Editing. All authors contributed to the article and approved the submitted version.

Funding

Nazarbayev University (CRP Research Grant No. 021220CRP2122) for all field and laboratory research works as well as student and post-doctoral salaries. Swanson Family Foundation for Dr. Holbrook's visit to Kazakhstan. This work is conducted with financial support from Nazarbayev University (CRP Research Grant No. 021220CRP2122) and funds from the Swanson Family Foundation. VY was also partially supported by the University of Oulu.

Acknowledgments

The authors most sincerely thank Geoterm Production Company LLP management for providing us with water samples from hard-to-access localities, Altyn-Emel National Park authorities for granting sampling permits within the park, Drs. Dulat Kalitov and Bas Den Brok for useful discussions about historical hydrogeology data and structural geology interpretation,

respectively. The authors also thank Ayana Karakozhayeva for assisting with the ICP-OES analysis. The thorough reviews and constructive suggestions provided by Drs. Richeng Liu, Kun Tu, Tianran Ma, and Dr. Jianwei Tian (Editor) have greatly enhanced the final version of the manuscript, and their contributions are sincerely appreciated.

Conflict of interest

Authors VZ and AiK were employed by Geoterm Production Company LLP.

The remaining authors declare that the research was conducted in the absence of any commercial or financial relationships that could be construed as a potential conflict of interest.

Publisher's note

Supplementary material

The Supplementary Material for this article can be found online at: https://www.frontiersin.org/articles/10.3389/feart.2023.1212064/full#supplementary-material

References

Absametov, M., Sagin, J., Adenova, D., Smolyar, V., and Murtazin, E. (2023). Assessment of the groundwater for household and drinking purposes in central Kazakhstan. *Groundw. Sustain. Dev.* 21 (December 2022), 100907. doi:10.1016/j.gsd.2023.100907

Akchulakov, U. A. (2012). *The comprehensive study of the sedimentary basins of Kazakhstan. Ily basin (book 1).*

Alexeiev, D. V., Cook, H. E., Buvtyshkin, V. M., and Golub, L. Y. (2009). Structural evolution of the Ural-Tian Shan junction: a view from Karatau ridge, South Kazakhstan. *Comptes Rendus - Geosci.* 341 (2–3), 287–297. doi:10.1016/j.crte.2008.12.004

Allen, M. B., Windley, B. F., Chi, Z., Zhong-Yan, Z., and Guang-Rei, W. (1991). Basin evolution within and adjacent to the tien Shan range, NW China. *J. Geol. Soc.* 148 (2), 369–378. doi:10.1144/gsjgs.148.2.0369

Anderson, S. P. (2007). Biogeochemistry of glacial landscape systems. *Annu. Rev. Earth Planet. Sci.* 35 (1), 375–399. doi:10.1146/annurev.earth.35.031306.140033

Beria, H., Larsen, J. R., Ceperley, N. C., Michelon, A., Vennemann, T., and Schaefli, B. (2018). Understanding snow hydrological processes through the lens of stable water isotopes. *Wiley Interdiscip. Rev. Water* 5 (6), e1311. doi:10.1002/wat2.1311

Boguslavsky, E., Vainblat, A., Daukeev, G., Movchan, I., Pevzne, L., Smyslov, A., et al. (1999). Geothermal resources of sedimentary basins in the Republic of Kazakhstan. *Bull. d'Hydrogelogie* (17), 123–131.

Bowen, G. J. (2022). WaterIsotopes.org. *version OIPC3.1* http://wateriso.utah.edu/waterisotopes/pages/data_access/oipc.html.

Bowen, G. J., Wassenaar, L. I., and Hobson, K. A. (2005). Global application of stable hydrogen and oxygen isotopes to wildlife forensics. *Oecologia* 143 (3), 337–348. doi:10.1007/s00442-004-1813-y

Burtman, V. S. (2012). Geodymanics of tibet, Tarim, and the tien Shan in the late cenozoic. *Geotectonics* 46 (3), 185–211. doi:10.1134/S0016852112030028

Campbell, G. E., Walker, R. T., Abdrakhmanov, K., Schwenninger, J., Jackson, J., Elliott, J. R., et al. (2013). The Dzhungarian fault Late Quaternary tectonics and slip rate of a major right-lateral strike-slip fault in the northern Tien Shan region. *J. Geophys. Res. Solid Earth* 118, 5681–5698. doi:10.1002/jgrb.50367

Chakabayev, S. E. (1960). Hydrochemical and thermal conditions of the Cretaceous and Tertiary formations of the eastern part of the Ily depression (in Russian). *Vestnik KazSSR Sci. Acad.* 1 (38).

Cording, A., Hetzel, R., Kober, M., and Kley, J. (2014). 10Be exposure dating of river terraces at the southern mountain front of the Dzungarian Alatau (SE Kazakhstan) reveals rate of thrust faulting over the past ~400ka. *Quat. Res. (United States)* 81 (1), 168–178. doi:10.1016/j.yqres.2013.10.016

Craig, H. (1961). Isotopic variations in meteoric waters. *Science* 133 (3465), 1702–1703.

Dar, T., Rai, N., and Kumar, S. (2022). Distinguishing Mountain front and mountain block recharge in an intermontane basin of the himalayan region. *Groundwater* 60 (4), 488–495. doi:10.1111/GWAT.13181

Daukeev, S. Z., Uzhkenov, B. S., Abdulin, A. A., Bespayev, H. A., Votsalevskiy, E. S., Lubetskiy, V. N., et al. (2002). *The deep structure and mineral resources of*. Kazakhstan.

Dickson, M. H., and Fanelli, M. (2003). *Geothermal background*. Paris: Geothermal Energy, Utilization and Technology, UNESCO, 125.

Dillinger, A. (2021). *Outcrop observations in the Zharkent area (Aktam, Kolzhat, Dikan locations) (unpublished field study report)*, 1–33.

Dipippo, R. (2016). *Geothermal power generation: developments and innovation*. Woodhead Publishing.

ESRI (2011). *Release 10*, 437. Redlands, CA: Environmental Systems Research Institute, 438.

Faulds, J., and Hinz, N. (2015). "Favorable tectonic and structural settings of geothermal systems in the Great Basin region, western USA: Proxies for discovering blind geothermal systems," in Proceedings World Geothermal Congress, Melbourne, Australia, April 19–25, 2015 (No. DOE-UNR-06731-02). University of Nevada, Reno: Nevada Bureau of Mines and Geology.

Faulds, J. E., Hinz, N. H., Coolbaugh, M. F., Craig, M., Siler, D. L., Shevenell, L. A., et al. (2016). *Discovering geothermal systems in the Great Basin region: an integrated geologic, geochemical, and geophysical approach for establishing geothermal play fairways*. 1–15.

Ferguson, G., Grasby, S. E., and Hindle, S. R. (2009). What do aqueous geothermometers really tell us? *Geofluids* 9 (1), 39–48. doi:10.1111/j.1468-8123.2008.00237.x

Filipyev, G. P. (1957). *Report on the exploration drilling in the Ily depression*, 1955–1956. *(in russian).*

Filipyev, G. P., and Rabkin, F. S. (1959). *Report on the results of the exploration drilling in the Zharkent depression in 1957,1958 and 9 months of 1959 (in Russian).*

Franke, R. (1982). Smooth interpolation of scattered data by local thin plate splines. *Comput. \& Math. Appl.* 8 (4), 273–281. doi:10.1016/0898-1221(82)90009-8

Frisch, K., Voigt, S., Voigt, T., Hellwig, A., Verestek, V., and Weber, Y. (2019). Extreme aridity prior to lake expansion deciphered from facies evolution in the Miocene Ili Basin, south-east Kazakhstan. *Sedimentology* 66 (5), 1716–1745. doi:10.1111/sed.12556

Gaillardet, J., Dupré, B., Louvat, P., and Allègre, C. J. (1999). Global silicate weathering and CO2 consumption rates deduced from the chemistry of large rivers. *Chem. Geol.* 159 (1–4), 3–30. doi:10.1016/S0009-2541(99)00031-5

Grützner, C., Campbell, G., Walker, R. T., Jackson, J., Mackenzie, D., Abdrakhmanov, K., et al. (2019). Shortening accommodated by thrust and strike-slip faults in the Ili Basin northern tien Shan. *Tectonics* 38, 2255–2274. doi:10.1029/2018TC005459

Han, X. Z., Li, S. H., Zheng, E. J., Li, X. G., Cai, Y. Q., and Chen, Z. L. (2004). Neotectonic activity characteristics of Yili Basin and its relation to the formation of sandstone-type uranium deposits. *Xinjiang Geol.* 22 (4), 378–381.

Hellwig, A., Voigt, S., and Mulch, A. (2018). *Late Oligocene to early Miocene humidity change recorded in terrestrial sequences in the Ili Basin*. south-eastern Kazakhstan , Central Asia, 517–539. doi:10.1111/sed.12390

Hellwig, A., Voigt, S., Mulch, A., Frisch, K., Bartenstein, A., Pross, J., et al. (2017). Late Oligocene to early Miocene humidity change recorded in terrestrial sequences in the Ili Basin (south-eastern Kazakhstan, Central Asia). *Sedimentology* 65, 517–539. doi:10.1111/sed.12390

Hoelzle, M., Barandun, M., Bolch, T., Fiddes, J., Gafurov, A., Muccione, V., et al. (2019). "The status and role of the alpine cryosphere in Central Asia," in *The Aral Sea Basin* (Taylor & Francis), 100–121. doi:10.4324/9780429436475-8

Huang, H., Cawood, P. A., Ni, S., Hou, M., Shi, Z., and Hu, X. (2018). Provenance of late paleozoic strata in the Yili Basin: implications for tectonic evolution of the South tianshan orogenic belt. *GSA Bull.* 130 (5–6), 952–974. doi:10.1130/b31588.1

Hubert, E., and Wolkersdorfer, C. (2015). Establishing a conversion factor between electrical conductivity and total dissolved solids in South African mine waters. *Water sa.* 41 (4), 490–500. doi:10.4314/wsa.v41i4.08

Jasechko, S., Perrone, D., Befus, K. M., Bayani Cardenas, M., Ferguson, G., Gleeson, T., et al. (2017). Global aquifers dominated by fossil groundwaters but wells vulnerable to modern contamination. *Nat. Geosci.* 10 (6), 425–429. doi:10.1038/ngeo2943

Jia, Y., Sun, J., Lü, L., Pang, J., and Wang, Y. (2020). Late Oligocene-Miocene intra-continental mountain building of the Harke Mountains, southern Chinese Tian Shan: evidence from detrital AFT and AHe analysis. *J. Asian Earth Sci.* 191, 104198. doi:10.1016/j.jseaes.2019.104198

Jóhannesson, T., Axelsson, G., Hauksdóttir, S., Chatenay, C., Benediktsson, D. Ö., and Weisenberger, T. B. (2019). Preliminary review of geothermal resources in Kazakhstan. Final Report. May Available at: https://rfc.kegoc.kz/media/Geothermal.resources.pdf.

Jolie, E., Scott, S., Axelsson, G., Gutiérrez-negrín, L. C., Regenspurg, S., Ziegler, M., et al. (2021). Geological controls on geothermal resources for power generation. *Nat. Rev. Earth Environ.* 2 (May), 324–339. doi:10.1038/s43017-021-00154-y

Jolivet, M., Dominguez, S., Charreau, J., Chen, Y., Li, Y., and Wang, Q. (2010). Mesozoic and Cenozoic tectonic history of the central Chinese Tian Shan: reactivated tectonic structures and active deformation. *Tectonics* 29 (6), 1–30. doi:10.1029/2010TC002712

Kalitov, D. K. (2016). *Exploration of geothermal groundwater at the Zharkunak site of the Zharkent basin in the Almaty region in order to assess the operational reserves of thermal groundwater for heat and power purposes (in Russian).*

Kendall, C., and Doctor, D. H. (2003). Stable isotope applications in hydrologic studies. *Treatise Geochem.* 5–9, 319–364. doi:10.1016/B0-08-043751-6/05081-7

Kharaka, Y. K., and Hanor, J. S. (2003). Deep fluids in the continents: I. Sedimentary basins. *Treatise Geochem.* 5, 605.

Kim, E. K., Kondratyeva, I. M., Kaltayev, M. K., Gorlenko, N. N., Losev, D. M., Malikov, V. D., et al. (1971). *Karadala groundwater field in the Uyghur district of the Almaty region (in Russian).*

Kober, M., Seib, N., Kley, J., and Voigt, T. (2013). Thick-skinned thrusting in the northern Tien Shan Foreland, Kazakhstan: structural inheritance and polyphase deformation. *Geol. Soc. Spec. Publ.* 377 (1), 19–42. doi:10.1144/SP377.7

Kong, Y., Pang, Z., Pang, J., Li, J., Lyu, M., and Pan, S. (2020). Fault-affected fluid circulation revealed by hydrochemistry and isotopes in a large-scale utilized geothermal reservoir. *Geofluids* 2020, 1–13. doi:10.1155/2020/2604025

Kozhagulova, A., Yapiyev, V., Kalitova, A., Zavaley, V., Dillinger, A., Karakozhayeva, A., et al. (2022). "Low salinity upper cretaceous formation potential for geothermal energy harvesting in the eastern Ily Basin," in 3rd EAGE Global Energy Transition Conference & Exhibition, 1–5. Kazakhstan.

Kraaijenbrink, P. D. A., Stigter, E. E., Yao, T., and Immerzeel, W. W. (2021). Climate change decisive for Asia's snow meltwater supply. *Nat. Clim. Change* 11 (July), 591–597. doi:10.1038/s41558-021-01074-x

Lee, K. C. (2001). Classification of geothermal resources by exergy. *Geothermics* 30 (4), 431–442. doi:10.1016/S0375-6505(00)00056-0

Lucas, S. G., Aubekerov, B. Z., Dzhamangaraeva, A. K., Bayshashov, B. U., and Tyutkova, L. A. (2000). *Cenozoic lacustrine deposits of the Ili Basin, southeastern Kazakhstan. Lake basins through space and time.* Tulsa: American Association of Petroleum Geologists, 59–64.

Lucas, S. G., Bayshashov, B. U., Tyutkova, L. A., Zhamangara, A. K., and Aubekerov, B. Z. (1997). Mammalian biochronology of the paleogene-neogene boundary at Aktau mountain, eastern Kazakhstan. *Paläontologische Z.* 71 (3), 305–314. doi:10.1007/bf02988498

Macaulay, E. A., Sobel, E. R., Mikolaichuk, A., Kohn, B., and Stuart, F. M. (2014). Cenozoic deformation and exhumation history of the Central Kyrgyz Tien Shan. *Tectonics* 33 (2), 135–165. doi:10.1002/2013TC003376

Mackenzie, D., Walker, R., Abdrakhmatov, K., Campbell, G., Carr, A., Gruetzner, C., et al. (2018). A creeping intracontinental thrust fault: past and present slip-rates on the Northern edge of the Tien Shan, Kazakhstan. *Geophys. J. Int.* 215 (2), 1148–1170. doi:10.1093/GJI/GGY339

Manning, A. H., and Solomon, D. K. (2005). An integrated environmental tracer approach to characterizing groundwater circulation in a mountain block. *Water Resour. Res.* 41 (12), 1–18. doi:10.1029/2005WR004178

Markovich, K. H., Manning, A. H., Condon, L. E., and McIntosh, J. C. (2019). Mountain-block recharge: a review of current understanding. *Water Resour. Res.* 55 (11), 8278–8304. doi:10.1029/2019WR025676

Mcintosh, J. C. (2021). *Deep Meteoric Water Circulation Earth ' s Crust Geophys. Res. Lett.* 1, 10. doi:10.1038/s41477-022-01198-8

Middleton, M. F. (1989). A model for the formation of intracratonic sag basins. *Geophys. J. Int.* 99 (3), 665–676. doi:10.1111/j.1365-246x.1989.tb02049.x

Mitáš, L., and Mitášová, H. (1988). General variational approach to the interpolation problem. *Comput. \& Math. Appl.* 16 (12), 983–992. doi:10.1016/0898-1221(88)90255-6

Mukhamedzhanov, S. M. (1989). *Hydrogeological and geophysical data analysis of the eastern Ily geothermal basin, the geological economic apprasal of the thermal water fields (based on the 1984-1988 work) (in Russian).*

Mukhamedzhanov, S. M. (1990). *Geothermal map of Kazakhstan (in Russian).*

Muraoka, H., Takahashi, M., Sundhoro, H., Dwipa, S., Soeda, Y., Momita, M., et al. (2010). Geothermal systems constrained by the Sumatran fault and its pull-apart basins in Sumatra, Western Indonesia. *World Geotherm. Congr. 2010ermal Congr.*, 25–29.

Rozanski, K., Araguás-Araguás, L., and Gonfiantini, R. (1993). Isotopic patterns in modern global precipitation. *Clim. Change Cont. Isotopic Rec.* 78, 1–36. doi:10.1029/gm078p0001

Ryan, W. B. F., Carbotte, M. S., Coplan, J. O., O'Hara, S., Melkonian, A., Arko, R., et al. (2009). Geochem Geophys Geosyst—2009—Ryan—Global Multi-Resolution Topography synthesis. doi:10.1029/2008GC002332

Saidaliyeva, Z., Shahgedanova, M., Yapiyev, V., Wade, A., Akbarov, F., Esenaman, M., et al. (2021). *Water isoscapes of central Asia.* doi:10.13140/RG.2.2.18428.21127

Sharp, M., and Tranter, M. (2017). Glacier biogeochemistry. *Geochem. Perspect.* 6 (2), 173–339. doi:10.7185/geochempersp.6.2

Shoedarto, R. M., Tada, Y., Kashiwaya, K., Koike, K., Iskandar, I., Malik, D., et al. (2022). Advanced characterization of hydrothermal flows within recharge and discharge areas using rare Earth elements, proved through a case study of wayang windu field, West Java, Indonesia. *SSRN Electron. J.* 105 (April), 102507. doi:10.2139/ssrn.4085439

Sobel, E. R., Chen, J., and Heermance, R. V. (2006). Late oligocene-early Miocene initiation of shortening in the southwestern Chinese tian Shan: implications for Neogene shortening rate variations. *Earth Planet. Sci. Lett.* 247 (1–2), 70–81. doi:10.1016/j.epsl.2006.03.048

Somers, L. D., and McKenzie, J. M. (2020). A review of groundwater in high mountain environments. *WIREs Water* 7. doi:10.1002/wat2.1475

Sutrisno, L., Bonte, D., Daud, Y., Smit, J., Beekman, F., Van Wees, J. D., et al. (2019). "Assessing the role of pull-apart basins for high-temperature geothermal resources in transcurrent tectonic setting: Sumatra and California compared," in *European Geothermal Congress. June*, 1–8.

Stepanov, P. P., and Yanushevich, M. A. (1971). "Gravimetric map of the USSR," in *Minstry of Geology of the USSR.*

Umralin, A. (2022). *Grain size, composition, and petrography of sandstone hosted geothermal aquifer: comparison of outcrop samples and drill cuttings from a deep well, Upper Cretaceous, Ily Basin, Eastern Kazakhstan (unplublished BSc field study report)*, 1–32.

Verestek, V., Appel, E., Voigt, S., and Frisch, K. (2018). Constrained magnetostratigraphic dating of a continental Middle Miocene section in the arid central Asia. *Front. Earth Sci.* 6, 49. doi:10.3389/feart.2018.00049

Voigt, S., Weber, Y., Frisch, K., Bartenstein, A., Hellwig, A., Petschick, R., et al. (2017). Climatically forced moisture supply, sediment flux and pedogenesis in Miocene mudflat deposits of south-east Kazakhstan, Central Asia. *Depositional Rec.* 3 (2), 209–232. doi:10.1002/dep2.34

Wang, B., Faure, M., Cluzel, D., Shu, L., Charvet, J., Meffre, S., et al. (2006). Late paleozoic tectonic evolution of the northern west Chinese tianshan belt. *Geodin. Acta* 19 (3–4), 237–247. doi:10.3166/ga.19.237-247

Wu, C., Wang, W., Zheng, W., Zhang, P., and Yu, Z. (2021). Opposite sense of strike-slip faulting and crustal rotation accommodating left-lateral shear between the tianshan mountains and Kazakh platform. *Geophys. Res. Lett.* 48 (24), 1–8. doi:10.1029/2021GL096442

Xing, Y., Yu, H., Liu, Z., Li, J., Liu, S., Han, S., et al. (2022). Study on chemical genesis of deep geothermal fluid in gaoyang geothermal field. *Front. Earth Sci.* 9, 1321. doi:10.3389/feart.2021.787222

Yapiyev, V., Wade, A. J., Shahgedanova, M., Saidaliyeva, Z., Madibekov, A., and Severskiy, I. (2021). The hydrochemistry and water quality of glacierized catchments in Central Asia: a review of the current status and anticipated change. *J. Hydrology Regional Stud.* 38 (November), 100960. doi:10.1016/j.ejrh.2021.100960

Yu, J., Walker, R. T., Rhodes, E. J., Zhang, P., Li, C., Wang, S., et al. (2021). East tacheng (qoqek) fault zone: late quaternary tectonics and slip rate of a left-lateral strike-slip fault zone North of the tian Shan. *Tectonics* 40 (2), e2020TC006377. doi:10.1029/2020tc006377

frontiers | Frontiers in Earth Science

TYPE Original Research
PUBLISHED 28 December 2023
DOI 10.3389/feart.2023.1264652

OPEN ACCESS

EDITED BY
Yingfeng Sun,
University of Science and Technology Beijing, China

REVIEWED BY
Arkoprovo Biswas,
Banaras Hindu University, India
Paolo Favali,
ERIC foundation, Italy

*CORRESPONDENCE
Jiulong Liu,
julon0920@163.com

RECEIVED 21 July 2023
ACCEPTED 21 November 2023
PUBLISHED 28 December 2023

CITATION
Xiang H, Yao Y, Gai S, Song J, Song W, Liu J and Feng Z (2023), The target selection and quantitative evaluation for deep geothermal resource zoning of typical geothermal fields in central Hebei of North China plain.
Front. Earth Sci. 11:1264652.
doi: 10.3389/feart.2023.1264652

The target selection and quantitative evaluation for deep geothermal resource zoning of typical geothermal fields in central Hebei of North China plain

Hong Xiang[1,2], Yahui Yao[1,2], Shaohua Gai[3], Jian Song[1,2], Wei Song[1,2], Jiulong Liu[1,2]* and Zhaolong Feng[1,2]

[1]Center for Hydrogeology and Environmental Geology Survey, China Geology Survey, Tianjin, China, [2]Tianjin Engineering Center of Geothermal Resources Exploration and Development, Tianjin, China, [3]CNOOC Research Institute Ltd., Beijing, China

With the rapid economic development in North China, the demand for geothermal energy is increasing. It is urgent to find favorable deep geothermal resource targets in North China. Although geothermal resources in the North China Plain are widely distributed, in order to develop deep geothermal resources in North China safely, stably and efficiently, it is essential to carry out the target selection and evaluation of geothermal resource zoning. This article takes the typical geothermal fields in the central Hebei region as the research object, and through the comprehensive collation of regional geothermal geological data, constructs an optimization evaluation indicator system for geothermal resource target areas from three aspects: resource conditions, mining potential, and heating demand. On this basis, it establishes a linear relationship between the attribute values and scores of each indicator, and uses the analytic hierarchy process to assign weights to each indicator and calculate the comprehensive weight. Then, the comprehensive evaluation value is obtained by weighted calculation of the scores and comprehensive weights of each block in the grid segmentation of the evaluation area. Finally, through the spatial analysis function of GIS, the comprehensive evaluation values of all blocks in the evaluation area were analyzed using kriging difference analysis, and a comprehensive evaluation map, the geothermal resource prospective target area map, was finally obtained. Using quantitative zoning evaluation methods, the target areas for exploration and development of deep geothermal resources in central Hebei Province have been delineated within a large region. The evaluation results indicate that the Cambrian-Ordovician reservoir target area is relatively large, and there are many favorable target areas with good reservoir conditions in the Middle-Upper Proterozoic. The excellent prospective target area of the Mesoproterozoic geothermal reservoir accounts for 56%, mainly located in the Xingji uplift and Gaoyang low uplift. Xiong'an New Area, Cangzhou, and the eastern part of Hengshui are excellent prospective target areas for the evaluation of the Mesoproterozoic geothermal reservoir in a single area. This evaluation method can provide a reference for the optimization of resource exploration and development target areas in key regions.

KEYWORDS

geothermal resource, target selection, zoning evaluation, prospect target area, central Hebei, North China plain

1 Introduction

As a kind of renewable green energy, the geothermal energy is abundant, stable and safe. China's geothermal property has made rapid development, with the"Double carbon" target, geothermal energy in the adjustment of the role of a significant increase in the energy structure. By the end of 2020, China's geothermal utilization is equivalent to about 40 million tons of standard coal, which is only 4.5% of non-fossil energy, and available space is very large.The deep geothermal heating area is up to 580 million square meters (Wang D. et al., 2022).The geothermal resources in the North China plain are widely distributed. With the rapid development of the capital economic circle, the demand for geothermal energy is increasing, and the North China Plain has become one of the most important mid-deep hydrothermal geothermal development zones in China (Mao et al., 2020). Geothermal reservoirs of the clastic rock pore type and carbonate rock karst cavern-fracture type are the main types in this area. Three geothermal reservoir types are mainly developed, including the Jixian Wumishan formation and Gaoyuzhuang formation carbonate karst geothermal reservoir, the Cambrian-Ordovician carbonate karst geothermal reservoir and the Neogene sandstone geothermal reservoir (Mao et al., 2020; Wang T. H. et al., 2022). The first two types of geothermal reservoir development zones are mainly concentrated in Jizhong depression, Cangxian uplift and the north-west area of Huanghua depression and Linqing depression. The Neogene sandstone geothermal reservoir development zones are mainly concentrated in Jizhong Depression, Huanghua Depression, Jiyang Depression, and Linqing Depression.

In recent years, with the increasing exploration and development of geothermal resources, the predecessors have done a lot of work on the zoning evaluation of medium-deep geothermal resources. In 1995, Dunshi Yan, Yingtai Yu and others did a lot of work on the geothermal distribution, type division, resource quantity calculation, development and utilization evaluation of the Beijing Tianjin Hebei oil and gas region (Yan and Yu, 2000). The current situation and potential of development and utilization were analyzed (Wang et al., 2017a). Lin et al. (2013) and Wang G. L. et al. (2020) used different evaluation methods to evaluate the potential of shallow geothermal energy, hydrothermal geothermal resources and dry hot rock resources for different types of geothermal resources in China, and Wang G. L. et al. (2020) analyzed the current situation and the economic and environmental benefits of the geothermal resources development and utilization. Pang et al. (2020) proposed an index system for evaluating the mining conditions of deep geothermal energy, assigned values to each single index by expert scoring, and then quantitatively calculated and evaluated the developing difficulty of deep geothermal energy resources by using fuzzy mathematics. Wang (2019) selected the geothermal exploration target areabased on the distribution characteristics of geothermal fields and geothermal resources in Shandong Province and combined with market conditions. Zhang et al. (2016a), Zhang et al. (2016b) selected multiple evidence factors such as earthquake epicenter, fault, Bouguer gravity anomaly, magnetic anomaly, intrusive rock and terrestrial heat flow, to build a fuzzy logic model in a typical geothermal site in Anatolia, Türkiye, and then apply it to the geothermal potential evaluation of Fujian Province. Liu Z. M. et al. (2022) constructed a evaluation system of 61 geological condition indicators, including basic geological conditions, geological environment elements, and geological resource elements, to evaluate the urban geological conditions of Beijing. Based on the development characteristics and utilization direction of geothermal resources in bedrock in Shandong Province, Gao (2009) has established a selection evaluation method based on resource and market conditions. Li et al. (2018) established a site selection evaluation index system based on the Analytic Hierarchy Process, which includes four aspects: resources, technology, safety, and economy. Feng and Cao (2007) predicted favorable areas for geothermal resource development and utilization by studying the distribution of geothermal anomalies, physical properties of thermal reservoirs, and water yield. According to the project selection, project establishment, construction and operation stages, Liu G. Y. et al. (2022) proposed a set of evaluation system for hydrothermal geothermal resources in the middle and deep layers of sedimentary basin. In 2018, Quinao and Zarrouk, (2018) used the workflow of experimental design and response surface methodology (ED and RSM) to study the Ngatamariki geothermal field in New Zealand as an example. This method not only solves the problem of multiple factors for sufficient testing of the model, but also uses response surfaces for thousands of probabilistic geothermal resource assessments. Ciriaco et al. (2020) improved the workflow of experimental design (ED) and response surface methodology (RSM) by using two-level and three-level full factors and Box Behnken design, and established a proxy numerical model for evaluating geothermal resources. In 2022, Ciriaco et al. (2022) also used experimental design and response surface methodology to select 6 uncertain parameters, implemented Plasckett Burman design, and established twelve versions of Wright reservoir models for uncertainty quantification and geothermal resource evaluation.

The evaluation methods in these studies include resource calculation, numerical simulation and comprehensive evaluation based on physical indicators. Although there are many methods and significant progress, they still remain based on the evaluation unit of tectonic units, and there has been no quantitative evaluation research on geothermal resources in the central region of Hebei in previous studies. On the basis of previous research methods, this article uses GIS to comprehensively evaluate the fusion of geothermal geological multi-source information data, and uses the Kriging method to analyze the grid division difference in the evaluation area, breaking through the previous situation of using structural units as evaluation units; At the same time, by using analytic hierarchy process (AHP), the index of deep geothermal resources exploration and development zoning is quantified, and the exploration and development target areas of deep geothermal resources in central Hebei Province have been delineated on a large regional scale through quantitative zoning evaluation method. The purpose is to construct the zoning evaluation method for geothermal resources, and to provide reference for the exploration and development of middle-deep geothermal resources in key areas. In order to effectively reduce the risk of geothermal resources development and provide a reliable basis for the planning and management of geothermal resources development and utilization.

2 Geologic setting

The central Hebei Province is located in the North China Plain, where the Bohai Bay basin is extremely rich in geothermal

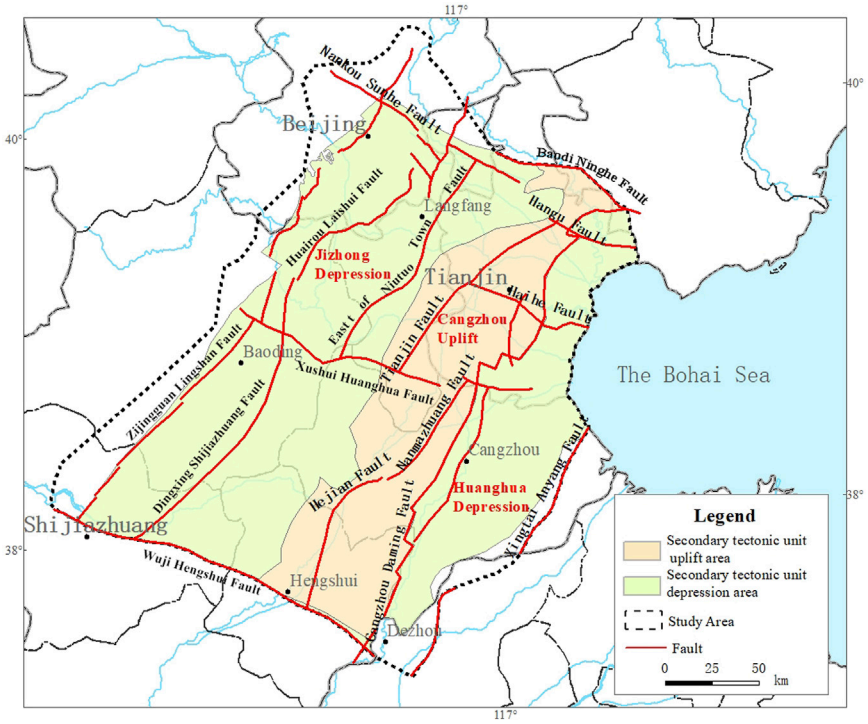

FIGURE 1
Tectonic map of the study area.

resources. It is one of the important mid deep hydrothermal geothermal development zones in China (Jiang et al., 2013). North China plain is a typical alluvial plain with low and flat terrain, sloping from the west to the east, and gradually lowering from the Taihang Mountains to the Bohai Bay (Chen, 1988). This area is mainly a huge Meso-Cenozoic depression, mostly low-lying land and lacustrine marsh, with a sedimentary thickness of 1,500–5000 m. It mainly develops three groups of faults in NNE-NE direction, NW direction and near EW direction (Liu et al., 2018; Zhang et al., 2023). The study area can be divided into three secondary structural units: Jizhong depression, Cangxian uplift and Huanghua depression (Figure 1) (Qiu, 2004; Gong, 2011). The overall structural pattern of NE-SW uplifts and depressions is presented. The sedimentary layer of this area is thick and wide, which has been formed a huge space for water and heat storage (Cai Y. H., 2004). There are two types of the developed geothermal reservoirs at the shallow depth of 4000 m in the study area: pore type and karst fissure type. From shallow to deep, five major geothermal reservoirs are mainly developed, including Minghuazhen formation, Guantao formation, Dongying formation, Cambrian-Ordovician and Middle-Upper Proterozoic (Wang et al., 2017b). Because it is more susceptible to be heated by a deep heat source, the temperature of deep bedrock geothermal reservoirs are higher, which are mainly existed in the Lower Paleozoic Cambrian-Ordovician and the Middle-Upper Proterozoic carbonate karst cavern-fractured geothermal reservoirs (Wang and Zhou, 1992). This study focuses on the deep karst fracture-type geothermal reservoirs.

2.1 Cambrian-ordovician geothermal reservoir

The Cambrian-Ordovician geothermal reservoir is mainly distributed in the Cangxian uplift, and other scattered areas are located near the boundary of the structural units, with a thickness of 600–800 m (Figure 2) (Chen et al., 1994; Zhang et al., 2018; Li and Zhang, (2018). Most of the buried depth of the Cambrian-Ordovician geothermal reservoir is buried under the Cenozoic stratum, and its developmental degree and the developmental thickness of the ancient weathering crust are affected by lithology, basement structure and the buried depth of the stratum, which is uneven. The roof interface of the Cambrian-Ordovician geothermal reservoir is controlled by the basement structure and fluctuates greatly. The degree of geothermal reservoir development varies greatly due to different top cover layers. The roof buried depth of the Cambrian-Ordovician geothermal reservoir is 2000–3000 m in Anxin, Fucheng, Shenze, and Cangxian in central Heibei (Chen et al., 1994; Liu et al., 2018). The proportion of reservoir thickness to formation thickness is about 20%, with an average effective porosity of about 3%. The water inflow of a single well is 150–1,500 m^3/d (Feng, 2018; Li et al., 2018). The temperature range in the middle of the heat storage is 25°C–110°C, and the highest temperature area is located in Gaoyang low swell, where the highest temperature is about 120°C.

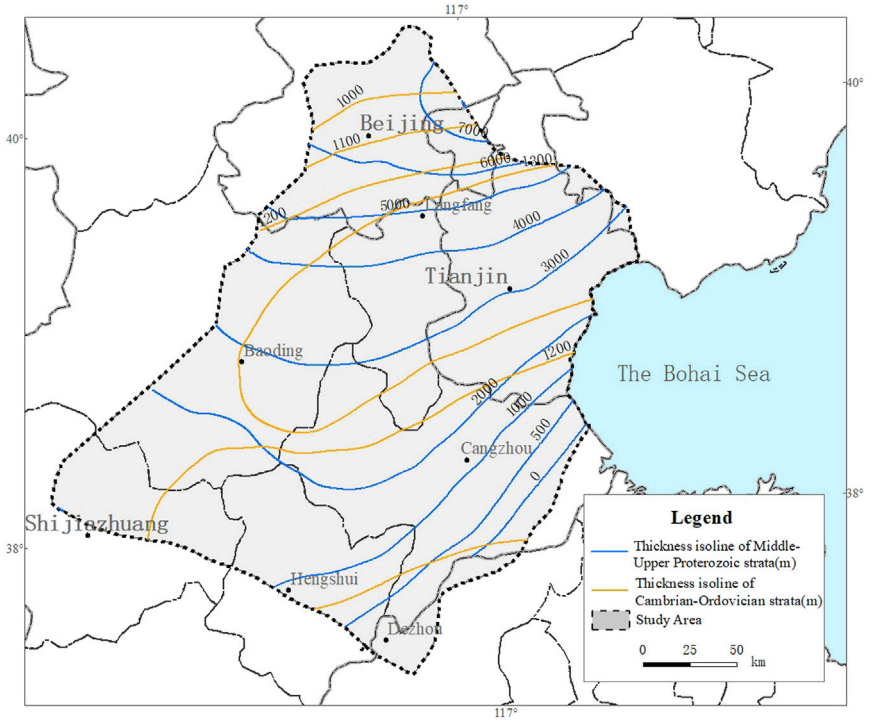

FIGURE 2
Thickness contour map of key areas in North China.

2.2 Middle-upper proterozoic geothermal reservoir

In the Beijing-Tianjin-Hebei plainStudy area, the dolomite carbonate rocks of the Jixian Wumishan formation and Gaoyuzhuang formation mainly were deposited. After the strong transformation in the later period, the karst fractures are extremely developed, and it is one of the most important geothermal reservoirs in the area. The geothermal reservoir is mainly distributed in the north-west of the Beijing-Tianjin-Hebei Plain, and the structural divisions include Jizhong depression, Cangxian uplift, and Huanghua depression, with a total thickness of 300–1000 m (Figure 2) (Chen et al., 1994; Wang et al., 2017b). In Gaoyang, Cangxian, Xianxian, and other areas in central Hebei, the overall burial depth is about 800–2000 m (Feng, 2018; Zhang et al., 2018). Due to the different geological and structural conditions, the buried depth of the geothermal reservoir is also different. Some are exposed to the surface to form peaks, and some are buried deeper than 3500 m. Karst fractures are developed and have good connectivity. The thickness of the thermal reservoir accounts for 25%–64.2% of the formation thickness, and the average effective porosity of the geothermal reservoir is 3%–6%. The water inflow of a single well is 400–1,500 m^3/d (Feng, 2018; Li et al., 2018).The geothermal reservoir temperature is generally greater than 60°C, and the highest temperature area is located in Niutuozhen swell, Xianxian swell, Dacheng swell and other places, the maximum temperature is about 130°C (Wang et al., 2017b; Feng, 2018).

3 Evaluation methods

Taking the central part of Hebei Province as an example, by selecting scientific evaluation methods, the exploration and development prospects of geothermal resources are divided into zones, which provides reliable basis for the planning and management of the middle and deep geothermal resources in north China (Liu J. L. et al., 2019). On the basis of comprehensive analysis of geothermal geological conditions in the evaluation area, this paper draws lessons from the previous technical evaluation experience of geothermal resources development and utilization suitability zoning (Liu et al., 2006; Xu C et al., 2009). The evaluation model of the analytic hierarchy process (AHP) is used to realize the quantization of division index (Liu et al., 2012).This method quantifies the decision-maker's experience and is more convenient to use when the target factors are complex and lack of necessary data, so it is widely used in practice (Guan et al., 2009). The specific analysis process mainly includes the following steps (Figure 3).

① Constructing an indicator evaluation system: By thoroughly understanding the geothermal geological background conditions and development and utilization needs of the study area, we will sort out and determine the evaluation indicators at various levels, and construct an indicator evaluation system.
② Assigning scores to each evaluation indicator: Based on the actual range of attribute values for each indicator in the study area, as well as relevant standards and experience, a grading

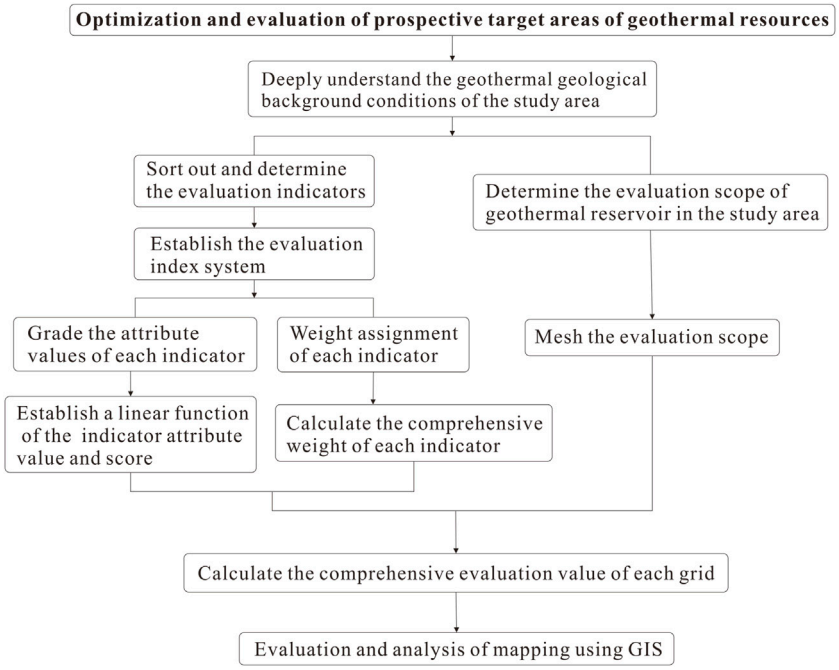

FIGURE 3
Evaluation process of prospective target areas for geothermal resources.

system is established. For each grade, a score is assigned, and a linear function is constructed between attribute values and scores to obtain the corresponding score for different attribute values.

③ Assigning weights to each evaluation indicator: Using the analytic hierarchy process to assign weights to each level of indicators and calculate the comprehensive weight value for each weight.

④ Calculating the comprehensive evaluation value of the evaluation area: Determine the evaluation scope of the thermal reservoir in the study area, and perform equal-area grid sectioning on the evaluation scope. Using the method of multi-source information superposition, that is, weighted calculation of the scores of all indicators in each grid and the corresponding comprehensive weight values in the evaluation area, the comprehensive evaluation value of each block can be obtained.

⑤ Mapping through GIS analysis: Using the spatial analysis function of GIS, the comprehensive evaluation values of each block are analyzed and mapped using kriging method, and areas with high scores are screened as prospective target areas for geothermal resources.

3.1 The determination of evaluation indicators

From the perspective of geothermal resource development, the target area for geothermal resources should have resource condition, development potential, and heating demand. Considering these three aspects, areas with good resource condition have abundant geothermal resources, high temperatures, large reservoir porosit (fissure) ratio, and reservoir effective thickness of the reservoir layer. Such areas have strong water productivity, better connectivity, and stronger heat conduction and water productivity. Areas with great development potential have better effluent capacity, shallower reservoir buried depth, and stronger economic development, areas with higher heat mining coefficients have greater development potential. Areas with high heating demand are a crucial part of the evaluation of geothermal resource development, which further strengthens the development and utilization of geothermal resources. Hebei Province is an important industrial province in China with relatively concentrated carbon emissions. In 2020, the carbon emissions were 794.18 million tons of carbon dioxide equivalent, ranking third in the country in total emissions. Therefore, areas with higher urbanization rate have a high demand for carbon neutrality. Through the above considerations, we further analyzed the geological background conditions and various factors that may be involved in the division of geothermal resources in central Hebei, summarized and classified the indicator levels, and constructed an evaluation indidicator system for the target area of geothermal resource development in central Hebei (Figure 4; Table 1). The system includes three primary evaluation indicators: the resource condition, the development potential, the heating demand; nine second-level evaluation indicators: the resources abundance, the reservoir temperature, the reservoir fissure ratio, the reservoir effective thickness, the water yield capacity, the reservoir buried depth, the heat mining coefficient, the carbon reduction quantity, the urbanization ratio.

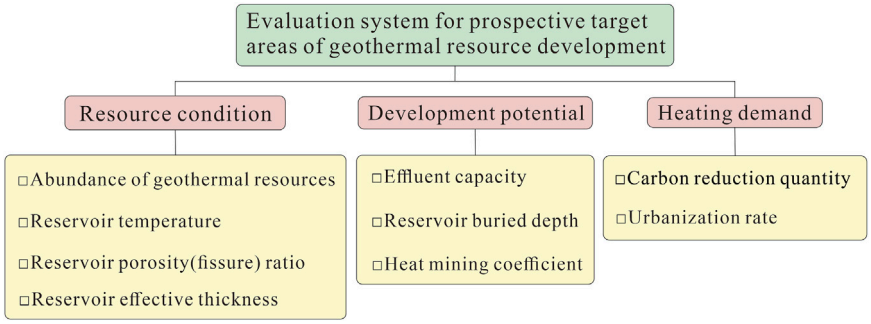

FIGURE 4
Evaluation system for prospective target areas of geothermal resource development.

TABLE 1 Grading evaluation table for evaluation indicators of prospective target areas for geothermal resources development.

First-level indicators	Second-level indicators	Level division				
		Excellent	Good	Medium	Poor	Extremely poor
Resource condition (U1)	Abundance of geothermal resources (10^{13} kJ/km^2)	Areas with excellent geothermal resources	Areas with good geothermal resources	Areas with Medium geothermal resources	Areas with poor geothermal resources	Areas with extremely poor geothermal resources
		≥8.0	[4.3, 8.0)	[2.8, 4.3)	[0.5, 2.8)	≤0.5
	Reservoir temperature (°C)	High temperature geothermal resources	Medium temperature geothermal resources	Low temperature geothermal resources		
				Hot water	Warm hot water	cool water
		≥110	[90, 110)	[60, 90)	[20, 60)	<25
	Reservoir porosity (fissure) ratio (%)	Excellent mining area	Good mining area	Medium mining area	Poor mining area	Extremely poor mining area
		≥10	[6, 10)	[3, 6)	[1, 3)	<1
	Reservoir effective thickness (m)	the area with very strong water abundance	the area with strong water abundance	he area with medium water abundance	the area with poor water abundance	the area with extremely poor water abundance
		≥500	[250, 500)	[180, 250)	[10, 180)	<10
Development potential (U2)	Effluent capacity (L/(s·m))	very strong water rich area	strong water rich area	medium water rich area	weak water rich area	very weak water rich area
		≥5	[2, 5)	[0.2, 2)	[0.1, 0.2)	<0.1
	Reservoir buried depth (m)	the most economical type	economical type	relatively economic type	economic risk type	serious economic risk type
		≤1,000	(1,000, 2000]	(2000, 3,000]	(3,000, 4,000]	>4,000
	Heat mining coefficient (%)	great exploitation potential area	good exploitation potential area	general exploitation potential area	basic equilibrium area	over exploitation potential area
		≤40	(40, 50]	(50, 70]	(70, 100]	>100
Heating Demand (U3)	Carbon reduction quantity/10^{13}kJ	excellent area of carbon emission reduction	good area of carbon emission reduction	medium area of carbon emission reduction	relatively poor area of carbon emission reduction	poor area of carbon emission reduction
		≥500	[300, 500)	[100, 300)	[50, 100)	<50
	Urbanization rate (%)	highly developed regions	developed regions	accelerated development regions	developing regions	starting development regions
		≥70	[60, 70)	[50, 60)	[40, 50)	<40

The abundance of geothermal resources (K_a): The calculation of the geothermal resources abundance is the most important scientific basis for the geothermal resources development and planning. This paper mainly uses the reservoir method to calculate the quantity of geothermal resources in accordance with the Code for Geological Exploration of Geothermal Resources (GB 11615-2010). Due to the uneven distribution of geothermal resources, the calculation of geothermal resources quantity alone cannot represent the water yield per unit area, so this paper further anchors the optimal target area by calculating the abundance of geothermal resources. The division of geothermal resource abundance (K_a) is mainly based on the background value of the geothermal resource abundance in central Hebei, which is divided into five levels.The $K_a \geq 8.0 \times 10^{13}$ kJ/km^2 is the area with excellent geothermal resources, the K_a within the range of 4.3×10^{13} kJ/km^2–8×10^{13} kJ/km^2 is the area with good geothermal resources, the K_a within the range of 2.8×10^{13} kJ/km^2–4.3×10^{13} kJ/km^2 is the area with medium geothermal resources, the K_a within the range of 0.5×10^{13} kJ/km^2–2.8×10^{13} kJ/km^2 is the area with poor geothermal resources, and when the K_a $<0.5 \times 10^{13}$ kJ/km^2 is the area with extremely poor geothermal resources. The abundance of geothermal resources is calculated according to the quantity of geothermal resources and the area of reservoir. As follows:

$$Q = C_r\rho_r(1-\varphi)V(T_1 - T_0) + C_w\rho_w q_w(T_1 - T_0) \quad (1)$$

$$K_a = Q/A \quad (2)$$

Where K_a (10^{13} kJ/km^2) is the abundance of geothermal resources, Q (kJ) is the quantity of geothermal resources, C_r (kJ/kg°C)is specific heat of heat storage rock, C_w (kJ/kg°C) 1is pecific heat of heat storage water, ρ_r (kg/m^3) is density of rock, ρ_w (kg/m^3) is density of water, φ is thermal reservoir rock porosity (or fracture rate), q_w (m^3) is fluid reserves (sum of static reserves and elastic reserves), T_1 (°C) is reservoir temperature, T_0 (°C) is temperature of constant temperature layer, V (m^3) is reservoir volume, A (km^2) is reservoir distribution area.

The reservoir temperature (T_Z): the reservoir temperature is an important parameter to measure the geothermal field, and usually has a certain corresponding relationship with the terrestrial heat flow and geothermal gradient on the plane. The higher the reservoir temperature is, the more conducive to the exploitation and utilization of geothermal resources (Kappelmeyer and Haenel, 1981). In this paper, the reservoir temperature of the bedrock top surface is obtained according to the pore-type reservoir temperature calculation method, and then the reservoir temperature from the bedrock top surface to the middle depth of the reservoir is obtained by using the bedrock geothermal gradient (generally 2.0°C/100 m), and then the two are added together, which is the temperature of the middle of the bedrock reservoir (Xu and Guo, 2009; Zhang et al., 2013).

The calculation of pore-type reservoir temperature is determined by the measured wellhead water temperature and geothermal gradient. Calculation formula:

$$T_Z = T_0 + \Delta T\left(\frac{H_1 + H_2}{2} - H_0\right) \quad (3)$$

where T_Z (°C)is the temperature in the middle of reservoir, T_0 (°C) is the temperature of constant temperature zone (same as reference temperature), ΔT (°C)is the ground temperature gradient, H_0 (m)is the depth of constant temperature zone (25 m), H_1 (m) is the buried depth of reservoir roof, H_2 (m) is the buried depth of reservoir floor.

The division of temperature in the evaluation process is based on the "GB 11615-2010 code for geological exploration of geothermal resources," $T_Z > 150$°C is high-temperature geothermal resources, 90°C< T_Z <150°C is medium temperature geothermal resources, and T_Z <90°C is low-temperature geothermal resources, of which 60°C< T_Z <90°C is hot water, 40°C< T_Z <60°C is warm hot water, and 25°C< T_Z <40°C is warm water. Medium and high temperature geothermal resources are suitable for power generation, drying and heating, and low temperature geothermal resources are suitable for bathing, aquaculture, etc,. During the evaluation process, due to the high temperature geothermal resources in the central Hebei region being around 110°C, in order to facilitate the evaluation, this article adjusted the geothermal temperature according to the specifications to $T_Z \geq 110$°C, 90°C ≤ T_Z < 110°C, 60°C ≤ T_Z < 90°C, 25°C ≤ T_Z < 60°C, and T_Z <25.

The reservoir porosity (fissure) ratio: The reservoir porosity is the proportion of pore volume per unit volume of rock (Zhou, 2005; Wang, 2013). The porosity of geothermal reservoir is one of the important parameters for evaluating geothermal resources (Yan et al., 2022), and the pore size, connectivity and filling material also have great influence on the heat transfer of rock (Wang and Sun, 2000), which reflects the water-rich nature of the thermal reservoir. According to the previous geophysical logging data and well testing data, this paper determines that the porosity of carbonate rocks in central Hebei is generally 1%–10%, so the porosity of geothermal reservoirs is divided into five levels: the reservoir porosity (fissure) ratio ≥10% is an excellent mining area, the reservoir porosity (fissure) ratio within the range of 6%–10% is a good mining area, the reservoir porosity (fissure) ratio within the range of 3%–6% is a medium mining area, the reservoir porosity (fissure) ratio within the range of 1%–3% is a poor mining area, and the reservoir porosity (fissure) ratio <1% is a very poor mining area.

The reservoir effective thickness: the reservoir effective thickness is the reservoir thickness containing geothermal fluid, which reflects the size of the thermal storage space of the geothermal reservoir. Under the same conditions, the unit area of water-rich strong in the thick section, conversely, weak. In this paper, the ratio of the bedrock geothermal reservoir thickness is based on the borehole data and referring to the regional value. Due to the uneven development of the karst fissures of the bedrock geothermal reservoir, the karst fissures near the top of the bedrock are relatively developed, With the increase of depth, its development degree gradually decreases, so when the thickness of bedrock geothermal reservoir is large, it is generally taken as a small value. The Cambrian-Ordovician reservoir thickness ratio is 20%, and the Middle-Upper Proterozoic reservoir thickness ratio is 25% (Zhang et al., 2013).

According to the calculation results of the reservoir effective thickness in central Hebei, it can be divided into five grades: the reservoir effective thickness ≥500 m is the area with very strong water abundance, the reservoir effective thickness within the range of 250–500 m is the area with strong water abundance, the reservoir effective thickness within the range of 180–250 m is the area with medium water abundance, the reservoir effective thickness within the range of 10–180 m is the area with poor water abundance, and

the reservoir effective thickness <10 m is the area with extremely poor water abundance.

The water yield capacity: the water yield capacity is reflected by the unit water inflow. The unit water inflow is the basic measurement to measure the pumping capacity of a well. The larger the value, the higher the water production capacity of the well. It is an important indicator to compare the water production capacity of the aquifer (Hudak, 2010; Zhai et al., 2013), which represents the water supply capacity of geothermal reservoir. Based on the statistics of pumping test data of geothermal wells in the study area, and according to the division of unit water inflow in the Exploration Specification of Hydrogeology and Engineering Geology in Mining Areas (GB12719-91), The water yield capacity in central Hebei is divided into five levels: the water yield capacity ≥5 $L/(s{\cdot}m)$ is a very strong water rich area; the water yield capacity within the range of 2–5 $L/(s{\cdot}m)$ is a strong water rich area; the water yield capacity within the range of 0.2–2 $L/(s{\cdot}m)$ is a medium water rich area, the water yield capacity within the range of 0.1–0.2 $L/(s{\cdot}m)$ is a weak water rich area, the water yield capacity <0.1 $L/(s{\cdot}m)$, it is a very weak water rich area.

The reservoir buried depth: the buried depth of geothermal reservoir directly affects the cost of geothermal resource exploitation. According to the Geothermal Resource Evaluation Method and Estimation Regulations (DZ/T0331-2020), if the depth is less than 1000 m, hot water above 40°C can be obtained in order to be used as an available resource (Xu and Guo, 2009). The reservoir depth is less than 1,000 m as an economic geothermal resource, while is 1,000–3,000 m as a sub economic geothermal resource. The lower limit of geothermal reservoir depth can reach 3,500 m–4,000 m. For geothermal reservoir depth greater than 3,000 m, there are significant differences in geothermal geological characteristics and utilization conditions, which is not conducive to the comprehensive evaluation of geothermal resources. According to the previous borehole data and geophysical interpretation thickness, this paper determines the buried depth of the reservoir, and then divides the buried depth of the geothermal reservoir into five levels according to the Geothermal Resource Evaluation Method and Estimation Regulations (DZ/T0331-2020), which are respectively: the reservoir buried depth ≤1,000 m is the most economical type, the reservoir buried depth within the range of 1,000–2,000 m is the economical type, the reservoir buried depth within the range of 2,000–3,000 m is the relatively economic type, the reservoir buried depth within the range of 3,000–4,000 m is the economic risk type, and the reservoir buried depth≥ 4,000 m is the serious economic risk type.

The geothermal exploitation coefficient ($\boldsymbol{C_E}$):this paper uses the geothermal exploitation coefficient of geothermal fluid index to measure the development and utilization potential of geothermal resources. The division of the geothermal exploitation coefficient is based on Geothermal Resource Evaluation Method and Estimation Regulations (DZ/T0331-2020) and the background value of the geothermal exploitation coefficient in central Hebei. $\boldsymbol{C_E}$ (%)≤40% is defined as the area with great exploitation potential, 50%≥ $\boldsymbol{C_E}$ (%)>40% as the area with good exploitation potential, 70% ≥ CE (%)>50% as the area with general exploitation potential, 100%≥ $\boldsymbol{C_E}$ (%)>70% as the area with basic equilibrium, and $\boldsymbol{C_E}$ (%) ≥100% as the area with over exploitation potential.The heat mining coefficient of geothermal fluid is calculated according to the following formula (Liu J. et al., 2019):

$$\boldsymbol{C_E = \frac{E_k}{E_y}} \tag{4}$$

where C_E (%)is heat mining coefficient; E_k (kJ/a) is exploitation heat of geothermal fluid; E_y (kJ/a) is allowable exploitation heat of geothermal fluid.

The carbon reduction quantity ($\boldsymbol{Q_k}$): The carbon emission reduction of geothermal development can be measured by the exploitable geothermal resources. When the data is less, can not determine the amount of recoverable, can be used to calculate the recovery method. According to the Evaluation Method and Estimation Regulation of Geothermal Resources (DZ/T0331 -2020), the recovery rate of karst fissure reservoir can be 15%–20%, The recovery rate of sandstone and Igneous rock fracture thermal storage can be 5%–10%. The formula for calculating the recoverable amount of geothermal resources:

$$\boldsymbol{Q_k = R_e{\cdot}Q} \tag{5}$$

where Q_k (kJ)is geothermal resource mining output, Re (%) is recovery rate, Q (kJ) is geothermal resource quantity.

The exploitable geothermal resources in this paper are calculated according to the background value of the actual exploitable geothermal resources in central Hebei, and then divided into five levels according to the range of the obtained values, which are: $\boldsymbol{Q_k}$ ≥ 500 kJ is an excellent area of carbon emission reduction, 500 kJ > $\boldsymbol{Q_k}$ ≥ 300 kJ is a good area of carbon emission reduction, 300 kJ > $\boldsymbol{Q_k}$ ≥100 kJ is a medium area of carbon emission reduction, 100 kJ > $\boldsymbol{Q_k}$ ≥ 50 kJ is a area with relatively poor of carbon emission reduction, and $\boldsymbol{Q_k}$ <50 kJ is a poor area of carbon emission reduction.

The urbanization rate: the urbanization rate is a measure of urbanization, usually using the demographics indicator, which is the proportion of the urban population in the total population (both agricultural and non-agricultural).The higher the degree of economic development, the higher the rate of urbanization, which reflects the extent of the regional demand for resources. The size of the urbanization rate reflects the heating scale degree for geothermal energy. Urbanization is closely related to urban energy consumption and its carbon emissions. For every 0.095% increase in urbanization, the total energy consumption increases by 1% (Wang Y. et al., 2020).With the development of urbanization in our country, the carbon emission presents a pattern of increasing from south to north and decreasing from east coast to inland (Wu and Jin, 2023).Therefore, geothermal resources are also an effective way to achieve dual-carbon targets in high-urbanization areas. The data of this paper is derived from the demographic data in 2019. The urbanization rate is divided into five levels: the urbanization rate ≥70 kJ are highly developed regions, the urbanization rate within the range of 60%–70% are developed regions, the urbanization rate within the range of 50%–60% are accelerated development regions, the urbanization rate within the range of 40%–50% are developing regions, and the urbanization rate <40% are starting development regions.

TABLE 2 Scoring table for evaluation indicators of prospective target areas for geothermal resource development.

First-level indicators	Second-level indicators	Evaluation grade	Attribute value interval division	Evaluation score range	Evaluation scoring algorithm
Resource condition (U1)	Abundance of geothermal resources (10^{13} kJ/km^2)	Excellent	≥8.0	9	9
		Good	[4.3, 8.0)	[7, 9)	9-2 (8-X)/(8-4.3)
		Medium	[2.8, 4.3)	[3, 7)	7-4 (4.3-X)/(4.3-2.8)
		Poor	[0.5, 2.8)	[1, 3)	3-2 (2.8-X)/(2.8-0.5)
		Extremely poor	<0.5	1	1
	Reservoir temperature (°C)	Excellent	≥110	9	9
		Good	[90, 110)	[7, 9)	9-2 (110-X)/(110-90)
		Medium	[60, 90)	[3, 7)	7-4 (90-X)/(90-60)
		Poor	[25, 60)	[1, 3)	3-2 (60-X)/(60-25)
		Extremely poor	<25	1	1
	Reservoir porosity (fissure) ratio (%)	Excellent	≥10	9	9
		Good	[6, 10)	[7, 9)	9-2 (10-X)/(10-6)
		Medium	[3, 6)	[3, 7)	7-4 (6-X)/(6-3)
		Poor	[1, 3)	[1, 3)	3-2 (3-X)/(3-1)
		Extremely poor	<1	1	1
	Reservoir effective thickness (m)	Excellent	≥500	9	9
		Good	[250, 500)	[7, 9)	9-2 (500-X)/(500-250)
		Medium	[180, 250)	[3, 7)	7-4 (250-X)/(250-180)
		Poor	[10, 180)	[1, 3)	3-2 (180-X)/(180-10)
		Extremely poor	<10	1	1
Development potential (U2)	Effluent capacity ($L/(s{\cdot}m)$)	Excellent	≥5	9	9
		Good	[2, 5)	[7, 9)	9-2 (5-X)/(5-2)
		Medium	[0.2, 2)	[3, 7)	7-4 (2-X)/(2-0.2)
		Poor	[0.1, 0.2)	[1, 3)	3-2 (0.2-X)/(0.2-0.1)
		Extremely poor	<0.1	1	1
	Reservoir buried depth (m)	Excellent	≤1,000	9	9
		Good	(1,000, 2000]	[7, 9)	9-2 (1000-X)/(1,000-2000)
		Medium	(2000, 3,000]	[3, 7)	7-4 (2000-X)/(2000-3,000)
		Poor	(3,000, 4,000]	[1, 3)	3-2 (3000-X)/(3,000-4,000)
		Extremely poor	>4,000	1	1
	Heat mining coefficient (%)	Excellent	≤40	9	9
		Good	(40, 50]	[7, 9)	9-2 (40-X)/(40-50)
		Medium	(50, 70]	[3, 7)	7-4 (50-X)/(50-70)
		Poor	(70, 100]	[1, 3)	3-2 (70-X)/(70-100)
		Extremely poor	>100	1	1
Heating Demand (U3)	Carbon reduction quantity/10^{13}kJ	Excellent	≥500	9	9
		Good	[300, 500)	[7, 9)	9-2 (500-X)/(500-300)
		Medium	[100, 300)	[3, 7)	7-4 (300-X)/(300-100)

(Continued on following page)

TABLE 2 (*Continued*) Scoring table for evaluation indicators of prospective target areas for geothermal resource development.

First-level indicators	Second-level indicators	Evaluation grade	Attribute value interval division	Evaluation score range	Evaluation scoring algorithm
		Poor	[50, 100)	[1, 3)	3-2 (100-X)/(100-50)
		Extremely poor	<50	1	1
	Urbanization rate (%)	Excellent	≥70	9	9
		Good	[60, 70)	[7, 9)	9-2 (70-X)/(70-60)
		Medium	[50, 60)	[3, 7)	7-4 (60-X)/(60-50)
		Poor	[40, 50)	[1, 3)	3-2 (50-X)/(50-40)
		Extremely poor	<40	1	1

Comments: The X in the table represents the attribute value of the indicator.

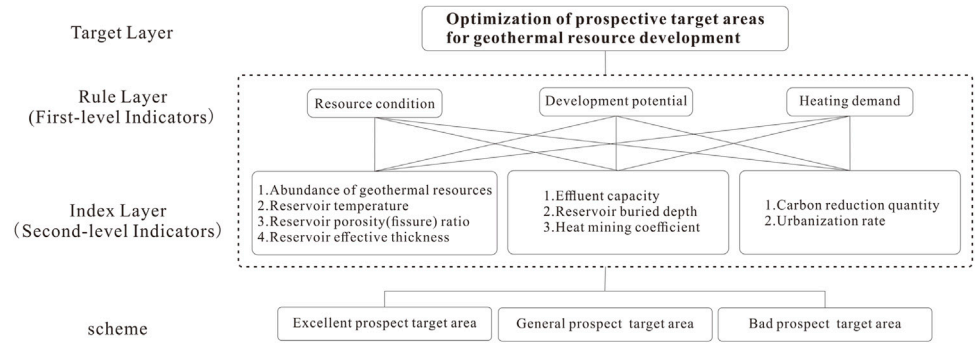

FIGURE 5
Analytic hierarchy process structure model.

3.2 The given evaluation score of the interval attribute

According to the above analysis, combined with the characteristics of deep carbonate geothermal reservoirs in central Hebei, fully considering the geothermal geological background conditions and factors affecting the development and utilization potential of geothermal resources in the central Hebei region, based on the background value of geothermal geological conditions in central Hebei, "the evaluation methods and specifications for geothermal resources" (DZ/T0331-2020), "the code for geological exploration of geothermal resources" (GB 11615-2010), "the code for hydrogeological and engineering geological survey of mining areas" (GB12719-91) and previous experience values have divided each indicator into 5 levels, (excellent, good, medium, poor, and extremely poor), and the scoring intervals of five levels are given respectively: excellent = 9, good ∈ [7–9), medium ∈ [3–7), poor ∈ [1–3), range = 1. Based on whether it is beneficial for the exploration and development of geothermal resources as a standard, the attribute interval data of each indicator is scored and quantified. The scoring algorithm is to establish a linear formula according to the evaluation interval division and evaluation score range of the indicator. Based on this, the scores corresponding to each indicator attribute value can be calculated (Table 2).

3.3 The quantification of evaluation factors weight

The weight is a quantized value which represents the effect of the lower sub-criteria relative to the upper one (Cai L., 2004). In order to ensure the reliability and credibility of the weight taken by each evaluation index factor, the analytic hierarchy process (AHP) evaluation model was used to calculate the weight of factors (Di et al., 2013). The weight of each evaluation index is evaluated comprehensively by expert scoring method and analytic hierarchy process. The analytic hierarchy process (AHP) is the relative value obtained by comparing the advantages of each index, that is the superiority weight (Zhang, 2000; Deng et al., 2012). The weight value is determined and tested by the judgment matrix. Cebi et al. (2023) used the DF-AHP method to determine the importance of pharmaceutical industry evaluation standards, Ma (2023) proposed a fuzzy hybrid AHP evaluation method for evaluating the risks of urban wind power enterprises, Deretarla et al. (2023) used Analytic Hierarchy Process (AHP) and Complex Proportional Assessment (COPRAS) to evaluate suppliers. AHP has been widely applied in various industries.

The analytic hierarchy process (AHP) is used to determine the weight of each layer in the index system, and the hierarchical structure of the evaluation index system for the optimization of geothermal resource exploration and development prospect area is

TABLE 3 The importance comparison judgment matrix of the evaluation indicators.

Optimization of prospective target areas for geothermal resource development consistency ratio of judgment matrix: 0.0032 The weight of the overall goal: 1.0000				
	Resource condition	Development potential	Heating demand	W1
Resource condition	1	1.5	2.5	0.4795
Development potential	0.6667	1	2	0.3398
Heating demand	0.4	0.5	1	0.1807
Resource condition (U1) Consistency ratio of judgment matrix: 0.0009 The weight of the overall goal: 0.4795				
Resource condition (U1)	Abundance of geothermal resources	Reservoir temperature	Reservoir porosity (fissure) ratio	Reservoir effective thickness	W2
Abundance of geothermal resources	1	0.5	0.7	1.2	0.1898
Reservoir temperature	2.0	1	1.5	2.5	0.3902
Reservoir porosity (fissure) ratio	1.4286	0.6667	1	1.5	0.2579
Reservoir effective thickness	0.8333	0.4	0.6667	1	0.1620
Development potential (U2) Consistency ratio of judgment matrix: 0.0002 The weight of the overall goal: 0.3398				
Development potential (U2)	Effluent capacity	Reservoir buried depth	Heat mining coefficient	W2
Effluent capacity	1	0.8	1.5	0.3438
Reservoir buried depth	1.25	1	1.8	0.4239
Heat mining coefficient	0.6667	0.5556	1	0.2323
Heating demand (U3) Consistency ratio of judgment matrix: 0.0000 The weight of the overall goal: 0.1807				
Heating demand (U3)	Carbon reduction quantity	Urbanization rate	W2	
Carbon reduction quantity	1	3	0.8000	
Urbanization rate	0.3333	1	0.2000	

10.3389/feart.2023.1264652

TABLE 4 The weights of evaluation indicator system.

First-level indicators	First-level weight	Second-level indicators	Second-level weight	Comprehensive weight
Resource condition	0.4795	Abundance of geothermal resources/10^{16} J/km^2	0.1898	0.091009
		Reservoir temperature (°C)	0.3902	0.187101
		Reservoir porosity (fissure) ratio (%)	0.2579	0.123663
		Reservoir effective thickness (m)	0.162	0.077679
Development potential	0.3398	Effluent capacity ($L/(s{\cdot}m)$)	0.3438	0.116823
		Reservoir buried depth (m)	0.4239	0.144041
		Heat mining coefficient (%)	0.2323	0.078936
Heating demand	0.1807	Carbon reduction quantity/10^{13}kJ	0.8	0.14456
		Urbanization rate/%	0.2	0.03614

designed, including the target layer, the rule layer (First-level indicators), the index layer (second-level indicators), and the scheme (Figure 5). The relative values between indicators are obtained through the comparison of priority and importance, and a pairwise comparison judgment matrix of importance is established. The 1–9 ratio scaling method is used to compare the importance of influencing factors. The consistency ratio of the comparison judgment matrix of the 9 evaluation indicators constructed in this evaluation is far less than 0.1, indicating satisfactory consistency, thus determining the weight values of each level. Calculate the comprehensive weight values of each indicator based on the results and interrelationships of the weight values of the two levels. The calculation method is as follows:

$$\textit{Comprehensive Weight} = \textit{First level Weight} \times \textit{Second level Weight} \tag{6}$$

According to the above method, the importance pairwise comparison judgment matrix of each level is constructed as shown in Table 3. From the calculation results, it can be seen from the calculation results that the importance of the first-level indicators in descending order is: Resource condition > Development potential > Heating demand, Weight value W1 = (0.4795, 0.3398, 0.1807); the importance of the second-level indicators in descending order is: Carbon reduction quantity > Reservoir buried depth > Reservoir temperature > Effluent capacity > Reservoir porosity (fissure) ratio > Heat mining coefficient > Urbanization rate > Abundance of geothermal > Reservoir effective thickness, Weight value W_2 = (0.8000, 0.4239, 0.3902, 0.3438, 0.2579, 0.2323, 0.2000, 0.1898, and 0.162). According to Formula 6, the comprehensive weight values of the nine indicators are obtained. From the calculation results, it can be seen that the weight values of reservoir temperature, carbon reduction quantity and reservoir buried depth are relatively high, as shown in Table 4.

3.4 The calculation of comprehensive evaluation value

In this paper, the analytic hierarchy process (AHP) and multi-source information superposition evaluation method based on GIS are applied to the zoning evaluation of hydrothermal geothermal target area. Through systemic analysis of hydrothermal geothermal influence factors, and according to the comprehensive weight of each influence factor, GIS is used to prepare single factor information map. The each single factor information map is registered and processed to form a composite superimposed evaluation model, and then the zoning evaluation map of the study area is carried out. Formula 7 is used for GIS spatial analysis and evaluation (Jin et al., 2004; Xu MJ et al., 2009).

$$\boldsymbol{P} = \sum\nolimits_{n=i} \boldsymbol{P_i A_i}\ (\boldsymbol{i} = \boldsymbol{1, 2, 3}. \ldots . \boldsymbol{n}) \tag{7}$$

Where P is the comprehensive evaluation value for the zoning of hydrothermal geothermal resource in the evaluation unit, n is the total number of the evaluation factors, P_i is the score given by the ith evaluation index, A_i is the weight of the number i evaluation index.

4 Results

Based on the in-depth understanding of the geothermal geological background conditions in the central region of Hebei Province, the evaluation indicators have been sorted out and determined, and an evaluation indicator system for the prospective target areas of geothermal resources in the study area has been constructed. Based on the principle that the higher the score is, the more favorable the mining is, the attribute values of each indicator have been classified into different levels, and a linear function between each attribute level and the scoring area has been established. According to this, the corresponding scores can be obtained based on different attribute values. The analytic hierarchy process is used to assign weights to each level of evaluation indicators, and the comprehensive weights of each evaluation indicator are calculated. While carrying out the above work, this article delineates the evaluation area based on the structural units in the study area, the cover layer with a geothermal gradient greater than 3°C/100 m, the depth of the geothermal reservoir less than 4000 m, and the distribution range of the geothermal reservoir as the boundary (Figures 6, 7). The evaluation area is divided into equal-area grids, and the weighted values of the scores and comprehensive weights of each indicator in

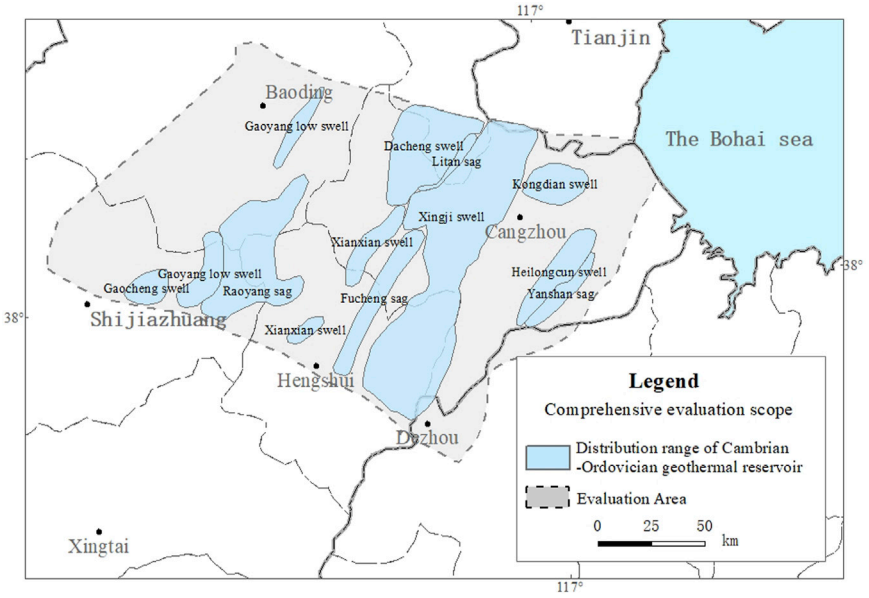

FIGURE 6
The distribution range of Cambrian-Ordovician geothermal reservoir with burial depth less than 4000 m.

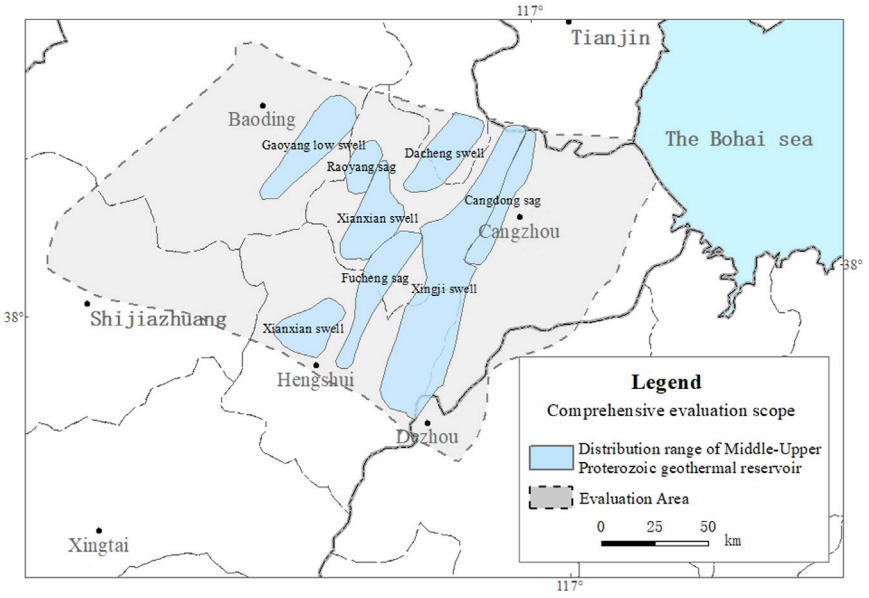

FIGURE 7
The distribution range of Middle-Upper Paleozoic geothermal reservoir with burial depth less than 4000 m.

each grid are calculated according to the formula x, which can obtain the comprehensive evaluation value of each grid. Then, using the spatial analysis function of GIS, the comprehensive evaluation value of each grid in the evaluation area is analyzed and mapped using the kriging difference method, and the geothermal resource zoning evaluation map is obtained (Figures 8, 9). From the calculation results, it is known that the regions with higher scores have a geothermal resource abundance greater than 6.0×10^{13} kJ/km^2 and an effective reservoir thickness greater than 500 m. However, the middle-upper Proterozoic geothermal reservoirs located in Xiongan New Area have a unit water inflow rate of basically greater than 5 $L/(s{\cdot}m)$, while the Cambrian-Ordovician thermal reservoirs have a unit water inflow rate of basically between 0.2 and 2 m^3 $L/(s{\cdot}m)$.

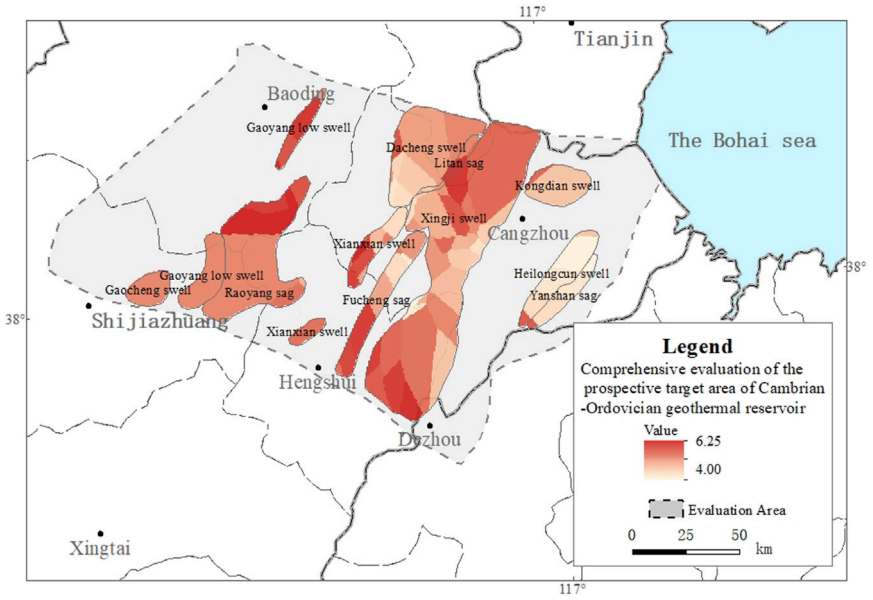

FIGURE 8
Comprehensive evaluation score of Cambrian-Ordovician geothermal reservoir. Evaluation unit in central Hebei.

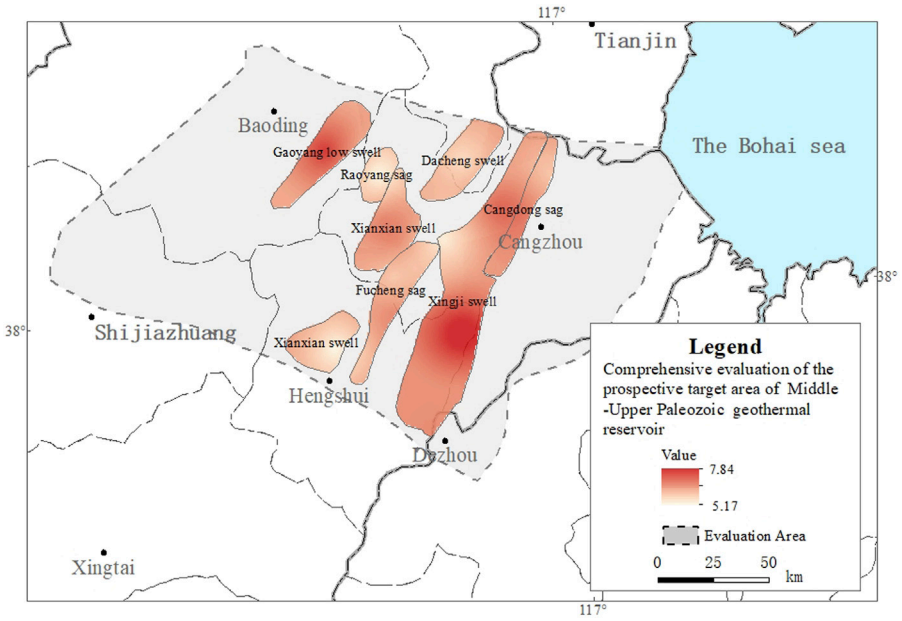

FIGURE 9
Comprehensive evaluation score of Middle-Upper Proterozoic geothermal reservoir. Evaluation unit in central Hebei.

5 Discussion

Finally, according to the evaluation results, the two sets of geothermal reservoirs are divided into three levels of prospect target areas (Figures 10, 11): the areas with evaluation score over 6.00 were classified as the excellent prospect target areas; the areas with evaluation score over 5.00 and less than 6.00 were classified as the general prospect target areas; and the areas with evaluation score less than 5.00 were classified as the bad prospect target areas. See Table 5 for the evaluation units included in the three levels of prospect target areas.

As can be seen from Figures 10, 11, due to regional differences in the characteristics of geothermal reservoirs, exploration and development prospects are not the same. The

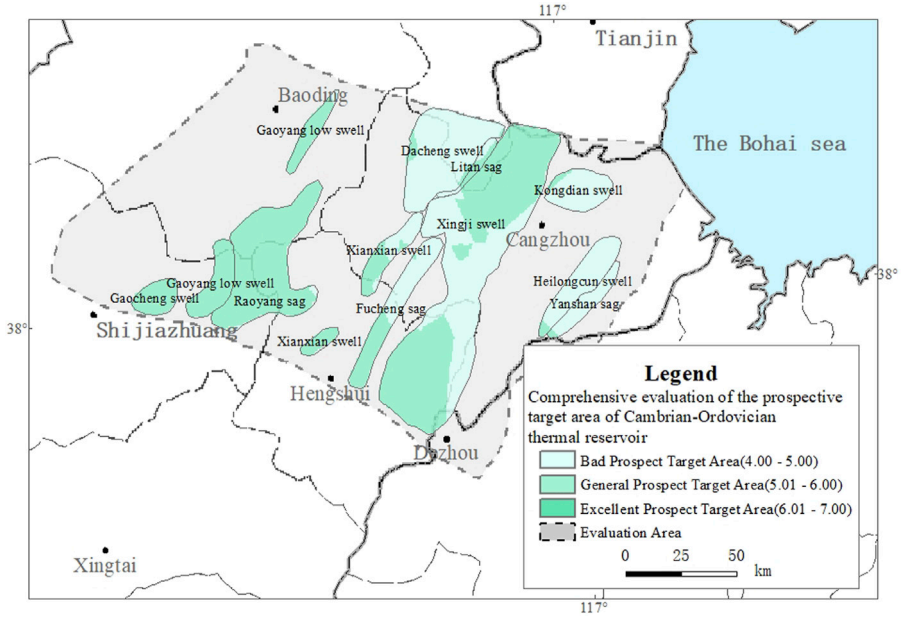

FIGURE 10
Prospective target areas of Cambrian-Ordovician geothermal reservoir.

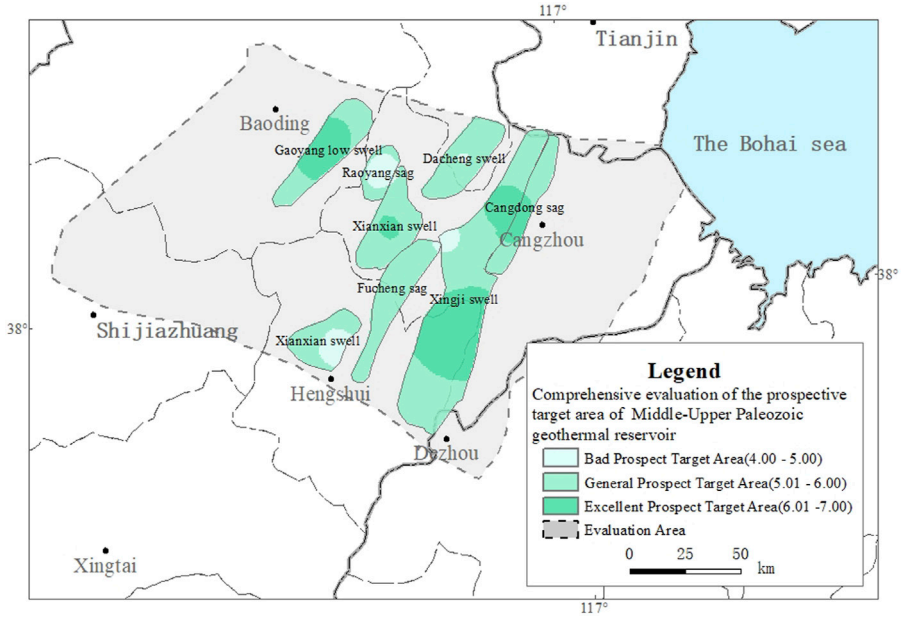

FIGURE 11
Prospective target areas of Middle-Upper Proterozoic geothermal reservoir.

Middle-Upper Proterozoic geothermal reservoir distribution area of the excellent prospect target area accounts for 56%, which is mainly located at Xingji swell, and Gaoyang low swell. For the Middle-Upper Proterozoic geothermal reservoir in the evaluation area, the regions with high geothermal abundance values are Xianxian and Dacheng. Among the Middle-Upper Proterozoic geothermal reservoirs, the geothermal resource potential in most areas of central Hebei have great exploitation potential and certain exploitation potential, including Cangxian in Cangzhou, Fucheng in Hengshui and Xiong'an New Area; There is no excellent prospective target area in the Cambrian-Ordovician

TABLE 5 Optimization selection of the prospect target area.

The target area zoning	Geothermal reservoir	Target area location
Excellent prospect target area	Middle-Upper Proterozoic	Xingji swell, Gaoyang low swell
General prospect target area	Middle-Upper Proterozoic	Xianxian swell, Dacheng swell, Fucheng sag, Xingji swell, Cangdong sag
	Cambrian-Ordovician	Raoyang sag, Gaoyang low swell, Gaocheng swell, Xianxian swell, Xingji swell
Bad prospect target area	Middle-Upper Proterozoic	Raoyang sag, Xianxian swell
	Cambrian-Ordovician	Litan sag, Yanshan sag, Xingji swell, Kongdian swell

geothermal reservoir, and the general prospective target area accounts for 54%. The northern part of Cangzhou, the northeastern part of Hengshui, and the border among the Shijiazhuang, and the junction of Shijiazhuang, Baoding and Hengshui all have certain exploitation potential.

According to the statistics of the distribution area of favorable areas of geothermal reservoirs at all levels, the geothermal reservoir distribution area of the excellent prospect target area accounts for 28%, and the Middle-Upper Proterozoic geothermal reservoirs mainly distributed in Xiong'an New Area, the eastern part of Hengshui, and the central part of Cangzhou; The geothermal reservoir distribution area of the general prospect target area accounts for 46%, and the distribution area of Cambrian-Ordovician geothermal reservoirs is slightly larger; The geothermal reservoir distribution of the bad prospect target area accounts for 26%, and the distribution area are mainly Cambrian-Ordovician geothermal reservoirs. From the comprehensive evaluation results, it can be seen that the Middle-Upper Proterozoic geothermal reservoir target area is relatively large, and the proportion of favorable target areas with better conditions is relatively large.

This article uses a quantitative zoning evaluation method to assess the prospective target areas for geothermal resources in the central Hebei region from the perspective of development and utilization. It delineates the exploration and development target areas for deep geothermal resources in the central Hebei region within a large area. This evaluation method is also applicable to the screening of resource development prospects in other regions, such as carbon sequestration, shallow geothermal energy resource development, and deep dry hot rock resource development.

From the perspective of resource utilization and sustainable development, in order to maximize the availability of geothermal resources for economic construction services, the reasonable planning and development of geothermal resources can greatly supplement the consumption of energy resources. This evaluation provides grounds for the sustainable development and utilization of the geothermal resources in North China Plain. Under the current situation, the large-scale and sustainable development and utilization of geothermal energy is part of the implementation of General Secretary Xi Jinping's National Energy Security Strategy, which is a response to global climate change. Implementing that strategy requires energy conservation and emission reduction via concrete measures to help achieve the goal of a "2030 carbon peak and 2060 carbon neutrality" (Liu et al., 2023).

6 Conclusion

(1) Based on the geothermal geological conditions in the central Hebei region, this article establishes a comprehensive evaluation index system for the favorable areas of deep geothermal development in the central Hebei region from three aspects: resource conditions, development potential, and heating demand. By combing the relevant indicators for the development and utilization of geothermal energy in the central Hebei region, a linear function is constructed based on the evaluation interval values of the indicator attributes and the corresponding score ranges. The analytic hierarchy process is used to assign weights to each indicator, which prepares for the weighted calculation of the comprehensive evaluation value of each block in the evaluation area. Finally, the GIS is used to analyze and evaluate each indicator by superimposing them, that is, to comprehensively weight and score each indicator in each section of the evaluation area, and to optimize the comprehensive score of the high-scoring areas as the prospective target areas.This evaluation method can provide a reference for optimizing the exploration and development goals of geothermal resources in key areas.

(2) According to the evaluation results, from the perspective of regional structure, the excellent prospective target areas of the Middle-Upper Proterozoic geothermal reservoirs are mainly located in the Xingji uplift and the Gaoyang low uplift, and the excellent prospective target areas of the Middle-Upper Cenozoic geothermal reservoirs account for 56%. The geothermal resource abundance in these areas is greater than 8.0×10^{13} kJ/km^2, with good resource development potential. It is suitable for the exploration and development of geothermal resources. From the perspective of geographical division, Xiong'an New Area, Cangzhou, and the eastern part of Hengshui are the excellent prospective target areas in the Middle-Upper Proterozoic geothermal reservoir evaluation unit.

(3) This assessment provides a reference basis for the sustainable development and exploitation of geothermal resources in the North China Plain. At the same time, it also provides new ideas for the optimization and evaluation of regional target areas in other resource and energy fields.

Data availability statement

The raw data supporting the conclusion of this article will be made available by the authors, without undue reservation.

Author contributions

HX: Data curation, Investigation, Methodology, Software, Writing–original draft, Writing–review and editing. YY: Investigation, Methodology, Writing–review and editing. SG: Investigation, Methodology, Writing–review and editing. JS: Investigation, Methodology, Writing–review and editing. WS: Data curation, Writing–review and editing. JL: Methodology, Project administration, Writing–review and editing. ZF: Data curation, Writing–review and editing.

Funding

The author(s) declare financial support was received for the research, authorship, and/or publication of this article. This research was supported by China Geological Survey project (DD20221680/DD20190127).

Acknowledgments

We thank the CNOOC Research Institute Ltd. and the individuals who contributed to this work.

Conflict of interest

Author SG was employed by CNOOC Research Institute Ltd.

The remaining authors declare that the research was conducted in the absence of any commercial or financial relationships that could be construed as a potential conflict of interest.

Publisher's note

References

Cai, L. (2004a). The fuzzy mathematics methods of determining weight in modeling and simulation. *Teach. Technol.* 2, 23–25.

Cai, Y. H. (2004b). *Geothermal direct utilization*. Tianjin: Tianjin Ancient Literature Press, 488–628.

Cebi, S., Gündoğdu, F. K., and Kahraman, C. (2023). Consideration of reciprocal judgments through Decomposed Fuzzy Analytical Hierarchy Process: a case study in the pharmaceutical industry. *Appl. Soft Comput.* 134, 110000. doi:10.1016/j.asoc.2023.110000

Chen, M. X. (1988). *North China geothermal*. Beijing: Science Press, 89–106.

Chen, M. X., Wang, J. Y., Deng, X., Hu, S. B., Huang, S. P., Pang, Z. H., et al. (1994). *China geothermal resources-formation characteristics and potential assessment*. Beijing: Science Press, 90–123.

Ciriaco, A. E., Uribe, M. H., Zarrouk, S. J., Downward, T., Omagbon, J. B., Austria, J. J. C., et al. (2022). Probabilistic geothermal resource assessment using experimental design and response surface methodology: the Leyte geothermal production field. *Geothermics* 103, 102426. doi:10.1016/j.geothermics.2022.102426

Ciriaco, A. E., Zarrouk, S. J., Zakeri, G., and Mannington, W. I. (2020). Refined experimental design and response surface methodology workflow using proxy numerical models for probabilistic geothermal resource assessment. *Geothermics* 88, 101911. doi:10.1016/j.geothermics.2020.101911

Deng, X., Li, J. M., Zeng, H. J., Chen, J. Y., and Zhao, J. F. (2012). Research on computation methods of AHP wight vector and its applications. *Math. Pract. Theory* 7, 93–99. doi:10.3969/j.issn.1000-0984.2012.07.012

Deretarla, Ö., Erdebilli, B., and Gündoğan, M. (2023). An integrated Analytic Hierarchy Process and Complex Proportional Assessment for vendor selection in supply chain management. *Decis. Anal. J.* 6, 100155. doi:10.1016/j.dajour.2022.100155

Di, Y. H., Wu, Y. L., and Jiang, H. (2013). Scheme optimization of geothermal project based on grey relational analysis and analytical hierarchy process. *Refrig. Air Cond.* 2, 164–169. doi:10.3969/j.issn.1671-6612.2017.02.011

Feng, B. B. (2018). *Geothermal resource potential research in central area of ji zhong depression*. master's thesis. Beijing: China University of Geosciences.

Feng, W. J., and Cao, B. (2007). Geoheat resources evaluation and target optimization in Gaoyou region of Jiangsu. *Jiangsu Geol.* 2, 130–133. doi:10.3969/j.issn.1674-3636.2007.02.010

Gao, Z. X. (2009). The summarization of geothermal resources and its exploitation and utilization in Shandong province. *J. Shandong Univ. Sci. Technol.* 28 (2), 1–7. doi:10.3969/j.issn.1672-3767.2009.02.001

Gong, Y. L. (2011). *Geothermal structure and thermal evolution of the Bohai Bay basin in eastern China*. Beijing: China Atomic Energy Press, 1–18.

Guan, S. Y., Long, Z. G., and Miao, Z. (2009). The adaptive partition of groundwater source heat pump system application in wuhan city. *City Surv.* 5, 143–146. doi:10.3969/j.issn.1672-8262.2009.05.043

Hudak, F. (2010). *Principles of Hydrogeology 3rd*. Milton Park: Taylor& Francis Group LLC, 73–84.

Jiang, D. D., Jiang, W. W., and Hu, J. W. (2013). Study of crustal structure and geodynamic characteristics around the Bohai Sea area. *Prog. Geophys.* 4, 1729–1738. CNKI:SUN:DQWJ.0.2013-04-015. doi:10.6038/pg20130413

Jin, J. L., Wei, Y. M., and Ding, J. (2004). Fuzzy comprehensive evaluation model based on i mproved analytic hierarchy process. *J. Hydraulic Eng.* 3, 65–75. doi:10.3321/j.issn:0559-9350.2004.03.011

Kappelmeyer, O., and Haenel, R. (1981). *Geothermics with special reference to application*. Beijing: Science Press, 23–28.

Li, J., and Zhang, Z. (2018). Characteristics of geothermal resources in Jizhong depression (Hebei region). *J.Hebei Univ. Technol.* 47 (2), 113–120. doi:10.14081/j.cnki.hgdxb.2018.02.020

Li, S. T., Zhang, S. Q., Jia, X. F., Xu, T. F., Ren, T., and Li, F. C. (2018). Index system research of project site selection for dry hot rocks exploration. *Geol. Surv. China* 2, 64–72. doi:10.19388/j.zgdzdc.2018.02.10

Lin, W. J., Liu, Z. M., Wang, W. L., and Wang, G. L. (2013). The assessment of geothermal resources potential of China. *Geol. China* 1, 312–321. doi:10.3969/j.issn.1000-3657.2013.01.021

Liu, C., Huang, L., Zhang, D., Zhao, J., Deng, Y., Guo, P., et al. (2018). Genetic causes of oil-rich and oil-poor reservoirs: implications from two Cenozoic basins in the eastern North China Craton. *Sci. China. Earth Sci.* 61, 1910–1931. doi:10.1007/s11430-017-9271-6

Liu, G. Y., Zhao, Z. X., Ren, L., and Meng, L. J. (2022b). Study and application of the evaluation system concerning the hydrothermal type geothermal resource at the middle and deep layers of sedimentary basin. *Oil, gas new energy* 2, 38–54. doi:10.3969/j.issn.2097-0021.2022.02.007

Liu, J., Han, S., Yang, F., and Yue, D. (2023). The hydraulic connection analysis of dongying geothermal fluid using hydrochemical information and isotope data in tianjin coastal regions. *Water-Sui.* 15, 1235. doi:10.3390/w15061235

Liu, J., Song, M. Y., Qin, L. H., Yu, Y., Lin, W., and Kang, N. (2019a). Division of potential geothermal resources zones in the Wumishan Formation in Tianjin. *Contributions Geol. Mineral Resour. Res.* 2, 321–325. CNKI:SUN:DZZK.0.2019-02-021. doi:10.6053/j.issn.1001-1412.2019.02.021

Liu, J. L., Lin, L., and Chen, W. Q. (2012). Suitability division evaluation of groundwater source heat pump system in Tianjin. *J. Jilin Univ. (Earth Sci. Ed.* 12, 380–386. doi:10.13278/j.cnki.jjuese.2012.s1.027

Liu, J. L., Wei, X. P., Chen, W. Q., Tian, G. H., Qin, L. H., and Wang, L. L. (2019b). Geothermal liquid enrichment conditions and exploration & production prospect division of Dongying geothermal resources in Tianjin Binhai New Area. *J. Hebei Geo Univ.* 2, 20–25. doi:10.13937/j.cnki.hbdzdxxb.2019.02.004

Liu, L. C., Wang, J. S., Zhang, N., and Guo, M. L. (2006). Suitability division for water source heat pumps in the central districts of Beijing. *Hydrogeology Eng. Geol.* 6, 15–17. doi:10.1016/S1872-2040(06)60004-2

Liu, Z. M., Liu, L. G., Zhen, G. L., Qi, R. Y., Wang, J. M., Zhao, Y., et al. (2022a). Study on suitability evaluation system of urban geological conditions in Beijing. *Urban Geol.* 2, 164–174. doi:10.3969/j.issn.1007-1903.2022.02.007

Ma, Y. (2023). Research on safety risk assessment method of wind power enterprises based on hybrid analytic hierarchy process. *J. Phys. Conf. Ser.* 2418, 012084. doi:10.1088/1742-6596/2418/1/012084

Mao, X., Luo, L., Wang, X. W., and Guo, D. B. (2020). Distribution characteristics of cenozoic volcanic rocks and its geothermal exploration potential in Bohai bay basin. *Geoscience* 4, 858–864. doi:10.19657/j.geoscience.1000-8527.2020.04.21

Pang, Z. H., Luo, J., Cheng, Y. Z., Duan, Z. F., Tian, J., Kong, Y. L., et al. (2020). Evaluation of geological conditions for the development of deep geothermal energy in China. *Earth Sci. Front.* 1, 134–151. doi:10.13745/j.esf.2020.1.15

Qiu, N. S. (2004). *Theory and application of geothermal regime in sedimentary basin*. Beijing: Petroleum Industry Press, 133–167.

Quinao, J. J. D., and Zarrouk, S. J. (2018). Geothermal resource assessment using experimental design and response surface methods: the Ngatamariki geothermal field, New Zealand. *Renew. Energ.* 116, 324–334. doi:10.1016/j.renene.2017.09.084

Wang, D., Liang, H. J., Huang, J. C., and Liu, R. (2022a). Development path of Chinese geothermal business under carbon peaking and carbon neutrality targets. *Petroleum&Petrochemical Today* 5, 6–15.

Wang, D. C. (2013). *Fundamentals of Hydrogeology*. Beijing: Geological Press, 15.

Wang, G. L., Liu, Y. G., Zhu, X., and Zhang, W. (2020a). The status and development trend of geothermal resources in China. *Earth Sci. Front.* 1, 1–9. doi:10.13745/j.esf.2020.1.1

Wang, G. L., Zhang, W., Liang, J. Y., Lin, W. J., and Wang, W. L. (2017a). Evaluation of geothermal resources potential in China. *Acta Geosci. Sin.* 4, 449–459. doi:10.3975/cagsb.2017.04.02

Wang, G. L., Zhang, W., Lin, W. J., Liu, F., Zhu, X., Liu, Y., et al. (2017b). Research on formation mode and development potential of geothermal resources in Beijing-Tianjin-Hebei region. *Geol. China* 6, 1074–1085. doi:10.12029/gc20170603

Wang, J., and Zhou, J. P. (1992). *Medium and low temperature geothermal resources in the North China Plain and its environmental impacts*. Beijing: Seismological Press, 1–4.

Wang, J. Y., and Sun, Z. X. (2000). *Magic geothermal*. Beijing: Tsinghua University Press, 18.

Wang, T. H. (2019). Evaluation of geothermal resources and target selection in Shandong province. *Explor. Dev.* 7, 114–115. doi:10.3969/j.issn.1006-0235.2019.07.062

Wang, T. H., Wang, X. W., Mao, X., Luo, L., Gao, N. A., Liu, H. Y., et al. (2022b). Characteristics and development potential of geothermal resources in northern Cangxian uplift. *Geol. China* 6, 1747–1764. doi:10.12029/gc20220604

Wang, Y., Tan, D., Zhang, J., Meng, N., Han, B., and Ouyang, Z. (2020b). The impact of urbanization on carbon emissions: analysis of panel data from 158 cities in China. *Acta Ecol. Sin.* 21, 7897. doi:10.5846/stxb201911292591

Wu, J. S., and Jin, X. R. (2023). Analysis of carbon emissions and influencing factors in China based on city scale. *Environ. Sci.* 5, 2974–2982. doi:10.13227/j.hjkx.202205326

Xu, C., Dai, F. C., Yao, X., Chen, J., and Wang, Z. (2009). GIS-based landslids susceptibility assessment using analytical hierarchy process in Wenchuan earthquake region. J. *Chin. J. Rock Mech. Eng.* 28, 3978–3985. doi:10.3321/j.issn:1000-6915.2009.z2.100

Xu, M. J., Jiang, Y., Xie, Z. H., and Wang, X. J. (2009). Study on division of the appr opriate rank of water source heat pumps based on AHP in Beijing plain. *Anal. Study* 1, 10–14. doi:10.3969/j.issn.1007-1903.2009.01.004

Xu, S. G., and Guo, Y. S. (2009). *Fundamentals of geothermal science*. Beijing: Science Press, 132–137.

Yan, D. S., and Yu, Y. T. (2000). *Evaluation and utilization of geothermal resources in Beijing-Tianjin-Hebei oil region*. Beijing: China University of Geosciences Press, 8–62.

Yan, J. H., Wang, S. J., and Yao, Y. H. (2022). *Evaluation and development practice of geothermal resources in oil region*. Beijing: Petroleum Industry Press, 19–20.

Zhai, Y. Z., Wang, J. S., Teng, Y. G., and Zuo, R. (2013). Humble opinion on assessment indices for groundwater renewability: applicability of renewal period and recharge rate. *Adv. Water Sci.* 24, 56–61. doi:10.14042/j.cnki.32.1309.2013.01.014

Zhang, D. Z., Liu, Z. G., and Lu, H. L. (2013). *Hebei geothermal energy*. Beijing: Geological Press, 100–125.

Zhang, D. Z., Ma, Y. Q., and Su, Y. Q. (2018). Study on the calculation of geothermal fluids recoverable quantity and the distribution law of karst geothermal reservoirs in Hebei Plain. *Geol. Surv. China* 5, 78–85. doi:10.19388/j.zgdzdc.2018.02.12

Zhang, J., Fang, G., and He, Y. B. (2023). The deep high temperature characteristics and geodynamic background of geothermal anomaly areas in Eastern China. *Earth Sci. Front.* 2, 316–332. doi:10.13745/j.esf.sf.2022.1.20

Zhang, J. J. (2000). Fuzzy analytical hierarchy process. *Fuzzy Syst. Math.* 2, 80–88. CNKI:SUN:MUTE.0.2000-02-015.

Zhang, Y. J., Yu, H., Li, J. M., Yu, Z., and Zhang, J. (2016a). Prediction models of deep hydrothemal geothermal potential areas based on GIS: ACase study of western Anatolia, Turkey. *J. Jilin Univ. (Earth Sci. Ed.* 3, 855–864. doi:10.13278/j.cnki.jjuese.201603207

Zhang, Y. J., Zhu, C. C., Yu, H., Lei, H. L., and Lü, T. Q. (2016b). Evaluation of geothermal resources potential on GIS and fuzzy logic theory. *J. Eng. Geol.* 24, 1173–1178. doi:10.13544/j.cnki.jeg.2016.s1.170

Zhou, N. L. (2005). *Practice book of geothermal resources development and utilization*. Beijing: Chinese geological Science Press, 73.

frontiers | Frontiers in Earth Science

TYPE Original Research
PUBLISHED 29 December 2023
DOI 10.3389/feart.2023.1277520

OPEN ACCESS

EDITED BY
Yingfeng Sun,
University of Science and Technology Beijing, China

REVIEWED BY
Chang'An Wang,
Xi'an Jiaotong University, China
Zhiqiang Wu,
Xi'an Jiaotong University, China

*CORRESPONDENCE
Pengfei Jiang,
jiangpf@xust.edu.cn

RECEIVED 14 August 2023
ACCEPTED 28 November 2023
PUBLISHED 29 December 2023

CITATION
Yang F, Jiang P, Duan Z, Cheng Z and Wang Z (2023), Quantitative characterization and analysis of pore-fractures in tar-rich coal under high-temperature pyrolysis based on micro-CT imaging.
Front. Earth Sci. 11:1277520.
doi: 10.3389/feart.2023.1277520

Quantitative characterization and analysis of pore-fractures in tar-rich coal under high-temperature pyrolysis based on micro-CT imaging

Fu Yang[1,2], Pengfei Jiang[1,2,3]*, Zhonghui Duan[1,2], Zhongyan Cheng[4] and Zhendong Wang[1,2]

[1]Key Laboratory of Coal Resources Exploration and Comprehensive Utilization, Ministry of Natural Resources, Xi'an, China, [2]Shaanxi Coal Geology Group Co., Ltd, Xi'an, China, [3]College of Geology and Environment, Xi'an University of Science and Technology, Xi'an, China, [4]School of Highway, Chang'an University, Xi'an, China

This study investigates pore distribution and permeability behavior of tar-rich coal following high-temperature pyrolysis at 500°C using X-ray computed tomography (CT) scanning. Coal samples post-pyrolysis were CT scanned, generating 1755 cross-sectional slices for three-dimensional reconstruction. An axial algorithm extracted pore distribution features, and geometric parameters were computed. An Equivalent Pore Network Model analyzed permeability characteristics. The results show that Post-pyrolysis pore distribution in tar-rich coal exhibited nonuniformity with a significant range in pore size distribution. Pores displayed concentrated spatial patterns. Total porosity was 14.24%, with 12.34% being connected. Most pores in Representative Elementary Volume (REV) regions fell within 10–50 μm in width and 20–60 μm in length, constituting over 40% of the total. Pore surface area peaked between 200–100 μm^2, also comprising over 40% of the total. The Pore Network Model showed distinct characteristics in two REV regions: REV-1 demonstrated an early stage of development with poor connectivity, while REV-2 displayed a well-developed network with a bimodal coordination number histogram. The study highlights nonuniform post-pyrolysis pore distribution and significant pore size variations in tar-rich coal. This study is crucial for understanding permeability behavior in tar-rich coal after high-temperature pyrolysis.

KEYWORDS

tar-rich coal, high temperature pyrolysis, pore structure, equivalent Pore Network Model, coordination number

1 Introduction

Coal, as the predominant global energy resource, finds extensive application in sectors such as power generation, heating, industrial production, and transportation (Li, 2021). In the realm of power generation, coal plays a pivotal role, constituting approximately 36% of the global energy mix (Wolde-Rufael and Yemane, 2010; Okoye-Chine and George, 2022). While many countries internationally are fostering the advancement and utilization of clean energy sources such as wind, solar, and

hydropower (Jiang et al., 2010), the staggering worldwide coal production remains noteworthy. According to estimations by the International Energy Agency, global coal reserves are estimated to be around 11.395 billion metric tons. Furthermore, coal stands as the world's second-largest energy resource, contributing to approximately a quarter of primary energy consumption, trailing only behind petroleum at 31.2% (IEA, 2018). Therefore, considering trends over recent decades, coal's development still presents substantial prospects.

In recent years, tar-rich coal has garnered increasing attention due to its high tar content and abundant oil and gas resources (Zhang et al., 2013; Ju et al., 2021). Research indicates that the pyrolysis of one metric ton of tar-rich coal generates approximately 10% oil and 500 cubic meters of combustible gas. Notably, China possesses substantial reserves of tar-rich coal, with the Shaanxi Province in western China alone harboring reserves of 150 billion metric tons (Ju et al., 2021). As a significant consumer of petroleum, China's abundant reserves of tar-rich coal, with their substantial tar resources, could offer an effective supplement to the nation's petroleum supply. Rational development and utilization of tar-rich coal have the potential to provide a valuable complement to China's petroleum supply. Relevant studies suggest that, considering a tar content of 10%, the potential petroleum resource from the exploitation of tar-rich coal in Shaanxi Province could reach up to 1.29 billion metric tons (Cheng, 2019).

Tar-rich coal, characterized by its abundant organic matter and tar content, exhibits a complex porous structure within its coal matrix (Xin et al., 2019). The porous network can be classified into four categories: micropores (diameter <10 nm), transitional pores (diameter 10–100 nm), mesopores (diameter 100–1,000 nm), macropores (diameter 1,000–10000 nm), and microcracks (diameter >10,000 nm) (Hodot, 1966). Among these, micropores, though smaller in size, possess a larger surface area, rendering them highly efficient and capable of accommodating substantial gas and liquid adsorption and storage (Mastalerz et al., 2008). Conversely, the presence of macroporous structures, characterized by larger diameters, confers advantages in gas storage and gas-liquid transport (Giffin, S et al., 2013). The extraction of tar involves *in-situ* underground pyrolysis, wherein tar-rich coal is heated to pyrolysis temperatures in its original geological layer and the resulting oil and gas products are subsequently extracted through drilling. The process of pyrolysis induces significant alterations in the pore structure of tar-rich coal, and the generated oil and gas products must flow through the high-temperature pyrolysis zone before they can be collected. Consequently, the investigation and quantitative characterization of the pore network structure during high-temperature pyrolysis of tar-rich coal hold paramount importance for optimizing and applying gas extraction, storage, and pyrolysis technologies.

With the advancement of technology, various research methods have emerged for studying pore network structures, including low-temperature gas adsorption, electron microscopy, mercury intrusion porosimetry, and nuclear magnetic resonance (Yao et al., 2008; Li et al., 2015; Nie et al., 2015; Zhao, 2017). CT technology is a non-destructive technique that does not damage the tested object, thus improving the accuracy of research data. It has significant advantages in studying the distribution characteristics of porous network structures and spatial flow features in objects. Therefore, CT technology is a more comprehensive and higher-resolution research method, facilitating the easier acquisition of relevant information about the porous structure of objects, particularly suitable for complex samples such as coal. Golab et al. (2013) utilized CT scanning to examine the three-dimensional distribution of minerals and pore fractures. Li et al. (2017) employed X-ray μ-CT to quantitatively analyze different pore sizes in bituminous and anthracite coal, establishing an equivalent pore network model to analyze permeability properties. Ni et al. (2017) quantitatively characterized large pores in coal using CT technology and performed numerical simulations of permeability based on three-dimensional reconstructions of coal samples. Currently, research on quantitative analysis of tar-rich coal after high-temperature pyrolysis using CT technology is relatively limited. This study aims to quantitatively characterize the pore structure of tar-rich coal after high-temperature pyrolysis, establish an equivalent network model, and analyze its permeability characteristics, providing guidance for *in-situ* pyrolysis processes of tar-rich coal.

In this study, Chinese tar-rich coal samples from Shanxi were selected for X-ray CT scanning after cooling to room temperature following pyrolysis at 500°C. A total of $1755^{-\Delta\Delta CT}$ slices were obtained and used for three-dimensional reconstruction. The pore distribution features of the coal samples after high-temperature pyrolysis were analyzed. Connected pores and isolated pores were extracted, their geometric parameters were analyzed, and a quantitative characterization was conducted. Subsequently, an equivalent pore network model (PNM) was established to investigate the developmental characteristics and pore flow properties of tar-rich coal after high-temperature pyrolysis. The aim of this study is to deepen the understanding of pore characteristics in tar-rich coal after high-temperature pyrolysis and to provide a scientific basis for the efficient development and utilization of tar-rich coal.

2 Experiment and method

2.1 Sample collection

The experimental samples were collected from the Jurassic coal seam in the Shenfu mining area of northern Shaanxi, China, at a burial depth of approximately 400 m. Industrial analysis and elemental analysis data are presented in Table 1. The original coal is cut and sanded to a smooth surface and polished to achieve a smooth surface, with dimensions approximately measuring 3.5 cm × 3.5 cm × 1.5 cm. The experimental specimens were subjected to heating under a nitrogen (N2) environment, reaching a temperature of 500°C over a duration of 2 h, followed by natural cooling to room temperature, yielding the tar-rich coal samples post high-temperature pyrolysis.

TABLE 1 Physical properties of tar-rich coal.

Industrial analysis (%)				Elemental analysis (%)			
Moisture content (M_{ad})	Ash content (A_{ad})	Volatile matter (V_{ad})	Fixed carbon (FC_{ad})	C_{ad}	H_{ad}	N_{ad}	S_{ad}
6.78	8.45	36.58	48.19	76.02	5.08	0.75	0.52

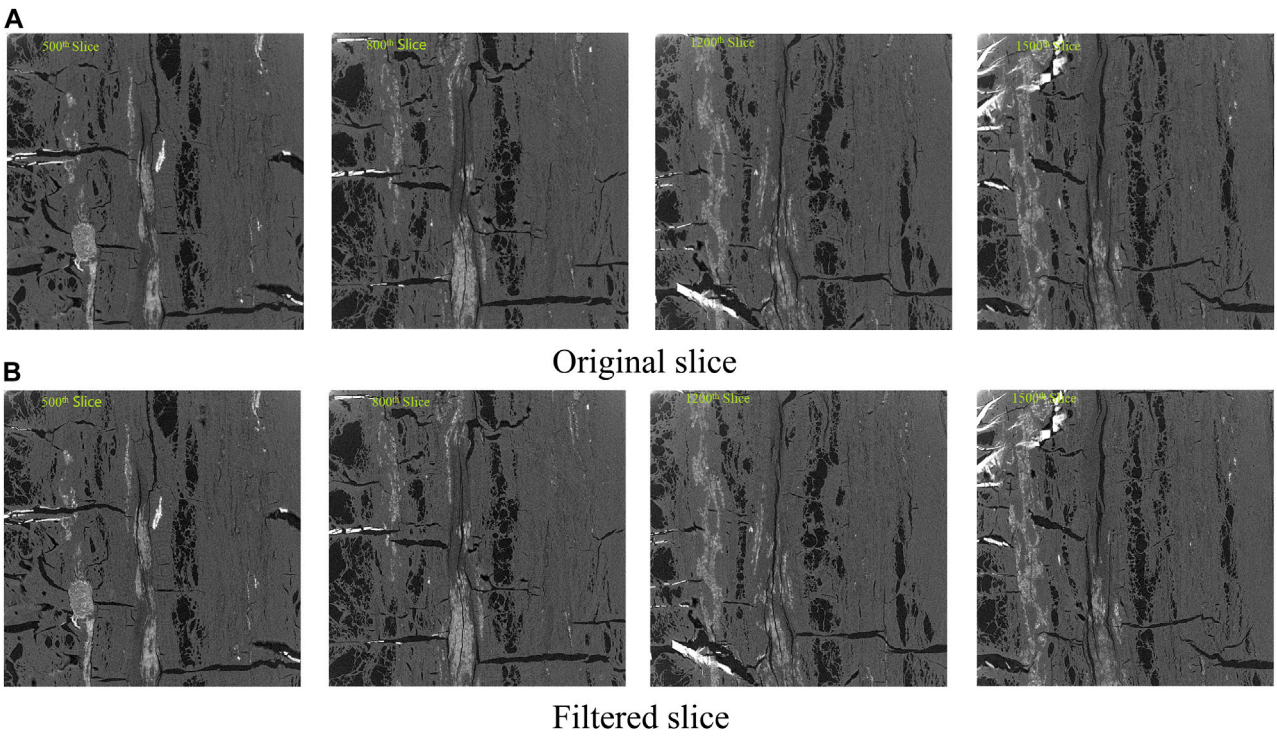

FIGURE 1
Original and filtered slice.

2.2 CT scan technical parameters

The CT scanning device employed in this study is the advanced Nikon XTH 320 X-ray inspection system. The test sample was a 7 mm cube sample. The instrument utilizes a cone-beam scanning mode, operating at a voltage of 119 kV and a current of 120 μA. Given the consideration of the high-temperature (500°C) pyrolyzed coal samples and the need for spatial resolution and noise control, This study determined that the spatial resolution of the CT scanner was 3.9 μm. The scanning process was conducted at a speed that resulted in an exposure time of 1 s per projection. Ultimately, a total of 1755 slices were acquired, each with a cross-sectional area of voxels and a thickness of 3.9 μm per slice.

2.3 CT digital image processing

2.3.1 Preprocessing of CT images

Due to the physical uncertainty of X-rays and the statistical limitations during the acquisition process, CT images inevitably exhibit noise. Therefore, it is crucial to apply filtering algorithms to CT images to eliminate noise, as this process significantly impacts subsequent image post-processing (Jing et al., 2017). Commonly used filtering algorithms include Convolution Filtering, Median Filtering, Gaussian Filtering, and Mean Filtering (Basran Parminder, 2011; Sun, 2022). The specific choice of filtering algorithm depends on the actual image characteristics. In this study, after performing calculations and trials with various algorithms, the unsharp masking algorithm was selected. One prominent feature of this algorithm is its ability to enhance image edges and details. This enables the capture of finer details during image post-processing, reducing errors in subsequent pore and crack threshold segmentation. The results of coal sample slicing are presented in Figure 1, where A represents the original slice and B depicts the slice after algorithm processing. The slices in Figure 1 consist of a series of grayscale images, with dark black representing pores and cracks, light black representing coal matrix, and white indicating high-density minerals. From the CT slices, a series of large-scale, elongated dark black pores and cracks can be observed, some of which are interconnected within the coal

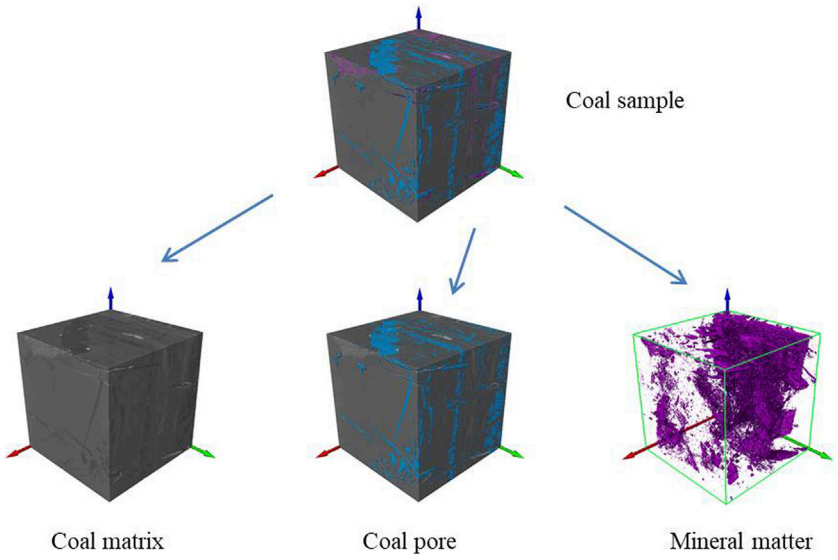

FIGURE 2
3D visualization of coal sample.

matrix. This phenomenon arises from the pyrolysis of organic matter within the coal at high temperatures, resulting in the formation of larger-scale pores and cracks. This differs from the pore and crack studies conducted by many researchers on coal samples at room temperature (Liu et al., 2017; Ju et al., 2018; Shi et al., 2018; Fan et al., 2020). In order to separately extract and three-dimensionally reconstruct pores, coal matrix, and minerals from the grayscale images, threshold segmentation processing is applied to the CT images. This study uses 16-bit images, which offer pixel grayscale values ranging from 0 to 65,535. Compared to 8-bit images, 16-bit images are more capable of capturing the finer details of pores and cracks, enhancing the precision and reliability of threshold segmentation results.

2.3.2 Three-dimensional visualization of tar-rich coal

After applying denoising to the original slices, not only can large-scale cracks be extracted but also the distribution of small pores can be captured. Consequently, based on the earlier threshold segmentation results, a three-dimensional reconstruction is performed. Many studies have presented three-dimensional visualizations of coal samples based on selected small regions for analysis (Ni et al., 2017; Fang et al., 2019). However, based on the analysis of CT data obtained from coal samples subjected to temperatures of 500°C, it has been ascertained that the distribution of pores and fractures cannot be adequately characterized within the confines of a single Region of Interest (ROI). Consequently, a supercomputing facility was harnessed to effectuate a comprehensive three-dimensional reconstruction of the entire coal specimen, thereby quantitatively delineating the post-pyrolysis state of the coal sample and the distribution profiles of various constituents. The result is shown in Figure 2.

Pores and cracks within the coal can be classified into connected pores and isolated pores. The axial algorithm functionality is employed for connectivity analysis of the threshold-segmented pores and cracks, resulting in the identification of connected and isolated pores. The outcomes of this analysis are depicted in Figure 3.

3 Results and discussions

3.1 Pore distribution at high temperatures

Many researchers have conducted in-depth studies on coal pores and cracks using CT technology (Li et al., 2017; Ju, 2021). However, much of this research has primarily focused on the natural distribution of pores and cracks within coal structures at normal temperature. There has been limited exploration of the pore structure of coal at high-temperature pyrolysis. Yet, pore structure generated during high temperature pyrolysis in coal structures plays a crucial role in determining gas molecule adsorption capacity, water and liquid storage capabilities, as well as the significance of interconnected pores in the extraction of oil and gas.

In Figure 2, the blue material represents the pores and cracks within the coal structure, while the red color signifies minerals. Due to the high content of coal matrix (which is not shown in RGB color representation), the natural color of coal is displayed in black using the CT processing software. In Figure 3, RGB colors are employed to represent connected pores and isolated pores, providing a more comprehensive visualization of the distribution of pore and crack structures after high temperatures.

From Figures 2, 3, it is evident that the pore and crack structure of coal after high temperatures pyrolysis exhibits a large-scale elongated distribution, with some areas displaying extensive interconnected patterns. Additionally, it is clear that isolated pores and cracks are not distributed in a punctate manner; instead, they still maintain a larger-scale distribution. This contrasts with findings from other studies (Li et al., 2017; Wang et al., 2019). To gain a deeper understanding of the distribution of

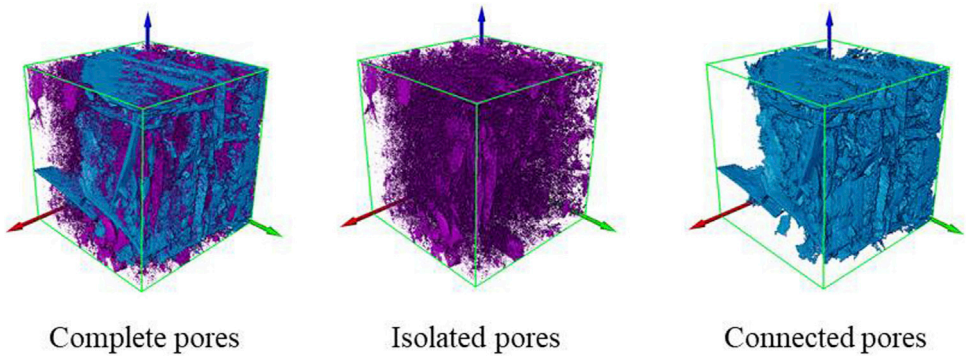

FIGURE 3
3D visualization of coal pores.

TABLE 2 Distribution of pore content in tar-rich coal.

Pore category	Volume fraction (%)	Volume of each category/μm^3	Voxels of each category
Complete pores	14.24	4.26×10^{19}	7.19×10^{8}
Connected pores	12.34	3.69×10^{19}	6.23×10^{8}
Isolated pores	1.90	5.70×10^{18}	9.62×10^{7}

pores and cracks, algorithmic statistics were performed on the volumes of connected pores and isolated pores, as summarized in Table 2.

The table clearly indicates that the porosity of coal is over 14%, with connected pores accounting for 12.3% of the total porosity, making up a significant proportion of 86.67%. This contrasts with other studies where the distribution of pores at room temperature CT coal structures mostly falls within 8% or lower. This difference highlights that the pyrolysis and volatilization of organic matter within coal at high temperatures lead to a rapid increase in coal porosity. Furthermore, it is worth noting that the distribution proportion of isolated pores is relatively low, accounting for only 1.9% of the entire coal sample. This suggests that at high temperatures pyrolysis, a portion of the organic matter in coal volatilizes and transforms into interconnected pores. Given that natural pores already exist in coal, these natural pores also gradually transform into interconnected pores at elevated temperatures.

3.2 Pore characterisation

3.2.1 REV selection

To further refine the characterization of pore structures in tar-rich coal after temperature pyrolysis, it is essential to quantitatively analyze the relevant geometric parameters of the pores, such as width, equivalent diameter, and shape factor. Therefore, the concept of the Representative Elementary Volume (REV) needs to be employed to capture the intrinsic features of the entire coal sample.

As discussed earlier, since the CT images are derived from coal samples at 500°C, the pore distribution may not necessarily follow a specific statistical probability distribution as seen in coal structures at room temperature. Through repeated attempts at pore data analysis, it is been challenging to extract a single effective REV that can represent the entire volume. In Figure 1, from various CT slices, it is evident that the pore structure of tar-rich coal does not exhibit a random distribution but rather shows aggregation and concentration patterns. On the left side of the slices, elongated and elliptical pores cluster together to form larger-scale pores; however, across different slices, there's a longitudinal anisotropy, and no consistent top-to-bottom interconnected distribution is observed. On the right side of the slices, a large-scale interconnected pore distribution can be observed, showing isotropy in the vertical direction as well as the XY plane, indicating that the pore distribution not only spans the XY plane but also extends vertically. This may be due to the pyrolysis of organic matter in this region at 500°C, resulting in a large-scale interconnected pore distribution.

Considering the pore distribution characteristics of the coal sample at high temperatures, the slice images are divided into two larger regions: the left and right sides. Region of Interest (ROI) are then selected for each region, followed by the extraction of Representative Elementary Volume (REV) to characterize these differences. For the selection of the two ROI, we chose the pore aggregation region on the left side and the interconnected pore region on the right side, each using voxel-sized cubic volumes for pore volume calculations (increasing by 10 voxels each time). Ultimately, it was found that the pore volume stabilizes when the voxel count reaches 240 voxels for the left region and 270 voxels for the right region. To facilitate comparison, representative cubic volumes of voxel-sized ROIs were chosen for both sides, labeled as REV-1 (left) and REV-2 (right). The three-dimensional representation of these results can be seen in Figure 4.

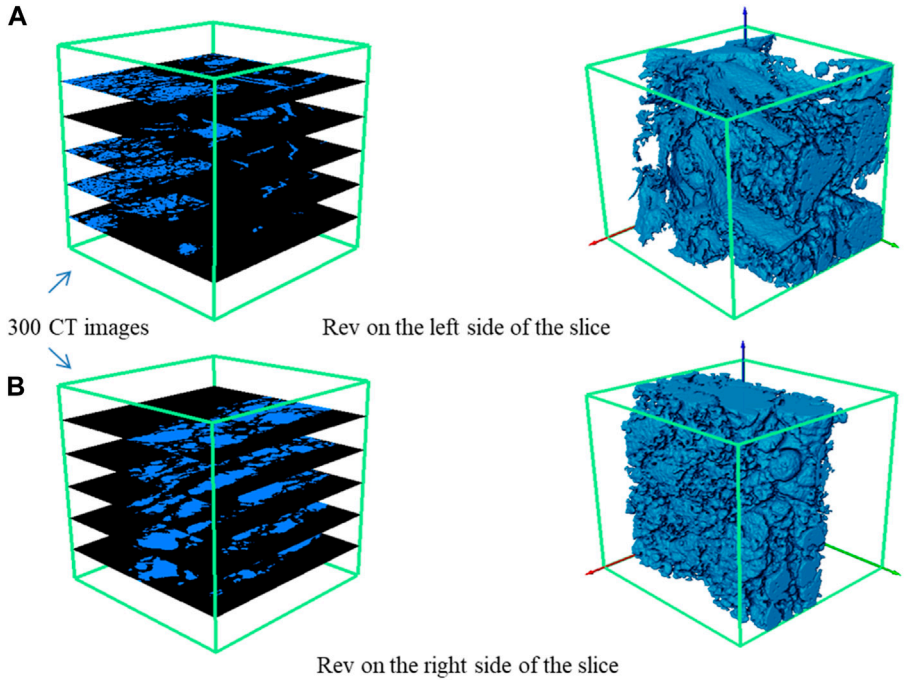

FIGURE 4
REV visualization. **(A)** Rev on the left side of the slice. **(B)** Rev on the right side of the slice.

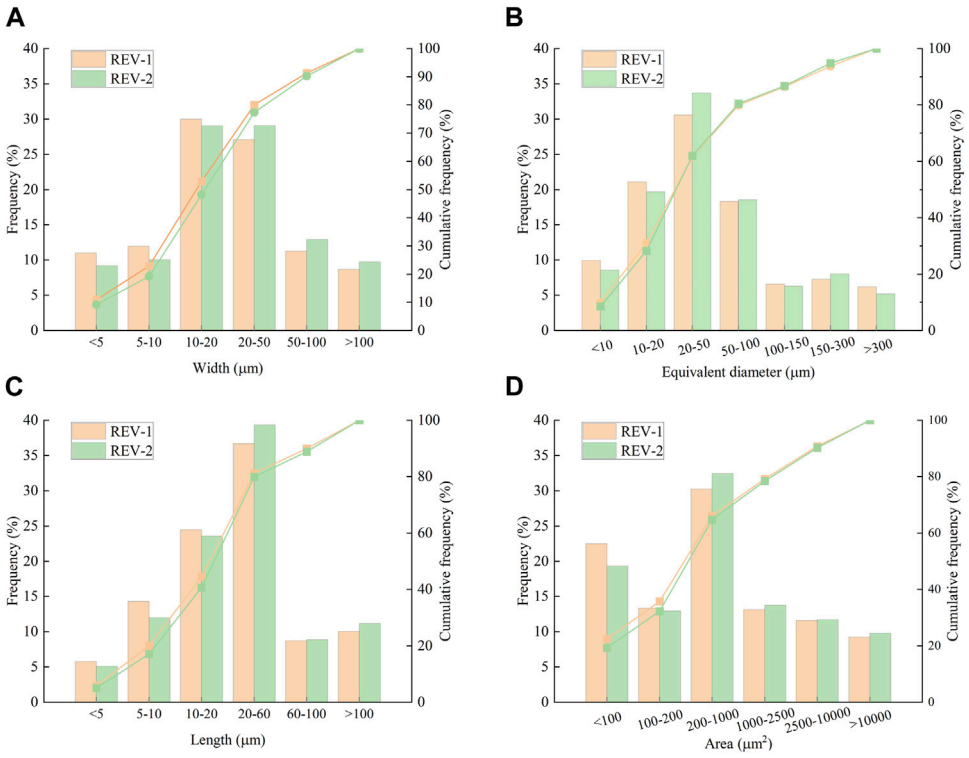

FIGURE 5
Frequency histogram of pore geometry parameters. **(A)** Frequency histogram of pore width in REV region; **(B)** Frequency histogram of pore equivalent diameter in REV region; **(C)** Frequency histogram of pore length in REV region; **(D)** Frequency histogram of pore area in REV region.

3.2.2 Geometrical characterisation of pores

Based on the previous discussions and the selection of two representative REV locations, in order to better characterize the pore characteristics of the entire coal structure after high temperatures pyrolysis, pore geometric parameters were introduced in the post-processing software of CT images. The introduced geometric parameters include pore length, width, equivalent diameter, and surface area. Pore length and equivalent diameter play a crucial role in fluid transport and permeability within the coal; pore width affects gas adsorption capacity, while different surface areas are closely related to gas storage capacity. The characterization of these parameters contributes to a deeper understanding of pore changes in tar-rich coal at high temperatures. The frequency histogram results of the geometric parameters are shown in Figure 5. The formula for the equivalent diameter is expressed as depicted in Eq. 1.

$$D_{eq} = \sqrt[3]{\frac{6 \times V}{\pi}} \tag{1}$$

Where, D_{eq} is the equivalent diameter, V is the volume of each pore, μm^3 After calculating the pore volumes for the two selected REV areas, it was found that the pore volume in REV-1 is 13%, while in REV-2 it is 22%. Surprisingly, the frequency distributions of the geometric parameters in both REV-1 and REV-2 exhibit strikingly similar patterns (as shown in Figure 5). This indicates that, despite the variations in pore distribution due to the differential thermal decomposition of different types of organic matter within the coal at high temperatures, their distributions at the scale level remain highly similar.

As observed in Figure 5, the distribution of geometric parameters for pores shows a noticeable change in scale compared to previous studies on coal pore structures at normal temperatures (Ju et al., 2018; Shi et al., 2018; Fang et al., 2019). This aligns with the conclusions drawn from the earlier discussions that the thermal decomposition of organic matter in tar-rich coal at 500°C leads to an enlargement of pores in terms of scale.

3.3 The establishment of the pore network model

3.3.1 PNM

In order to further quantitatively describe the spatial connectivity characteristics of the pore network structure, the introduction of a Pore Network Model (PNM) is utilized to analyze the flow characteristics of tar-rich coal. The PNM is a tool used to study fluid flow and transport in porous media at the microscale. This model equivalently represents the pore network in porous media as a network structure composed of interconnected pores and throats. In this representation, the connections between pores are depicted as sticks, representing the throats, while the largest sphere volume within a pore structure is represented by a sphere. The Pore Network Model allows for the quantitative characterization of structural parameters involved in the flow within interconnected pores. These parameters encompass geometric attributes of the participating pores, microscopic properties of the throats, and coordination numbers. The coordination number represents the number of throats connected to a pore node. A higher coordination number signifies more pathways for fluid flow, leading to a more complex flow path and better connectivity within the pore network. This metric serves as a powerful indicator to measure the connectivity of the pore and fracture network.

In accordance with the preceding discussions, considering the non-uniform distribution of pore structures in the coal sample at high temperature pyrolysis, we have selected the two aforementioned Regions of Interest (REV) to perform Pore Network Model (PNM) analysis. This enables us to quantitatively characterize the spatial connectivity characteristics. The resulting PNM models, as depicted in Figure 6, reveal that the REV-1 model comprises 40 pores and 57 throats, while the REV-2 model includes 59 pores and 191 throats. In the figure, the diameter of the rod-like structures represents the size of the throats, while the size of the spheres represents the volume of the pores. The variation in the throats and the sizes of the pore spheres are depicted using different RGB colors.

3.3.2 Parametric analysis of the PNM

A statistical analysis of the lengths, equivalent diameters, and coordination numbers of throats in the Pore Network Model (PNM) is presented in Figure 7. Noticeable differences in coordination numbers between the two designated REV areas within the PNM permeability models are observed (Figures 7A, D). In the REV-1 area, coordination numbers predominantly fall within the range of 1–5, with a prominent concentration at a coordination number of 3. Notably, there are no interconnected pore with coordination numbers exceeding 6. Conversely, the coordination number histogram for the REV-2 area exhibits a bimodal distribution. The first peak occurs at a coordination number of 4, with the coordination number range primarily spanning from 1 to 5. The second peak appears at a coordination number of 8, covering a broader range from 6 to 17. Moreover, the cumulative frequency of coordination numbers exceeding 6 reaches 50%. It is important to highlight that the most intense temperature range for the pyrolysis of tar-rich coal generally falls between 450°C and 500°C. Beyond this range, organic matter within the coal gradually begins to volatilize, leading to the development of coal's pore structure. The coal sample utilized in this study was subjected to a temperature of 500°C, placing the pore network structure in a transitional phase from development to more advanced stages.

Therefore, it can be reasonably inferred that the pore network structure in the REV-1 area is likely in a developmental state, resulting in lower coordination numbers and poor connectivity. On the other hand, the REV-2 area is in a phase of pore network development, with some pores still not fully matured within the region. This leads to a concentration of coordination numbers within the range of 1–5, consistent with the recently developed REV-1 region. Consequently, the bimodal structure of the coordination number histogram in the REV-2 area emerges. However, the cumulative frequency of coordination numbers exceeding 6 in the REV-2 area surpasses 50%. This observation suggests that despite the differing stages of pore structure development between the two REV regions, the REV-2 area exhibits notably improved connectivity due to a significant proportion of pores with coordination numbers exceeding 6.

However, it should be noted that an examination of Figures 7B, C, E, F reveals a relatively close distribution range for equivalent throat diameters and throat lengths, with similar shapes in the cumulative frequency curves. The primary divergence between the

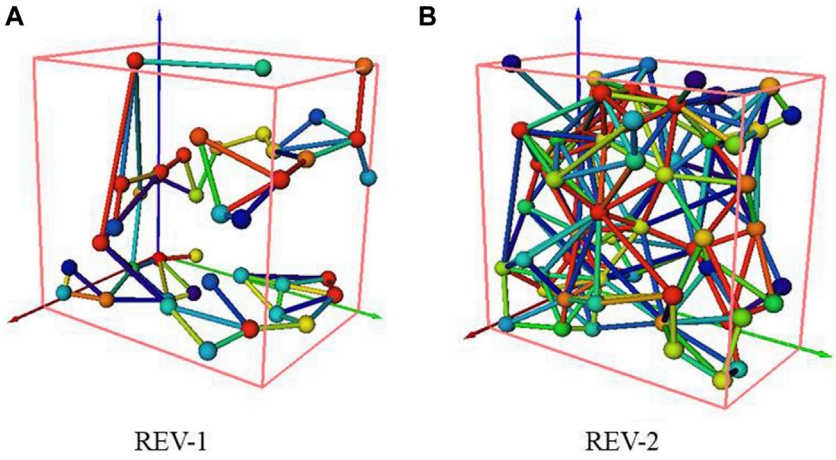

FIGURE 6
Pore network model. Note: For the comparison of REV-1 and. REV-2, a uniform range of colormap was chosen for the RGB color characterization of the throat and pore sizes in the PNM model.

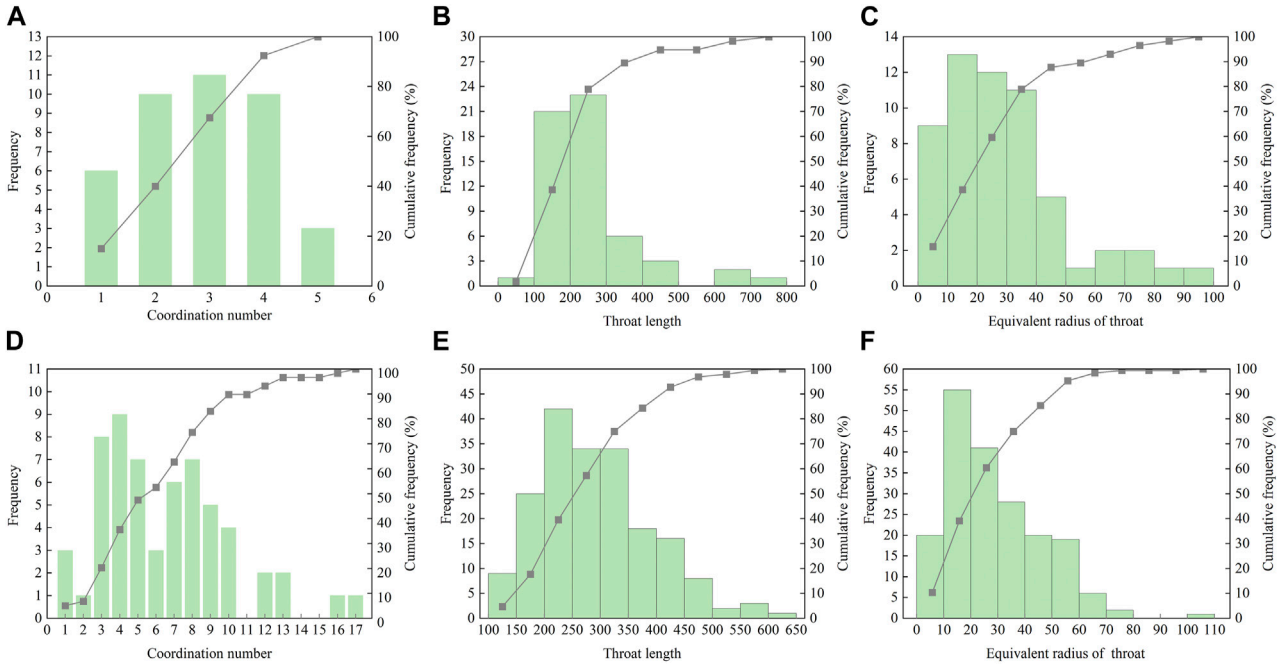

FIGURE 7
Histograms of PNM parameters. **(A–C)** for REV-1; **(D–F)** for REV-2.

two lies in the frequency of parameter occurrence and the uniformity of interval distributions, where the frequencies differ by approximately a factor of two.

4 Conclusion

In this study, X-ray computed tomography (CT) scanning was employed to examine the 500°C pyrolyzed tar-rich coal. A total of 1755 slices were obtained, with a sample dimension of. Utilizing a threshold segmentation algorithm, the two-dimensional grayscale images were processed to extract the coal matrix, mineral components, and coal pores for subsequent three-dimensional reconstruction. Geometric parameters of the pores were extracted, and an Equivalent Pore Network Model (PNM) was employed to further investigate the permeability characteristics of the tar-rich coal after high-temperature pyrolysis. Subsequently, relevant parameter analyses were performed.

(1) The samples used in this study were tar-rich coal after pyrolyzed at 500°C. Based on observations from two-dimensional CT slices, the pores of the high-temperature pyrolysis in tar-rich coal exhibit non-uniformity, a distribution skewed towards larger scales, and a pronounced connectivity concentration in spatial distribution. The pore volume fraction was determined to be 14.24%.

(2) The medial axis algorithm was employed for pore extraction, resulting in the identification and subsequent three-dimensional reconstruction of connected and isolated pores. Among these, connected pores accounted for 12.34% of the total pore volume, while mineral components comprised 1.90%. Considering the entire pore structure, connected pores contributed to 86.67% of the pore volume. Due to the non-uniform and clustered distribution of pores in the tar-rich coal after high-temperature pyrolysis, two Representative Elementary Volume (REV) units were selected: REV-1 and REV-2. Despite a significant disparity in pore volume fractions between these two REV units, their geometric parameter frequency distributions exhibited a high degree of similarity. The geometric parameters of the pores were generally larger in scale compared to those at room temperature. Most pore widths were concentrated within the range of 10–50 μm, with a peak range of pore lengths at 20–60 μm, accounting for over 40% of the distribution. Similarly, the peak range of pore surface areas was 200–1,000 μm^2, contributing to over 40% of the distribution.

(3) Based on the analysis of the equivalent pore network models for the two REV regions, the pore network structure of REV-1 was found to be in the developmental stage, with coordination numbers distributed within the range of 1–5, and no pores with coordination numbers exceeding 6, indicating poor connectivity. The pore network structure of REV-2 was in a progressively developing stage, with a bimodal distribution of coordination numbers. The first peak was in the range of 1–5, and the second peak was in the range of 5–17, with a peak coordination number of 8. Pores with coordination numbers exceeding 6 accounted for more than 50% of all pores, with nearly 10% of pores having coordination numbers exceeding 10. The frequency distribution of pore parameters (equivalent diameter and pore length) in the two REV regions exhibited relatively similar ranges, with the frequency difference approximately 2 times.

This study conducted an in-depth investigation into the pore distribution characteristics and permeability properties of tar-rich coal after high-temperature pyrolysis. This enhances our understanding of the evolution of pore structure in tar-rich coal under high-temperature pyrolysis. Furthermore, it will serve as a reference for optimizing the *in-situ* pyrolysis process of tar-rich coal to improve the efficiency of oil and gas extraction.

Data availability statement

The original contributions presented in the study are included in the article/supplementary material, further inquiries can be directed to the corresponding author.

Author contributions

FY: Conceptualization, Data curation, Funding acquisition, Supervision, Writing–original draft. PJ: Conceptualization, Methodology, Supervision, Writing–review and editing. ZD: Funding acquisition, Supervision, Writing–review and editing. ZC: Data curation, Software, Writing–original draft. ZW: Data curation, Software, Writing–original draft.

Funding

The author(s) declare financial support was received for the research, authorship, and/or publication of this article. This work was supported by the Key Scientific Research Project of Shaanxi Coal Geology (SMDZ-2020ZD-1); Shaanxi Province Young Science and Technology Nova Project (2022KJXX-24); Key R&D program of Shaanxi Province (2022GY-155); the Qinchuangyuan Scientist and Engineer Team Project of Shaanxi Province.

Conflict of interest

Authors FY, PJ, ZD and ZW were employed by the company Shaanxi Coal Geology Group Co., Ltd.

The remaining author declares that the research was conducted in the absence of any commercial or financial relationships that could be construed as a potential conflict of interest.

Publisher's note

References

Basran Parminder, S., Robertson, A., and Wells, D. (2011). CT image artifacts from brachytherapy seed implants: a postprocessing 3D adaptive median filter. *Med. Phys.* 38 (2), 712–718. doi:10.1118/1.3539648

Capuano, L. (2018). *International energy outlook 2018 (IEO2018)*. Washington, DC, USA 2018: US Energy Information Administration EIA, 21.

Cheng, Q. (2019). "Technological innovation leads energy transformation," in *China petrochemical news* (Beijing, China: Sinopec Group), 5. (in Chinese).

Fan, N., Wang, J., Deng, C., Fan, Y., Wang, T., and Guo, X. (2020). Quantitative characterization of coal microstructure and visualization seepage of macropores using CT-based 3D reconstruction. *J. Nat. Gas Sci. Eng.* 81, 103384. doi:10.1016/j.jngse.2020.103384

Fang, H.-H., Sang, S.-X., and Liu, S.-Qi (2020). Three-dimensional spatial structure of the macro-pores and flow simulation in anthracite coal based on X-ray μ-CT scanning data. *Petroleum Sci.* 17, 1221–1236. doi:10.1007/s12182-020-00485-3

Giffin, S., Littke, R., Klaver, J., and Urai, J. (2013). Application of BIB–SEM technology to characterize macropore morphology in coal. *Int. J. Coal Geol.* 114, 85–95. doi:10.1016/j.coal.2013.02.009

Golab, A., Ward, C. R., Permana, A., Lennox, P., and Botha, P. (2013). High-resolution three-dimensional imaging of coal using microfocus X-ray computed tomography, with special reference to modes of mineral occurrence. *Int. J. coal Geol.* 113, 97–108. doi:10.1016/j.coal.2012.04.011

Hodot, B. B. (1966). *Outburst of coal and coalbed gas (Chinese Translation)*. Beijing, China: China Coal Industry Press, 318.

Jiang, B., Sun, Z., and Liu, M. (2010). China's energy development strategy under the low-carbon economy. *Energy* 35 (11), 4257–4264. doi:10.1016/j.energy.2009.12.040

Jing, Yu, Armstrong, R. T., Ramandi, H. L., and Mostaghimi, P. (2017). Topological characterization of fractured coal. *J. Geophys. Res. solid earth* 122 (12), 9849–9861. doi:10.1002/2017jb014667

Ju, Y., Xi, C., Zhang, Y., Mao, L., Gao, F., and Xie, H. (2018). Laboratory *in situ* CT observation of the evolution of 3D fracture networks in coal subjected to confining pressures and axial compressive loads: a novel approach. *Rock Mech. Rock Eng.* 51, 3361–3375. doi:10.1007/s00603-018-1459-4

Ju, Y., Zhu, Y., Zhou, H., and Xie, H. (2021). Microwave pyrolysis and its applications to the *in situ* recovery and conversion of oil from tar-rich coal: an overview on fundamentals, methods, and challenges. *Energy Rep.* 7 (2021), 523–536. doi:10.1016/j.egyr.2021.01.021

Li, Q. (2021). The view of technological innovation in coal industry under the vision of carbon neutralization. *Int. J. Coal Sci. Technol.* 8 (6), 1197–1207. doi:10.1007/s40789-021-00458-w

Li, Z., Liu, D., Cai, Y., Ranjith, P., and Yao, Y. (2017). Multi-scale quantitative characterization of 3-D pore-fracture networks in bituminous and anthracite coals using FIB-SEM tomography and X-ray μ-CT. *Fuel* 209, 43–53. doi:10.1016/j.fuel.2017.07.088

Li, Z., Liu, D., Cai, Y., Yao, Y., and Wang, H. (2015). Pore structure and compressibility of coal matrix with elevated temperatures by mercury intrusion porosimetry. *Energy Explor. Exploitation* 33 (6), 809–826. doi:10.1260/0144-5987.33.6.809

Liu, S., Li, X., Wang, D., Wu, M., Yin, G., and Li, M. (2020). Mechanical and acoustic emission characteristics of coal at temperature impact. *Nat. Resour. Res.* 29, 1755–1772. doi:10.1007/s11053-019-09562-w

Liu, S., Sang, S., Wang, G., Ma, J., Wang, X., Wang, W., et al. (2017). FIB-SEM and X-ray CT characterization of interconnected pores in high-rank coal formed from regional metamorphism. *J. Petroleum Sci. Eng.* 148, 21–31. doi:10.1016/j.petrol.2016.10.006

Mastalerz, M., Drobniak, A., Strąpoć, D., Solano Acosta, W., and Rupp, J. (2008). Variations in pore characteristics in high volatile bituminous coals: implications for coal bed gas content. *Int. J. Coal Geol.* 76 (3), 205–216. doi:10.1016/j.coal.2008.07.006

Ni, X., Miao, J., Lv, R., and Lin, X. (2017). Quantitative 3D spatial characterization and flow simulation of coal macropores based on μCT technology. *Fuel* 200, 199–207. doi:10.1016/j.fuel.2017.03.068

Nie, B., Liu, X., Yang, L., Meng, J., and Li, X. (2015). Pore structure characterization of different rank coals using gas adsorption and scanning electron microscopy. *Fuel* 158, 908–917. doi:10.1016/j.fuel.2015.06.050

Okoye-Chine, George, C., Shiba, N., Rashama, C., Ugwu, S. N., Onyeaka, H., et al. (2022). Conversion of carbon dioxide into fuels—a review. *J. CO2 Util.* 62 (2022), 102099. doi:10.1016/j.jcou.2022.102099

Shi, X., Pan, J., Hou, Q., Jin, Y., Wang, Z., Niu, Q., et al. (2018). Micrometer-scale fractures in coal related to coal rank based on micro-CT scanning and fractal theory. *Fuel* 212, 162–172. doi:10.1016/j.fuel.2017.09.115

Sun, L., Zhang, C., Wang, G., Huang, Q., and Shi, Q. (2022). Research on the evolution of pore and fracture structures during spontaneous combustion of coal based on CT 3D reconstruction. *Energy* 260 (2022), 125033. doi:10.1016/j.energy.2022.125033

Wang, G., Qin, X., Han, D., and Liu, Z. (2021). Study on seepage and deformation characteristics of coal microstructure by 3D reconstruction of CT images at high temperatures. *Int. J. Min. Sci. Technol.* 31 (2), 175–185. doi:10.1016/j.ijmst.2020.11.003

Wang, G., Shen, J., Liu, S., Jiang, C., and Qin, X., Three-dimensional modeling and analysis of macro-pore structure of coal using combined X-ray CT imaging and fractal theory. *Int. J. Rock Mech. Min. Sci.*, 2019, 123: 104082, doi:10.1016/j.ijrmms.2019.104082

Wolde-Rufael, and Yemane, (2010). Coal consumption and economic growth revisited. *Appl. Energy* 87 (1), 160–167. doi:10.1016/j.apenergy.2009.05.001

Xin, F., Xu, H., Tang, D., Yang, J., Chen, Y., Cao, L., et al. (2019). Pore structure evolution of low-rank coal in China. *Int. J. Coal Geol.* 205, 126–139. doi:10.1016/j.coal.2019.02.013

Yao, Y., Liu, D., Tang, D., Tang, S., and Huang, W. (2008). Fractal characterization of adsorption-pores of coals from North China: an investigation on CH4 adsorption capacity of coals. *Int. J. Coal Geol.* 73 (1), 27–42. doi:10.1016/j.coal.2007.07.003

Zhang, Y., Wang, Y., Cai, L., Yao, C., Gao, S., Li, C. Z., et al. (2013). Dual bed pyrolysis gasification of coal: process analysis and pilot test. *Fuel* 112, 624–634. doi:10.1016/j.fuel.2012.01.038

Zhao, Y., Sun, Y., Liu, S., Wang, K., and Jiang, Y. (2017). Pore structure characterization of coal by NMR cryoporometry. *Fuel* 190, 359–369. doi:10.1016/j.fuel.2016.10.121

Frontiers in Earth Science

Investigates the processes operating within the major spheres of our planet

Advances our understanding across the earth sciences, providing a theoretical background for better use of our planet's resources and equipping us to face major environmental challenges.

Discover the latest Research Topics

See more →

Frontiers

Avenue du Tribunal-Fédéral 34
1005 Lausanne, Switzerland
frontiersin.org

Contact us

+41 (0)21 510 17 00
frontiersin.org/about/contact